

Washington University in St. Louis

Washington University Open Scholarship

All Theses and Dissertations (ETDs)

5-24-2011

Simulation Of The Undiseased Human Cardiac Ventricular Action Potential: Model Formulation, Experimental Validation And Application

Thomas O'Hara
Washington University in St. Louis

Follow this and additional works at: <https://openscholarship.wustl.edu/etd>

Recommended Citation

O'Hara, Thomas, "Simulation Of The Undiseased Human Cardiac Ventricular Action Potential: Model Formulation, Experimental Validation And Application" (2011). *All Theses and Dissertations (ETDs)*. 873. <https://openscholarship.wustl.edu/etd/873>

This Dissertation is brought to you for free and open access by Washington University Open Scholarship. It has been accepted for inclusion in All Theses and Dissertations (ETDs) by an authorized administrator of Washington University Open Scholarship. For more information, please contact digital@wumail.wustl.edu.

WASHINGTON UNIVERSITY IN ST. LOUIS
School of Engineering and Applied Sciences
Department of Biomedical Engineering

Dissertation Examination Committee:

Yoram Rudy, Chair

Jianmin Cui

Igor Efimov

Colin Nichols

Dan Ory

Rick Schuessler

Simulation of the Undiseased Human Cardiac Ventricular Action Potential: Model Formulation,
Experimental Validation and Application

by

Thomas James O'Hara IV

A dissertation presented to the
Graduate School of Engineering
of Washington University in
partial fulfillment of the
requirements for the degree
of Doctor of Philosophy

August 2011

Saint Louis, Missouri

Abstract

Creation of an accurate model for the undiseased human ventricular action potential (AP) which reproduces a broad range of physiological behaviors requires extensive experimental data, of which essential elements have been unavailable. We developed and validated such a model using new experimental data from endocardium of 140 undiseased human hearts. 78 were from male (56%). Average age was 41 with standard deviation of 12 years. New experiments include: Ca^{2+} versus voltage dependent inactivation of L-type Ca^{2+} current; kinetics for the transient outward, rapid delayed rectifier, $\text{Na}^+/\text{Ca}^{2+}$ exchange, and inward rectifier currents; AP recordings at all physiological cycle lengths; steady state rate dependence and restitution of AP duration. The model was used to investigate the “silent” Long-QT mutation Q357R in KCNQ1.

Acknowledgements

This work was supported by NIH/National Heart, Lung, and Blood Institute grants R01-HL049054-18 and R01-HLR01033343-26, Fondation Leducq Award to the Alliance for CaMK Signaling in Heart Disease, and National Science Foundation grant CBET-0929633 (all to Yoram Rudy); American Heart Association Predoctoral Fellowship 0815539G (to Thomas O'Hara). Yoram Rudy is the Fred Saigh Distinguished Professor at Washington University.

Discussions and feedback from Yoram Rudy and my colleagues in the Rudy lab have been invaluable. Thanks to Yoram and current Rudy lab members Leonid Livshitz, Ashwin Mohan, Ali Nekouzadeh, Pan Li, Namit Gaur, Jordi Heijman, JiaJing Xu, and Smiruthi Ramasubramanian. Thanks to former Rudy lab members Tom Hund, Greg Faber, Jon Silva, Keith Decker, Yong Wang, Subham Ghosh, and Lina El-Esber. Thanks to Maya Bera, Kim Smith, Li Li, Jennifer Godwin-Wyer, Debra Adams, Ellen Harken and Marlene Siegal. Thanks to Glen Reitz, Amanda Carr, Karen Teasdale and Frank Yin.

Thanks to the following, who generously shared valuable experimental data, facilities, equipment and tissue: András Varró and colleagues László Virág and Norbert Jost of the University of Szeged in Hungary; David Van Wagoner and colleagues Rashmi Ram and Laurie Castel of the Cleveland Clinic; Igor Efimov and Jianmin Cui of Washington University.

Thanks to Paul Volders of the University of Maastricht, and to Gail Robertson of the University of Wisconsin, Madison, who provided opportunities for me to contribute to their publications.

This work is dedicated to Lúnia Dadarlat.

Table of Contents

Abstract	ii
Acknowledgements	iii
Table of Contents	iv
List of Figures	x
Abbreviations	xiii
Currents ($\mu\text{A}/\mu\text{F}$)	xv
Time Dependent Gates	xv
Fluxes (milliMol/Liter/ms)	xvi
Calcium Buffers	xvii
Chapter 1: Background and Introduction	1
Species Differences	2
<i>Species Dependence of AP Changes Due to Block of Delayed Rectifier K^+ Currents</i>	3
<i>APD Rate Dependence</i>	4
<i>Role of $[\text{Na}^+]$ Accumulation in AP Rate Dependence</i>	4
The Case for a New Human Specific Model	5
Unique Access to Undiseased Human Ventricular Measurements	6
Thesis Objectives	6
Designation of Contribution	7
Chapter 2: Simulation of the Undiseased Human Cardiac Ventricular Action Potential: Model Formulation and Experimental Validation	10
Introduction	10
Results	11

Results Subsection 1: Formulation, Validation and Properties of Simulated Currents.....	11
<i>L</i> -type Ca^{2+} Current (I_{CaL})	11
Transient Outward K^+ Current (I_{to})	13
$\text{Na}^+/\text{Ca}^{2+}$ Exchange Current (I_{NaCa})	15
Inward Rectifier K^+ Current (I_{K1})	16
Rapid Delayed Rectifier K^+ Current (I_{Kr}).....	17
Slow Delayed Rectifier K^+ Current (I_{Ks}).....	18
Fast Na^+ Current	18
Late Na^+ Current	19
Na^+/K^+ Pump Current (I_{NaK}).....	20
Results Subsection 2: Human AP Characteristics and APD	21
Transmural Heterogeneity.....	23
Early Afterdepolarization (EAD)	24
Na^+ and Ca^{2+} Rate Dependence.....	25
Ca^{2+} Cycling and CaMK.....	26
Alternans.....	26
Currents Participating in Steady State APD Rate Dependence and APD Restitution.....	27
Ionic Basis for APD Rate Dependence and Restitution.....	29
Results Subsection 3: Comparison with Other Human Ventricular AP Models.....	31
Discussion.....	32
EADs and Repolarization Rate	33
Steady State APD Rate Dependence.....	34
APD Restitution.....	36
Ca^{2+} Cycling, CaMK and Alternans.....	37
Transmural Heterogeneity.....	38
APD Accommodation.....	39
Parameter Sensitivity.....	39

<i>Computational Tractability and Model Stability</i>	40
<i>Limitations</i>	41
Materials and Methods.....	43
<i>Characteristics of Human Tissue</i>	43
<i>Tissue Preparation</i>	43
<i>Myocyte Isolation</i>	44
<i>Electrophysiology</i>	44
<i>Ca²⁺ Transient Florescence</i>	45
<i>Pacing Protocols</i>	45
<i>Population Based CaMK effects</i>	46
<i>Relative Weights in a Two Time Constant Scheme</i>	46
<i>Transmural Wedge Simulation</i>	46
<i>Equations, Computers, and Software</i>	47
Figures.....	48
Chapter 2 Supplementary Material.....	74
ORd Human Model Basic Parameters.....	74
<i>Stimulus</i>	74
<i>External Concentrations</i>	74
<i>ORd Model Initial Conditions</i>	74
<i>Reversal Potentials</i>	76
<i>Cell Geometry</i>	76
ORd Human Model Currents.....	76
<i>Sodium Current (I_{Na})</i>	77
<i>Transient Outward Potassium Current (I_{to})</i>	79
<i>L-type Calcium Current (I_{CaL})</i>	80
<i>Rapid Delayed Rectifier Potassium Current (I_{Kr})</i>	83
<i>Slow Delayed Rectifier Potassium Current (I_{Ks})</i>	84

<i>Inward Rectifier Potassium Current (I_{K1})</i>	85
<i>Sodium-Calcium Exchange Current (I_{NaCa})</i>	85
<i>Sodium-Potassium Pump Current (I_{NaK})</i>	87
<i>Background Currents (I_{Nab}, I_{Cab}, I_{Kb}) and Sarcolemmal Calcium Pump Current (I_{pCa})</i>	89
<i>Voltage</i>	90
<i>Calcium/Calmodulin-Dependent Protein Kinase (CaMK)</i>	90
ORd Human Model Fluxes.....	91
<i>Diffusion Fluxes ($J_{diff,Na}$, $J_{diff,Ca}$, $J_{diff,K}$)</i>	91
<i>SR Calcium Release Flux, via Ryanodine Receptor (J_{rel})</i>	91
<i>Calcium Uptake via SERCA Pump (J_{up})</i>	92
<i>Calcium Translocation from NSR to JSR (J_{tr})</i>	93
ORd Human Model Concentrations and Buffers.....	93
ORd Human Model Transmural Heterogeneity.....	95
Computational Methodology.....	95
<i>Hardware and Software</i>	95
<i>Rapid Integration</i>	96
Chapter 2 Supplementary Figures.....	98
<i>Additional Details for Currents</i>	98
<i>APD Rate Dependence in Homogeneous Multicellular Fiber</i>	106
<i>Transmural AP Simulations Compared with Nonfailing Human Optical Mapping Experiments</i>	107
<i>Alternans Simulation in Coupled Tissue</i>	108
<i>Alternans were Eliminated by SERCA2a Upregulation</i>	109
<i>Effects of H^+, CO_2 and HCO_3^- on Na^+ Handling, I_{NaK} and APD Rate Dependence</i>	110
<i>Effect of KCNE1 Heterogeneity on Transmural I_{Ks} and AP Simulations</i>	112
<i>APD Accommodation</i>	114
<i>Parameter Sensitivity Analysis</i>	115

Chapter 3: Multiple Hits Evince Arrhythmic Phenotype in Subclinical Long QT Syndrome:	
Simulation Studies of the Silent KCNQ1 Mutation Q357R	120
Introduction	120
Methods.....	121
<i>Markov I_{Ks} and Human Ventricular Myocyte Models.....</i>	121
<i>β-Adrenergic Stimulation by Isoproterenol (ISO)</i>	121
Results	122
<i>Silent Mutant Q357R Kinetics and Behavior.....</i>	122
<i>Heterotetramer Assembly and Function</i>	123
<i>Validation of WT, Q357R, and het models.....</i>	123
<i>β-Adrenergic Stimulation.....</i>	124
<i>Phenotype is Silent under Basal Conditions.....</i>	125
<i>Multiple Hits Cause AP Prolongation and Early Afterdepolarizations (EADs).....</i>	125
<i>Silent Mutant I_{Ks} Gating Kinetics in Presence of Multiple Hits</i>	126
<i>Mechanisms</i>	127
<i>Heterogeneous Transmural Wedge.....</i>	128
<i>Onset of Emotional/Physical Stress or Exercise.....</i>	129
Discussion.....	129
<i>Clinical Attributes Determine Protocols.....</i>	130
<i>Dominant Negative Loss of Available Reserve.....</i>	130
<i>Cell Type and Pacing Rate</i>	131
<i>Limitations</i>	132
Figures	133
Chapter 3 Supplementary Material	142
Markov I_{Ks} Models	142
Simulations Using the O'Hara-Rudy dynamic (ORd) Human Ventricular Model.....	142

Equations for PKA Phosphorylation.....	143
<i>L-type Ca²⁺ Current: I_{CaL}</i>	143
<i>Slow Delayed Rectifier K⁺ Current: I_{Ks}</i>	144
<i>Background K⁺ Current: I_{Kb}</i>	144
<i>Fast Na⁺ Current: I_{Na}</i>	144
<i>SR Ca²⁺ Release Flux, via Ryanodine Receptor: J_{rel}</i>	144
<i>Calcium Uptake via SERCa Pump: J_{up}</i>	144
<i>Troponin</i>	145
<i>Na⁺/K⁺ ATPase Current: I_{NaK}</i>	145
Chapter 3 Supplementary Figures.....	146
Chapter 4: Insights and Conclusions.....	149
APD with Dynamic Pacing in Human.....	149
Role of I_{Ks} in Human.....	151
Transmural Heterogeneity.....	151
Species Differences and the Need for an Accurate Human Specific Model.....	152
<i>Species Differences in the Role of Delayed Rectifier K⁺ Currents</i>	153
<i>Species Differences in APD Steady State Rate Dependence</i>	154
References.....	155

List of Figures

1.01 Species dependence of delayed rectifier K^+ current block	8
1.02 Simulation of interspecies comparison of steady state APD rate dependence	9
2.01 Undiseased human I_{CaL} experiments and model validation	49
2.02 Undiseased human I_{to} , I_{NaCa} , and I_{K1} experiments and model validation	51
2.03 Undiseased human I_{Kr} and I_{Ks} experiments and model validation	52
2.04 Nonfailing human fast I_{Na} and late I_{Na} experiments and model validation	54
2.05 Schematic diagram of human ventricular myocyte model	55
2.06 Undiseased human endocardial AP traces from experiments (small tissue preparations) and model simulations	57
2.07 Undiseased human endocardial AP response to pacing protocols from experiments (small tissue preparations) and model simulations.....	58
2.08 Pacing protocols with block of various currents.....	59
2.09 Rate dependence of currents at steady state	60
2.10 Transmural heterogeneity and validation of transmural cell type models.....	61
2.11 Early afterdepolarizations (EADs).....	63
2.12 Rate dependence of intracellular ion concentrations.....	64
2.13 CaMK and Ca^{2+} cycling.....	65
2.14 AP and Ca^{2+} alternans at fast pacing.....	66
2.15 I-V curves during steady state rate dependent pacing at various CLs and S1S2 restitution at various DIs	68
2.16 Major causes of steady state APD rate dependence and S1S2 APD restitution	69
2.17 I_{Kr} deactivation is important for APD restitution at very short DIs	71
2.18 Comparison with other human ventricular AP models.....	73
2.S01 Human I_{NaCa} model faithfully reproduces Kang and Hilgemann observations.....	99
2.S02 Human I_{NaCa} model faithfully reproduces observations of Weber et al.....	100
2.S03 Human I_{NaCa} model faithfully reproduces Weber et al. intracellular Na^+ dependence under AP and Ca^{2+} clamp conditions	101

2.S04 I_{K1} shows voltage dependence, but not rate dependence	102
2.S05 I_{Kr} shows voltage dependence, but not rate dependence	103
2.S06 Schematic diagram of the human I_{NaK} model, modified from Smith and Crampin	104
2.S07 Human I_{NaK} model faithfully reproduces major observations of Nakao and Gadsby	105
2.S08 APD rate dependence in homogeneous multicellular fiber	106
2.S09 Transmural AP simulations compared with nonfailing human optical mapping experiments	107
2.S10 Alternans simulation in coupled tissue	108
2.S11 Alternans were eliminated by upregulation of SERCA2a	109
2.S12 Effects of H^+ , CO_2 and HCO_3^- on Na^+ handling, I_{NaK} and APD rate dependence	111
2.S13 Effect of KCNE1 Heterogeneity on Transmural I_{Ks} and AP Simulations	113
2.S14 APD accommodation	114
2.S15 Parameter sensitivity of steady state APD rate dependence	115
2.S16 Parameter sensitivity of S1S2 restitution of APD	116
2.S17 Parameter sensitivity of rate dependence of peak $[Ca^{2+}]_i$	117
2.S18 Parameter sensitivity of rate dependence of intracellular $[Na^+]_i$	118
2.S19 Parameter sensitivity of steady state rate dependence of APD in the different transmural cell types	119
3.01 Markov models for I_{Ks}	133
3.02 Validation for WT, Q357R, and het I_{Ks}	134
3.03 Validation of the effects of ISO on target channels and processes in human	135
3.04 Transmural cell type dependence of the Q357R mutation at normal pacing rate	137
3.05 Effect of pacing, ISO and partial I_{Kr} block on the AP in epi cells	138
3.06 Mechanism by which layered hits reveal pathology	139
3.07 Effects of ISO and I_{Kr} reduction on the transmural wedge pseudo-ECG	140
3.08 Emotional/physical stress or exercise onset	141
3.S01 M-cell dependence of the Q357R mutation at fast pacing rate	146
3.S02 Effect of reduced conductance versus kinetics changes in the silent mutation	147

3.S03 In guinea pig simulations(Faber, Silva et al. 2007), Q357R mutation is not silent..... 148

Abbreviations

ORd model	O'Hara-Rudy dynamic human ventricular cell model
TP model	ten-Tusscher-Panfilov(Ten Tusscher and Panfilov 2006) human ventricular cell model
GB model	Grandi-Bers(Grandi, Pasqualini et al. 2010) human ventricular cell model
AP	action potential
APD	action potential duration (ms)
APDX	action potential duration to X% of resting membrane potential (ms)
CL	pacing cycle length (ms)
DI	diastolic interval, relative to APD90 (ms)
I-V Curve	current voltage relationship
CDI	Ca ²⁺ dependent inactivation of L-type Ca ²⁺ current
VDI	voltage dependent inactivation of L-type Ca ²⁺ current
RyR	ryanodine receptor
V, or V _m	membrane voltage (mV)
R	gas constant, 8314 J/kmol/K
T	temperature (310° K)
F	Faraday constant, 96485 coul/mol
C _M	total membrane capacitance, 1 μF
E _S	reversal potential for ion S (mV)
R _{CG}	ratio between capacitive and geometric membrane areas (= 2)
A _{geo}	geometric area (cm ²)
A _{cap}	capacitive area (cm ²)
v _S	volume of compartment S (μL)
s _∞	steady state value of gate S
τ _S	time constant of gate S (ms)
τ _{S,fast} , τ _{S,slow}	fast/slow time constant of gate S (ms)

$A_{s,fast}, A_{s,slow}$	fraction of channels with gate S undergoing fast/slow process
z_s	valence of ion S
I_{stim}	stimulus current ($\mu A/\mu F$)
I_s	current through ion channel S ($\mu A/\mu F$)
\overline{G}_s	maximum conductance of ion channel S ($mS/\mu F$)
$K_{m,S}$	half-saturation concentration of molecule S (mM)
\overline{I}_s	maximum current carried through ion channel S ($\mu A/\mu F$)
P_s	permeability to ion S (cm/s)
$PR_{Q,S}$	permeability ratio of ion Q to ion S
γ_s	activity coefficient of ion S
J_s	ion flux S (mM/ms)
$[S]_Q$	concentration of ion S, in sub-cellular compartment Q (mM)
$\overline{[S]}$	maximum concentration of buffer S (mM)
myo	myoplasmic compartment (also abbreviated by small letter “i”)
ss	subspace compartment (representing submembrane space near t-tubules)
SR	sarcoplasmic reticulum
jsr	junctional SR compartment
nsr	network SR compartment
Y	compartment Y (e.g. “i”, “ss”), as in I_{NaCa} equations
CaMK	Ca^{2+} /calmodulin-dependent protein kinase II
$CaMK_{bound}$	fraction of CaMK binding sites bound to Ca^{2+} /calmodulin
$CaMK_{trap}$	fraction of autonomous CaMK binding sites with trapped calmodulin
$CaMK_{active}$	fraction of active CaMK binding sites
$CaMK_o$	fraction of active CaMK binding sites at equilibrium
$\alpha_{CaMK}, \beta_{CaMK}$	(de)phosphorylation rates of CaMK (ms^{-1})
PLB	phospholamban
$\emptyset_{S,CaMK}$	fraction of channels of type S phosphorylated by CaMK

Currents ($\mu\text{A}/\mu\text{F}$)

I_{Na}	Na^+ current
I_{to}	transient outward K^+ current
I_{CaL}	Ca^{2+} current through the L-type Ca^{2+} channel
I_{CaNa}	Na^+ current through the L-type Ca^{2+} channel
I_{CaK}	K^+ current through the L-type Ca^{2+} channel
I_{Kr}	rapid component of the delayed rectifier K^+ current
I_{Ks}	slow component of the delayed rectifier K^+ current
I_{K1}	inward rectifier K^+ current
$I_{\text{NaCa,i}}$	myoplasmic component of Na^+ - Ca^{2+} exchange current
$I_{\text{NaCa,ss}}$	subspace component of Na^+ - Ca^{2+} exchange current
I_{NaCa}	total Na^+ - Ca^{2+} exchange current
I_{NaK}	Na^+ - K^+ pump current
I_{Nab}	Na^+ background current
I_{Cab}	Ca^{2+} background current
I_{Kb}	K^+ background current
I_{pCa}	sarcolemmal Ca^{2+} pump current

Time Dependent Gates

m	activation for fast I_{Na}
h_{fast}	fast development of inactivation for fast I_{Na}
h_{slow}	slow development of inactivation for fast I_{Na}
j	recovery from inactivation for fast I_{Na}
$h_{\text{CaMK,fast}}$	fast development of inactivation for CaMK phosphorylated fast I_{Na}
$h_{\text{CaMK,slow}}$	slow development of inactivation for CaMK phosphorylated fast I_{Na}
j_{CaMK}	recovery from inactivation for CaMK phosphorylated fast I_{Na}

m_L	activation for late I_{Na}
h_L	inactivation for late I_{Na}
$h_{L,CaMK}$	inactivation for CaMK phosphorylated late I_{Na}
a	activation for I_{to}
i_{fast}	fast inactivation for I_{to}
i_{slow}	slow inactivation for I_{to}
a_{CaMK}	activation for CaMK phosphorylated I_{to}
$i_{CaMK,fast}$	fast inactivation for CaMK phosphorylated I_{to}
$i_{CaMK,slow}$	slow inactivation for CaMK phosphorylated I_{to}
d	activation for I_{CaL}
f_{fast}	fast voltage dependent inactivation for I_{CaL}
f_{slow}	slow voltage dependent inactivation for I_{CaL}
$f_{Ca,fast}$	fast development of Ca^{2+} dependent inactivation for I_{CaL}
$f_{Ca,slow}$	slow development of Ca^{2+} dependent inactivation for I_{CaL}
j_{Ca}	recovery from Ca^{2+} dependent inactivation for I_{CaL}
n	fraction in Ca^{2+} dependent inactivation mode for I_{CaL}
$f_{CaMK,fast}$	fast development of Ca^{2+} dependent inactivation for CaMK phosphorylated I_{CaL}
$f_{Ca,CaMK,fast}$	slow development of Ca^{2+} dependent inactivation for CaMK phosphorylated I_{CaL}
$x_{r,fast}$	fast activation for I_{Kr}
$x_{r,slow}$	slow activation for I_{Kr}
x_{s1}	activation for I_{Ks}
x_{s2}	deactivation for I_{Ks}
x_{K1}	inactivation for I_{K1}

Fluxes (milliMol/Liter/ms)

$J_{diff,Na}$	diffusion of Na^+ from subspace to myoplasm
$J_{diff,K}$	diffusion of K^+ from subspace to myoplasm
$J_{diff,Ca}$	diffusion of Ca^{2+} from subspace to myoplasm

$J_{rel,NP}$	non-phosphorylated Ca^{2+} release, via ryanodine receptors, from jsr to myoplasm
$J_{rel,CaMK}$	CaMK phosphorylated Ca^{2+} release, via ryanodine receptors, from jsr to myoplasm
J_{rel}	total Ca^{2+} release, via ryanodine receptors, from jsr to myoplasm
$J_{up,NP}$	non-phosphorylated Ca^{2+} uptake, via SERCA pump, from myoplasm to nsr
$J_{up,CaMK}$	CaMK phosphorylated Ca^{2+} uptake, via SERCA pump, from myoplasm to nsr
J_{up}	total Ca^{2+} uptake, via SERCA pump, from myoplasm to nsr
J_{leak}	Ca^{2+} leakage from nsr to myoplasm
J_{tr}	Ca^{2+} translocation from nsr to jsr

Calcium Buffers

CMDN	calmodulin, Ca^{2+} buffer in myoplasm
TRPN	troponin, Ca^{2+} buffer in myoplasm
BSR	anionic SR binding sites for Ca^{2+} in subspace
BSL	anionic sarcolemmal binding sites for Ca^{2+} buffer in subspace
CSQN	calsequestrin, Ca^{2+} buffer in JSR
β_Y	buffer factor for compartment Y

Chapter 1: Background and Introduction

Since 1921, cardiovascular disease (CVD) has been the leading cause of death in the United States(Keenan and Shaw 2011). In recent years, it was the cause of one third of all U.S. deaths(Roger, Go et al. 2011). The most common deadly form of CVD is sudden cardiac death, SCD(Zheng, Croft et al. 2001). Typically, ventricular arrhythmia is the first clinical symptom of SCD. With sudden appearance and high lethality, preventative measures are the most effective treatment for SCD. However, prevention requires hard-won mechanistic understanding of the underlying principles of arrhythmia formation. Basic investigations into human cardiac electrophysiology can fill gaps in our understanding of such mechanisms. This is the key to prevention(Myerburg 2002).

In recent decades, computers have revolutionized medicine and basic scientific research of all kinds. In biology, and electrophysiology in particular, computers have allowed scientists to assemble mathematical descriptions of discrete and relatively simple processes into larger, much more complex interacting systems. A famous early example of these methods(Hodgkin and Huxley 1952) revealed remarkable new insights into the basic functioning of the neuronal action potential (AP); insights that could not have been discovered by experimental methods alone. Hodgkin and Huxley manually cranked a Brunsviga mechanical calculator for months(Noble 2007) in order to solve the coupled differential equations comprising their axon model. Their effort was motivated by an understanding that mathematical models are extraordinarily powerful tools. The squid giant axon model won them the 1963 Nobel Prize in Physiology or Medicine, and was the dawn of “systems biology”, where integration methods replace reductionist methods (i.e. investigating the whole based on its parts rather than the parts abstracted from the whole). To study mechanisms, and test hypotheses to explain emergent phenomena, integrative methods are crucial.

Regarding SCD, where mechanistic understanding is essential for prevention, computer modeling and systems approaches have been widely employed(Winslow, Cortassa et al. 2010).

For the clinically relevant case of undiseased or nonfailing human electrocardiology, due to limited access to tissue and myocytes, these methods are especially useful (Rudy, Ackerman et al. 2008). With this as motivation, we worked to create a computer model that is faithful to the detailed processes underlying the ventricular AP in human. The model was constructed as none before; it was based exclusively on undiseased and nonfailing human ventricular whole cell measurements. We assumed as little similarity to other mammalian species as possible and reformulated all major processes responsible for the generation of the AP, making the model human ventricle specific. The human ventricle specific model revealed explanations for basic mechanisms particular to human rhythmic and arrhythmic behavior. It was with an interest in understanding, predicting, and preventing the development of SCD arrhythmia in the human heart, that this project was designed.

Species Differences

Studies of basic cardiac electrophysiology, arrhythmia and SCD are usually performed with experiments in non-human hearts (dog or small rodents) or isolated cells. However, ion channel currents which determine the ventricular AP are species dependent (Zicha, Moss et al. 2003; Akar, Wu et al. 2004; Blechschmidt, Haufe et al. 2008). Moreover, so too are arrhythmia mechanisms (e.g. (Wang, Pelletier et al. 1990)). The fact that species differences exist seems trivial. However, the consequences of these differences with respect to arrhythmia mechanisms are not trivial, and because of the complex interrelatedness of bio-electrical processes (Rudy and Silva 2006), it is impossible to predict how findings from dog, or guinea pig should apply to human. Broadly, it is important to ask: how does ion channel function differ across species, and how do these differences affect the AP in response to dynamic pacing and/or drugs? Species-specific mathematical models, based on extensive and quantitative validation, can provide a platform from which to investigate these questions.

It is instructive to compare human cellular electrophysiology mechanisms and AP properties with other species. A species comparison was conducted using previously developed

and validated mathematical models for dog(Decker, Heijman et al. 2009) and guinea pig(Faber, Silva et al. 2007) ventricular myocytes. For the human case, we used the new human model, described in detail and extensively validated in Chapter 2 (all epicardial cell types). Response to delayed rectifier current block and underlying mechanisms of AP duration (APD) rate dependent adaptation were species dependent. The differences between species highlighted the fact that great caution should be used when extrapolating results from non-human experiments to human cellular electrophysiology, arrhythmic behaviors, response to drugs and strategies for SCD prevention. These issues emphasize the importance of an accurate human model.

Species Dependence of AP Changes Due to Block of Delayed Rectifier K⁺ Currents

Species dependence of pharmacological responses was illustrated using delayed rectifier K⁺ current block (rapid and slow, I_{Kr} and I_{Ks}, respectively). This simulates effects of certain mutations in the arrhythmic long QT syndrome. The hERG protein, forming I_{Kr} α -subunits, has extraordinary affinity for many channel blocking drugs(Sanguinetti and Tristani-Firouzi 2006). Recent FDA rejected examples include clinically useful non-cardiac drugs such as anti-histamines (e.g. terfenadine, fexofenadine), antipsychotics (e.g. risperidone, sertindole), antibiotics (e.g. erythromycin) and prokinetics (e.g. cisapride)(Brown 2004). Drug-induced I_{Kr} block or mutations associated with I_{Kr} reduction cause QT prolongation (long QT syndrome, acquired or inherited), leading to torsade de pointes arrhythmias(Roden 2004). I_{Ks} reduction mutations have similar consequences (Schwartz, Priori et al. 2001). There is an interplay between these currents: I_{Kr} loss indirectly affects I_{Ks} (via V_m), while I_{Ks} can prevent excessive AP prolongation(Jost, Virag et al. 2005) in the face of reduced I_{Kr} (e.g.(Rodén and Yang 2005), and simulations in Chapter 3). For these reasons, it is important to know how I_{Kr} and I_{Ks} block affect human AP in particular, and how the effects differ from those in experimental animals.

Figure1.01 shows simulations and corresponding experiments(Jost, Virag et al. 2004) for the species dependence of delayed rectifier K⁺ current block. For I_{Kr} block (panel A), simulated APD was substantially prolonged in human (80%, 172 ms prolongation). Block consequence was

comparatively small for dog (30%, 65 ms APD prolongation) and guinea pig (20%, 35 ms APD prolongation). In panel B, I_{Ks} block (90% block) was essentially of no consequence for both human (4%, 10 ms APD prolongation) and dog (2%, 3 ms APD prolongation). By contrast, it substantially prolonged APD in guinea pig (26%, 43 ms APD prolongation, using only 50% block). Simulation results agree with experiments (Jost, Virag et al. 2004), shown at the top of each panel.

APD Rate Dependence

APD was longest for human. As shown in Figure 1.02A, at cycle length (CL) = 1000 ms, APD was 226 ms for human, 191 ms for dog, and 166 ms for guinea pig. Human AP repolarization rate was the most gradual. At CL = 1000 ms, the time difference between APD at 30% and APD at 90% completion (APD90 – APD30) was 49 ms for human, 43 ms for dog, and 24 ms for guinea pig. The range of APD90 over CLs from 300 to 2000 ms was 54 ms for human, 45 ms for dog, and 60 ms for guinea pig.

Role of $[Na^+]$ Accumulation in AP Rate Dependence

We clamped Na^+ concentrations in myoplasmic and subspace compartments of the models ($[Na^+]_i$ and $[Na^+]_{ss}$, respectively) to 5 mM during the final paced beat at CL = 300 ms and CL = 2000 ms. In absence of $[Na^+]$ clamp, $[Na^+]_i$ is 10.0 mM, 10.0 mM, and 14.5 mM at CL = 300 ms and 6.6 mM, 7.4 mM, and 9.7 mM at CL = 2000 ms in human, dog, and guinea pig, respectively. Figure 1.02B shows the AP, the difference between slow and fast rate APs (ΔV_m), and Na^+/K^+ -ATPase current (I_{NaK}) for these simulations. When $[Na^+]$ was clamped to 5 mM, APD increased relative to control in all species, at both CL = 300 and 2000 ms. The percent increase in APD was always larger at CL = 300 than at 2000 ms. With $[Na^+]$ clamp, APD90 was 40%, 59%, and 24% longer for human, dog, and guinea pig, respectively at CL = 300 ms. At CL =

2000 ms, APD90 was only 8%, 25%, and 11% longer for human, dog, and guinea pig, respectively. For human and dog, ΔV_m was greatly reduced by $[Na^+]$ clamp, indicating that rate dependent $[Na^+]$ changes play an important role in rate dependent AP changes. In other words, when $[Na^+]$ is clamped, slow and fast rate APs are similar. However, for guinea pig, ΔV_m remained large despite $[Na^+]$ clamp, indicating a minor role for $[Na^+]$ in AP rate dependence.

Change in I_{NaK} is greatest for guinea pig. However, its effect on AP is the smallest because it occurs on the background of a large slow delayed rectifier K^+ current, I_{Ks} (Faber and Rudy 2000). I_{Ks} is much larger in guinea pig than in the other species (see Figure 1.01). It is the net change in the balance of currents that alters the AP.

The Case for a New Human Specific Model

As just described with experiments and simulations, species differences lead to different effects of drugs and explanations for rate dependent phenomena. Thus, experiments from human are needed. Accordingly, more and more, data describing the electrophysiology of the undiseased or nonfailing human ventricular cell are becoming available. However, previously published data have been insufficient to generate a model of the normal human ventricular AP that can be experimentally validated to the same extent as the current paradigm: the Luo-Rudy dynamic guinea pig type AP model (LRd) (Luo and Rudy 1994; Zeng, Laurita et al. 1995; Viswanathan, Shaw et al. 1999; Faber and Rudy 2000). Nevertheless, several research groups have published human ventricular AP models.

Excluding our own efforts, there are four major publications presenting models of the human ventricular AP. The first to be published was developed by Priebe and Beuckelmann (Priebe and Beuckelmann 1998) in 1998 (PB model). The second model, published in 2004, is by ten Tusscher et al. (ten Tusscher, Noble et al. 2004); the TP model. ten Tusscher published a revised version of their model in 2006 (Ten Tusscher and Panfilov 2006). Third, Iyer et al. (Iyer, Mazhari et al. 2004) contributed by publishing a model in 2004. Finally, Grandi et al.

published a model in 2010(Grandi, Pasqualini et al. 2010). However, these models were all lacking critical human ventricle specific validation. Details follow in Chapter 2.

Unique Access to Undiseased Human Ventricular Measurements

It is exceedingly rare to have regular access to undiseased or nonfailing human ventricular tissue for use in studies such as we present here. Throughout our work on this project, we have been in close contact with such a laboratory: that of András Varró and colleagues at the University of Szeged, Hungary. The previously unpublished measurements shown for human model validation were measured by A. Varró's group in the undiseased human ventricle at 37° C. Varró's extensive, high quality, experimental dataset was a major source of novelty for the new model.

Thesis Objectives

(1) To design a detailed mathematical model describing the ionic currents which make up the AP in the human ventricle. We emphasized undiseased human ventricle specificity in our model and appropriately choose data from which the model was constructed and validated in order to maximize fidelity.

(2) To study pacing rate dependent phenomena in the human ventricle. The phenomena of interest include steady state rate dependence of A) AP morphology, B) AP duration (APD), C) intracellular Ca^{2+} concentration, and D) intracellular Na^+ concentration. The model should reproduce the induction of Ca^{2+} and APD alternans seen at very rapid pacing rates in human. In addition, the model should reproduce S1S2 restitution of the APD for different diastolic intervals. We aim to investigate the underlying ionic mechanisms involved in these behaviors.

(3) To study transmural dispersion of AP repolarization in the human ventricle by designing and using human ventricular cell models of the different transmural cell types. These models can be

used to explain both the basis and arrhythmogenic consequences of transmural AP differences in the human ventricle.

(4) To apply the human model in a clinically interesting investigation: subclinical or “silent” channelopathy in human. We choose as an example the long QT syndrome missense mutation Q357R in KCNQ1. Challenges to the repolarization reserve, including β -adrenergic stimulation, transmural cell type, pacing rate, and simulated drug block were tested.

Designation of Contribution

All mathematical model development, model validation and computer simulations were performed by Thomas O'Hara under the guidance of Yoram Rudy. András Varró and colleagues at the Department of Pharmacology and Pharmacotherapy at the University of Szeged performed all previously unpublished undiseased human heart experiments. New measurements of undiseased human ventricular L-type Ca^{2+} current were performed by László Virág at the University of Szeged Department of Pharmacology and Pharmacotherapy. L-type Ca^{2+} current protocols used by László Virág were designed and tested by Thomas O'Hara. The use of “we” in what follows refers to these individuals as a collective, according to the roles designated here.

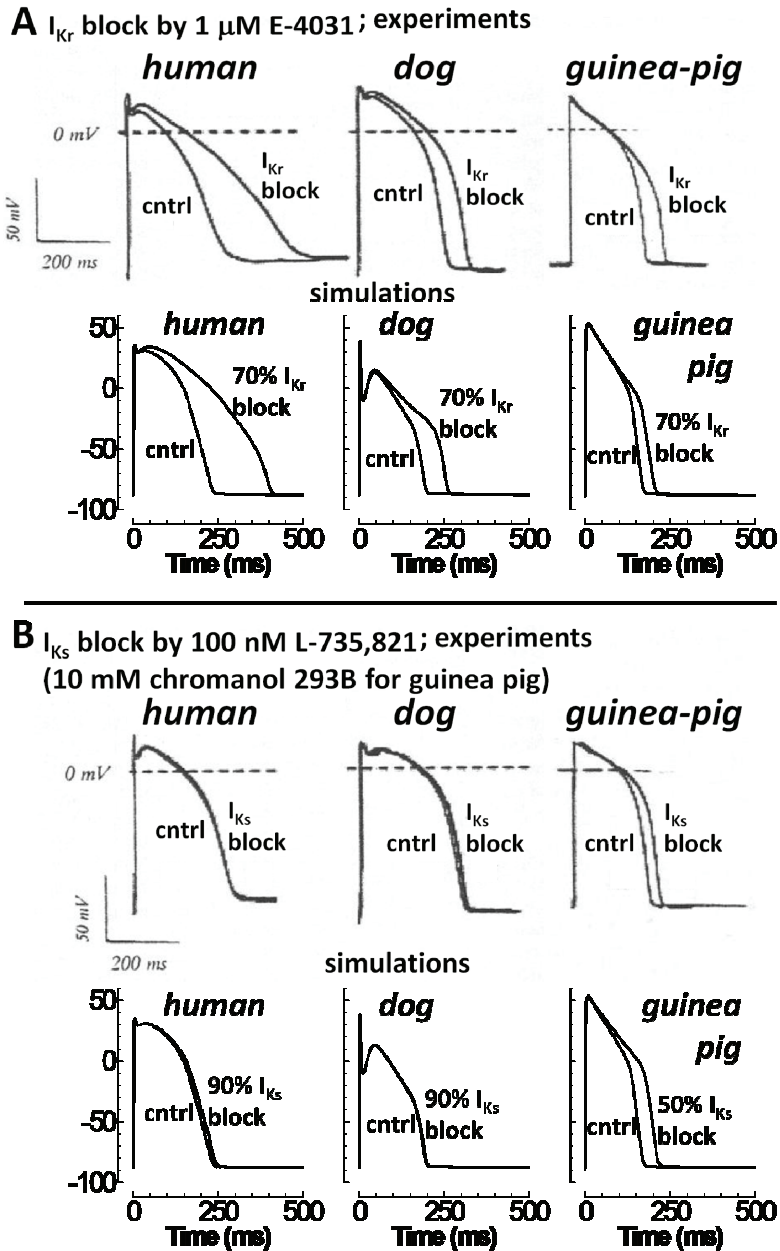


Figure 1.01 Species dependence of delayed rectifier K^+ current block. A) I_{Kr} block. B) I_{Ks} block. Results from human, dog, and guinea pig are shown from left to right. Shown are steady state APs at CL = 1000 ms for control and K^+ current block. Experiments from Jost et al. (Jost, Virag et al. 2004) are shown above simulations.

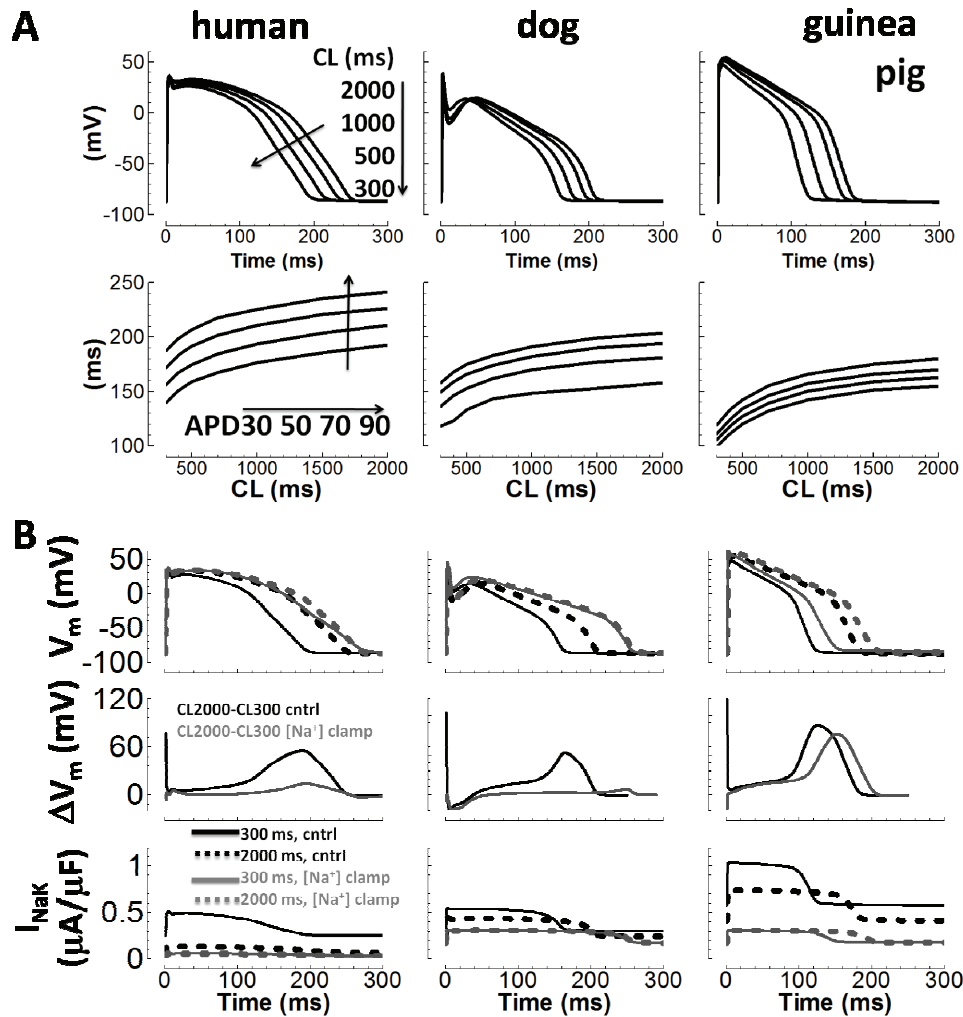


Figure 1.02 Simulation of interspecies comparison of steady state APD rate dependence.

Human, dog, and guinea pig results are left, middle, and right, respectively. A) Top) APs at different rates. CL changes are indicated by the arrows. Bottom) APD rate dependence.

APD30-90 are indicated the arrows. B) Effect of intracellular [Na⁺] Clamp to 5 mM during the final paced beat. The AP, the difference between slow and fast rate APs (ΔV_m), and Na⁺/K⁺ pump current (I_{NaK}) are shown on the top, middle and bottom rows, respectively. Solid black – CL = 300 ms, no [Na⁺] clamp; Dashed black – CL = 2000 ms, no [Na⁺] clamp; Solid gray – CL = 300 ms, [Na⁺] clamp; Dashed gray – CL = 2000 ms, [Na⁺] clamp.

Chapter 2: Simulation of the Undiseased Human Cardiac Ventricular Action Potential: Model Formulation and Experimental Validation

Introduction

The first step toward preventing sudden cardiac death is understanding the basic mechanisms of ventricular arrhythmias at the level of ion channel currents and the single myocyte action potential (AP), using both experiments(Myerburg 2002) and theoretical models(Winslow, Cortassa et al.). Obtaining ventricular myocytes from human hearts for the study of arrhythmia mechanisms is both rare and technically challenging. Consequently, these mechanisms are usually studied with human channels expressed in non myocytes, or with non human (rodent or other mammalian) myocytes. However, these approaches have limitations, because functionally important accessory subunits and anchoring proteins native to ventricular myocytes(Ackerman and Mohler 2010) are absent in expression systems, and even among mammalian ventricular myocytes, ion channel kinetics(Zicha, Moss et al. 2003; Akar, Wu et al. 2004; Blechschmidt, Haufe et al. 2008) and consequently arrhythmia mechanisms are strongly species dependent.

These issues limit the applicability of results from animal studies to human cardiac electrophysiology and clinical arrhythmia(Rudy, Ackerman et al. 2008). Measurements from undiseased human ventricular myocytes are a requisite for understanding human cell electrophysiology. Here, we present data from over 100 undiseased human hearts for steady state rate dependence, and restitution of the ventricular AP. Importantly, we also obtained essential new measurements for the L-type Ca^{2+} current, K^+ currents, and $\text{Na}^+/\text{Ca}^{2+}$ exchange current from undiseased human ventricle. These previously unavailable data are critically important for correct formulation of mathematical models for simulation of electrophysiology and cellular arrhythmia mechanisms(Rudy and Silva 2006). Using the new data together with previously published experiments, a detailed mathematical model of undiseased human ventricular myocyte electrophysiology and Ca^{2+} cycling was developed and thoroughly validated over the entire range of physiological frequencies. This model is referred to as the ORd (O'Hara-

Rudy dynamic) model throughout the text. Model comparisons are conducted with the ten Tusscher-Panfilov (TP) model(Ten Tusscher and Panfilov 2006), and the Grandi-Bers (GB) model(Grandi, Pasqualini et al. 2010).

The ORd model was used to describe cellular electrophysiology mechanisms specific to human ventricular myocytes. Underlying mechanisms of AP duration (APD) rate dependence and APD restitution were investigated. The effects of Ca^{2+} /calmodulin-dependent protein kinase II (CaMK) on known ionic current and Ca^{2+} cycling targets were incorporated and studied. Early afterdepolarizations (EADs) and alternans were reproduced by the model. These are important arrhythmogenic phenomena that must be reproduced in order to study the mechanisms of cardiac arrhythmias in human and simulate clinical interventions such as drugs.

Results

Throughout Chapter 2, new undiseased human ventricle experimental data are represented by white circles or white squares for isolated myocyte or small tissue preparation measurements, respectively. Previously published nonfailing human ventricle experimental data are shown with black symbols. Other data classification schemes are provided case by case in figure legends.

Results Subsection 1: Formulation, Validation and Properties of Simulated Currents

L-type Ca^{2+} Current (I_{CaL})

Data for I_{CaL} in the undiseased human ventricle are from Magyar et al.(Magyar, lost et al. 2000) and Fulop et al.(Fulop, Banyasz et al. 2004) (both at 37 °C, model validation in Figure 2.01C). Magyar et al. measured steady state activation, steady state inactivation, and the current voltage (I-V) curve. Fulop et al. measured recovery from inactivation. However, neither study

separated Ca^{2+} dependent inactivation (CDI) from voltage dependent inactivation (VDI). In fact, no published data are available which separate CDI and VDI in the undiseased or nonfailing human ventricle. For this measurement, we made new recordings in undiseased human ventricular myocytes at 37 °C (Figure 2.01, current traces and white circles).

Measurements were carried out with Ca^{2+} as charge carrier, allowing both CDI and VDI, or with Ba^{2+} as charge carrier, allowing only VDI. Results for Sr^{2+} were similar to those for Ba^{2+} . From holding potential of -60 mV, 75 ms steps were to potentials ranging from -40 to +50 mV (10 mV increments, 3 second interpulse interval, Figure 2.01A). 75 ms was sufficient for comparison of CDI and VDI, since it is in the early phase of decay in which CDI effects are most prominent (Aggarwal and Boyden 1995). Simulated current traces for CDI+VDI and for VDI-alone, were similar to the experiments.

Fractional remaining current (FRC, at time t and voltage V_m , $\text{FRC}(t, V_m) = I(t, V_m) / I_{\text{peak}}(V_m)$) quantified the voltage and time dependence of inactivation for comparison between charge carriers. Figure 2.01B compares FRC for Ba^{2+} (experiments top left, simulations right), and Ca^{2+} (experiments bottom left, simulations right). With Ba^{2+} as the charge carrier, FRC monotonically decreased with increasing voltage at all times after peak current. This finding is consistent with dependence of inactivation on voltage alone. In contrast, for Ca^{2+} currents, FRC did not decrease monotonically with increasing voltage. Rather, Ca^{2+} current FRC curves appear to be effectively voltage independent. FRC for CDI+VDI was statistically different from FRC for VDI-alone at the more hyperpolarized potentials (-20 to 0 mV, unpaired two-tailed t-test, $p < 0.01$). Ca^{2+} ions caused additional inactivation at these voltages, where VDI-alone was relatively weak. Since the only difference between Ca^{2+} and Ba^{2+} cases was the charge carrier, it follows that Ca^{2+} ions themselves are the source of the additional inactivation. This is evidence that currents carried by Ba^{2+} inactivate due to VDI only, while Ca^{2+} currents inactivate due to both VDI and CDI (Findlay 2002). There is evidence that Ba^{2+} can cause ion dependent inactivation (Grandi, Morotti et al. 2010). However, Ba^{2+} -dependent inactivation was estimated to be 100-fold weaker than CDI (Ferreira, Yi et al. 1997), and its effects were not appreciable in FRC experiments.

To modulate VDI versus CDI in the model, the n gate was introduced, the value of which represents the fraction of channels operating in CDI mode. Under physiological conditions, I_{CaL} inactivation is caused by a combination of both CDI and VDI. That is, n is between 0 (all VDI) and 1 (all CDI). This model was based on experiments by Kim et al. (Kim, Ghosh et al. 2004), where CDI was observed to function as a faster VDI, activated by elevated Ca^{2+} . Thus, both CDI and VDI are voltage dependent. The rate of decay in CDI mode is faster than that in VDI mode. The Mahajan et al. (Mahajan, Shiferaw et al. 2008) and Decker et al. (Decker, Heijman et al. 2009) I_{CaL} models work similarly.

The n gate is diagrammed in Figure 2.01E. Rates k_1 and k_{-1} represent binding/unbinding of Ca^{2+} to channel bound calmodulin (CaM) (Peterson, DeMaria et al. 1999). There are four identical binding sites. Rates k_2 and k_{-2} represent activation/deactivation of CDI mode (black circle, asterisk), which occurs when all Ca^{2+} binding sites are occupied. We considered that the four Ca^{2+} binding transitions are in rapid equilibrium and solved the reversible two state reaction of Ca^{2+} /CaM binding and CDI mode activation to obtain the differential equation describing the n gate (Chapter 2 Supplement).

In both CDI and VDI modes, there are two weighted time constants for inactivation (time constant weighting described in Methods). We determined time constants for CDI and n gate kinetics in an attempt to represent the shape and magnitude of the FRC measurements (i.e. CDI reduced FRC, particularly at negative potentials). Time constants for VDI gates were determined by inactivation of Ba^{2+} currents (Figure 2.01C). AP clamp simulations using the formulated I_{CaL} model were similar to AP clamp experiments, where I_{CaL} was defined as the 1 μ M nisoldipine sensitive current (Figure 2.01D). Specifically, currents showed spike and dome morphology. In experiments, peak current was $-3.0 \mu A/\mu F$. It was $-2.7 \mu A/\mu F$ in simulations. Fast inactivation was 2.5 fold faster when phosphorylated by CaMK, similar to the Decker et al. dog I_{CaL} model (Decker, Heijman et al. 2009) and as measured experimentally (Dzhura, Wu et al. 2000).

Transient Outward K^+ Current (I_{to})

The model for I_{to} was formulated based on newly measured experimental data. The measurements were from isolated undiseased human ventricular myocytes at 37 °C (Figure 2.02A, white circles), and were carried out with the addition of 1 μ M nisoldipine to the standard bath solution (see Methods) to block I_{CaL} . The holding potential was -90 mV. Currents were activated by a 300 ms step to various potentials. Inactivation time constants were determined from exponential fits to decay of these traces. To measure steady state inactivation, 500 ms steps from -90 mV to various potentials were followed by test pulses to 50 mV. Recovery from inactivation was determined at -90 mV, using P1/P2 pulses of 200 ms to 50 mV at varying interpulse intervals in a double pulse protocol.

The time constant for activation was determined by fitting time to peak from a digitized current trace ((Amos, Wettwer et al. 1996), their Figure 12C, in undiseased human ventricle at 37 °C; $\tau_a = 2.645$ ms at $V_m = +40$ mV). Greenstein et al.(Greenstein, Wu et al. 2000) showed time to peak for hKv4.3 expressed in mouse fibroblast cells. The model provides a qualitative match to these data (considering temperature and expression system differences). That is, the model activation time constant decreases from a peak value of 6.5 to 1.5 ms in near linear fashion with increasing voltage from -20 to 60 mV.

The inactivation gate has two time constants, each with voltage dependent weighting. Inactivation kinetics and the I-V curve are accurate to the experimental data. A small divergence between simulations and experiments was observed at hyperpolarized potentials along the I-V curve (simulated current was less than in experiments). This may be due to the fact that experimentally measured currents were small and difficult to measure at these potentials. In fact, current was not measureable in 21, 11, 5, and 1 out of 23 cells at $V_m = -40, -30, -20,$ and -10 mV, respectively. Currents with zero values were not included in the experimental I-V averages. However, these currents were included in averages for obtaining steady state activation and steady state inactivation curves in the model. This prevented over representation of the window current (small, appearing late during phase-3 of the AP, shown later). The conductance of the I_{to} model was set so that phase-1 behavior of the simulated AP would be similar to undiseased human endocardium experiments (small in endocardium; maximum value $\sim 1 \mu A/\mu F$). Measured

endocardial APs showed rapid phase-1 repolarization, but did not show positive time derivatives during phase-1 (true notching was generally not observed). Thus, model I_{to} conductance was set to the maximum level which did not violate these observations ($\sim 1 \mu A/\mu F$ peak current at $CL = 1000$ ms).

CaMK effects on I_{to} were incorporated based on measurements by Tessier et al. (Tessier, Karczewski et al. 1999) and Wagner et al. (Wagner, Hacker et al. 2009). As in Tessier et al., CaMK shifted the voltage dependence of steady state activation 10 mV in the depolarization direction, and the time constant for development of inactivation was increased (multiplicative factor fit to match the voltage dependent increase). Wagner et al. showed that the time constant for recovery from inactivation was affected by CaMK (~ 2 fold faster).

Na^+/Ca^{2+} Exchange Current (I_{NaCa})

The I_{NaCa} model was formulated using measurements from undiseased human ventricular myocytes at 37 °C (Figure 2.02B, white circles). The model was based on the framework established by Kang and Hilgemann (Kang and Hilgemann 2004), which allows for unlikely occurrence of inward Na^+ leak, without Ca^{2+} exchange. The Hilgemann model shows $Na^+:Ca^{2+}$ exchange stoichiometry slightly greater than 3.0, as has been observed by others (Fujioka, Komeda et al. 2000; Dong, Dunn et al. 2002). Though the Hilgemann model is mechanistically novel in this way, it can still reproduce all Na^+ , Ca^{2+} and voltage dependent properties observed by Weber et al. (Weber, Piacentino et al. 2003) in the nonfailing human ventricle. Compare Hilgemann and Weber data to our simulated reproductions in Chapter 2 Supplement Figures 2.S01-2.S03. As in the Faber-Rudy (Faber, Silva et al. 2007) and Hund-Decker-Rudy models (Hund and Rudy 2004; Decker, Heijman et al. 2009), we included 20% of the exchanger in the Ca^{2+} diffusion subspace (Frank, Mottino et al. 1992; Kieval, Bloch et al. 1992). The choice to include 20% in the subspace in human is validated based on its effect on the rate dependence of peak $[Ca^{2+}]_i$ (results in Chapter 2 Supplement Figure 2.S17). Values above or below 20% disrupt

the demonstrated correspondence of peak $[Ca^{2+}]_i$ rate dependence with experiments (see section on Na^+ and Ca^{2+} rate dependence).

Inward Rectifier K^+ Current (I_{K1})

The model for I_{K1} was constructed based primarily on new experimental data, measured at 37 °C in undiseased isolated human ventricular myocytes as the 0.5 mM $BaCl_2$ sensitive current (Figure 2.02C, white circles). Current was elicited with steps from -90 mV to various potentials for 300 ms. The current that remained at the end of the steps was recorded as I_{K1} .

Two gates were used in the model: R_{K1} , the instantaneous rectification gate, and x_{K1} , the time dependent inactivation gate. Importantly, previous models (Priebe and Beuckelmann 1998; Iyer, Mazhari et al. 2004; Ten Tusscher and Panfilov 2006; Grandi, Pasqualini et al. 2010) have ignored both inactivation gating, and detailed $[K^+]_o$ -dependence of I_{K1} (exception, I_{K1} equations by Fink et al. (Fink, Noble et al. 2008)). There are nonfailing human ventricular measurements which we utilized to include these effects (Konarzewska, Peeters et al. 1995; Bailly, Mouchoniere et al. 1998).

Steady state rectification was determined by dividing current by driving force, then normalizing. Rectification was shown to be $[K^+]_o$ -dependent in the nonfailing human ventricle by Bailly et al. (Bailly, Mouchoniere et al. 1998). A linear shift in $V_{1/2}$ for rectification toward more depolarized potentials with elevated $[K^+]_o$ was incorporated, as was shown experimentally (compare to Bailly et al., their Figure 4B). Bailly also showed the voltage and $[K^+]_o$ -dependence of inactivation. We introduced the time dependent x_{K1} gate, based on these data. As was shown experimentally, both $V_{1/2}$ and the slope factor for inactivation depend linearly on $[K^+]_o$. The time constant for inactivation was based on measurements in nonfailing human ventricular myocytes by Konarzewska et al. (Konarzewska, Peeters et al. 1995) (their Figure 1C). Conductance was observed to be in proportion to the square root of $[K^+]_o$ in the human ventricle (Bailly, Mouchoniere et al. 1998). When assembled, the I_{K1} model demonstrated correspondence with the measured amplitude and rectification profile, and with Bailly data for $[K^+]_o$ -dependence. As in Jost et

al.(Jost, Acsai et al. 2009), I_{K1} was voltage dependent, but not pacing rate dependent (Chapter 2 Supplement Figure 2.S04)

Rapid Delayed Rectifier K⁺ Current (I_{Kr})

The model for I_{Kr} was constructed using experimental data measured in isolated undiseased human ventricular myocytes at 37 °C (Figure 2.03A, white circles). Measurements were carried out with/without addition of 1 μ M E-4031 to the standard bath solution in order to obtain the difference current. Tail currents were elicited by stepping from -40 mV to various potentials for 1000 ms, and then stepping back down to -40 mV. The deactivation time constant was determined by fitting the tail current decay. The time constant for activation was found by stepping from -40 mV to various potentials for various durations preceding a step back to -40 mV. The rate with which the envelope of tail currents developed at different voltages was measured with an exponential fit to obtain the time constant for activation. Since this process was well fit by a single exponential, we made the fast and slow time constants in the model converge on the activation limb, at depolarized potentials. The steady state activation curve was determined from the I-V curve, after dividing by the driving force, assuming maximal activation at the time of peak tail current. Slow deactivation of I_{Kr} (experiments and simulations, Figure 2.03B), suggests its participation in AP shortening during steady state pacing at fast rate and at short diastolic intervals during restitution; this hypothesis will be explored in a later section. The fast inactivation (rectification, instantaneous in the model) R_{Kr} gate was determined so that current profile matched experiments using a human AP voltage clamp (Figure 2.03C). Important features of the experimental AP clamp trace that the model reproduced include 1) the early recovery phase, where approximately half maximal current appeared by the beginning of the AP plateau, followed by 2) quasi-linear current increase until peak current was reached during late phase-3 of the AP.

Since enzymes used to disaggregate myocytes can significantly degrade I_{Kr} (Rajamani, Anderson et al. 2006), conductance was scaled to provide correct APD90 in control and with I_{Kr} block, measured in small tissue preparations. Indeed, APD90 was a function of I_{Kr} conductance

(parameter sensitivity, Chapter 2 Supplement Figure 2.S15). As in undiseased human ventricle experiments(Jost, Acsai et al. 2009), I_{Kr} was voltage dependent, but not pacing rate dependent (Chapter 2 Supplement Figure 2.S05).

Slow Delayed Rectifier K⁺ Current (I_{Ks})

Data from Virág et al.(Virag, lost et al. 2001), measured in isolated undiseased human ventricular myocytes at 37 °C, were used to construct the model for I_{Ks} (Figure 2.03D). The model has two gates, x_{s1} and x_{s2} . The x_{s1} gate is responsible for activation. Deactivation was controlled by x_{s2} . Activation/deactivation separation was based on the fact that activation was much slower than deactivation. Setting $\tau_{x1} \gg \tau_{x2}$ at hyperpolarized potentials, where deactivation dominated, and $\tau_{x2} \ll \tau_{x1}$ at depolarized potentials, where activation dominated, allowed for separation of these processes as two gates. As in the case of I_{Kr} , it is understood that I_{Ks} is damaged (reduced) by enzymatic disaggregation of myocytes(Li, Feng et al. 1996). Therefore, we used I_{Ks} specific drug block (1 μ M HMR-1556) effects on APD90, measured in small tissue preparations, to determine the correct conductance. Ca^{2+} dependence of I_{Ks} was incorporated(Tohse 1990). The effect of this dependence was negligible under physiological Ca^{2+} concentration conditions.

Fast Na⁺ Current

Fast I_{Na} was formulated using nonfailing human ventricular data from Sakakibara et al.(Sakakibara, Furukawa et al. 1993) (Figure 2.04A). Since the Sakakibara experiments were performed at 17° C, a temperature adjustment was used to obtain the final model equations, representing behavior at 37° C. The effect of temperature on steady state gating was shown by Nagatomo et al.(Nagatomo, Fan et al. 1998). For activation, $V_{1/2}$ shift with temperature change from 23 to 33° C was +4.3 mV. For inactivation, the shift was +4.7 mV. We shifted $V_{1/2}$ by twice

these amounts, assuming linearity (adjust to 37° C from data taken at 17° C, a change of 20° C; Nagatomo showed a change of 10° C). Time constants were adjusted to 37° C using Q_{10} . We set $Q_{10} = 2$ since Q_{10} was given as “about two” by Nagatomo.

Hanck and Sheets (Hanck and Sheets 1992) documented a shift in $V_{1/2}$ with the passage of time after patch clamp commencement. For activation, the shift was -0.47 mV/min. It was -0.41 mV/min for inactivation. Sakakibara reported the time elapsed between patching and measurement for steady state activation and inactivation as between 10 and 20 min, ~15 min for both. Thus, we reversed the time dependent shifts in $V_{1/2}$.

CaMK effects on I_{Na} were based on available data (Wagner, Dybkova et al. 2006). We took into account the measured -6.2 mV $V_{1/2}$ shift in steady state inactivation, the roughly 3-fold slowing of current decay, and the 1.46-fold slowing of recovery from inactivation.

The non-temperature adjusted model I-V curve matches Sakakibara data at 17° C. We determined appropriate channel conductance at 37° C based on conduction velocity, and maximum dV_m/dt . Conduction velocity in a one dimensional fiber simulation was 45 cm/s during pacing at CL = 1000 ms, consistent with available (dog) experiments (Spach, Heidlage et al. 2000). It was 70 cm/s when stimulated from quiescence, consistent with *in vivo* measurements in nonfailing human hearts (Taggart, Sutton et al. 2000). Maximum dV_m/dt was 254 mV/ms in single cells at 1 Hz pacing, consistent with measurements from nonfailing human ventricular myocytes at 37° C (234 ± 28 V/second) (Drouin, Charpentier et al. 1995).

Late Na⁺ Current

Data used in the formulation of late I_{Na} were from Maltsev et al. (Maltsev, Sabbah et al. 1998), measured in the nonfailing human ventricle (Figure 2.04B), functionally defined in experiments and simulations as the Na⁺ current remaining after 200 ms from the onset of depolarization. Steady state activation was derived from the I-V curve (current divided by driving force, then normalized). The time constant for activation of late I_{Na} was identical to that for fast I_{Na} . It is not possible to measure the time to peak for late I_{Na} because of the interfering effects of

the much larger I_{Na} . However, in the model scheme, the measurement is irrelevant for the same reason.

The h_L gate is responsible for both development of and recovery from inactivation. The time constant for development was adjusted using $Q_{10} = 2.2$, as measured by Maltsev et al. (Maltsev and Undrovinas 2006) (hNav1.5 channels expressed heterologously). The time constant was voltage independent (Maltsev, Sabbah et al. 1998). Maltsev et al. (Maltsev, Sabbah et al. 1998) reported a maximum late I_{Na} of -0.356 pA/pF in nonfailing human ventricular myocytes (average current between 200 and 220 ms during step to -30 mV from -120 mV, their Table 2, donor heart average). We scaled the Maltsev I-V curve to the donor value and used it to determine the model conductance.

We do not consider fast and late Na^+ currents to be separate channels. Rather, they have long been understood to represent different gating modes (experiments (Maltsev and Undrovinas 2006), and simulations by our group (Clancy and Rudy 1999)), separated functionally in time. In experiments, and in simulated reproductions of experiments, late I_{Na} was functionally defined as the I_{Na} current persisting 200 ms after onset of depolarization. CaMK dependence was implemented (-6.2 mV $V_{1/2}$ shift in steady state inactivation, and 3-fold slowing of inactivation time constant, as measured (Wagner, Dybkova et al. 2006)).

Na⁺/K⁺ Pump Current (I_{NaK})

The model for I_{NaK} was reformulated based on the work of Smith and Crampin (Smith and Crampin 2004). The Smith and Crampin model includes more detail than standard formulations employed by other ventricular AP models (Priebe and Beuckelmann 1998; Iyer, Mazhari et al. 2004; Ten Tusscher and Panfilov 2006; Grandi, Pasqualini et al. 2010). Importantly, the Smith and Crampin framework includes $[K^+]_i$ dependence and inputs for ATP and pH sensitivity. Here, we set ATP and pH values to normal physiological levels (pH was dynamic when stated). Dynamically changing $[K^+]_i$ is a known and meaningful pump regulator that is a functioning part of

this model. High $[K^+]_i$ (combined with low ATP) can make the pump reverse, bringing Na^+ in, as has been observed in isolated hearts (Jansen, Shen et al. 2003).

The Smith and Crampin model (schematized in Chapter 2 Supplement Figure 2.S06) was adjusted to reproduce the basic findings of Nakao and Gadsby (Nakao and Gadsby 1989), demonstrating $[Na^+]_o$ dependence, $[Na^+]_i$ dependence with high and low $[Na^+]_o$, and $[K^+]_o$ dependence with high and low $[Na^+]_o$ (Chapter 2 Supplement Figure 2.S07). To determine human ventricle appropriate conductance for I_{NaK} , we used $[Na^+]_i$ -frequency data presented by Pieske et al. (Pieske, Maier et al. 2002) as a target (nonfailing human left ventricular myocytes at 37°C).

The I_{NaK} formulation is based on known biophysical properties (Smith and Crampin 2004); its behavior reproduces available experimental observations (Nakao and Gadsby 1989) (Chapter 2 Supplement Figure 2.S07). However, no direct measurement of I_{NaK} has been made in the nonfailing or undiseased human ventricle. To endow human ventricle specificity to I_{NaK} , our strategy was indirect; reproducing the rate dependence of intracellular Na^+ concentration, $[Na^+]_i$, measured in the nonfailing human ventricle was the target. This choice assumes that the major role for I_{NaK} is maintenance of physiological $[Na^+]_i$. In the model, $[Na^+]_i$ and its relative changes with pacing rate are controlled by I_{NaK} conductance (~0.5 mM change per 20% change in I_{NaK} conductance, Chapter 2 Supplement Figure 2.S18). In the absence of direct human ventricle I_{NaK} measurements, validation of the I_{NaK} formulation employs this relationship.

Results Subsection 2: Human AP Characteristics and APD

Figure 2.05 shows a schematic diagram of the human ventricular AP model. The scheme was largely unchanged from the recent dog ventricular model by Decker et al. (Decker, Heijman et al. 2009). However, additional targets for CaMK were included, as described above, based on new findings. Currents were reformulated based on new undiseased or published nonfailing human experiments. These are colored gray in Figure 2.05. Currents and fluxes colored white in the figure were based on human specific measurements of rate dependence of

intracellular Na^+ and Ca^{2+} concentrations ($[\text{Na}^+]_i$ and $[\text{Ca}^{2+}]_i$, respectively), which these currents/fluxes affect. Equations for currents and fluxes were not adopted from other human or animal models without substantive modification; all equations were reformulated with the exceptions of Ca^{2+} buffers, CaMK kinetics, and background currents, for which we used Decker et al.(Decker, Heijman et al. 2009) formulations and adjusted conductances. Model equations for all major currents were completely reformulated (i.e. fast I_{Na} , late I_{Na} , I_{to} , I_{CaL} , I_{Kr} , I_{Ks} , I_{K1} , I_{NaCa} , and I_{NaK}). Relevant details precede equations in the Chapter 2 Supplement.

Microelectrode AP recordings from undiseased human ventricular endocardium at 37 °C were used to validate basic human model AP characteristics. Figure 2.06A shows simulated APs and experimentally measured example APs for comparison during steady state pacing at the cycle lengths (CLs) indicated. We also compared simulated values for resting voltage, maximum voltage, and the maximum upstroke velocity, dV_m/dt , with experiments (Figure 2.06B). These comparisons were made for a single beat, stimulated from the quiescent state.

For steady state rate dependence, we compared APD30-90 after pacing at different CLs (Figure 2.07A). For restitution, we compared APD30-90 after steady state S1 pacing at CL = 1000 ms, followed by a single S2 extrasystolic stimulus delivered at various diastolic intervals (DIs, measured relative to APD90, Figure 2.07B). Model AP repolarization from 30 to 90% quantitatively reproduced this extensive dataset (simulation results were within experimental error bars). Generally, electrotonic effects of tissue coupling were minor (see Discussion and Chapter 2 Supplement Figure 2.S08).

The rate of repolarization in the model was gradual, as in experiments (APD30-90 were well separated in time, Figure 2.07C). Other models repolarized more rapidly and late compared to these experiments (simulations were all endocardial cell types).

Koller et al.(Koller, Maier et al. 2005) measured dynamic restitution in the nonfailing human ventricle with monophasic AP electrodes. Following the Koller protocol (explained in Methods), the human model matched Koller results (Figure 2.07D). Simulations predict a bifurcation (alternans) at shortest DIs (< 90 ms), which is also observed in the experiments.

Steady state rate dependence and restitution of the undiseased human ventricular APD were also measured in the presence of channel-specific blockers (Figure 2.08, white squares, see Methods for further details). In Figure 2.08, drugs and applied doses are provided for each experiment. Simulated block was based on experimental dose-response measurements (E-4031(Sanguinetti and Jurkiewicz 1990), HMR-1556(Gogelein, Bruggemann et al. 2000), nisoldipine(Walsh, Zhang et al. 2007), BaCl₂(Warren, Guha et al. 2003), ryanodine(Nanasi, Sarkozi et al. 2000), and mexiletine(Wang, Yazawa et al. 1997), for block of I_{Kr}, I_{Ks}, I_{CaL}, I_{K1}, J_{rel}, and late I_{Na}, respectively). Simulations matched these experiments; that is, simulation results were within experimental error bars.

As pacing CL was decreased from 2000 to 300 ms, currents in the human ventricular AP model changed accordingly (Figure 2.09). Due to increased refractoriness at faster rates, maximum fast I_{Na}, late I_{Na}, and I_{to} were reduced. By contrast, peak I_{CaL} increased, due in part to CaMK-phosphorylation induced facilitation(Yuan and Bers 1994). I_{Kr} and I_{K1} were largely rate independent. Mild I_{Ks} accumulation(Silva and Rudy 2005) caused rate dependent increase in current. I_{NaK} became larger due to intracellular Na⁺ accumulation at fast pacing (details below). I_{NaCa,i} and I_{NaCa,ss} became more inward, in order to remove increasing Ca²⁺.

Transmural Heterogeneity

Changes in mRNA and protein expression across the transmural wall using undiseased human ventricles were measured(Szabo, Szentandrassy et al. 2005; Gaborit, Le Bouter et al. 2007; Soltysinska, Olesen et al. 2009). Functional data for transmural changes in I_{to} were measured in nonfailing human ventricular myocytes(Nabauer, Beuckelmann et al. 1996). These results were compiled to create a complete dataset for transmural differences between endocardial (endo), mid-myocardial (M), and epicardial (epi) cell types. We considered transmural differences in Nav1.5, Cav1.2, HERG1, KvLQT1, Kir2.1, NCX1, Na/KATPase, Kv1.5, RyR2, SERCA2, and CALM3 to be represented in the model by late I_{Na}, I_{CaL}, I_{Kr}, I_{Ks}, I_{K1}, I_{NaCa}, I_{NaK}, I_{Kb}, J_{rel}, J_{up}, and CMDN, respectively. Whenever an expression ratio was not available, we chose

unity. Using this analysis, models for M and epi cells were derived from the thoroughly validated endo model (Figure 2.10A-2.10D; equations in the Chapter 2 Supplement).

In Figure 2.10E1, our experimental measurements for endo APD90 were scaled by M/endo and epi/endo APD90 ratios measured by Drouin et al.(Drouin, Charpentier et al. 1995) and compared to simulations. Drouin experiments did not show results for CL < 1000 ms. Epi simulations seem to deviate from Drouin experiments at faster pacing rates. However, epi simulations were consistent with nonfailing human epi experimental measurements at fast pacing rates (CL < 1000 ms) recorded using optical mapping by Glukhov et al.(Glukhov, Fedorov et al. 2010) (panel E2). The rate dependence of simulated AP morphology in the different cell types (Figure 2.10F) was similar to Drouin recordings(Drouin, Charpentier et al. 1995). Relative shape and duration of simulated transmural APs were also consistent with those recorded by Glukhov et al.(Glukhov, Fedorov et al. 2010) from the heart of a 20 year old healthy human male (Chapter 2 Supplement Figure 2.S09). The transmural repolarization gradient direction was such that the pseudo-ECG T-wave was upright and rate dependent(Shimizu and Antzelevitch 1998) as expected (Figure 2.10G).

Early Afterdepolarization (EAD)

Experiments from Guo et al.(Guo, Liu et al. 2011) in isolated nonfailing human ventricular endocardial myocytes showed EADs when paced very slowly (CL = 4000 ms) in the presence of the I_{Kr} blocker dofetilide (0.1 μ M dose, ~85% I_{Kr} block(Thomsen, Volders et al. 2003)). In Figure 2.11A, we display Guo experimental results and simulation results of the same protocol using the ORd model, and the GB and TP models (all for endo cells at steady state). As in the experiment, the ORd model produced an EAD when paced at slow rate (CL = 4000 ms) with block of I_{Kr} (85%). Experiments and simulations both show a single, large EAD deflection. The GB and TP models failed to produce an EAD following the same protocol (CL = 4000 ms), even with complete block of I_{Kr} (100%).

EADs in the ORd model were caused by I_{Kr} block induced prolongation of the time at plateau voltages, allowing I_{CaL} reactivation. When I_{CaL} recovery was prevented, the EAD was eliminated (inactivation gate clamping protocol, Figure 2.11B). This mechanism is the same as shown previously in other species (Zeng and Rudy 1995).

Na⁺ and Ca²⁺ Rate Dependence

Using data from nonfailing human ventricle, we validated rate dependent changes in concentrations of intracellular Na⁺ and Ca²⁺. For $[Na^+]_i$ changes with pacing rate, we used data from Pieske et al. (Pieske, Maier et al. 2002), measured in the nonfailing human ventricle, normalized to 0.25 Hz pacing rate (Figure 2.12A). Reproduction of this curve implied that I_{NaK} magnitude was accurate (I_{NaK} conductance controls intracellular Na⁺, thus rate dependence of relative accumulation, Chapter 2 Supplement Figure 2.S18). For Ca²⁺, we used data from Schmidt et al. (Schmidt, Hajjar et al. 1998), normalized to the value at 0.5 Hz pacing rate. A personal correspondence with senior author J. Gwathmey revealed that pacing in the experiments was for about 100 beats (long enough to reach apparent steady state). Following this protocol, we showed the reduction in peak Ca²⁺ observed at the fastest pacing rates (Figure 2.12B). However, at true steady state, peak Ca²⁺ increased monotonically with pacing rate (shown in Figure 2.13).

Using Fura-2-AM fluorescence data measured in an undiseased isolated human ventricular myocyte at 37 °C, we determined that the human ventricular cell model showed accurate intracellular Ca²⁺ decay (Figure 2.12C and 2.12D). Time constant fits were a single exponential decay from time of peak Ca²⁺. The decrease in decay time constant observed with increase in pacing rate is a measure of frequency dependent acceleration of relaxation, an important validation of Ca²⁺ cycling.

Ca²⁺ Cycling and CaMK

As pacing rate increased, so did the CaMK active fraction (CaMK_{active}, Figure 2.13A, validated previously (Hund and Rudy 2004; Livshitz and Rudy 2007)). CaMK was important for controlling rate dependence of Ca²⁺ cycling in the model. In the absence of CaMK: Ca²⁺ transient amplitude was reduced, diastolic Ca²⁺ was elevated, JSR Ca²⁺ content and evacuation were rate independent, and Ca²⁺ reuptake (J_{up}) and release (J_{rel}) were severely blunted (Figure 2.13B).

Alternans

Koller et al. (Koller, Maier et al. 2005) showed that in the nonfailing human ventricle (*in vivo*, monophasic AP recordings), APD alternans appeared at CLs < 300 ms (> 200 bpm). The amplitude of APD alternans was ~10 ms. These findings were reproduced by the human model (APD alternans of 11 ms at CL = 250 ms, Figure 2.14). Pacing at rates faster than 230 ms in the model caused 2 to 1 block (i.e. failed APs every other beat), because APD began to encroach upon the pacing cycle length, leading to enhanced refractoriness of Na⁺ current due to incomplete repolarization.

Since Koller measurements were performed in intact hearts, electrotonic coupling effects would have played a role. Therefore, simulations in a strand of 100 coupled endo cells were conducted to test whether alternans occurred in coupled tissue as well. Indeed, during CL = 280 ms steady state pacing, alternans developed in the multicellular fiber; Chapter 2 Supplement Figure 2.S10.

As in Livshitz et al. (Livshitz and Rudy 2007), beat to beat alternans in the Ca²⁺ subsystem were the cause of the APD alternans in the model. Longer APs coincided with larger Ca²⁺ transients. For steady state pacing at 250 ms pacing cycle length (shown in Figure 2.14A), we found that clamping the subspace Ca²⁺ concentration to either the odd or even beat waveforms eliminated alternans, but clamping of the voltage, myoplasmic Ca²⁺, I_{CaL}, or I_{NaCa} did not eliminate alternans (odd or even beat clamp, not shown).

Cutler et al.(Cutler, Wan et al. 2009) demonstrated that 30% SERCa upregulation eliminated alternans. Similarly, in our human model, a 20% increase in J_{up} magnitude eliminated alternans (shown in Chapter 2 Supplement Figure 2.S11). CaMK suppression also eliminated alternans in the model (Figure 2.14A and 2.14B, gray traces). At slower pacing rates, APD was minimally affected by CaMK suppression. However, the peak Ca^{2+} concentration was markedly reduced, especially at faster rates (Figure 2.14C).

Currents Participating in Steady State APD Rate Dependence and APD Restitution.

In order to describe the mechanisms underlying steady state rate dependence and restitution of the APD in the model, it is instructive to first systematically determine which currents participate in these phenomena. In Figure 2.15, currents were plotted versus V_m during steady state and S1S2 restitution pacing for a variety of CLs and DIs, respectively. If I-V curves are CL or DI independent (i.e. curves overlap), then that current did not participate in steady state rate dependence or restitution, respectively. Conversely, if I-V curves depended greatly on CL or DI, then that current played at least some role in these phenomena.

As CL or DI decreased, fast I_{Na} , responsible for the maximum AP upstroke velocity and maximum V_m , was reduced (see Figure 2.09, and principles detailed in Luo and Rudy(Luo and Rudy 1991)). This is because shortened time at resting potential between beats prevents complete recovery from inactivation. Thus, at fast pacing rates, and short DIs, maximum V_m and upstroke velocity were reduced, explaining some of what follows.

During steady state pacing, I_{Ks} was strongly rate dependent (Figure 2.15A). The I-V curves were dramatically different at different pacing CLs. However, I_{Ks} was a relatively small contributor to the rate dependence of APD because I_{Ks} density in human ventricle is small under basal conditions (no β -adrenergic stimulation), and changes relative to slow rate values produced minimal additional outward current at fast rates.

Late I_{Na} , I_{CaL} , I_{NaCa} and I_{NaK} also showed CL dependent changes during steady state pacing (Figure 2.15A). I_{NaK} became more outward at fast rates. The changes in I_{NaK} were

dramatic, and the current density was relatively large. Thus, I_{NaK} was an important contributor to APD shortening at fast pacing rates. Late I_{Na} became dramatically less inward at fast rates, making it a secondary contributor to APD shortening at fast rates. Changes in I_{CaL} and I_{NaCa} opposed APD shortening at fast rates; these currents became more inward at short CLs. I_{NaCa} increased to match the increased Ca^{2+} extrusion burden. Importantly, I_{CaL} increased despite reduced channel availability. I_{CaL} inactivation gates recovered less between beats as pacing rate increased (~20% less at CL = 300 ms compared to CL = 2000 ms). The same mechanism caused reduced late I_{Na} at fast rates (availability at CL = 300 ms was ~1/3 that at CL = 2000 ms). However, influences of increased CaMK facilitation combined with increased driving force (reduced maximum V_m) actually caused I_{CaL} to become larger at fast rates.

If Na^+ is clamped to small values associated with slow pacing ($[Na^+]_i$ and $[Na^+]_{ss} = 6.2$ mM at CL = 2000 ms), preventing its accumulation at fast rates, I_{NaK} remains small and CL independent (this mechanism is described later in detail), causing plateau voltages to become relatively CL independent. Thus, with Na^+ clamp, I_{CaL} changes with pacing rate are different than under control conditions. CL independent plateau voltages confer CL independence to the driving force for plateau I_{CaL} . Na^+ clamping reduced Ca^{2+} (via I_{NaCa}) which reduced activated CaMK and thus I_{CaL} facilitation. An interesting consequence is that with Na^+ clamp, I_{CaL} changes with CL help to cause APD shortening at fast rates, whereas in control (i.e. no Na^+ clamp), I_{CaL} changes with CL oppose APD shortening.

During restitution, late I_{Na} , I_{to} , I_{CaL} , I_{Ks} and I_{NaCa} showed DI dependent changes (Figure 2.15B). Dramatically less inward late I_{Na} at short DIs helped shorten the APD. The mechanism was reduced availability due to residual inactivation at the start of the S2 beat. I_{CaL} was reduced for the same reason. This was evident during the plateau. CaMK facilitation did not depend on DI because Ca^{2+} accumulation (necessary for CaMK activation) is slow, occurring only after long term pacing to steady state. Similarly, Na^+ did not accumulate at short DIs, which kept I_{NaK} constant. Therefore, plateau potentials and I_{CaL} driving force during the plateau were relatively DI independent. Just as in the case of Na^+ clamp, these properties combined to allow reduced availability of I_{CaL} at short DI to dominate the behavior. However, reduced maximum V_m

increased the driving force during the time of peak I_{CaL} , which caused peak current to generally increase at short DIs. At extreme DI of 5 ms, the slow AP upstroke (i.e. reduced dV_m/dt) caused mild I_{CaL} inactivation coincident with activation, so the peak current was reduced compared to DI = 10 ms.

Changes in other currents (I_{to} , I_{Ks} and I_{NaCa}), though nonzero, were relatively minor due to timing. DI dependent changes that increased or reduced current during phase-1 of the AP had little effect on final repolarization time. The exception is I_{Kr} . I_{Kr} is large enough that early spiking helped shorten APD at very short DIs (detailed simulations follow).

Ionic Basis for APD Rate Dependence and Restitution

Steady state rate dependence of the APD was largely caused by accumulation of intracellular Na^+ at fast rates. This is illustrated in Figure 2.16A. When $[Na^+]_i$ and $[Na^+]_{ss}$ were clamped to values from steady state pacing at CL = 2000 ms, APD lost much of its sensitivity to pacing rate and remained relatively long. Conversely, when the clamp was to $[Na^+]_i$ and $[Na^+]_{ss}$ from steady state pacing at CL = 300 ms, the APD remained relatively short at all rates. Pacing rate dependent $[Na^+]_i$ and $[Na^+]_{ss}$ changes are linked to the AP via I_{NaK} , which responds to $[Na^+]_i$ levels. I_{NaK} increased with $[Na^+]_i$ at fast rate. However it did not increase, regardless of the pacing rate, when $[Na^+]_i$ and $[Na^+]_{ss}$ were kept low (Na^+ at CL = 2000 ms; Figure 2.16C, right). Moreover, APD remained long at all CLs when I_{NaK} was clamped to its slow rate waveform (not shown).

Steady state APD rate dependence was not completely eliminated by Na^+ clamp alone. That is, clamping $[Na^+]_i$ and $[Na^+]_{ss}$ to slow rate values did not cause APD curves to become absolutely flat with respect to CL, especially at fast pacing rates (Figure 2.16A, shaded box CL = 300 to 700 ms, solid gray line). This signifies that other mechanisms are involved. When in addition to clamping $[Na^+]_i$ and $[Na^+]_{ss}$ to their slow rate values, we also reset the inactivation gates for late I_{Na} , and especially for both late I_{Na} and I_{CaL} to their CL = 2000 ms values at the start of each beat, the APD curve flattened further at fast rates (Figure 2.16A, dashed gray and

dashed-dot-dot gray lines, respectively). Importantly, resetting these inactivation gates alone, without also clamping Na^+ , had little effect on APD rate dependence (Figure 2.16B).

As described previously, without Na^+ clamp, fast pacing caused late I_{Na} reduction and I_{CaL} increase; the former helped while the latter opposed APD shortening. However, with Na^+ clamp, both currents became less inward with fast pacing. Thus, resetting I_{CaL} inactivation gates to slow rate values had different effects with, versus without Na^+ clamping. Na^+ clamp prolonged the APD. The prolongation and changed I_{CaL} behavior after Na^+ clamp rendered late I_{Na} and I_{CaL} gate resetting more potent effectors of further AP prolongation; especially at fast rates where residual inactivation between beats was substantial.

Rate dependent Na^+ changes only occurred with the steady state pacing protocol due to slow ion accumulation after lengthy pacing regimes. For APD restitution, clamping $[\text{Na}^+]_i$ and $[\text{Na}^+]_{\text{ss}}$ to values from S1 pacing during the S2 beat did not affect APD (Figure 2.16E). However, restitution was dramatically affected by resetting inactivation gates for late I_{Na} and/or I_{CaL} to their S1 starting values at the start of the S2 beat (Figure 2.16D). APD remained long for all DIs. Conversely, when late I_{Na} and/or I_{CaL} inactivation gates were reset to S2 starting values for DI = 5 ms, APD remained short for all DIs. Again, resetting these inactivation gates to their slow rate values had only minor effects on steady state APD rate dependence (Figure 2.16B).

At very short DIs, I_{Kr} played an important role in APD restitution. In Figure 2.17A, the fast and slow time dependent deactivation gates (x_{rfast} and x_{rslow} , respectively) were reset to their value at DI = S1 = 1000 ms (dashed gray line, compare to control solid black line). Deactivation of I_{Kr} is slow (Figure 2.03B). For DI = S1, deactivation was complete between beats. At short DIs, it was incomplete at the start of the S2 beat, enhancing I_{Kr} availability (early I_{Kr} spiking, Figure 2.17B, bottom) and outward current that contributes to APD shortening. The enhanced availability only mattered at very short DIs, because at these DIs APD was short enough that increased outward current during phase-1 of the AP affected final repolarization time. Changes to currents during later AP phases 2 and 3 (during the plateau and early repolarization, e.g. late I_{Na} and I_{CaL}), generally have greater impact on the APD. Early I_{Kr} spiking reduced maximum V_m , which affected all other currents, including late I_{Na} and I_{CaL} .

Results Subsection 3: Comparison with Other Human Ventricular AP Models

Several important differences exist between the ORd model presented here and other human models (e.g. TP(Ten Tusscher and Panfilov 2006) and GB(Grandi, Pasqualini et al. 2010) models). Notably, model differences in the rate of repolarization and EAD formation were examined in direct comparison with experiments (Figures 2.07C, and Figure 2.11A, respectively). Readers wishing to simulate the human ventricular AP have a choice of models. To help further differentiate the models, additional comparisons are shown in Figure 2.18.

Undiseased human ventricular measurements of steady state rate dependence of APD90, 70, 50 and 30 were accurately reproduced by the ORd model (Figure 2.18A, same data as in Figure 2.07A). Rate dependence of APD90 is fairly accurate in the TP model. However, rate dependence of APD70, 50 and especially APD30 are not accurate. The GB model repolarization rate is more accurate, but divergence from the measurements is large for APD30. At fast pacing rates, GB model APD90 is accurate. Slow pacing APD90 is long compared with experiments (at CL = 2000 ms, APD90 is ~40 ms longer than in experiments). In addition, APD rate dependence does not plateau at CL = 2000 ms.

In Figure 2.18B, the AP, major currents, and $[Na^+]_i$ and $[Ca^{2+}]_i$ were compared between models. Simulations were in single endo cells paced to steady state at CL = 1000 ms. Of note, the TP and GB models do not include late I_{Na} . The width of the I_{CaL} peak and the morphology were model dependent. It was “cigar shaped” in the TP model. In the GB model, the I_{CaL} peak was broad and poorly defined. The ORd model I_{CaL} peak was sharp, as seen in undiseased human ventricle experiments (AP clamp, Figure 2.01D). I_{Kr} was relatively small in the GB model, but shared a similar morphology with the ORd model. The TP I_{Kr} morphology is characterized by an early spike and a wider late spike. The I_{Ks} density in the TP model was much larger than in the other models (~10 fold larger). Density and morphology of I_{NaCa} was model dependent. I_{NaCa} was smallest in the ORd model (based on undiseased human measurements, Figure 2.02B). I_{NaK} was roughly 1.5 and 2 fold greater in GB and TP models, respectively, compared with ORd. The

Ca^{2+} transient peak was much larger in the TP model than in the other models, which were similar to each other. The decay rate of $[\text{Ca}^{2+}]_i$ was somewhat slower in the ORd model (accurate to undiseased human measurements; Figure 2.12 panels C and D). Model $[\text{Na}^+]_i$ was 7.2, 8.2, and 9.7 mM in ORd, GB, and TP models, respectively.

Discussion

Though the available undiseased human ventricle dataset has been missing essential elements, several human ventricle AP models have been developed and published. The Priebe and Beuckelmann model (Priebe and Beuckelmann 1998) lacks human specific data for reformulation of major currents, and so was based in large part on its guinea pig predecessor (Luo and Rudy 1994). The TP model (ten Tusscher, Noble et al. 2004) and updated version (Ten Tusscher and Panfilov 2006) is easy to use, includes many reformulated currents, and simulates physiological restitution and alternans. However, both the TP and GB (Grandi, Pasqualini et al. 2010) models lack sufficient I_{CaL} data for validation, and cannot produce EADs. The GB model includes K^+ current reformulations using undiseased human data for validation, but does not produce AP or Ca^{2+} transient alternans. EADs and alternans are both important mechanisms of arrhythmogenesis and should be reproduced in simulation studies of human arrhythmias. The Iyer et al. model (Iyer, Mazhari et al. 2004) is based almost entirely on data from human channels expressed in non myocytes. Though the expressed channels are human, native myocyte ion channels in the ventricle are composed of a variety of protein isoform combinations, auxiliary subunits, cytoskeletal elements, and membrane lipid composition, all of which may influence channel behavior. Anchoring and other regulatory proteins present in native cells also define the local environment for I_{CaL} in particular (Kobayashi, Yamada et al. 2007), but are not present in expression systems.

Fink et al. modified the TP model (Fink, Noble et al. 2008) to include updated I_{Kr} and I_{K1} (with $[\text{K}^+]_o$ dependence) formulations, based on undiseased human ventricular measurements. The rate of AP repolarization in this modified scheme is more accurate compared with the original

TP model. For these advantages, the model sacrifices runtime speed (Markov formulation is used for I_{Kr}). Other core issues of the TP model carry over to this modified version (incorrect I_{CaL} , non-physiologically large I_{Ks} , and no EAD generation under appropriate conditions).

We believe that the new undiseased human data presented here are essential, and substantially increase human specific model accuracy. Due to extensive validation using these new data, our model reproduces all of the following important physiological behaviors: 1) CDI versus VDI inactivation of I_{CaL} ; 2) reformulated, detailed and accurate kinetics (using weighted time constants) for I_{to} , I_{NaCa} , I_{K1} , I_{Kr} , I_{Ks} , fast I_{Na} , and late I_{Na} ; 3) AP repolarization rate from 30% to 90% repolarization; 4) APD at all physiological pacing rates with/without block of major currents, 5) APD restitution with/without block of delayed rectifier currents; 6) transmural heterogeneity causing upright pseudo-ECG T-wave; 7) early afterdepolarizations (EADs); 8) effects of CaMK; and 9) AP and Ca^{2+} transient alternans.

EADs and Repolarization Rate

One of the most important aspects of the model is its close correspondence to experimental measurements of not only APD90, but also to APD30, 50 and 70 at all physiologically relevant pacing rates and for S1S2 restitution. This large pool of data has previously been unavailable. Accurate repolarization rate (i.e. time between APD30 and 90) for the restitution protocol is crucial for simulating any phenomenon related to reentrant arrhythmia, where head-tail interactions determine refractoriness and vulnerability (Hund, Otani et al. 2000). Use of new undiseased data for currents that are active during the plateau and phase-3 of the AP (I_{CaL} , I_{NaCa} , I_{Kr} and I_{Ks}) contributed to the correct repolarization rate.

The rate of repolarization and its effects on I_{CaL} control EAD formation in this model, as in canonical EAD explanations (Zeng and Rudy 1995; Weiss, Garfinkel et al. 2010). Failure of the TP and GB models to reproduce EADs may be due in part to their accelerated repolarization rates (Figure 2.07C). It may also be caused by inaccurate formulation of I_{CaL} inactivation, developed in absence of the essential undiseased human data presented here.

Steady State APD Rate Dependence

Due to the small amplitude and rapid deactivation kinetics of I_{Ks} in the human ventricle in absence of β -adrenergic stimulation, it does not play a major role in determining APD, APD rate dependence, or APD restitution under basal conditions (Jost, Virag et al. 2005) (Figure 2.08). This is in contrast to guinea pig ventricle, where slower deactivation and larger amplitude I_{Ks} make it the most important current for steady state APD rate dependence (simulations (Faber and Rudy 2000) and experiments (Rocchetti, Besana et al. 2001)). Phosphorylation by PKA in the case of β -adrenergic stimulation greatly enhances both the activation rate and amplitude of I_{Ks} (Volders, Stengl et al. 2003). With β -adrenergic stimulation, I_{Ks} plays an important role in steady state APD rate dependence (Heijman, Volders et al. 2011). Clearly, I_{Ks} is important under various circumstances – the AP repolarizes in human ventricle experiments even when I_{Kr} is blocked (Jost, Virag et al. 2005), and clinical long QT syndrome type 1 is caused by I_{Ks} loss of function (Roden 2008). Typically, isolated myocyte patch clamp experiments underestimate I_{Ks} due to enzymatic degradation (Li, Feng et al. 1996). In ORd, the role of I_{Ks} was validated using small tissue preparations, where selective I_{Ks} block prolonged APD, but only very modestly under basal (no β -adrenergic stimulation) conditions (<15 milliseconds in experiments and simulations at CL = 1000 ms, Figure 2.08).

Block of I_{Kr} caused the most severe changes to the human AP (rate dependence and restitution, Figure 2.08). However, Chapter 2 Supplement Figure 2.S05, and Figure 2.15A show that I_{Kr} is rate independent, as in experiments (Jost, Acsai et al. 2009) and therefore was not responsible for causing APD changes with pacing rate. Rather, our simulations identified rate dependent changes in I_{NaK} secondary to $[Na^+]_i$ accumulation as a primary cause of APD rate dependence (Figure 2.16A, 2.16C). This finding is not new. Simulations in dog ventricle (Decker, Heijman et al. 2009), human atrium (Koivumaki, Korhonen et al. 2011), and in the GB human ventricle (Grandi, Pasqualini et al. 2010) models all led to this conclusion. However, findings from

the Iyer human model(Iyer, Mazhari et al. 2004) differ, at least in part, regarding this mechanism. In the Iyer model, $[Na^+]_i$ affected APD rate dependence via I_{NaCa} , which is primarily outward at fast rates. Rate dependence in the TP model(Ten Tusscher and Panfilov 2006) is less $[Na^+]_i$ dependent because, as Grandi discussed(Grandi, Pasqualini et al. 2010), I_{Ks} is exaggerated. Experiments by Pieske et al.(Pieske, Maier et al. 2002) investigated $[Na^+]_i$ in heart failure, versus nonfailing human ventricular myocytes. Pieske experiments demonstrate that rate dependent $[Na^+]_i$ accumulation is an important phenomenon in health and disease. However, additional experiments are needed to determine whether and how $[Na^+]_i$ affects I_{NaK} and APD in human ventricle.

In addition to I_{NaK} and I_{NaCa} (both included in the ORd model), intracellular Na^+ is also mediated by fluxes related to H^+ , CO_2 , and HCO_3^- homeostasis. Exchangers and cotransporters move Na^+ ions down the electrochemical gradient in order to offset the cost of H^+ and CO_2 and HCO_3^- pumping. Na^+ rate dependent handling and consequently I_{NaK} should be affected by these processes, which were not explicitly included in the ORd model. In the absence of H^+ , CO_2 , and HCO_3^- fluxes, it is possible that the role of I_{NaK} might have been over estimated. It is important to address this because I_{NaK} and its response to Na^+ accumulation was a major cause of APD rate dependence in the model. Thus, we performed simulations where H^+ , CO_2 , and HCO_3^- effects on Na^+ were explicitly included, using Crampin and Smith equations(Crampin and Smith 2006) (Chapter 2 Supplement Figure 2.S12).

Quantitative details of Na^+ handling, I_{NaK} and APD rate dependence were affected when we included H^+ , CO_2 , and HCO_3^- handling processes. However, the qualitative outcomes were not affected. I_{NaK} increase with fast pacing, secondary to Na^+ accumulation, was still the primary determinant of APD rate dependence during steady state pacing.

Removal of the effects of Na^+ accumulation on steady state APD rate dependence by clamping $[Na^+]_i$ and $[Na^+]_{ss}$ did not completely eliminate APD rate dependence. Especially at fast rates (Figure 2.16A, shaded box CL = 300 to 700 ms, solid gray line), APD was not absolutely flat with respect to CL. APD rate dependence was largely unaffected by resetting inactivation gates for late I_{Na} , and/or I_{CaL} to their slow rate values at the start of each beat (Figure 2.16B).

Interestingly, if these gates were reset while also clamping Na^+ to slow rate values, the APD-CL curve became almost completely flat, even at fast rates (Figure 2.16A, dashed gray and dashed-dot-dot gray lines, respectively). Thus, accumulation of Na^+ and consequent effects on I_{NaK} is a major cause of APD rate dependence, however, not the only cause. Other currents also participate at fast pacing rates. Though the GB model (Grandi, Pasqualini et al. 2010) demonstrated the $\text{Na}^+/I_{\text{NaK}}/\text{APD}$ rate dependence mechanism, it did not show the additional effects of late I_{Na} and I_{CaL} . The GB model cannot show these multi-factorial causes of APD rate dependence because it does not include late Na^+ current (Figure 2.18), and because I_{CaL} kinetics are inaccurate due to lack of experimental data.

Due to charge conservation, accumulation of $[\text{Na}^+]_i$ is associated with an equal reduction in $[\text{K}^+]_i$ and a volume converted $[\text{K}^+]_o$ increase in tissue clefts and interstitial spaces (Livshitz and Rudy 2009). This can affect behavior by increasing I_{K1} (its $[\text{K}^+]_o$ sensitivity is included in this model), which depolarizes resting voltage and reduces excitability. However, our simulations represent experiments in an isolated myocyte in a large bath, where $[\text{K}^+]_o$ is constant. Even *in vivo*, $[\text{K}^+]_o$ is tightly controlled via regulation by the lymphatic system and kidneys.

APD Restitution

We showed that in contrast to steady state rate dependence, $[\text{Na}^+]_i$ had no effect on APD restitution. Rather, restitution was primarily caused by the time course of recovery from inactivation of late I_{Na} and I_{CaL} ; processes which had little effect on steady state-rate dependence of APD (absent Na^+ clamp). At very short DIs, slow deactivation of I_{Kr} caused increased availability and spiking, which helped shorten the APD. APD rate dependence was caused primarily by concentration changes, while APD restitution was caused by gating kinetics. Previous studies have not made this important distinction between steady state rate dependence and restitution mechanisms in human. The role of I_{CaL} and its inactivation kinetics in APD restitution reiterates the primacy of I_{CaL} in determining basic physiological behaviors, highlighting

the importance of the new I_{CaL} experimental data, presented here, to model development and validation.

A role for late I_{Na} in restitution could not have been hypothesized using TP or GB models, which have no late I_{Na} . The density of late I_{Na} was constrained in the ORd model by experiments from nonfailing human ventricular myocyte measurements by Maltsev et al. (Maltsev, Sabbah et al. 1998), where the late current was measured 200 ms after the start of the voltage clamp step ($\sim 0.35 \mu A/\mu F$ I-V curve maximum). The maximum late I_{Na} during the free running AP model was much smaller ($\sim 0.15 \mu A/\mu F$, about half the I-V curve maximum) even at slow pacing rates, where late I_{Na} was largest. Late current is difficult to measure directly, and it is possible that the current density was overestimated due to selection bias. That is, late I_{Na} is small, and not all cells produced measurable late current (2 of 3 myocytes (Maltsev, Sabbah et al. 1998)). However, we consider the model density of late I_{Na} to be accurate based on model reproduction of experiments which consistently showed substantial APD90 shortening following application of 10 μM mexiletine in undiseased human myocardium (90% late I_{Na} block in simulations, Figure 2.08A).

Ca²⁺ Cycling, CaMK and Alternans

Previously published human ventricle AP models have not incorporated the CaMK signaling pathway. Our human simulations show, as in dog simulations (Hund and Rudy 2004; Livshitz and Rudy 2007), that CaMK plays an important role in determining frequency dependence of Ca²⁺ cycling (Figure 2.13). The model also shows that the integrated electrophysiological consequence of CaMK effects on target channels is minimal. That is, CaMK suppression had only minor effects on APD rate dependence and AP morphology. At very fast pacing (CLs < 300 ms), the Ca²⁺ cycling consequences of CaMK phosphorylation were central to alternans formation. Suppression of CaMK eliminated alternans. CaMK related findings are in agreement with simulations using other models developed by our group (Livshitz and Rudy 2007), models from other groups (Iribe, Kohl et al. 2006), and experiments (Ji, Zhao et al. 2006).

However, experiments showing the effects of pharmacological suppression of CaMK on rate dependent behaviors (e.g. by Wehrens et al. (Wehrens, Lehnart et al. 2004) with KN-93 in rabbit) should be performed in human ventricular myocytes to validate model predictions.

Transmural Heterogeneity

The method used for implementation of the transmural cell types (M and epi cell), based on the thoroughly validated endo cell framework, was simplistic. That is, we considered that channel conductance was proportional to transmural gradients in mRNA or protein expression for alpha subunits of ion channels. Only in the case of I_{to} were functional current measurement data available (Nabauer, Beuckelmann et al. 1996). Staying within error bars for mRNA or protein data (Szabo, Szentandrassy et al. 2005; Gaborit, Le Bouter et al. 2007; Soltysinska, Olesen et al. 2009), channel conductances were modulated so that the simulated transmural AP differences were consistent with experiments (Drouin, Charpentier et al. 1995; Glukhov, Fedorov et al. 2010).

The effect of transmural heterogeneity of accessory β -subunits was not considered in the transmural cell type definitions. However, in the case of I_{Ks} , the KCNE1 β -subunit is transmurally heterogeneous. KCNE1 protein was about two times greater in M-cells compared to epi cells (Szabo, Szentandrassy et al. 2005). The presence of KCNE1 carries two important functional consequences 1) ~5 fold slower activation and 2) ~5 fold larger conductance (Sanguinetti, Curran et al. 1996). Therefore, theoretically, twice as much KCNE1 in M-cells may increase the variable stoichiometry ratio of KCNE1 to alpha subunit KCNQ1 (Nakajo, Ulbrich et al. 2010), slowing activation and increasing conductance. We conducted simulations to evaluate the influence of KCNE1 heterogeneity on I_{Ks} and the AP (Chapter 2 Supplement Figure 2.S13 and related text). Due to the small amplitude of human I_{Ks} in the absence of β -adrenergic stimulation, implementation of KCNE1 heterogeneity did not appreciably affect the AP (Chapter 2 Supplement Figures 2.S13 and 2.S19, where transmural APDs are shown to be relatively insensitive to changes in I_{Ks} conductance). Interestingly, the simulated effects of KCNE1 on activation rate and conductance offset one another. That is, slowed activation and larger

conductance in M-cells yielded I_{Ks} current that was remarkably close to the control case. Similar results were found for epi cell simulations: the effects of faster activation and reduced conductance were offsetting such that their combined effect was minimal.

APD Accommodation

Steady state rate dependence of APD and APD restitution were the focus of the simulations and experiments in this study. However, the time course of APD response to abrupt changes in pacing rate has been shown in human by Franz et al.(Franz, Swerdlow et al. 1988), and simulated in the TP model by Pueyo et al.(Pueyo, Husti et al. 2010) as a marker for arrhythmia risk. Simulations of APD accommodation in our model compare favorably to Franz experiments (same pacing protocols used in experiments were used in the simulations, Chapter 2 Supplement Figure 2.S14). Single exponential curves were fit to the time dependence of APD changes. For abrupt CL reduction from 750 to 480 ms, the time constant was 250 and 284 seconds in experiments and simulations, respectively. Time constants were 300 and 299 seconds in experiments and simulations, respectively, when CL was abruptly returned to 750 ms. When the CL reduction was more severe, from CL = 750 to 410 ms, the time constants were 252 and 165 seconds, in experiments and simulations, respectively. For return to CL = 750 ms, the time constants were 350 and 289 seconds, respectively. Pueyo used time to 90% accommodation to compare model with experiments demonstrating similar accuracy. Both simulation studies also show initial overshoot, or “notching”, as observed and described by Franz.

Parameter Sensitivity

As in Romero et al.(Romero, Pueyo et al. 2009), we performed a sensitivity analysis to determine factors participating in important model outputs, including 1) steady state APD90 rate dependence (Chapter 2 Supplement Figure 2.S15), 2) S1S2 APD90 restitution (Chapter 2

Supplement Figure 2.S16), 3) rate dependence of maximum (systolic) intracellular Ca^{2+} concentration (Chapter 2 Supplement Figure 2.S17), 4) rate dependence of intracellular Na^+ concentration (Chapter 2 Supplement Figure 2.S18), and 5) transmural cell type APD90 at steady state (Chapter 2 Supplement Figure 2.S19).

The findings from our analysis were similar to those shown by Romero et al. using the TP human AP model (Romero, Pueyo et al. 2009). That is, in ORd and TP models, I_{Kr} and I_{CaL} affect APD90 while I_{CaL} , I_{NaCa} , and I_{NaK} affect peak $[\text{Ca}^{2+}]_i$. One important difference is the role for I_{Ks} . A much larger role was played by I_{Ks} in the TP model (~10 fold larger density than in other human models, Figure 2.18B). In the TP model, I_{Ks} is responsible for steady state rate dependence of the APD (shown by Grandi et al. (Grandi, Pasqualini et al. 2010)).

I_{Kr} conductance changes affect APD90 substantially in our model. This was expected, since I_{Kr} is the largest outward current (also in experiments, Figure 2.08, and in Romero's analysis using the TP model). Though I_{Kr} affects APD, it is not responsible for its rate dependence. Conductance changes in I_{NaK} did not substantially affect APD90 because I_{NaK} is a relatively small current. Yet, rate dependent changes in I_{NaK} (secondary to Na^+ accumulation at fast rate) were the primary determinant of APD rate dependence. $[\text{Na}^+]_i$ at different pacing rates, and thus its relative changes with rate, was by far most sensitive to I_{NaK} conductance (Chapter 2 Supplement Figure 2.S18). This supports our strategy for setting I_{NaK} conductance to reproduce rate dependence of $[\text{Na}^+]_i$ in nonfailing human myocytes (Pieske, Maier et al. 2002).

Computational Tractability and Model Stability

To keep the ORd model computationally efficient and parameters well constrained, the Hodgkin-Huxley formalism was used in formulating current equations. This choice was made as a design principal with the thought that interested users can modularly replace any current or flux with more detailed Markov formulations of mutation or drug effects as desired (e.g. (Clancy and Rudy 1999; Silva and Rudy 2005)). Similarly, intracellular Ca^{2+} handling can be modified (e.g. more spatial detail, Markov ryanodine receptor implementation), or various signaling pathways

and related effects on ion channels can be added (e.g.(Hund and Rudy 2004; Saucerman, Healy et al. 2004; Heijman, Volders et al. 2011)). The basic ORd model has 41 state variables. In the absence of CaMK and its effects on target currents and fluxes, the number of state variables is 31.

Exclusion of Markov models increases parameter constraint. It also prevents the system of differential-algebraic equations from being overly stiff. This promotes model stability and computational tractability. Using the rapid integration technique described in the Chapter 2 Supplement (Computational Methodology section), the model arrives at true and accurate steady state in under one minute of runtime (~1000 beats are needed, depending on the CL, Visual C++ running on a desktop PC; more details in Chapter 2 Supplement). ORd equations are all smoothly varying functions, free of singularities and “if” conditionals. Thus, the model can readily be implemented in any of a variety of automated numerical integrators, such as Matlab (The MathWorks Inc.), CellML (<http://www.cellml.org/>), CHASTE(Bernabeu, Bordas et al. 2009), or CARP (CardioSolv LLC.).

Limitations

Direct measurement of I_{NaK} in the undiseased or nonfailing human ventricular myocyte is lacking. Therefore, I_{NaK} was validated by reproduction of important biophysical properties (Chapter 2 Supplement Figure 2.S07), and by reproduction of $[Na^+]_i$ rate dependence measured in nonfailing human ventricular myocytes ((Pieske, Maier et al. 2002), Figure 2.12A). However, independent and direct experimental measurement of I_{NaK} in undiseased or nonfailing human ventricular myocytes would provide additional support for the mechanistic conclusion that I_{NaK} changes secondary to Na^+ accumulation at fast pacing rates is a major determinant of steady state APD rate dependence. This conclusion is consistent with several other modeling studies which proposed the same mechanism (dog ventricle(Decker, Heijman et al. 2009), human atrium(Koivumaki, Korhonen et al. 2011), and human ventricle(Grandi, Pasqualini et al. 2010)). The relationship between $[Na^+]_i$, I_{NaK} and steady state APD rate dependence was robust. It was

not disrupted by including the effects of Na^+/H^+ and $\text{Na}^+/\text{HCO}_3^-$ exchange fluxes on Na^+ handling (Crampin and Smith equations(Crampin and Smith 2006), Chapter 2 Supplement Figure 2.S12). Na^+ accumulation and I_{NaK} response were not the only cause of APD rate dependence in the ORd model. At fast pacing rates (CL = 300 to 700 ms), late I_{Na} and I_{CaL} were also involved (Figure 2.16A, and related discussion).

Measurements of undiseased human endocardial APs were performed in small tissue preparations (1-3 gram pieces). This was to avoid possible enzymatic degradation of K^+ channel proteins(Li, Feng et al. 1996; Rajamani, Anderson et al. 2006), affecting currents and the AP. However, electrical loading in tissue subtly affects behavior(Decker, Heijman et al. 2009). We performed simulations using a multicellular fiber model to include loading effects, which had only minor consequences (Figure 2.S08).

APD was ~275 ms in our human endo preparations at CL = 1000 ms, well matched by the model (273 ms). *In vivo* noninvasive electrocardiographic imaging of the activation-recovery interval, an indicator of the cellular epi APD, was ~260 ms in healthy adults(Ramanathan, Jia et al. 2006). Human monophasic AP measurements are also in this range(Koller, Maier et al. 2005). Measurements from Drouin et al. showed longer APDs (~350 ms in endo cells on the cut transmural face at CL = 1000 ms). Having validated the endo model based on more than 100 of our own endo AP measurements, we thought it reasonable to use Drouin transmural APD ratios, rather than the uniformly longer APDs themselves, for validation of the transmural cell type models.

The presence of M cell APs in the nonfailing human heart was observed by Drouin et al.(Drouin, Charpentier et al. 1995), and more recently by Glukhov et al.(Glukhov, Fedorov et al. 2010). However, there is controversy regarding the M cell definition and its role in human. Our M cell model was based on data where the M cell was defined by its transmural location. The resulting simulated M cell AP corresponded with the “max cell” observed by Glukhov.

Recently, Sarkar and Sobie developed a method for quantitative analysis of parameter constraint and relationships between parameters and target outputs in AP models(Sarkar and Sobie 2010). We did not apply this analysis during model development. However, the extensive

validation of channel kinetics and the emergent response of the AP to a variety of dynamic pacing protocols, used in development and validation of the model, ensures sufficient parameter constraint. The parameter sensitivity tests we performed were instructive, though relatively limited (conductance changes only). Application of the Sarkar and Sobie's analysis to our model is beyond the scope of this paper, but should provide worthwhile insights regarding inter-relatedness of processes in the human ventricle, in addition to formally testing parameter constraint.

Materials and Methods

Characteristics of Human Tissue

During the last 15 years, undiseased hearts were donated for research in compliance with the Declaration of Helsinki and were approved by the Scientific and Research Ethical Committee of the Medical Scientific Board of the Hungarian Ministry of Health (ETT-TUKEB), under ethical approval No 4991-0/2010-1018EKU (339/PI/010). Data from 140 hearts were used in this study. Of these, 78 were from male donors (56%). The average donor age was 41 years old with standard deviation of 12 years.

Tissue Preparation

Tissue transport and ventricular endocardial preparations were performed as previously described (Jost, Virag et al. 2005). Tissue was carefully pinned and placed in a modified Tyrodes superfusate (in mM: NaCl 115, KCl 4, CaCl₂ 1.8, MgCl₂ 1, NaHCO₃ 20, and glucose 11, pH 7.35, 37° C), and point stimulation was via bipolar platinum electrodes. Drug solutions were made fresh on the day of use. Drugs included in this study were, in μM: E-4031 1, HMR-1556 1, nisoldipine 1, BaCl₂ 100, ryanodine 5, mexiletine 10. Simulated application of these drugs was

70% I_{Kr} (Sanguinetti and Jurkiewicz 1990), and 90% I_{Ks} (Gogelein, Bruggemann et al. 2000), I_{CaL} (Walsh, Zhang et al. 2007), I_{K1} (Warren, Guha et al. 2003), RyR (Nanasi, Sarkozi et al. 2000), and late I_{Na} (Wang, Yazawa et al. 1997) block, respectively.

Myocyte Isolation

Tissue transport and myocyte isolation for the undiseased donor hearts were as previously described (Jost, Virag et al. 2005). Myocyte isolation commenced immediately upon arrival in the laboratory, using the perfusion disaggregation procedure, previously described (Jost, Virag et al. 2005).

Electrophysiology

Data were obtained using conventional whole cell patch-clamp techniques. Micropipette fabrication and data acquisition were as described previously for undiseased donor heart (Jost, Virag et al. 2005). Axopatch 200 amplifiers, Digidata 1200 converters, and pClamp software were used (Axon Instruments/Molecular Devices). Experiments were performed at 37° C.

The standard bath solution contained, in mM: NaCl 144, NaH_2PO_4 0.33, KCl 4.0, CaCl_2 1.8, MgCl_2 0.53, Glucose 5.5, and HEPES 5.0 at pH of 7.4, and pipette solutions contained K-aspartate 100, KCl 25, K_2ATP 5, MgCl_2 1, EGTA 10 and HEPES 5. The pH was adjusted to 7.2 by KOH (+15-20 mM K^+).

For L-type Ca^{2+} current measurement, the bath solution contained in mM: tetraethylammonium chloride (TEA-Cl) 157, MgCl_2 0.5, HEPES 10, and 1 mM CaCl_2 , or BaCl_2 , or SrCl_2 (pH 7.4 with CsOH). The pipette solution contained (in mM) CsCl 125, TEA-Cl 20, MgATP 5, creatine phosphate 3.6, EGTA 10, and HEPES 10 (pH 7.2 with CsOH).

For $\text{Na}^+/\text{Ca}^{2+}$ exchange current measurement, the bath solution contained, (in mM): NaCl 135, CsCl 10, CaCl_2 1, MgCl_2 1, BaCl_2 0.2, NaH_2PO_4 0.33, TEACl 10, HEPES 10, glucose 10

and (in μM) ouabain 20, nisoldipine 1, lidocaine 50, pH 7.4. The pipette solution contained (in mM): CsOH 140, aspartic acid 75, TEACl 20, MgATP 5, HEPES 10, NaCl 20, EGTA 20, CaCl₂ 10 (pH 7.2 with CsOH).

Ca²⁺ Transient Florescence

Isolated myocytes from the undiseased donor hearts were used to measure the Ca²⁺ transient during point stimulation via bipolar platinum electrodes, indicated by Fura-2-AM, as was described previously (Acsai, Kun et al. 2007). Bath temperature was 37° C.

Pacing Protocols

For both experiments and simulations, we determined APD at 30, 50, 70 and 90% of complete repolarization (APD₃₀₋₉₀, in ms). The start of the AP was the time of maximum dV_m/dt . The time of APD_X occurred once membrane voltage was X% of the resting value. Resting voltage was measured immediately prior to each paced beat. For APD rate dependence, pacing was to steady state. For APD restitution (S1S2, or static restitution), S1 pacing was at cycle length (CL) = 1000 ms. The S2 beat was delivered at variable diastolic intervals (DIs), measured relative to APD₉₀.

The dynamic restitution protocol was simulated as in experiments by Koller et al. (Koller, Maier et al. 2005). Pacing was at a variety of rates (30 seconds at CLs from 230 to 1000 ms, no S2 beats). APD₉₅ was plotted against DI (where DI = CL – APD₉₅). Unlike static S1S2 restitution, the dynamic restitution protocol allows for more than one APD to be associated with a given DI. This is significant because bifurcation in the dynamic restitution curve is believed to be arrhythmogenic (Watanabe, Otani et al. 1995).

Population Based CaMK effects

For all channels affected by CaMK, we created separate models for the fully CaMK phosphorylated channels, and the totally non phosphorylated channels. Then, based on the degree of CaMK activation ($\text{CaMK}_{\text{active}}$), we determined the proportion of channels affected by CaMK. To calculate the CaMK affected current (or flux), we added the weighted sum of fully affected and totally unaffected channels, using the proportionality. The model employed for CaMK activity was validated previously (Hund and Rudy 2004; Livshitz and Rudy 2007).

Relative Weights in a Two Time Constant Scheme

When measurements called for a gating process to be represented by both a fast and a slow process, we included separate fast and slow gates. However, we did not simply multiply fast and slow gates to modulate conductance as others have done previously. To do so allows the fast process alone to completely control deactivation/inactivation, and the slow process alone to completely control activation/recovery. Rather, since measurements of bi-exponential behaviors provide the relative weight of fast/slow processes, we modeled the measurements literally, and used the weighted sum of fast and slow processes.

Transmural Wedge Simulation

We computed the pseudo-ECG using a 1-dimensional model of the transmural wedge preparation (Yan and Antzelevitch 1996; Gima and Rudy 2002). In brief, the spatially weighted sum of the voltage gradient was determined at a point 2 cm from the epi end of a heterogeneous multicellular fiber, along the fiber axis. Cells 1-60 were endo, 61-105 were M, and 106-165 were epi. The stimulus was delivered to cell 1. Cells 15 from both ends of the fiber were excluded

from the gradient measurement due to confounding edge effects. Pacing was for 100 beats using steady state initial conditions from paced single cells.

Equations, Computers, and Software

All model equations, hardware and software used, and rapid integration methods are provided in the Chapter 2 Supplement. Model code can be downloaded from the research section of our website: <http://rudylab.wustl.edu>.

Figures

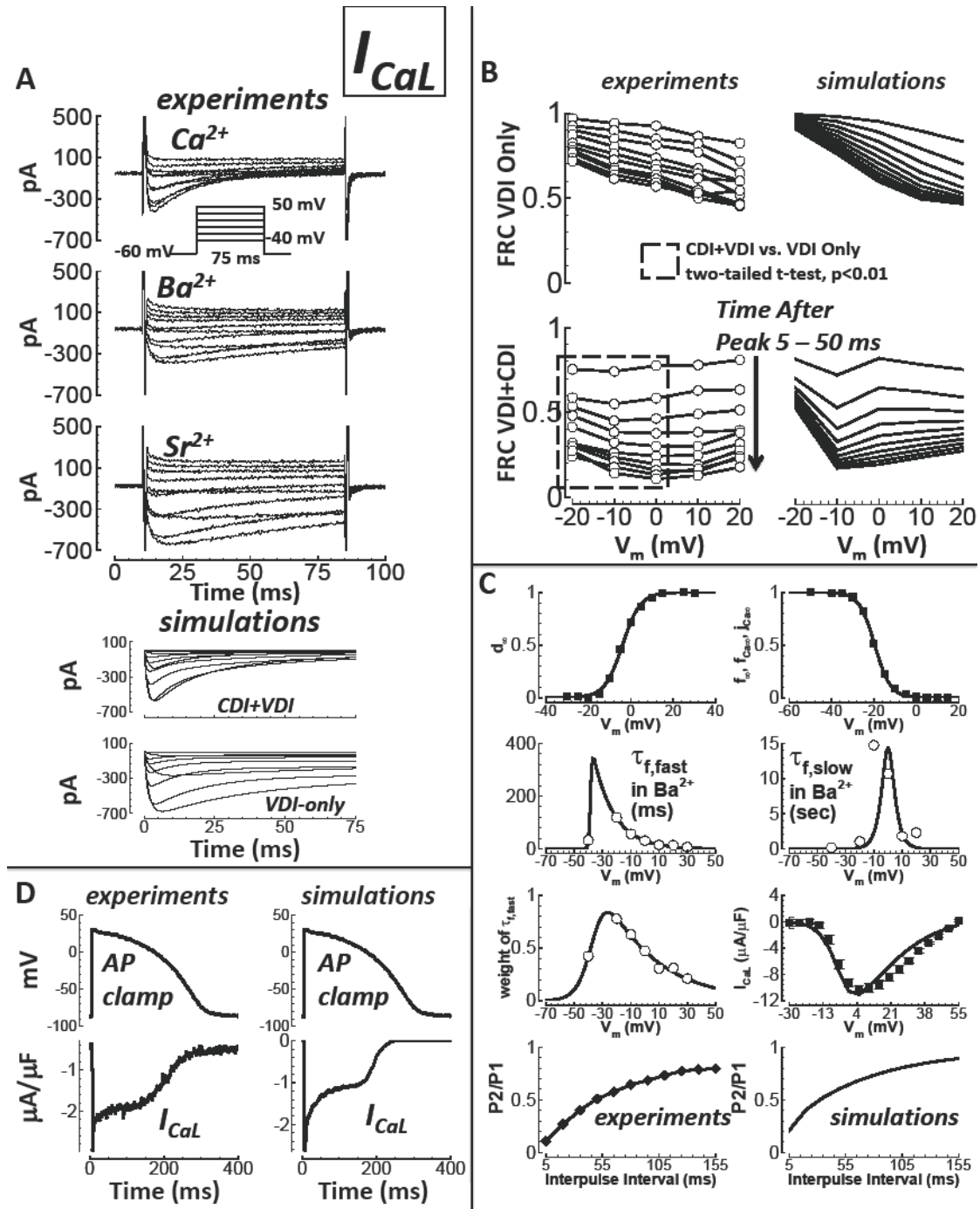


Figure 2.01. Undiseased human I_{CaL} experiments and model validation. A) Experiments: I_{CaL} traces for currents carried by Ca^{2+} (top), Ba^{2+} (middle), and Sr^{2+} (bottom). The voltage protocol is below the Ca^{2+} traces. Ca^{2+} current decay was visibly more rapid than decay for Ba^{2+} or Sr^{2+} currents. Simulations: I_{CaL} in response to the same voltage protocol with CDI (CDI+VDI, top), and without CDI (VDI-only, bottom). B) Experimental data are on the left (white circles, N=5, from 3 hearts). Simulation results are on the right (solid lines). FRC is fractional remaining current. Times after peak current shown are from 5 to 55 ms, in 5 ms steps (indicated by arrow). Top left) Experiments showing the voltage and time dependence of FRC with Ba^{2+} as charge carrier (VDI only). Top right) Simulations of FRC, with n-gate=0 (representing VDI only; see text and panel E). Bottom left) Experiments showing FRC with Ca^{2+} as charge carrier (CDI and VDI are concurrent). FRC for CDI+VDI was significantly smaller at more hyperpolarized potentials ($V_m = -20$ to 0 mV, dashed box) than FRC for VDI-alone. Bottom right) Simulations of FRC with free running n-gate, allowing both CDI and VDI to occur. C) Data are from Magyar et al. (Magyar, lost et al. 2000) (black squares), Fulop et al. (Fulop, Banyasz et al. 2004) (black diamonds), and previously unpublished (white circles, N=5, from 3 hearts). Simulation results are solid lines. From left to right, top to bottom: steady state activation, steady state inactivation, fast time constant for VDI, slow time constant for VDI, relative weight of the fast component for VDI, I-V curve, experiments showing recovery from inactivation, and corresponding simulations. D) Human AP clamp waveform, used to elicit 1 μ M nisoldipine sensitive current (I_{CaL} , experiments, left) and comparison to simulations using the same AP clamp (right). E) Schematic diagram for the n-gate, representing the fraction of L-type channels undergoing CDI. Calmodulin (CaM) is constitutively attached to the L-type channel. Ca^{2+} ions bind to CaM (on-rate k_1 and off-rate k_{-1}). With Ca^{2+} ions bound, the Ca^{2+} /CaM/channel complex may activate CDI mode (asterisk and black color indicate CDI activation, on-rate k_2 and off-rate k_{-2}).

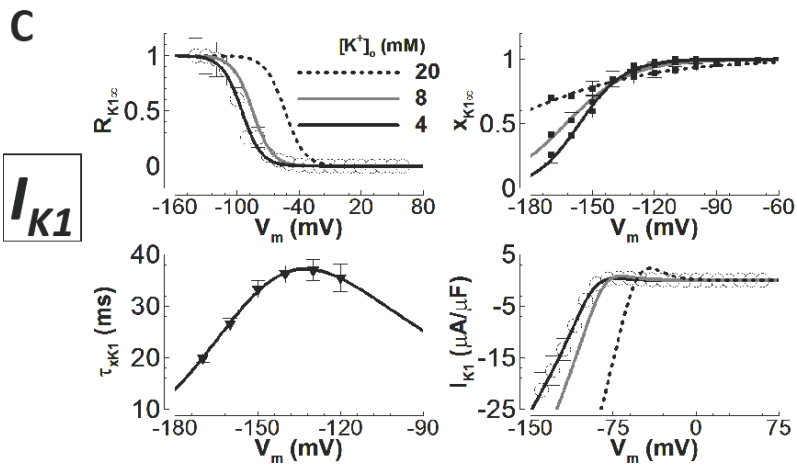
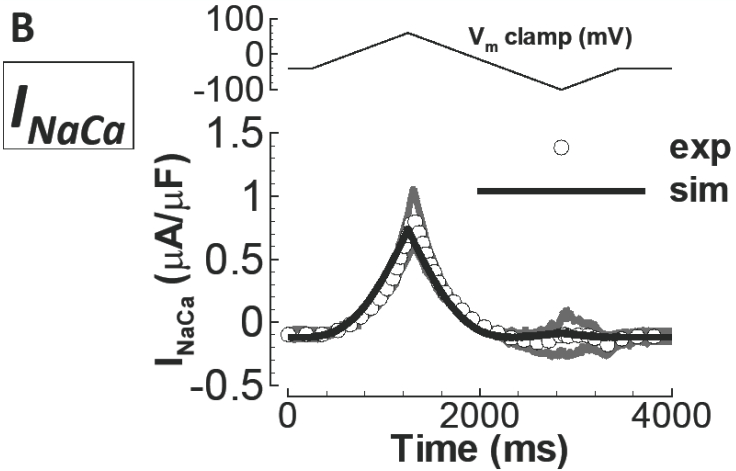
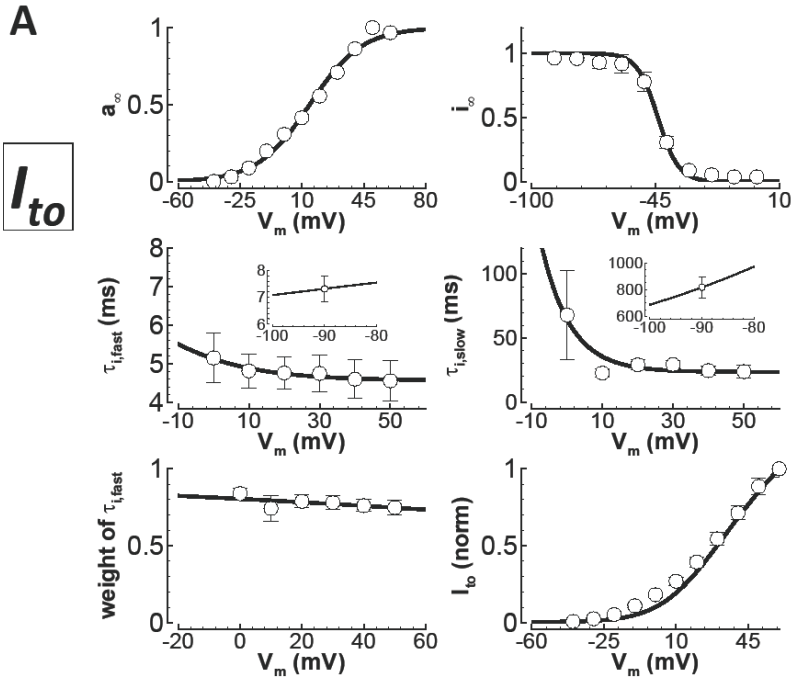


Figure 2.02. Undiseased human I_{to} , I_{NaCa} , and I_{K1} experiments and model validation. A) I_{to} . Experimental data are white circles (N=8 from 5 hearts for inactivation time constants, N=10 from 5 hearts for recovery time constants, N=9 from 6 hearts for steady state inactivation, and N=23 from 8 hearts for the I-V curve). Simulation results are solid lines. From left to right, top to bottom: steady state activation, steady state inactivation, fast time constant for inactivation, slow time constant for inactivation (insets show fast and slow recovery from inactivation), relative weight of the fast component for inactivation and the I-V curve (normalized). B) I_{NaCa} . Experimental data are digitally averaged time traces (N=3 from 2 hearts, white circles, gray is standard error of the mean). Simulation results are the solid line. Top) Voltage clamp protocol. Bottom) I_{NaCa} in response to the clamp. C) I_{K1} . Experimental data are previously unpublished (white circles, N=21 from 12 hearts), from Bailly et al. (Bailly, Mouchoniere et al. 1998) (black squares) and Konarzewska et al. (Konarzewska, Peeters et al. 1995) (black triangles). Simulation results are solid lines (black, gray and dashed black for $[K^+]_o = 4, 8$ and 20 mM). Top left) Voltage and $[K^+]_o$ dependence of steady state rectification. Top right) Voltage and $[K^+]_o$ dependence of steady state inactivation. Bottom left) Time constant for inactivation. Bottom right) I-V curve, and its $[K^+]_o$ dependence.

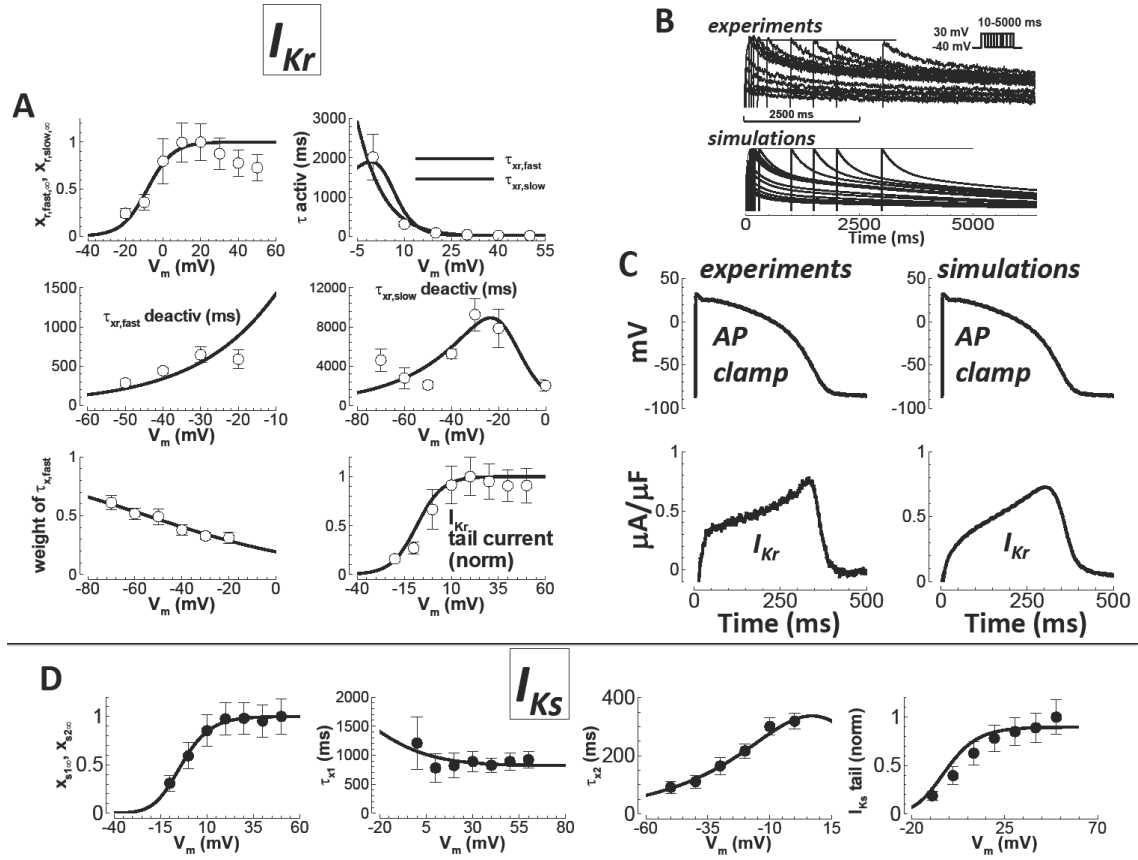


Figure 2.03. Undiseased human I_{Kr} and I_{Ks} experiments and model validation. A) I_{Kr} . Experimental data are white circles (N=10 from 7 hearts for steady state activation, N=7 from 3 hearts for activation and from 2 hearts for deactivation time constants and weights, and N=10 from 7 hearts for tail currents). Simulation results are lines. From left to right, top to bottom: steady state activation, time constant for activation (fast (solid) and slow (dashed) time constants converge), fast time constant for deactivation, slow time constant for deactivation, relative weight of the fast component for deactivation, and the I-V curve for normalized tail currents. B) Activation/deactivation profiles in response to the voltage steps shown (-40 mV holding potential to +30 mV steps of various duration, followed by a return to -40 mV, top right inset). Experiments are above. Simulations are below. Activation is rapid, occurring within tens of milliseconds. Deactivation is slow, occurring after several seconds. C) Human AP clamp waveform (top), used to elicit 1 μ M E-4031 sensitive current (I_{Kr} , bottom); experiments are on the left, and comparison to simulations using the same AP clamp is on the right. D) I_{Ks} . Data are from Virág et al. (Virag,

lost et al. 2001) (black circles). Simulation results are solid lines. From left to right: steady state activation, time constant for activation (much slower than deactivation at depolarized potentials), time constant for deactivation (much faster than activation at hyperpolarized potentials), and the I-V curve, showing normalized tail currents.

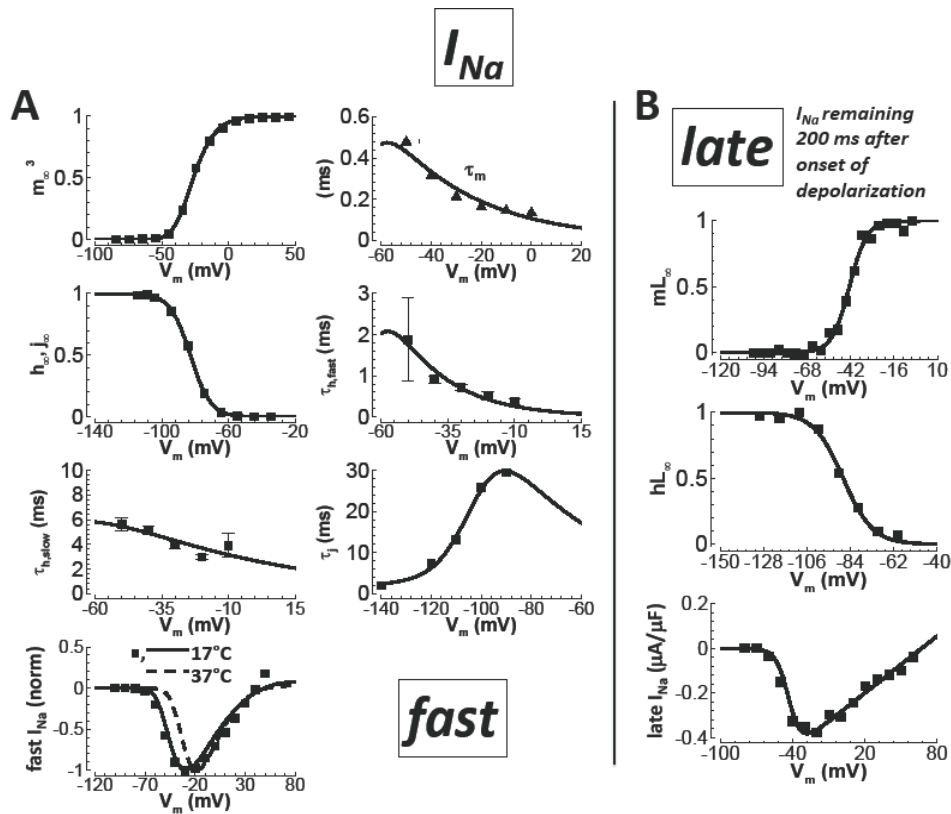


Figure 2.04. Nonfailing human fast I_{Na} and late I_{Na} experiments and model validation. A) Fast I_{Na} . Experiments are from Sakakibara et al.(Sakakibara, Furukawa et al. 1993) (black squares) and Nagatomo et al.(Nagatomo, Fan et al. 1998) (black triangles). Simulation results are solid lines. From left to right, top to bottom: steady state activation, time to peak (experiment) and activation time constant (simulation), steady state inactivation, fast time constant for development of inactivation, slow time constant for development of inactivation, relative weight of the fast component for development of inactivation, time constant for recovery from inactivation, and the I-V curve (solid line simulation and data at 17° C, dashed line simulation at 37° C). In other panels, simulations and data were adjusted to 37° C. Time to peak was fit at 33° C. B) Late I_{Na} . Experiments are from Maltsev et al.(Maltsev, Sabbah et al. 1998) (black squares). Simulation results are solid lines. Top) Steady state activation. Middle) Steady state inactivation. Bottom) I-V curve.

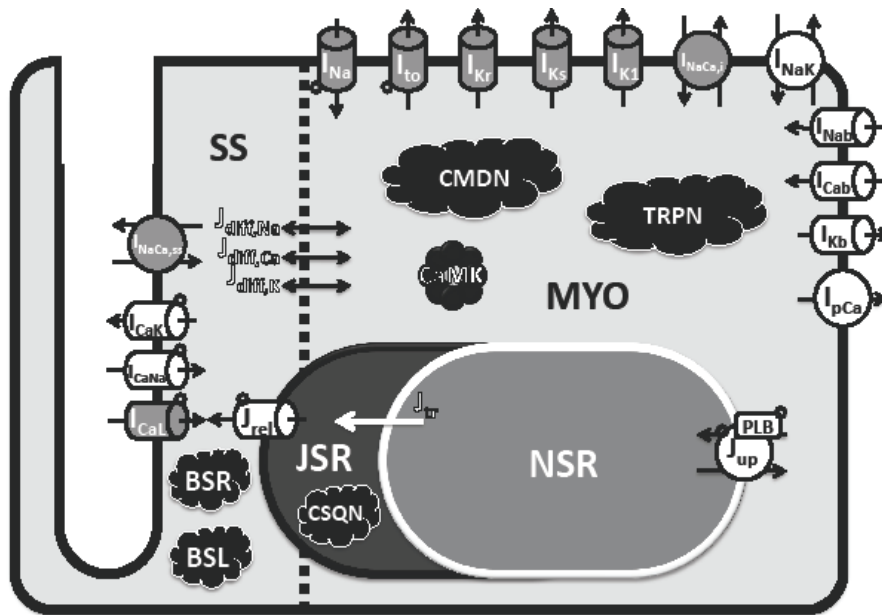


Figure 2.05. Schematic diagram of human ventricular myocyte model. Formulations for all currents and fluxes were based either directly (gray) or indirectly (white) on undiseased or nonfailing human experimental data. Model includes four compartments: 1) bulk myoplasm (myo), 2) junctional sarcoplasmic reticulum (JSR), 3) network sarcoplasmic reticulum (NSR), and 4) subspace (SS), representing the space near the T-tubules. Currents into the myoplasm: Na^+ current (I_{Na} ; representing both fast and late components), transient outward K^+ current (I_{to}), rapid delayed rectifier K^+ current (I_{Kr}), slow delayed rectifier K^+ current (I_{Ks}), inward rectifier K^+ current (I_{K1}), 80% of $\text{Na}^+/\text{Ca}^{2+}$ exchange current ($I_{\text{NaCa,i}}$), Na^+/K^+ pump current (I_{NaK}), background currents (I_{Nab} , I_{Cab} , and I_{Kb}), and sarcolemmal Ca^{2+} pump current (I_{pCa}). Currents into subspace: L-type Ca^{2+} current (I_{CaL} , with Na^+ and K^+ components I_{CaNa} , I_{CaK}), and 20% of $\text{Na}^+/\text{Ca}^{2+}$ exchange current ($I_{\text{NaCa,ss}}$). Ionic fluxes: Ca^{2+} through ryanodine receptor (J_{rel}), NSR to JSR Ca^{2+} translocation (J_{tr}), Ca^{2+} uptake into NSR via SERCA2a/PLB (J_{up} ; PLB - phospholamban), diffusion fluxes from subspace to myoplasm ($J_{\text{diff,Na}}$, $J_{\text{diff,Ca}}$, and $J_{\text{diff,K}}$). Ca^{2+} Buffers: calmodulin (CMDN), troponin (TRPN), calsequestrin (CSQN), anionic SR binding sites for Ca^{2+} (BSR), anionic sarcolemmal binding sites for Ca^{2+} (BSL). Ca^{2+} /calmodulin-dependent protein kinase II (CaMK) and its targets are labeled.

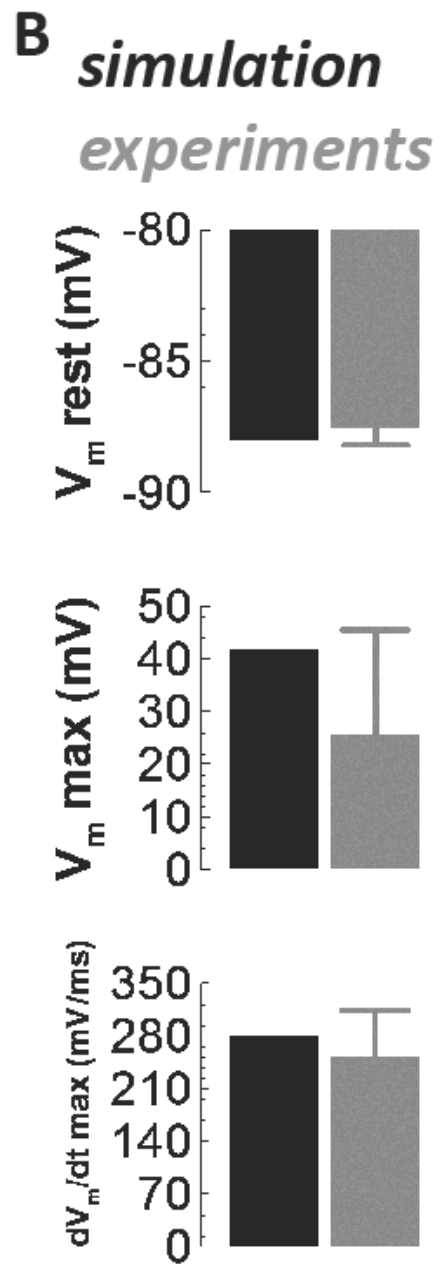
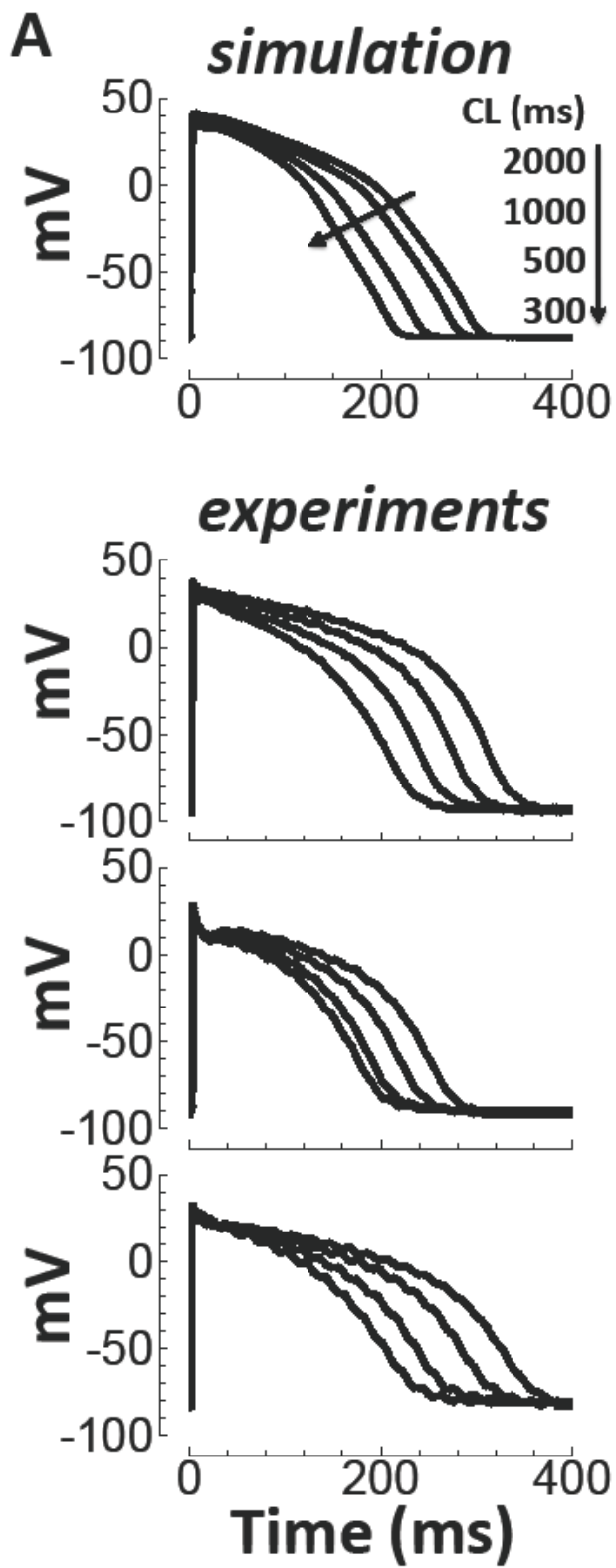


Figure 2.06. Undiseased human endocardial AP traces from experiments (small tissue preparations) and model simulations. Simulated APs for a range of pacing frequencies (top) and corresponding examples of experimentally recorded APs at 37°C (below). Arrows indicate cycle length (CL) changes. B) Comparison of simulation (black) and experimentally measured (gray, small tissue preparations) basic AP parameters for a single paced beat from quiescence (37°C, N=32 from 32 hearts). Shown, from top to bottom, are the resting membrane potential (V_m rest), maximum upstroke potential (V_m max), and maximum upstroke velocity (dV_m/dt max).

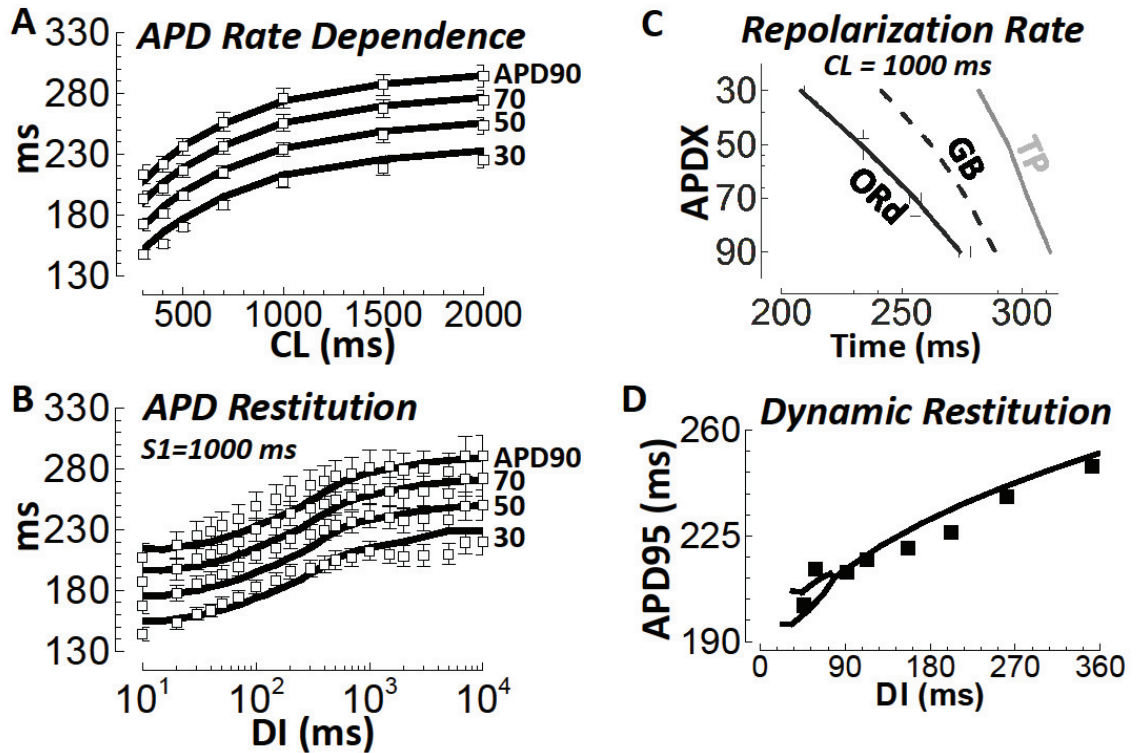


Figure 2.07. Undiseased human endocardial AP response to pacing protocols from experiments (small tissue preparations) and model simulations. A) Steady state APD rate dependence. B) S1S2 APD restitution (DI – diastolic interval). APD30-90 are labeled at right. Solid lines are simulation results; white squares are experiments at 37°C (N=140 hearts in panel A, N=50 hearts in panel B). C) Repolarization rate at CL = 1000 ms. Trajectory of APD30 to APD90 is accurate in the ORd model (circles are experimental data); less so in other models. D) Dynamic restitution protocol (see Methods). Experiments are from Koller et al. (Koller, Maier et al. 2005), measured in nonfailing human hearts with monophasic AP electrodes (black squares). Simulated results are the black line. At very short diastolic intervals (DI < 90 ms), the model shows APD bifurcation (alternans).

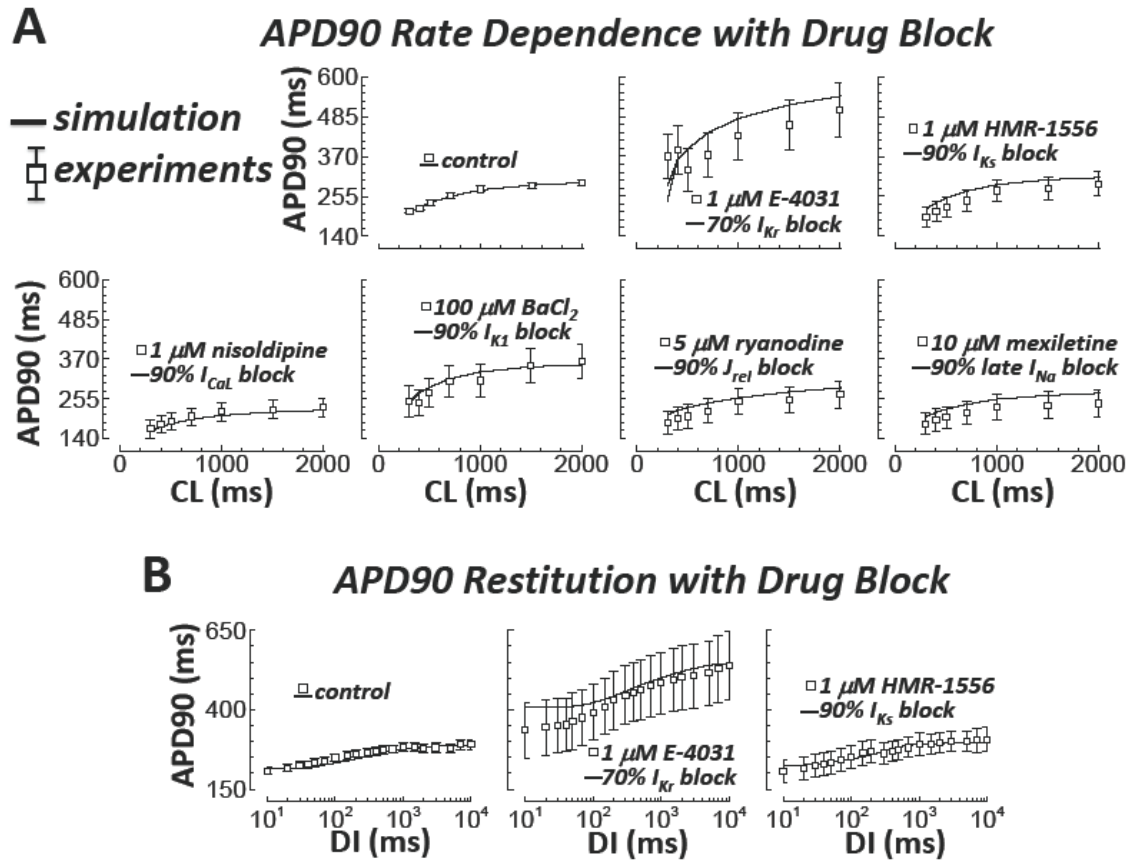


Figure 2.08. Pacing protocols with block of various currents. Experimental data (small tissue preparations) are white squares. A) Steady state APD90 rate dependence. From left to right, top to bottom: N=140, 5, 5, 5, 5, 4, and 4 hearts. Shown are control, I_{Kr} , I_{Ks} , I_{CaL} , I_{K1} , RyR, and late I_{Na} block. B) APD90 restitution (S1 = 1000 ms). From left to right: N=50, 3, and 4 hearts. Shown are control, I_{Kr} , and I_{Ks} block.

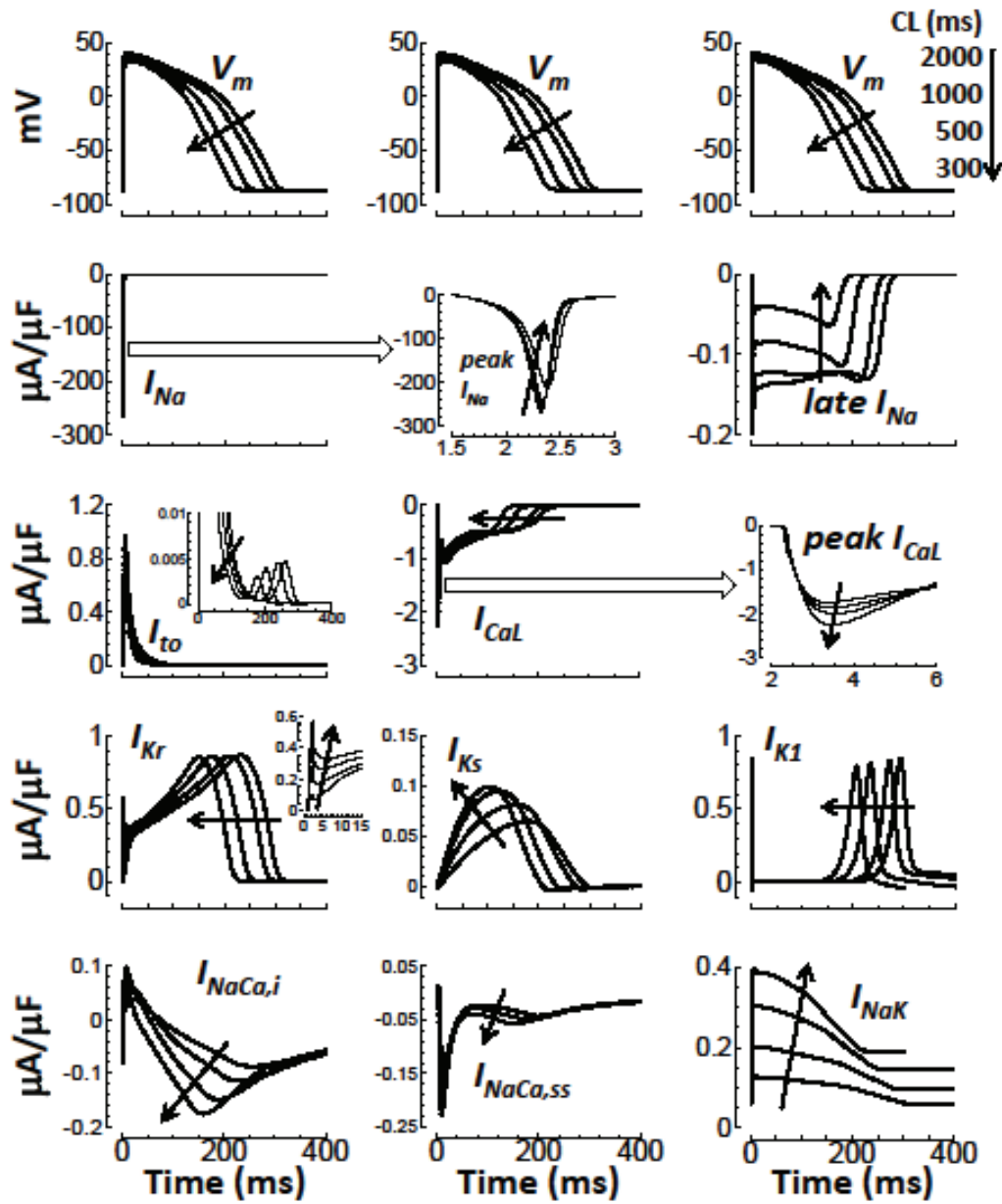


Figure 2.09. Rate dependence of currents at steady state. Black arrows indicate CL decrease (rate increase). Top Row) Simulated APs, repeated in each column for timing purposes. Lower Rows (left to right, top to bottom): I_{Na} , peak I_{Na} detailed time course, late I_{Na} , I_{to} , I_{CaL} , I_{CaL} increasing peaks with increasing pacing rate, I_{Kr} , I_{Ks} , I_{K1} , $I_{NaCa,i}$, $I_{NaCa,ss}$, and I_{NaK} . Insets show greater detail of late small I_{to} window current, and early I_{Kr} spiking at fast rates.

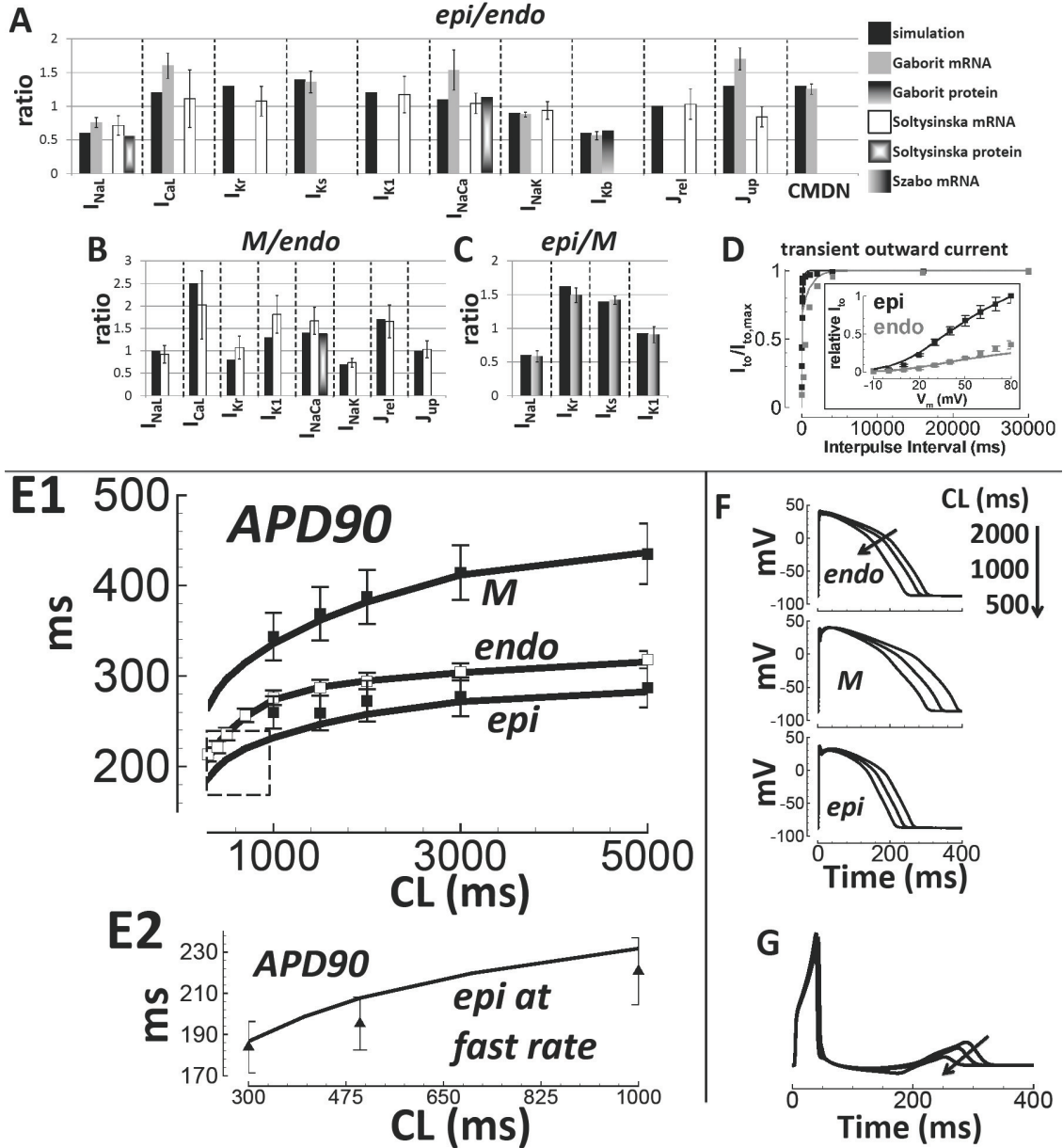


Figure 2.10. Transmural heterogeneity and validation of transmural cell type models. A-C) Expression ratio in the model (black bars) compared to experimental data from undiseased human hearts (grayscale bars, labeled). Data are from Gaborit et al. (Gaborit, Le Bouter et al. 2007), Soltysinska et al. (Soltysinska, Olesen et al. 2009), Szabo et al. (Szabo, Szentandrássy et al. 2005), and Nabauer et al. (for I_{to} , panel D, (Nabauer, Beuckelmann et al. 1996)). D) Transmural heterogeneity of I_{to} ; simulations are lines, experiments are squares. Results for endo are gray; those for epi are black. E1) Rate dependence of APD90 in endo, M, and epi cell types. Epi and M data were obtained by scaling endo data (white squares) by epi/endo and M/endo

APD90 ratios from Drouin et al.(Drouin, Charpentier et al. 1995) (black squares). Simulations are black lines. E2) Same format as panel E1, showing epi APD90 at faster pacing rates. Data are from Glukhov et al.(Glukhov, Fedorov et al. 2010), (epi/endo scaling, black triangles). F) Top to bottom: Rate-dependence of endo, M, and epi APs. G) Pseudo-ECG, using a simulated transmural wedge. CL changes are indicated by arrows.

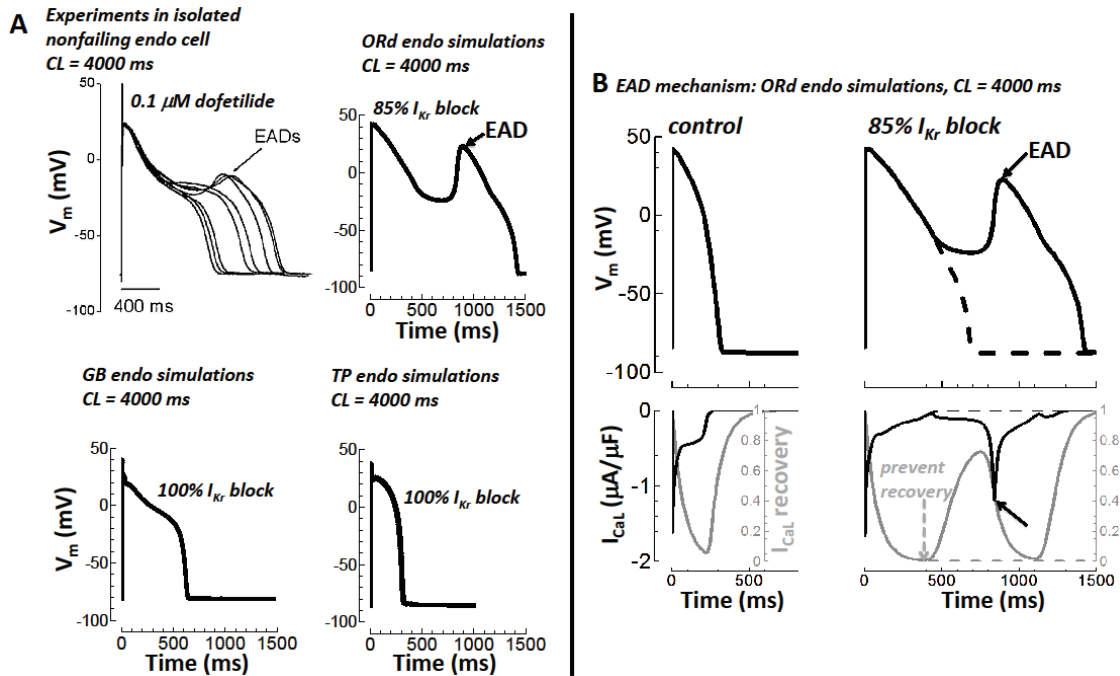


Figure 2.11. Early afterdepolarizations (EADs). A) Top left) Experiments in isolated nonfailing human endo myocytes from Guo et al.(Guo, Liu et al. 2011) showed EADs with slow pacing (CL = 4000 ms) in the presence of I_{Kr} block ($0.1 \mu\text{M}$ dofetilide, $\sim 85\%$ I_{Kr} block(Thomsen, Volders et al. 2003), reproduce with permission). Top right) Following the experimental protocol of Guo et al. (CL = 4000 ms, 85% I_{Kr} block) the ORd model accurately showed a single large EAD. Bottom) GB (left) and TP (right) models failed to generate EADs (CL = 4000 ms, even with 100% I_{Kr} block). B) EAD mechanism. APs are on top. I_{CaL} (black) and I_{CaL} recovery gate (gray) are below. Slow pacing alone (CL = 4000 ms) did not cause an EAD (left). Slow pacing plus I_{Kr} block (85%) caused an EAD (solid lines, right). The EAD was depolarized by I_{CaL} reactivation during the slowly repolarizing AP plateau (solid lines, solid arrows). When I_{CaL} recovery was prevented, the EAD was eliminated (dashed lines and dashed arrow).

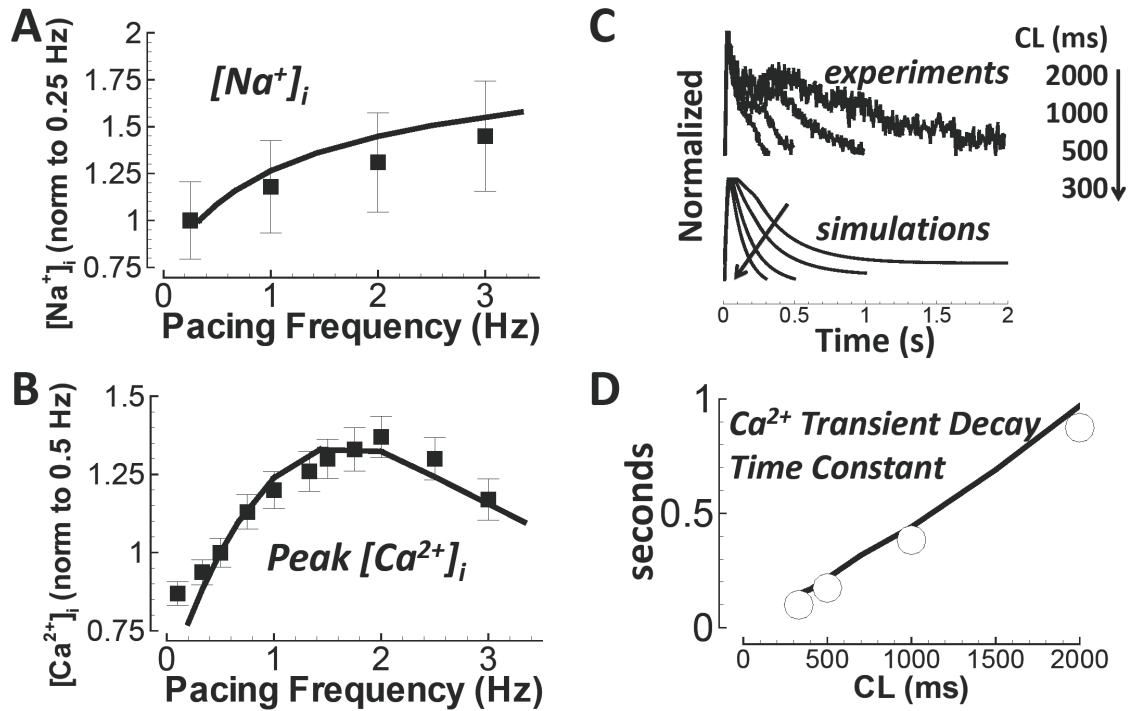


Figure 2.12. Rate dependence of intracellular ion concentrations. Simulation results are solid lines. A) $[Na^+]_i$ versus pacing frequency (normalized to 0.25 Hz). Experiments are from nonfailing myocytes (Pieske et al.(Pieske, Maier et al. 2002), black squares). B) Peak Ca^{2+} transient (normalized to 0.5 Hz). Experiments are from nonfailing myocytes (Schmidt et al.(Schmidt, Hajjar et al. 1998), black squares). C) Ca^{2+} transients from experiments (Fura-2-AM) and simulations. Results are normalized to illustrate the time course of decay. The arrow indicates pacing CL changes. D) Frequency dependent acceleration of relaxation. Undiseased human experimental data are white circles. Simulations are the black line.

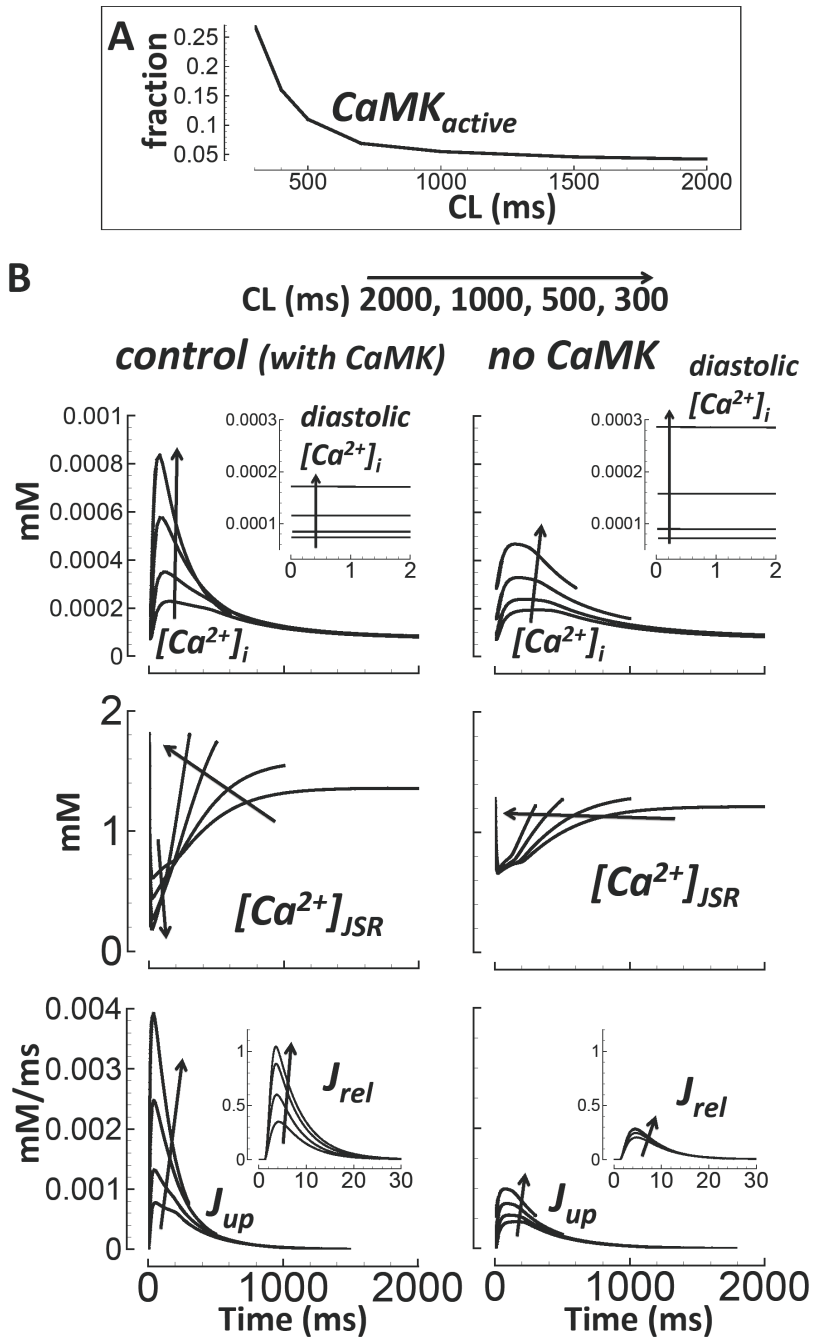


Figure 2.13. CaMK and Ca^{2+} cycling. A) Rate dependence of CaMK active fraction. B) Ca^{2+} cycling under control conditions (left) and without CaMK (right). CL changes are indicated by arrows. Top) $[Ca^{2+}]_i$ and diastolic values (inset). Middle) $[Ca^{2+}]_{JSR}$. Bottom) J_{up} and J_{rel} (inset, expanded time scale).

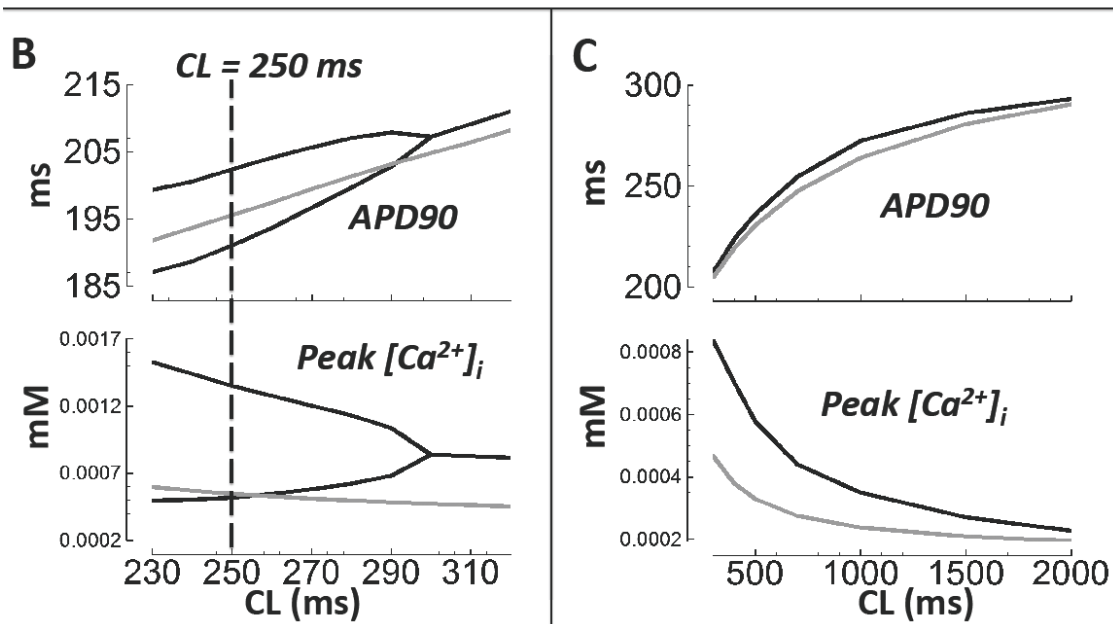
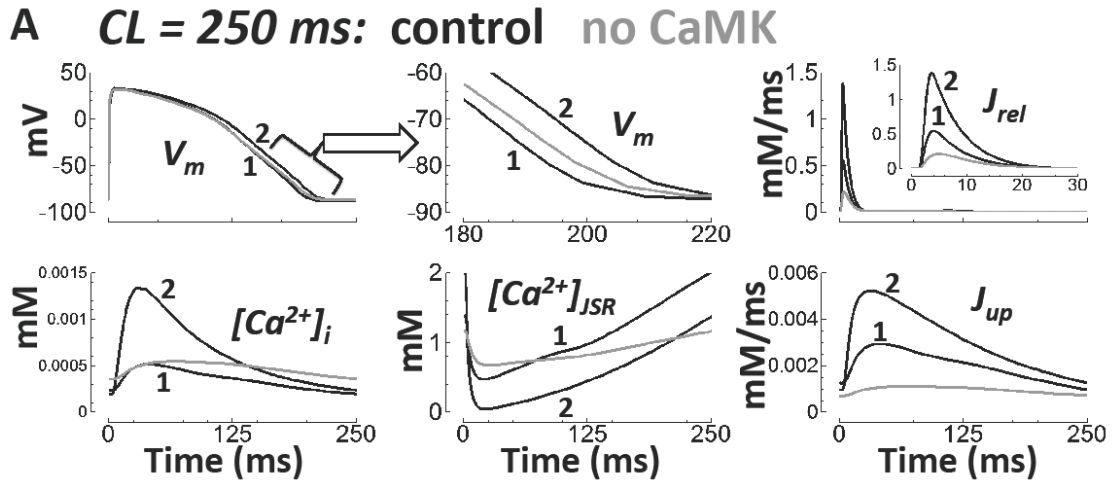


Figure 2.14. AP and Ca^{2+} alternans at fast pacing. Black lines are control. Gray lines are without CaMK. The two consecutive beats are labeled 1 and 2. A) Pacing at $CL = 250$ ms. From left to right, top to bottom: AP, expanded time scale showing AP repolarization, J_{rel} (inset is expanded time scale), $[\text{Ca}^{2+}]_i$, $[\text{Ca}^{2+}]_{JSR}$, and J_{up} . B) Rate dependence of APD (top) and peak $[\text{Ca}^{2+}]_i$ (bottom) at fast rates (alternans bifurcations disappear without CaMK). C) Same as panel B, but at slower rates (no bifurcations).

Figure 2.15. I-V curves during steady state rate dependent pacing at various CLs (panel A), and S1S2 restitution at various DIs (panel B). Arrows indicate decreasing CL or DI. From left to right, top to bottom, results for late I_{Na} , I_{to} , I_{CaL} , I_{Kr} , I_{Ks} , zoom of plateau I_{CaL} (dashed box section), I_{K1} , I_{NaCa} , and I_{NaK} are shown.

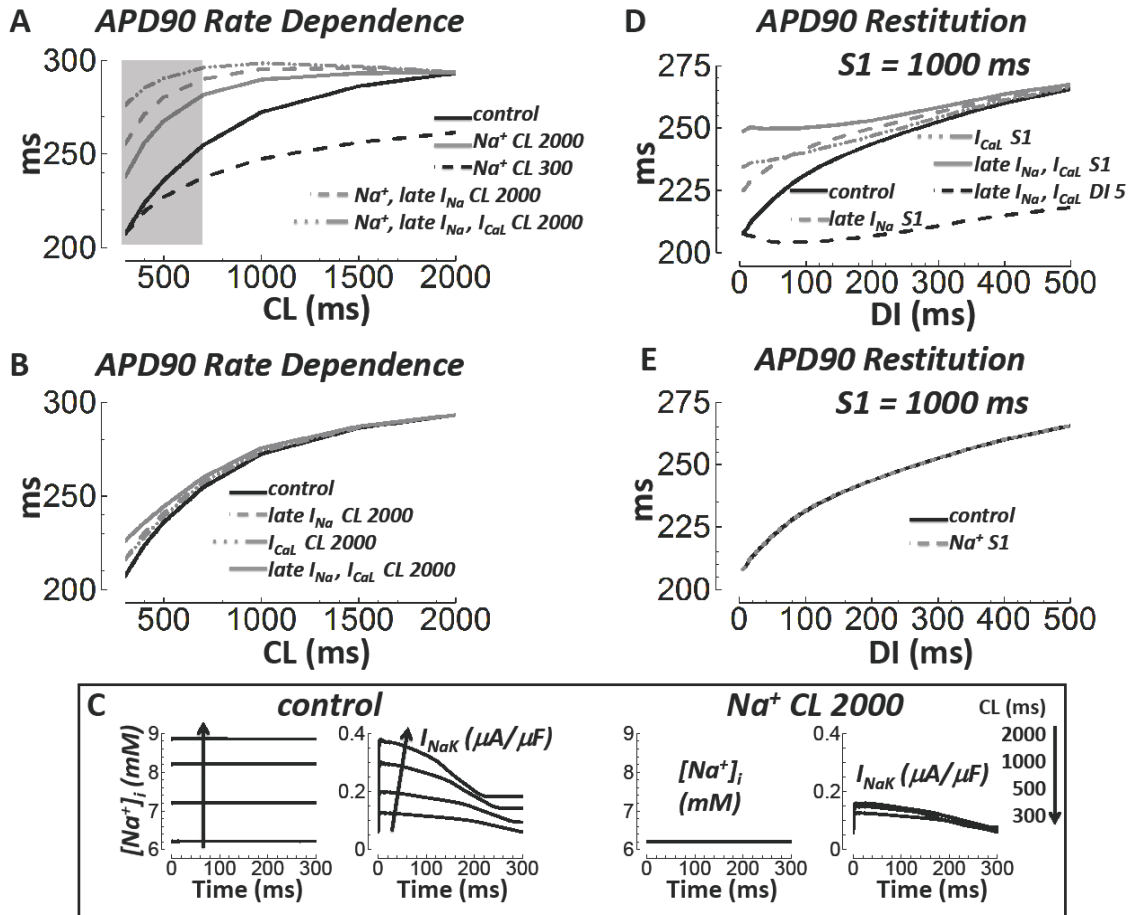


Figure 2.16. Major causes of steady state APD rate dependence and S1S2 APD restitution. A) APD rate dependence in control (solid black), and with $[Na^+]_i$ and $[Na^+]_{ss}$ clamped to slow rate (solid gray) or fast rate (dashed black) values. When late I_{Na} (dashed gray) or both late I_{Na} and I_{CaL} inactivation gates were reset to their slow rate values (dash-dot-dot gray) in addition to $[Na^+]_i$ and $[Na^+]_{ss}$ slow rate clamp, APD lost almost all rate dependence. Note that slow rate $[Na^+]_i$ and $[Na^+]_{ss}$ clamp alone left residual APD rate dependence, especially at fast rates (CL = 300 to 700 ms, shaded box). B) APD rate dependence (control, solid black) was largely unaffected by resetting inactivation gates for late I_{Na} (dashed gray), I_{CaL} (dash-dot-dot gray), or late I_{Na} and I_{CaL} (solid gray) to their slow rate values (no $[Na^+]_i$ and $[Na^+]_{ss}$ clamping to slow rate values). C) $[Na^+]_i$ and I_{NaK} increase with pacing rate under control conditions (left). When $[Na^+]_i$ and $[Na^+]_{ss}$ are clamped to slow rate values, I_{NaK} is small and rate independent (right). D) APD restitution in control (solid black), and when inactivation gates were reset to S1 values upon S2 delivery (late I_{Na} reset – dashed gray, I_{CaL} reset – dash-dot-dot gray, late I_{Na} and I_{CaL} reset – solid gray). Shown

in dashed black is resetting late I_{Na} and I_{CaL} inactivation to the $DI = 5$ ms value. E) $[Na^+]_i$ and $[Na^+]_{ss}$ clamp to S1 values (dashed gray) did not affect APD restitution (control, solid black).

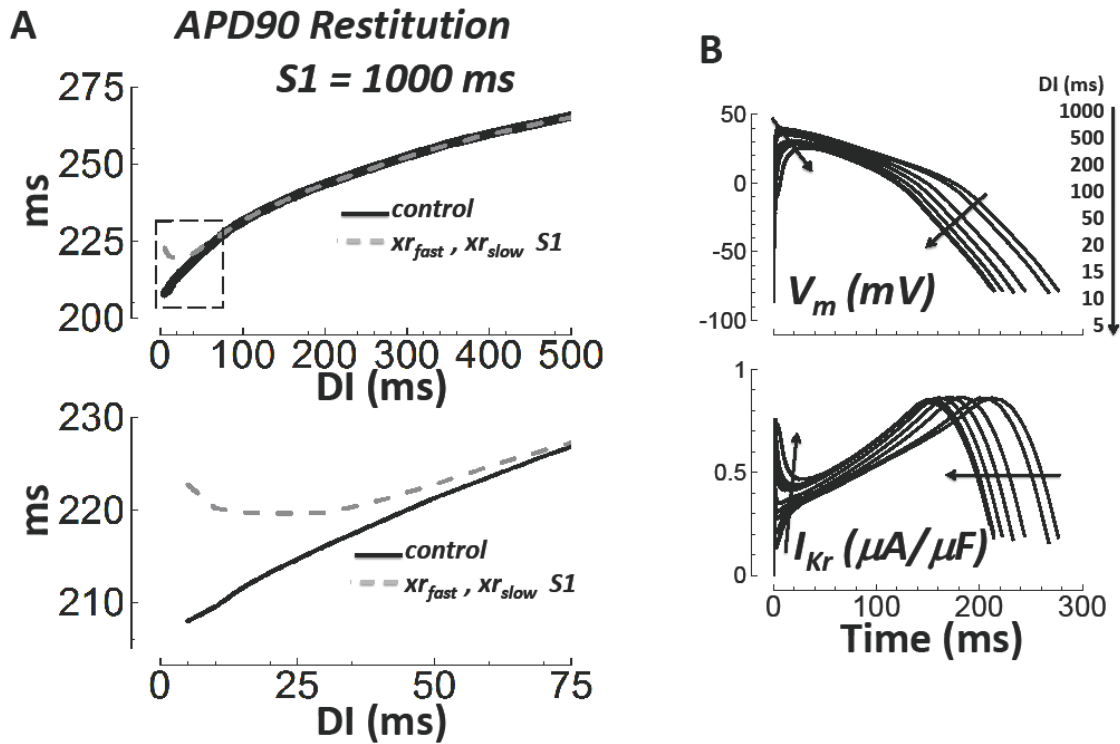


Figure 2.17. I_{Kr} deactivation is important for APD restitution at very short DIs. A) APD restitution in control (solid black), and when the fast and slow deactivation gates (xr_{fast} and xr_{slow}) were reset to the $DI = S1 = 1000$ ms value at the start of the S2 beat (dashed gray). Bottom) Zoom in to more clearly show the consequence of deactivation resetting at short DIs (section outlined by dashed box above). B) Traces for the AP (top) and I_{Kr} (bottom) during the S2 beat at different DIs (indicated by arrows). Spiking in I_{Kr} occurred early during the AP at short DI. Spiking was caused by slow deactivation, increasing availability of I_{Kr} .

$\overline{\text{ORd}}$
 $\overline{\text{TP}}$
 $\overline{\text{GB}}$

A *endo cells, steady state APD rate dependence*

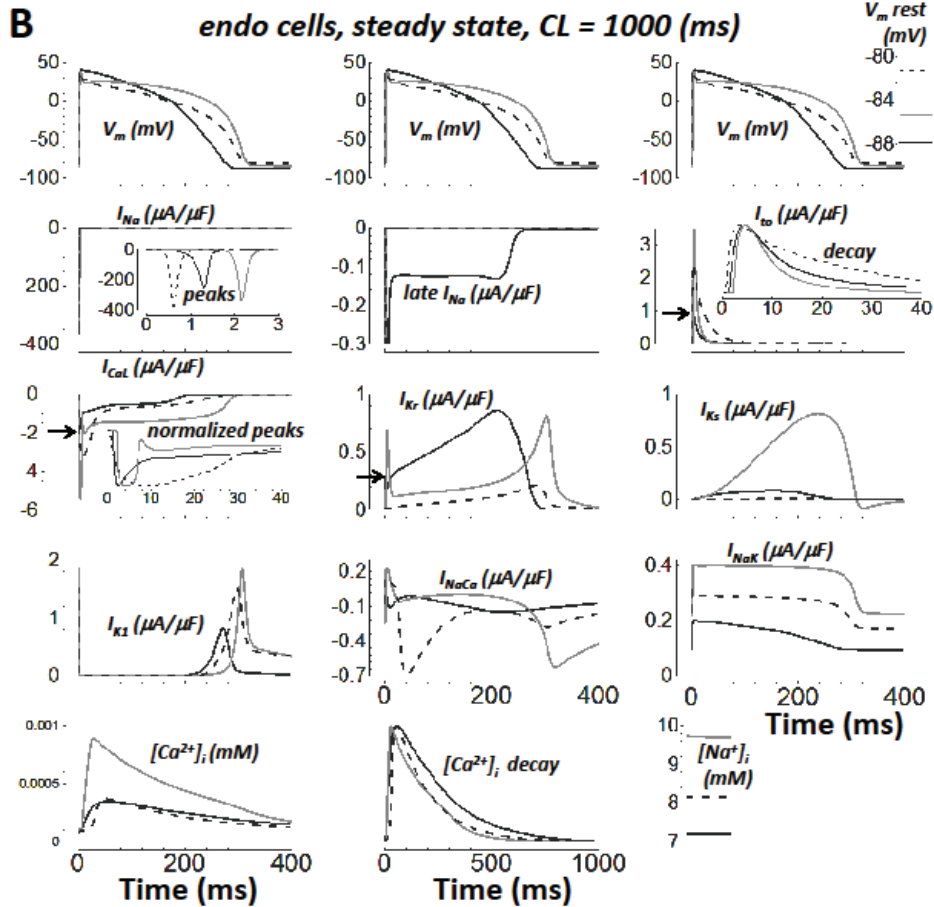
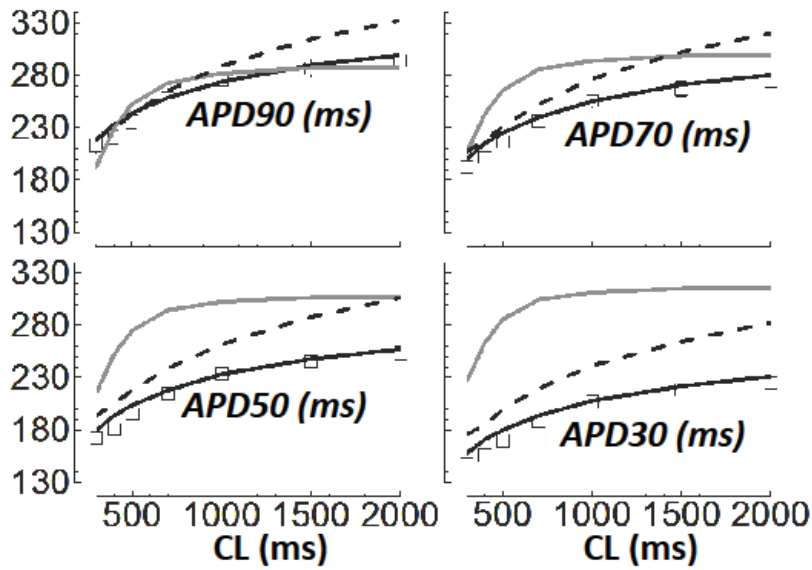


Figure 2.18. Comparison with other human ventricular AP models. Single endo cell simulations from ORd, TP, and GB models are solid black, gray, and dashed black lines, respectively. Experimental results (small tissue preparations) are white squares. A) APD rate dependence. Results for APD₉₀, 70, 50 and 30 are shown top left, top right, bottom left, and bottom right, respectively. B) The AP, major currents, and intracellular Na⁺ and Ca²⁺ concentrations at steady state for CL = 1000 ms. From left to right, top to bottom: AP (with V_m rest inset at far right), I_{Na} (inset shows peaks), late I_{Na} (not present in TP or GB models), I_{to} (inset to show decay rate), I_{CaL} (arrow shows ORd peak magnitude; inset shows normalized peaks, which are wide in TP and GB), I_{Kr} (arrow shows ORd early spike peak magnitude), I_{Ks}, I_{K1}, I_{NaCa}, I_{NaK}, intracellular Ca²⁺ concentration [Ca²⁺]_i, [Ca²⁺]_i decay rate, and intracellular Na⁺ concentration, [Na⁺]_i.

Chapter 2 Supplementary Material

ORd Human Model Basic Parameters

Stimulus

$$\text{amplitude} = -80.0 \frac{\mu\text{A}}{\mu\text{F}}, \quad \text{duration} = 0.5 \text{ ms}$$

For charge conservation sake, stimulus has K^+ identity as described by Hund et al. (Hund, Kucera et al. 2001).

External Concentrations

$$[\text{Na}^+]_o = 140 \text{ mM}$$

$$[\text{Ca}^{2+}]_o = 1.8 \text{ mM}$$

$$[\text{K}^+]_o = 5.4 \text{ mM}$$

ORd Model Initial Conditions

Single endocardial cell, at 1 Hz steady state, in diastole. There are 41 state variables.

$$V = -87.84 \text{ mV}$$

$$[\text{Na}^+]_i = 7.23 \text{ mM}$$

$$[\text{Na}^+]_{ss} = 7.23 \text{ mM}$$

$$[\text{K}^+]_i = 143.79 \text{ mM}$$

$$[\text{K}^+]_{ss} = 143.79 \text{ mM}$$

$$[\text{Ca}^{2+}]_i = 8.54 \cdot 10^{-5} \text{ mM}$$

$$[\text{Ca}^{2+}]_{ss} = 8.43 \cdot 10^{-5} \text{ mM}$$

$$[\text{Ca}^{2+}]_{nsr} = 1.61 \text{ mM}$$

$$[\text{Ca}^{2+}]_{jsr} = 1.56 \text{ mM}$$

$$m = 0.0074621$$

$h_{\text{fast}} = 0.692591$
 $h_{\text{slow}} = 0.692574$
 $j = 0.692477$
 $h_{\text{CaMK,slow}} = 0.448501$
 $j_{\text{CaMK}} = 0.692413$
 $m_L = 0.000194015$
 $h_L = 0.496116$
 $h_{L,\text{CaMK}} = 0.265885$
 $a = 0.00101185$
 $i_{\text{fast}} = 0.999542$
 $i_{\text{slow}} = 0.589579$
 $a_{\text{CaMK}} = 0.000515567$
 $i_{\text{CaMK,fast}} = 0.999542$
 $i_{\text{CaMK,slow}} = 0.641861$
 $d = 2.43015 \cdot 10^{-9}$
 $f_{\text{fast}} = 1.0$
 $f_{\text{slow}} = 0.910671$
 $f_{\text{Ca,fast}} = 1.0$
 $f_{\text{Ca,slow}} = 0.99982$
 $j_{\text{Ca}} = 0.999977$
 $n = 0.00267171$
 $f_{\text{CaMK,fast}} = 1.0$
 $f_{\text{Ca,CaMK,fast}} = 1.0$
 $x_{r,\text{fast}} = 8.26608 \cdot 10^{-6}$
 $x_{r,\text{slow}} = 0.453268$
 $x_{s1} = 0.270492$
 $x_{s2} = 0.0001963$
 $x_{K1} = 0.996801$

$$J_{\text{rel,NP}} = 2.53943 \cdot 10^{-5} \text{ mM/ms}$$

$$J_{\text{rel,CaMK}} = 3.17262 \cdot 10^{-7} \text{ mM/ms}$$

$$\text{CaMK}_{\text{trap}} = 0.0124065$$

Reversal Potentials

$$E_{\text{Na}} = \frac{RT}{F} \cdot \ln \left(\frac{[\text{Na}^+]_o}{[\text{Na}^+]_i} \right)$$

$$E_{\text{K}} = \frac{RT}{F} \cdot \ln \left(\frac{[\text{K}^+]_o}{[\text{K}^+]_i} \right)$$

$$\text{PR}_{\text{Na,K}} = 0.01833, \quad E_{\text{KS}} = \frac{RT}{F} \cdot \ln \left(\frac{[\text{K}^+]_o + \text{PR}_{\text{Na,K}} \cdot [\text{Na}^+]_o}{[\text{K}^+]_i + \text{PR}_{\text{Na,K}} \cdot [\text{Na}^+]_i} \right)$$

Cell Geometry

Cell geometry was approximated by a cylinder. Cell length (L) was about ten times longer than the radius (Forbes and Sperelakis 1989).

$$L = 0.01 \text{ cm}, \quad r = 0.0011 \text{ cm}$$

$$v_{\text{cell}} = \pi \cdot r^2 \cdot L = 38 \cdot 10^{-6} \mu\text{L}$$

$$A_{\text{geo}} = 2\pi \cdot r^2 + 2\pi \cdot r \cdot L = 0.767 \cdot 10^{-4} \text{ cm}^2$$

$$A_{\text{cap}} = R_{\text{CG}} \cdot A_{\text{geo}} = 2 \cdot A_{\text{geo}} = 1.534 \cdot 10^{-4} \text{ cm}^2$$

$$v_{\text{myo}} = 0.68 \cdot v_{\text{cell}} = 25.84 \cdot 10^{-6} \mu\text{L}$$

$$v_{\text{nsr}} = 0.0552 \cdot v_{\text{cell}} = 2.098 \cdot 10^{-6} \mu\text{L}$$

$$v_{\text{jsr}} = 0.0048 \cdot v_{\text{cell}} = 0.182 \cdot 10^{-6} \mu\text{L}$$

$$v_{\text{ss}} = 0.02 \cdot v_{\text{cell}} = 0.76 \cdot 10^{-6} \mu\text{L}$$

ORd Human Model Currents

Sodium Current (I_{Na})

$$m_{\infty} = \frac{1}{1 + \exp\left(\frac{-(V + 39.57)}{9.871}\right)}$$

$$\tau_m = \frac{1}{6.765 \cdot \exp\left(\frac{V + 11.64}{34.77}\right) + 8.552 \cdot \exp\left(\frac{-(V + 77.42)}{5.955}\right)}$$

$$\frac{dm}{dt} = \frac{m_{\infty} - m}{\tau_m}$$

$$h_{\infty} = \frac{1}{1 + \exp\left(\frac{V + 82.9}{6.086}\right)}$$

$$\tau_{h,fast} = \frac{1}{1.432 \cdot 10^{-5} \cdot \exp\left(\frac{-(V + 1.196)}{6.285}\right) + 6.149 \cdot \exp\left(\frac{V + 0.5096}{20.27}\right)}$$

$$\tau_{h,slow} = \frac{1}{0.009764 \cdot \exp\left(\frac{-(V + 17.95)}{28.05}\right) + 0.3343 \cdot \exp\left(\frac{V + 5.730}{56.66}\right)}$$

$$A_{h,fast} = 0.99, \quad A_{h,slow} = 0.01$$

$$\frac{dh_{fast}}{dt} = \frac{h_{\infty} - h_{fast}}{\tau_{h,fast}}$$

$$\frac{dh_{slow}}{dt} = \frac{h_{\infty} - h_{slow}}{\tau_{h,slow}}$$

$$h = A_{h,fast} \cdot h_{fast} + A_{h,slow} \cdot h_{slow}$$

$$j_{\infty} = h_{\infty}$$

$$\tau_j = 2.038 + \frac{1}{0.02136 \cdot \exp\left(\frac{-(V + 100.6)}{8.281}\right) + 0.3052 \cdot \exp\left(\frac{V + 0.9941}{38.45}\right)}$$

$$\frac{dj}{dt} = \frac{j_{\infty} - j}{\tau_j}$$

$$h_{CaMK,\infty} = \frac{1}{1 + \exp\left(\frac{V + 89.1}{6.086}\right)}$$

$$\tau_{h,CaMK,slow} = 3.0 \cdot \tau_{h,slow}$$

$$A_{h,CaMK,fast} = A_{h,fast}, \quad A_{h,CaMK,slow} = A_{h,slow}$$

$$h_{CaMK,fast} = h_{fast}$$

$$\frac{dh_{\text{CaMK,slow}}}{dt} = \frac{h_{\text{CaMK},\infty} - h_{\text{CaMK,slow}}}{\tau_{h,\text{CaMK,slow}}}$$

$$h_{\text{CaMK}} = A_{h,\text{CaMK,fast}} \cdot h_{\text{CaMK,fast}} + A_{h,\text{CaMK,slow}} \cdot h_{\text{CaMK,slow}}$$

$$j_{\text{CaMK},\infty} = j_{\infty}$$

$$\tau_{j,\text{CaMK}} = 1.46 \cdot \tau_j$$

$$\frac{dj_{\text{CaMK}}}{dt} = \frac{j_{\text{CaMK},\infty} - j_{\text{CaMK}}}{\tau_{j,\text{CaMK}}}$$

$$K_{m,\text{CaMK}} = 0.15, \quad \phi_{\text{INa,CaMK}} = \frac{1}{1 + \frac{K_{m,\text{CaMK}}}{\text{CaMK}_{\text{active}}}}$$

$$\overline{G_{\text{Na,fast}}} = 75 \text{ mS}/\mu\text{F}$$

$$I_{\text{Na,fast}} = \overline{G_{\text{Na,fast}}} \cdot (V - E_{\text{Na}}) \cdot m^3 \cdot \left((1 - \phi_{\text{INa,CaMK}}) \cdot h \cdot j + \phi_{\text{INa,CaMK}} \cdot h_{\text{CaMK}} \cdot j_{\text{CaMK}} \right)$$

$$m_{L,\infty} = \frac{1}{1 + \exp\left(\frac{-(V + 42.85)}{5.264}\right)}$$

$$\tau_{m,L} = \tau_m$$

$$\frac{dm_L}{dt} = \frac{m_{L,\infty} - m_L}{\tau_{m,L}}$$

$$h_{L,\infty} = \frac{1}{1 + \exp\left(\frac{V + 87.61}{7.488}\right)}$$

$$\tau_{h,L} = 200 \text{ ms}$$

$$\frac{dh_L}{dt} = \frac{h_{L,\infty} - h_L}{\tau_{h,L}}$$

$$h_{L,\text{CaMK},\infty} = \frac{1}{1 + \exp\left(\frac{V + 93.81}{7.488}\right)}$$

$$\tau_{h,L,\text{CaMK}} = 3 \cdot \tau_{h,L}$$

$$\frac{dh_{L,\text{CaMK}}}{dt} = \frac{h_{L,\text{CaMK},\infty} - h_{L,\text{CaMK}}}{\tau_{h,L,\text{CaMK}}}$$

$$K_{m,\text{CaMK}} = 0.15, \quad \phi_{\text{INaL,CaMK}} = \frac{1}{1 + \frac{K_{m,\text{CaMK}}}{\text{CaMK}_{\text{active}}}}$$

$$\overline{G_{Na,late}} = 0.0075 \text{ mS}/\mu\text{F}$$

$$I_{Na,late} = \overline{G_{Na,late}} \cdot (V - E_{Na}) \cdot m_L \cdot \left((1 - \phi_{INaL,CaMK}) \cdot h_L + \phi_{INaL,CaMK} \cdot h_{L,CaMK} \right)$$

$$I_{Na} = I_{Na,fast} + I_{Na,late}$$

Transient Outward Potassium Current (I_{to})

$$a_{\infty} = \frac{1}{1 + \exp\left(\frac{-(V - 14.34)}{14.82}\right)}$$

$$\tau_a = \frac{1.0515}{\frac{1}{1.2089 \cdot \left(1 + \exp\left(\frac{-(V - 18.41)}{29.38}\right)\right)} + \frac{3.5}{1 + \exp\left(\frac{V + 100}{29.38}\right)}}$$

$$\frac{da}{dt} = \frac{a_{\infty} - a}{\tau_a}$$

$$i_{\infty} = \frac{1}{1 + \exp\left(\frac{V + 43.94}{5.711}\right)}$$

$$\tau_{i,fast} = 4.562 + \frac{1}{0.3933 \cdot \exp\left(\frac{-(V + 100)}{100}\right) + 0.08004 \cdot \exp\left(\frac{V + 50}{16.59}\right)}$$

$$\tau_{i,slow} = 23.62 + \frac{1}{0.001416 \cdot \exp\left(\frac{-(V + 96.52)}{59.05}\right) + 1.7808 \cdot 10^{-8} \cdot \exp\left(\frac{V + 114.1}{8.079}\right)}$$

$$A_{i,fast} = \frac{1}{1 + \exp\left(\frac{V - 213.6}{151.2}\right)}, \quad A_{i,slow} = 1 - A_{i,fast}$$

$$\frac{di_{fast}}{dt} = \frac{i_{\infty} - i_{fast}}{\tau_{i,fast}}$$

$$\frac{di_{slow}}{dt} = \frac{i_{\infty} - i_{slow}}{\tau_{i,slow}}$$

$$i = A_{i,fast} \cdot i_{fast} + A_{i,slow} \cdot i_{slow}$$

$$a_{CaMK,\infty} = \frac{1}{1 + \exp\left(\frac{-(V - 24.34)}{14.82}\right)}$$

$$\tau_{a,CaMK} = \tau_a$$

$$\frac{da_{\text{CaMK}}}{dt} = \frac{a_{\text{CaMK},\infty} - a_{\text{CaMK}}}{\tau_{a,\text{CaMK}}}$$

$$i_{\text{CaMK},\infty} = i_{\infty}$$

$$\delta_{\text{CaMK,develop}} = 1.354 + \frac{10^{-4}}{\exp\left(\frac{V - 167.4}{15.89}\right) + \exp\left(\frac{-(V - 12.23)}{0.2154}\right)}$$

$$\delta_{\text{CaMK,recover}} = 1 - \frac{0.5}{1 + \exp\left(\frac{V + 70}{20}\right)}$$

$$\tau_{i,\text{CaMK,fast}} = \tau_{i,\text{fast}} \cdot \delta_{\text{CaMK,develop}} \cdot \delta_{\text{CaMK,recover}}$$

$$\tau_{i,\text{CaMK,slow}} = \tau_{i,\text{slow}} \cdot \delta_{\text{CaMK,develop}} \cdot \delta_{\text{CaMK,recover}}$$

$$A_{i,\text{CaMK,fast}} = A_{i,\text{fast}}, \quad A_{i,\text{CaMK,slow}} = A_{i,\text{slow}}$$

$$\frac{di_{\text{CaMK,fast}}}{dt} = \frac{i_{\text{CaMK},\infty} - i_{\text{CaMK,fast}}}{\tau_{i,\text{CaMK,fast}}}$$

$$\frac{di_{\text{CaMK,slow}}}{dt} = \frac{i_{\text{CaMK},\infty} - i_{\text{CaMK,slow}}}{\tau_{i,\text{CaMK,slow}}}$$

$$i_{\text{CaMK}} = A_{i,\text{CaMK,fast}} \cdot i_{\text{CaMK,fast}} + A_{i,\text{CaMK,slow}} \cdot i_{\text{CaMK,slow}}$$

$$K_{m,\text{CaMK}} = 0.15, \quad \phi_{\text{Ito,CaMK}} = \frac{1}{1 + \frac{K_{m,\text{CaMK}}}{\text{CaMK}_{\text{active}}}}$$

$$\overline{G_{\text{to}}} = 0.02 \text{ mS}/\mu\text{F}$$

$$I_{\text{to}} = \overline{G_{\text{to}}} \cdot (V - E_K) \cdot \left((1 - \phi_{\text{Ito,CaMK}}) \cdot a \cdot i + \phi_{\text{Ito,CaMK}} \cdot a_{\text{CaMK}} \cdot i_{\text{CaMK}} \right)$$

L-type Calcium Current (I_{CaL})

$$d_{\infty} = \frac{1}{1 + \exp\left(\frac{-(V + 3.940)}{4.230}\right)}$$

$$\tau_d = 0.6 + \frac{1}{\exp(-0.05 \cdot (V + 6.0)) + \exp(0.09 \cdot (V + 14.0))}$$

$$\frac{dd}{dt} = \frac{d_{\infty} - d}{\tau_d}$$

$$f_{\infty} = \frac{1}{1 + \exp\left(\frac{V + 19.58}{3.696}\right)}$$

$$\tau_{f,fast} = 7.0 + \frac{1}{0.0045 \cdot \exp\left(\frac{-(V+20.0)}{10.0}\right) + 0.0045 \cdot \exp\left(\frac{V+20.0}{10.0}\right)}$$

$$\tau_{f,slow} = 1000 + \frac{1}{0.000035 \cdot \exp\left(-\frac{V+5.0}{4.0}\right) + 0.000035 \cdot \exp\left(\frac{V+5.0}{6.0}\right)}$$

$$A_{f,fast} = 0.6, \quad A_{f,slow} = 1 - A_{f,fast}$$

$$\frac{df_{fast}}{dt} = \frac{f_{\infty} - f_{fast}}{\tau_{f,fast}}$$

$$\frac{df_{slow}}{dt} = \frac{f_{\infty} - f_{slow}}{\tau_{f,slow}}$$

$$f = A_{f,fast} \cdot f_{fast} + A_{f,slow} \cdot f_{slow}$$

$$f_{Ca,\infty} = f_{\infty}$$

$$\tau_{f,Ca,fast} = 7.0 + \frac{1}{0.04 \cdot \exp\left(-\frac{V-4.0}{7.0}\right) + 0.04 \cdot \exp\left(\frac{V-4.0}{7.0}\right)}$$

$$\tau_{f,Ca,slow} = 100 + \frac{1}{0.00012 \cdot \exp\left(\frac{-V}{3.0}\right) + 0.00012 \cdot \exp\left(\frac{V}{7.0}\right)}$$

$$A_{f,Ca,fast} = 0.3 + \frac{0.6}{1.0 + \exp\left(\frac{V-10.0}{10.0}\right)}, \quad A_{f,Ca,slow} = 1 - A_{f,Ca,fast}$$

$$\frac{df_{Ca,fast}}{dt} = \frac{f_{Ca,\infty} - f_{Ca,fast}}{\tau_{f,Ca,fast}}$$

$$\frac{df_{Ca,slow}}{dt} = \frac{f_{Ca,\infty} - f_{Ca,slow}}{\tau_{f,Ca,slow}}$$

$$f_{Ca} = A_{f,Ca,fast} \cdot f_{Ca,fast} + A_{f,Ca,slow} \cdot f_{Ca,slow}$$

$$j_{Ca,\infty} = f_{Ca,\infty}$$

$$\tau_{j,Ca} = 75.0$$

$$\frac{dj_{Ca}}{dt} = \frac{j_{Ca,\infty} - j_{Ca}}{\tau_{j,Ca}}$$

$$f_{CaMK,\infty} = f_{\infty}$$

$$\tau_{f,CaMK,fast} = 2.5 \cdot \tau_{f,fast}$$

$$A_{f,CaMK,fast} = A_{f,fast}, \quad A_{f,CaMK,slow} = A_{f,slow}$$

$$\frac{df_{\text{CaMK,fast}}}{dt} = \frac{f_{\text{CaMK},\infty} - f_{\text{CaMK,fast}}}{\tau_{f,\text{CaMK,fast}}}$$

$$f_{\text{CaMK,slow}} = f_{\text{slow}}$$

$$f_{\text{CaMK}} = A_{f,\text{CaMK,fast}} \cdot f_{\text{CaMK,fast}} + A_{f,\text{CaMK,slow}} \cdot f_{\text{CaMK,slow}}$$

$$f_{\text{Ca,CaMK},\infty} = f_{\infty}$$

$$\tau_{f,\text{Ca,CaMK,fast}} = 2.5 \cdot \tau_{f,\text{Ca,fast}}$$

$$A_{f,\text{Ca,CaMK,fast}} = A_{f,\text{Ca,fast}}, \quad A_{f,\text{Ca,CaMK,slow}} = A_{f,\text{Ca,slow}}$$

$$\frac{df_{\text{Ca,CaMK,fast}}}{dt} = \frac{f_{\text{Ca,CaMK},\infty} - f_{\text{Ca,CaMK,fast}}}{\tau_{f,\text{Ca,CaMK,fast}}}$$

$$f_{\text{Ca,CaMK,slow}} = f_{\text{Ca,slow}}$$

$$f_{\text{Ca,CaMK}} = A_{f,\text{Ca,CaMK,fast}} \cdot f_{\text{Ca,CaMK,fast}} + A_{f,\text{Ca,CaMK,slow}} \cdot f_{\text{Ca,CaMK,slow}}$$

$$K_{m,n} = 0.002, \quad k_{+2,n} = 1000.0, \quad k_{-2,n} = j_{\text{Ca}} \cdot 1.0$$

$$\alpha_n = \frac{1.0}{\frac{k_{+2,n}}{k_{-2,n}} + \left(1 + \frac{K_{m,n}}{[\text{Ca}^{2+}]_{ss}}\right)^{4.0}}$$

$$\frac{dn}{dt} = \alpha_n \cdot k_{+2,n} - n \cdot k_{-2,n}$$

$$P_{\text{Ca}} = 0.0001 \frac{\text{cm}}{\text{s}}$$

$$\gamma_{\text{Cai}} = 1.0, \quad \gamma_{\text{Cao}} = 0.341, \quad z_{\text{Ca}} = 2$$

$$\Psi_{\text{Ca}} = z_{\text{Ca}}^2 \cdot \frac{VF^2}{RT} \cdot \frac{\gamma_{\text{Cai}} \cdot [\text{Ca}^{2+}]_{ss} \cdot \exp\left(\frac{z_{\text{Ca}}VF}{RT}\right) - \gamma_{\text{Cao}} \cdot [\text{Ca}^{2+}]_o}{\exp\left(\frac{z_{\text{Ca}}VF}{RT}\right) - 1.0}$$

$$\overline{I_{\text{CaL}}} = P_{\text{Ca}} \cdot \Psi_{\text{Ca}}$$

$$P_{\text{CaNa}} = 0.00125 \cdot P_{\text{Ca}}, \quad \gamma_{\text{Nai}} = 0.75, \quad \gamma_{\text{Nao}} = 0.75, \quad z_{\text{Na}} = 1$$

$$\Psi_{\text{CaNa}} = z_{\text{Na}}^2 \cdot \frac{VF^2}{RT} \cdot \frac{\gamma_{\text{Nai}} \cdot [\text{Na}^+]_{ss} \cdot \exp\left(\frac{z_{\text{Na}}VF}{RT}\right) - \gamma_{\text{Nao}} \cdot [\text{Na}^+]_o}{\exp\left(\frac{z_{\text{Na}}VF}{RT}\right) - 1.0}$$

$$\overline{I_{\text{CaNa}}} = P_{\text{CaNa}} \cdot \Psi_{\text{CaNa}}$$

$$P_{\text{CaK}} = 3.574 \cdot 10^{-4} \cdot P_{\text{Ca}}, \quad \gamma_{\text{Ki}} = 0.75, \quad \gamma_{\text{Ko}} = 0.75, \quad z_{\text{K}} = 1$$

$$\Psi_{CaK} = z_K^2 \cdot \frac{VF^2}{RT} \cdot \frac{\gamma_{Ki} \cdot [K^+]_{ss} \cdot \exp\left(\frac{z_K VF}{RT}\right) - \gamma_{Ko} \cdot [K^+]_o}{\exp\left(\frac{z_K VF}{RT}\right) - 1.0}$$

$$\overline{I_{CaK}} = P_{CaK} \cdot \Psi_{CaK}$$

$$P_{Ca,CaMK} = 1.1 \cdot P_{Ca}$$

$$\overline{I_{CaL,CaMK}} = P_{Ca,CaMK} \cdot \Psi_{Ca}$$

$$P_{CaNa,CaMK} = 0.00125 \cdot P_{Ca,CaMK}$$

$$\overline{I_{CaNa,CaMK}} = P_{CaNa,CaMK} \cdot \Psi_{CaNa}$$

$$P_{CaK,CaMK} = 3.574 \cdot 10^{-4} \cdot P_{Ca,CaMK}$$

$$\overline{I_{CaK,CaMK}} = P_{CaK,CaMK} \cdot \Psi_{CaK}$$

$$K_{m,CaMK} = 0.15, \quad \phi_{ICaL,CaMK} = \frac{1}{1 + \frac{K_{m,CaMK}}{CaMK_{active}}}$$

$$I_{CaL} = \overline{I_{CaL}} \cdot d \cdot (1 - \phi_{ICaL,CaMK}) \cdot (f \cdot (1 - n) + f_{Ca} \cdot n \cdot j_{Ca}) + \overline{I_{CaL,CaMK}} \cdot d \cdot \phi_{ICaL,CaMK} \cdot (f_{CaMK} \cdot (1 - n) + f_{Ca,CaMK} \cdot n \cdot j_{Ca})$$

$$I_{CaNa} = \overline{I_{CaNa}} \cdot d \cdot (1 - \phi_{ICaL,CaMK}) \cdot (f \cdot (1 - n) + f_{Ca} \cdot n \cdot j_{Ca}) + \overline{I_{CaNa,CaMK}} \cdot d \cdot \phi_{ICaL,CaMK} \cdot (f_{CaMK} \cdot (1 - n) + f_{Ca,CaMK} \cdot n \cdot j_{Ca})$$

$$I_{CaK} = \overline{I_{CaK}} \cdot d \cdot (1 - \phi_{ICaL,CaMK}) \cdot (f \cdot (1 - n) + f_{Ca} \cdot n \cdot j_{Ca}) + \overline{I_{CaK,CaMK}} \cdot d \cdot \phi_{ICaL,CaMK} \cdot (f_{CaMK} \cdot (1 - n) + f_{Ca,CaMK} \cdot n \cdot j_{Ca})$$

Rapid Delayed Rectifier Potassium Current (I_{Kr})

$$x_{r,\infty} = \frac{1}{1 + \exp\left(\frac{-(V + 8.337)}{6.789}\right)}$$

$$\tau_{xr,fast} = 12.98 + \frac{1}{0.3652 \cdot \exp\left(\frac{V - 31.66}{3.869}\right) + 4.123 \cdot 10^{-5} \cdot \exp\left(\frac{-(V - 47.78)}{20.38}\right)}$$

$$\tau_{xr,slow} = 1.865 + \frac{1}{0.06629 \cdot \exp\left(\frac{V - 34.70}{7.355}\right) + 1.128 \cdot 10^{-5} \cdot \exp\left(\frac{-(V - 29.74)}{25.94}\right)}$$

$$A_{x_r,fast} = \frac{1}{1 + \exp\left(\frac{V + 54.81}{38.21}\right)}, \quad A_{x_r,slow} = 1 - A_{x_r,fast}$$

$$\frac{dx_{r,fast}}{dt} = \frac{x_{r,\infty} - x_{r,fast}}{\tau_{x_r,fast}}$$

$$\frac{dx_{r,slow}}{dt} = \frac{x_{r,\infty} - x_{r,slow}}{\tau_{x_r,slow}}$$

$$x_r = A_{x_r,fast} \cdot x_{r,fast} + A_{x_r,slow} \cdot x_{r,slow}$$

$$R_{Kr} = \frac{1}{\left(1 + \exp\left(\frac{V + 55}{75}\right)\right) \cdot \left(1 + \exp\left(\frac{V - 10}{30}\right)\right)}$$

$$\overline{G_{Kr}} = 0.046 \text{ mS}/\mu\text{F}$$

$$I_{Kr} = \overline{G_{Kr}} \cdot \sqrt{\frac{[K^+]_o}{5.4}} \cdot x_r \cdot R_{Kr} \cdot (V - E_K)$$

Slow Delayed Rectifier Potassium Current (I_{Ks})

$$x_{s1,\infty} = \frac{1}{1 + \exp\left(\frac{-(V + 11.60)}{8.932}\right)}$$

$$\tau_{x,s1} = 817.3 + \frac{1}{2.326 \cdot 10^{-4} \cdot \exp\left(\frac{V + 48.28}{17.80}\right) + 0.001292 \cdot \exp\left(\frac{-(V + 210.0)}{230.0}\right)}$$

$$\frac{dx_{s1}}{dt} = \frac{x_{s1,\infty} - x_{s1}}{\tau_{x,s1}}$$

$$x_{s2,\infty} = x_{s1,\infty}$$

$$\tau_{x,s2} = \frac{1}{0.01 \cdot \exp\left(\frac{V - 50}{20}\right) + 0.0193 \cdot \exp\left(\frac{-(V + 66.54)}{31}\right)}$$

$$\frac{dx_{s2}}{dt} = \frac{x_{s2,\infty} - x_{s2}}{\tau_{x,s2}}$$

$$\overline{G_{Ks}} = 0.0034 \text{ mS}/\mu\text{F}$$

$$I_{Ks} = \overline{G_{Ks}} \cdot \left(1 + \frac{0.6}{1 + \left(\frac{3.8 \cdot 10^{-5}}{[Ca^{2+}]_i}\right)^{1.4}}\right) \cdot x_{s1} \cdot x_{s2} \cdot (V - E_{Ks})$$

Inward Rectifier Potassium Current (I_{K1})

$$x_{K1,\infty} = \frac{1}{1 + \exp\left(-\frac{V + 2.5538 \cdot [K^+]_o + 144.59}{1.5692 \cdot [K^+]_o + 3.8115}\right)}$$

$$\tau_{x,K1} = \frac{122.2}{\exp\left(\frac{-(V + 127.2)}{20.36}\right) + \exp\left(\frac{V + 236.8}{69.33}\right)}$$

$$\frac{dx_{K1}}{dt} = \frac{x_{K1,\infty} - x_{K1}}{\tau_{x,K1}}$$

$$R_{K1} = \frac{1}{1 + \exp\left(\frac{V + 105.8 - 2.6 \cdot [K^+]_o}{9.493}\right)}$$

$$\overline{G_{K1}} = 0.1908 \text{ mS}/\mu\text{F}$$

$$I_{K1} = \overline{G_{K1}} \cdot \sqrt{[K^+]_o} \cdot x_{K1} \cdot R_{K1} \cdot (V - E_K)$$

Sodium-Calcium Exchange Current (I_{NaCa})

For, $Y \in \{i, ss\}$

$$k_{Na1} = 15 \text{ mM}, \quad k_{Na2} = 5 \text{ mM}, \quad k_{Na3} = 88.12 \text{ mM}, \quad k_{asymm} = 12.5$$

$$\omega_{Na} = 6 \cdot 10^4 \text{ Hz}, \quad \omega_{Ca} = 6 \cdot 10^4 \text{ Hz}, \quad \omega_{NaCa} = 5 \cdot 10^3 \text{ Hz}$$

$$k_{Ca,on} = 1.5 \cdot 10^6 \frac{\text{mM}}{\text{ms}}, \quad k_{Ca,off} = 5 \cdot 10^3 \text{ Hz}$$

$$q_{Na} = 0.5224, \quad q_{Ca} = 0.1670$$

$$h_{Ca} = \exp\left(\frac{q_{Ca}VF}{RT}\right), \quad h_{Na} = \exp\left(\frac{q_{Na}VF}{RT}\right)$$

$$h_1 = 1 + \frac{[Na^+]_Y}{k_{Na3}}(1 + h_{Na})$$

$$h_2 = \frac{[Na^+]_Y \cdot h_{Na}}{k_{Na3} \cdot h_1}$$

$$h_3 = \frac{1}{h_1}$$

$$h_4 = 1 + \frac{[Na^+]_Y}{k_{Na1}} \left(1 + \frac{[Na^+]_Y}{k_{Na2}}\right)$$

$$h_5 = \frac{[\text{Na}^+]_Y^2}{h_4 \cdot k_{\text{Na}1} \cdot k_{\text{Na}2}}$$

$$h_6 = \frac{1}{h_4}$$

$$h_7 = 1 + \frac{[\text{Na}^+]_o}{k_{\text{Na}3}} \left(1 + \frac{1}{h_{\text{Na}}} \right)$$

$$h_8 = \frac{[\text{Na}^+]_o}{k_{\text{Na}3} \cdot h_{\text{Na}} \cdot h_7}$$

$$h_9 = \frac{1}{h_7}$$

$$h_{10} = k_{\text{asymm}} + 1 + \frac{[\text{Na}^+]_o}{k_{\text{Na}1}} \left(1 + \frac{[\text{Na}^+]_o}{k_{\text{Na}2}} \right)$$

$$h_{11} = \frac{[\text{Na}^+]_o^2}{h_{10} \cdot k_{\text{Na}1} \cdot k_{\text{Na}2}}$$

$$h_{12} = \frac{1}{h_{10}}$$

$$k_1 = h_{12} \cdot [\text{Ca}^{2+}]_o \cdot k_{\text{Ca,on}}$$

$$k_2 = k_{\text{Ca,off}}$$

$$k'_3 = h_9 \cdot \omega_{\text{Ca}}$$

$$k''_3 = h_8 \cdot \omega_{\text{NaCa}}$$

$$k_3 = k'_3 + k''_3$$

$$k'_4 = \frac{h_3 \cdot \omega_{\text{Ca}}}{h_{\text{Ca}}}$$

$$k''_4 = h_2 \cdot \omega_{\text{NaCa}}$$

$$k_4 = k'_4 + k''_4$$

$$k_5 = k_{\text{Ca,off}}$$

$$k_6 = h_6 \cdot [\text{Ca}^{2+}]_Y \cdot k_{\text{Ca,on}}$$

$$k_7 = h_5 \cdot h_2 \cdot \omega_{\text{Na}}$$

$$k_8 = h_8 \cdot h_{11} \cdot \omega_{\text{Na}}$$

$$x_1 = k_2 \cdot k_4 \cdot (k_7 + k_6) + k_5 \cdot k_7 \cdot (k_2 + k_3)$$

$$x_2 = k_1 \cdot k_7 \cdot (k_4 + k_5) + k_4 \cdot k_6 \cdot (k_1 + k_8)$$

$$x_3 = k_1 \cdot k_3 \cdot (k_7 + k_6) + k_8 \cdot k_6 \cdot (k_2 + k_3)$$

$$x_4 = k_2 \cdot k_8 \cdot (k_4 + k_5) + k_3 \cdot k_5 \cdot (k_1 + k_8)$$

$$E_1 = \frac{x_1}{x_1 + x_2 + x_3 + x_4}$$

$$E_2 = \frac{x_2}{x_1 + x_2 + x_3 + x_4}$$

$$E_3 = \frac{x_3}{x_1 + x_2 + x_3 + x_4}$$

$$E_4 = \frac{x_4}{x_1 + x_2 + x_3 + x_4}$$

$$K_{mCaAct} = 150 \cdot 10^{-6} \text{ mM}$$

$$\text{allo}_Y = \frac{1}{1 + \left(\frac{K_{mCaAct}}{[Ca^{2+}]_Y} \right)^2}$$

$$J_{NaCa,Na,Y} = 3 \cdot (E_4 \cdot k_7 - E_1 \cdot k_8) + E_3 \cdot k_4'' - E_2 \cdot k_3''$$

$$J_{NaCa,Ca,Y} = E_2 \cdot k_2 - E_1 \cdot k_1$$

$$z_{Na} = 1, \quad z_{Ca} = 2$$

$$\overline{G_{NaCa}} = 0.0008 \text{ } \mu\text{A}/\mu\text{F}$$

$$I_{NaCa,i} = \overline{G_{NaCa}} \cdot 0.8 \cdot \text{allo}_i \cdot (z_{Na} \cdot J_{NaCa,Na,i} + z_{Ca} \cdot J_{NaCa,Ca,i})$$

$$I_{NaCa,ss} = \overline{G_{NaCa}} \cdot 0.2 \cdot \text{allo}_{ss} \cdot (z_{Na} \cdot J_{NaCa,Na,ss} + z_{Ca} \cdot J_{NaCa,Ca,ss})$$

$$I_{NaCa} = I_{NaCa,i} + I_{NaCa,ss}$$

Sodium-Potassium Pump Current (I_{NaK})

$$k_1^+ = 949.5 \text{ Hz}, \quad k_1^- = 182.4 \text{ mM}^{-1}, \quad k_2^+ = 687.2 \text{ Hz}, \quad k_2^- = 39.4 \text{ Hz}$$

$$k_3^+ = 1899 \text{ Hz}, \quad k_3^- = 79300 \text{ Hz} \cdot \text{mM}^{-2}, \quad k_4^+ = 639.0 \text{ Hz}, \quad k_4^- = 40 \text{ Hz}$$

$$K_{Na,i}^0 = 9.073 \text{ mM}, \quad K_{Na,o}^0 = 27.78 \text{ mM}$$

$$\Delta = -0.1550$$

$$K_{Na,i} = K_{Na,i}^0 \cdot \exp\left(\frac{\Delta \cdot V \cdot F}{3 \cdot R \cdot T}\right), \quad K_{Na,o} = K_{Na,o}^0 \cdot \exp\left(\frac{(1 - \Delta) \cdot V \cdot F}{3 \cdot R \cdot T}\right)$$

$$K_{Ki} = 0.5 \text{ mM}, \quad K_{Ko} = 0.3582 \text{ mM}$$

$$[\text{MgADP}] = 0.05, \quad [\text{MgATP}] = 9.8$$

$$K_{\text{MgATP}} = 1.698 \cdot 10^{-7} \text{ mM}$$

$$[\text{H}^+] = 10^{-7} \text{ mM}$$

$$[\Sigma\text{P}] = 4.2 \text{ mM}$$

$$K_{\text{H,P}} = 1.698 \cdot 10^{-7} \text{ mM}, \quad K_{\text{Na,P}} = 224 \text{ mM}, \quad K_{\text{K,P}} = 292 \text{ mM}$$

$$[\text{P}] = [\Sigma\text{P}] / \left(1 + \frac{[\text{H}^+]}{K_{\text{H,P}}} + \frac{[\text{Na}^+]_i}{K_{\text{Na,P}}} + \frac{[\text{K}^+]_i}{K_{\text{K,P}}} \right)$$

$$\alpha_1 = \frac{k_1^+ \left(\frac{[\text{Na}^+]_i}{K_{\text{Nai}}} \right)^3}{\left(1 + \frac{[\text{Na}^+]_i}{K_{\text{Nai}}} \right)^3 + \left(1 + \frac{[\text{K}^+]_i}{K_{\text{Ki}}} \right)^2 - 1}$$

$$\beta_1 = k_1^- \cdot [\text{MgADP}]$$

$$\alpha_2 = k_2^+$$

$$\beta_2 = \frac{k_2^- \left(\frac{[\text{Na}^+]_o}{K_{\text{Nao}}} \right)^3}{\left(1 + \frac{[\text{Na}^+]_o}{K_{\text{Nao}}} \right)^3 + \left(1 + \frac{[\text{K}^+]_o}{K_{\text{Ko}}} \right)^2 - 1}$$

$$\alpha_3 = \frac{k_3^+ \left(\frac{[\text{K}^+]_o}{K_{\text{Ko}}} \right)^2}{\left(1 + \frac{[\text{Na}^+]_o}{K_{\text{Nao}}} \right)^3 + \left(1 + \frac{[\text{K}^+]_o}{K_{\text{Ko}}} \right)^2 - 1}$$

$$\beta_3 = \frac{k_3^- \cdot [\text{P}] \cdot [\text{H}^+]}{1 + \frac{[\text{MgATP}]}{K_{\text{MgATP}}}}$$

$$\alpha_4 = \frac{k_4^+ \cdot \frac{[\text{MgATP}]}{K_{\text{MgATP}}}}{1 + \frac{[\text{MgATP}]}{K_{\text{MgATP}}}}$$

$$\beta_4 = \frac{k_4^- \left(\frac{[\text{K}^+]_i}{K_{\text{Ki}}} \right)^2}{\left(1 + \frac{[\text{Na}^+]_i}{K_{\text{Nai}}} \right)^3 + \left(1 + \frac{[\text{K}^+]_i}{K_{\text{Ki}}} \right)^2 - 1}$$

$$x_1 = \alpha_4 \cdot \alpha_1 \cdot \alpha_2 + \beta_2 \cdot \beta_4 \cdot \beta_3 + \alpha_2 \cdot \beta_4 \cdot \beta_3 + \beta_3 \cdot \alpha_1 \cdot \alpha_2$$

$$x_2 = \beta_2 \cdot \beta_1 \cdot \beta_4 + \alpha_1 \cdot \alpha_2 \cdot \alpha_3 + \alpha_3 \cdot \beta_1 \cdot \beta_4 + \alpha_2 \cdot \alpha_3 \cdot \beta_4$$

$$x_3 = \alpha_2 \cdot \alpha_3 \cdot \alpha_4 + \beta_3 \cdot \beta_2 \cdot \beta_1 + \beta_2 \cdot \beta_1 \cdot \alpha_4 + \alpha_3 \cdot \alpha_4 \cdot \beta_1$$

$$x_4 = \beta_4 \cdot \beta_3 \cdot \beta_2 + \alpha_3 \cdot \alpha_4 \cdot \alpha_1 + \beta_2 \cdot \alpha_4 \cdot \alpha_1 + \beta_3 \cdot \beta_2 \cdot \alpha_1$$

$$E_1 = \frac{x_1}{x_1 + x_2 + x_3 + x_4}$$

$$E_2 = \frac{x_2}{x_1 + x_2 + x_3 + x_4}$$

$$E_3 = \frac{x_3}{x_1 + x_2 + x_3 + x_4}$$

$$E_4 = \frac{x_4}{x_1 + x_2 + x_3 + x_4}$$

$$z_{Na} = 1, \quad z_K = 1$$

$$J_{NaK,Na} = 3 \cdot (E_1 \cdot \alpha_3 - E_2 \cdot \beta_3)$$

$$J_{NaK,K} = 2 \cdot (E_4 \cdot \beta_1 - E_3 \cdot \alpha_1)$$

$$I_{NaK} = 30 \cdot (z_{Na} \cdot J_{NaK,Na} + z_K \cdot J_{NaK,K})$$

Background Currents (I_{Nab} , I_{Cab} , I_{Kb}) and Sarcolemmal Calcium Pump Current (I_{pCa})

The formulations for I_{Nab} , I_{Cab} , I_{Kb} , and I_{pCa} were taken from the Hund-Decker-Rudy model (Hund and Rudy 2004; Decker, Heijman et al. 2009). I_{Kb} represents small amplitude, rapidly activating K^+ current observed in the ventricle (I_{kp} -like (Yue and Marban 1988) or I_{kur} -like (Sridhar, da Cunha et al. 2007) current). The amplitudes of these currents were reduced compared to values used by Decker et al. (Decker, Heijman et al. 2009). These choices were made consistent with the following: 1) so that resting $[Na^+]_i$ would be similar to values shown in nonfailing human ventricle at 37 °C by Pieske et al. (Pieske, Maier et al. 2002) at very slow pacing rates (0.25 Hz), 2) so that the resting $[Ca^{2+}]_i$ would be similar to values shown in nonfailing human ventricle at 37 °C by Schmidt et al. (Schmidt, Hajjar et al. 1998), and 3) so that the generally lower major current conductances used to match human data in construction of this model would be properly balanced.

$$P_{Nab} = 3.75 \cdot 10^{-10} \text{ cm/s}, \quad z_{Na} = 1$$

$$I_{Nab} = P_{Nab} \cdot z_{Na}^2 \cdot \frac{VF^2}{RT} \cdot \frac{[Na^+]_i \cdot \exp\left(\frac{z_{Na}VF}{RT}\right) - [Na^+]_o}{\exp\left(\frac{z_{Na}VF}{RT}\right) - 1.0}$$

$$P_{Cab} = 2.5 \cdot 10^{-8} \text{ cm/s}, \quad \gamma_{Cai} = 1.0, \quad \gamma_{Cao} = 0.341, \quad z_{Ca} = 2$$

$$I_{\text{Cab}} = P_{\text{Cab}} \cdot z_{\text{Ca}}^2 \cdot \frac{VF^2}{RT} \cdot \frac{\gamma_{\text{Cai}} \cdot [\text{Ca}^{2+}]_i \cdot \exp\left(\frac{z_{\text{Ca}}VF}{RT}\right) - \gamma_{\text{Cao}} \cdot [\text{Ca}^{2+}]_o}{\exp\left(\frac{z_{\text{Ca}}VF}{RT}\right) - 1.0}$$

$$x_{\text{Kb}} = \frac{1}{1 + \exp\left(\frac{-(V - 14.48)}{18.34}\right)}$$

$$\overline{G_{\text{Kb}}} = 0.003 \text{ mS}/\mu\text{F}$$

$$I_{\text{Kb}} = \overline{G_{\text{Kb}}} \cdot x_{\text{Kb}} \cdot (V - E_{\text{K}})$$

$$\overline{G_{\text{pCa}}} = 0.0005 \text{ mS}/\mu\text{F}$$

$$I_{\text{pCa}} = \overline{G_{\text{pCa}}} \cdot \frac{[\text{Ca}^{2+}]_i}{0.0005 + [\text{Ca}^{2+}]_i}$$

Voltage

$$C_m = 1.0 \mu\text{F}$$

$$\frac{dV_m}{dt} = -\frac{1}{C_m} \cdot (I_{\text{Na}} + I_{\text{to}} + I_{\text{CaL}} + I_{\text{CaNa}} + I_{\text{CaK}} + I_{\text{Kr}} + I_{\text{Ks}} + I_{\text{K1}} + I_{\text{NaCa}} + I_{\text{NaK}} + I_{\text{Nab}} + I_{\text{Cab}} + I_{\text{Kb}} + I_{\text{pCa}} + I_{\text{stim}})$$

Calcium/Calmodulin-Dependent Protein Kinase (CaMK)

The CaMK model is equivalent to that used in the Hund-Decker-Rudy dog model (Hund and Rudy 2004; Decker, Heijman et al. 2009). We assumed that CaMK kinetics are similar in human and dog, in the absence of human ventricle specific measurements.

$$\alpha_{\text{CaMK}} = 0.05 \text{ ms}^{-1}, \quad \beta_{\text{CaMK}} = 0.00068 \text{ ms}^{-1}$$

$$\text{CaMK}_0 = 0.05, \quad K_{\text{mCaM}} = 0.0015 \text{ mM}$$

$$\text{CaMK}_{\text{bound}} = \text{CaMK}_0 \cdot \frac{1 - \text{CaMK}_{\text{trap}}}{1 + \frac{K_{\text{mCaM}}}{[\text{Ca}^{2+}]_{\text{ss}}}}$$

$$\text{CaMK}_{\text{active}} = \text{CaMK}_{\text{bound}} + \text{CaMK}_{\text{trap}}$$

$$\frac{d\text{CaMK}_{\text{trap}}}{dt} = \alpha_{\text{CaMK}} \cdot \text{CaMK}_{\text{bound}} \cdot (\text{CaMK}_{\text{bound}} + \text{CaMK}_{\text{trap}}) - \beta_{\text{CaMK}} \cdot \text{CaMK}_{\text{trap}}$$

ORd Human Model Fluxes

Diffusion Fluxes ($J_{\text{diff,Na}}$, $J_{\text{diff,Ca}}$, $J_{\text{diff,K}}$)

$$\tau_{\text{diff,Na}} = \tau_{\text{diff,K}} = 2.0 \text{ ms}, \quad \tau_{\text{diff,Ca}} = 0.2 \text{ ms}$$

$$J_{\text{diff,Na}} = \frac{[\text{Na}^+]_{\text{ss}} - [\text{Na}^+]_{\text{i}}}{\tau_{\text{diff,Na}}}$$

$$J_{\text{diff,Ca}} = \frac{[\text{Ca}^{2+}]_{\text{ss}} - [\text{Ca}^{2+}]_{\text{i}}}{\tau_{\text{diff,Ca}}}$$

$$J_{\text{diff,K}} = \frac{[\text{K}^+]_{\text{ss}} - [\text{K}^+]_{\text{i}}}{\tau_{\text{diff,K}}}$$

The time constant for Na^+ and K^+ diffusion fluxes are larger than the time constant for Ca^{2+} diffusion flux. Physiologically, this amounts to reduced diffusivity for Na^+ and K^+ as they exit the subspace.

SR Calcium Release Flux, via Ryanodine Receptor (J_{rel})

Ca^{2+} release channels (ryanodine receptors, RyRs, formulation similar to that in Livshitz et al. (Livshitz and Rudy 2007)) have been split into two separate populations in this model according to CaMK phosphorylation state, based on observations in dog ventricle (Witcher, Kovacs et al. 1991). There is a non-phosphorylated release ($J_{\text{rel,NP}}$) and a CaMK phosphorylated release ($J_{\text{rel,CaMK}}$). When RyR channels are phosphorylated by CaMK, release amplitude is 1.25 times larger, and the decay time constant is 1.25 times longer. The proportion of the RyR population that behaves in the phosphorylated state is regulated by active CaMK.

$$\beta_{\tau} = 4.75 \text{ ms}$$

$$\alpha_{\text{rel}} = 0.5 \cdot \beta_{\tau}$$

$$J_{\text{rel,NP},\infty} = \frac{\alpha_{\text{rel}} \cdot (-I_{\text{CaL}})}{1 + \left(\frac{1.5}{[\text{Ca}^{2+}]_{\text{jSR}}} \right)^8}$$

$$\tau_{\text{rel,NP}} = \frac{\beta_{\tau}}{1 + \left(\frac{0.0123}{[\text{Ca}^{2+}]_{\text{jSR}}} \right)}, \quad \tau_{\text{rel,NP}} \geq 0.001$$

$$\frac{dJ_{\text{rel,NP}}}{dt} = \frac{J_{\text{rel,NP},\infty} - J_{\text{rel,NP}}}{\tau_{\text{rel,NP}}}$$

$$\beta_{\tau,\text{CaMK}} = 1.25 \cdot \beta_{\tau}$$

$$\alpha_{\text{rel,CaMK}} = 0.5 \cdot \beta_{\tau,\text{CaMK}}$$

$$J_{\text{rel,CaMK},\infty} = \frac{\alpha_{\text{rel,CaMK}} \cdot (-I_{\text{CaL}})}{1 + \left(\frac{1.5}{[\text{Ca}^{2+}]_{\text{jsr}}} \right)^8}$$

$$\tau_{\text{rel,CaMK}} = \frac{\beta_{\tau,\text{CaMK}}}{1 + \left(\frac{0.0123}{[\text{Ca}^{2+}]_{\text{jsr}}} \right)}, \tau_{\text{rel,CaMK}} \geq 0.001$$

$$\frac{dJ_{\text{rel,CaMK}}}{dt} = \frac{J_{\text{rel,CaMK},\infty} - J_{\text{rel,CaMK}}}{\tau_{\text{rel,CaMK}}}$$

$$K_{\text{m,CaMK}} = 0.15, \quad \phi_{\text{rel,CaMK}} = \frac{1}{1 + \frac{K_{\text{m,CaMK}}}{\text{CaMK}_{\text{active}}}}$$

$$J_{\text{rel}} = (1 - \phi_{\text{rel,CaMK}}) \cdot J_{\text{rel,NP}} + \phi_{\text{rel,CaMK}} \cdot J_{\text{rel,CaMK}}$$

Calcium Uptake via SERCA Pump (J_{up})

Ca^{2+} uptake channels (SERCA pumps) are phosphorylated by CaMK (Hawkins, Xu et al. 1994; Toyofuku, Curotto Kurzydowski et al. 1994). Here, we used two separate Ca^{2+} uptake populations: those not-phosphorylated ($J_{\text{up,NP}}$) and those phosphorylated by CaMK ($J_{\text{up,CaMK}}$). Ca^{2+} leakage from the NSR was identical to the formulation used in the Hund-Decker-Rudy model. However, leak magnitude was reduced by ~10%.

$$J_{\text{up,NP}} = \frac{0.004375 \cdot [\text{Ca}^{2+}]_i}{0.00092 + [\text{Ca}^{2+}]_i}$$

$$\overline{\Delta K_{\text{m,PLB}}} = 0.00017 \text{ mM}$$

$$\overline{\Delta J_{\text{up,CaMK}}} = 1.75$$

$$J_{\text{up,CaMK}} = \left(1 + \overline{\Delta J_{\text{up,CaMK}}} \right) \cdot \frac{0.004375 \cdot [\text{Ca}^{2+}]_i}{0.00092 - \overline{\Delta K_{\text{m,PLB}}} + [\text{Ca}^{2+}]_i}$$

$$K_{\text{m,CaMK}} = 0.15, \quad \phi_{\text{up,CaMK}} = \frac{1}{1 + \frac{K_{\text{m,CaMK}}}{\text{CaMK}_{\text{active}}}}$$

$$J_{\text{leak}} = \frac{0.0039375 \cdot [\text{Ca}^{2+}]_{\text{nsr}}}{15.0}$$

$$J_{\text{up}} = (1 - \phi_{\text{up,CaMK}}) \cdot J_{\text{up,NP}} + \phi_{\text{up,CaMK}} \cdot J_{\text{up,CaMK}} - J_{\text{leak}}$$

Calcium Translocation from NSR to JSR (J_{tr})

Sobie et al. (Sobie, Song et al. 2005) showed that Ca^{2+} spark recovery required 91 ms.

This measurement informed our choice of 100 ms for translocation time constant (τ_{tr}).

$$\tau_{\text{tr}} = 100 \text{ ms}$$

$$J_{\text{tr}} = \frac{[\text{Ca}^{2+}]_{\text{nsr}} - [\text{Ca}^{2+}]_{\text{jsr}}}{\tau_{\text{tr}}}$$

ORd Human Model Concentrations and Buffers

In the absence of human ventricle specific measurements, we take Ca^{2+} buffering equations and kinetics from the Hund-Decker-Rudy model.

$$[\overline{\text{CMDN}}] = 0.05 \text{ mM}, \quad K_{\text{m,CMDN}} = 0.00238 \text{ mM}$$

$$[\overline{\text{TRPN}}] = 0.07 \text{ mM}, \quad K_{\text{m,TRPN}} = 0.0005 \text{ mM}$$

$$[\overline{\text{BSR}}] = 0.047 \text{ mM}, \quad K_{\text{m,BSR}} = 0.00087 \text{ mM}$$

$$[\overline{\text{BSL}}] = 1.124 \text{ mM}, \quad K_{\text{m,BSL}} = 0.0087 \text{ mM}$$

$$[\overline{\text{CSQN}}] = 10.0 \text{ mM}, \quad K_{\text{m,CSQN}} = 0.8 \text{ mM}$$

$$\frac{d[\text{Na}^+]_i}{dt} = -(I_{\text{Na}} + I_{\text{NaL}} + 3 \cdot I_{\text{NaCa,i}} + 3 \cdot I_{\text{NaK}} + I_{\text{Nab}}) \cdot \frac{A_{\text{cap}}}{F \cdot v_{\text{myo}}} + J_{\text{diff,Na}} \cdot \frac{v_{\text{ss}}}{v_{\text{myo}}}$$

$$\frac{d[\text{Na}^+]_{\text{ss}}}{dt} = -(I_{\text{CaNa}} + 3 \cdot I_{\text{NaCa,ss}}) \cdot \frac{A_{\text{cap}}}{F \cdot v_{\text{ss}}} - J_{\text{diff,Na}}$$

$$\frac{d[\text{K}^+]_i}{dt} = -(I_{\text{to}} + I_{\text{Kr}} + I_{\text{Ks}} + I_{\text{K1}} + I_{\text{Kur}} + I_{\text{stim}} - 2 \cdot I_{\text{NaK}}) \cdot \frac{A_{\text{cap}}}{F \cdot v_{\text{myo}}} + J_{\text{diff,K}} \cdot \frac{v_{\text{ss}}}{v_{\text{myo}}}$$

$$\frac{d[\text{K}^+]_{\text{ss}}}{dt} = -I_{\text{CaK}} \cdot \frac{A_{\text{cap}}}{F \cdot v_{\text{ss}}} - J_{\text{diff,K}}$$

$$\beta_{\text{Cai}} = \frac{1}{1 + \frac{[\text{CMDN}] \cdot K_{\text{m,CMDN}}}{(K_{\text{m,CMDN}} + [\text{Ca}^{2+}]_i)^2} + \frac{[\text{TRPN}] \cdot K_{\text{m,TRPN}}}{(K_{\text{m,TRPN}} + [\text{Ca}^{2+}]_i)^2}}$$

$$\frac{d[\text{Ca}^{2+}]_i}{dt} = \beta_{\text{Cai}} \cdot \left(-(I_{\text{pCa}} + I_{\text{Cab}} - 2 \cdot I_{\text{NaCa,i}}) \cdot \frac{A_{\text{cap}}}{2 \cdot F \cdot v_{\text{myo}}} - J_{\text{up}} \cdot \frac{v_{\text{nsr}}}{v_{\text{myo}}} + J_{\text{diff,Ca}} \cdot \frac{v_{\text{ss}}}{v_{\text{myo}}} \right)$$

$$\beta_{\text{Cass}} = \frac{1}{1 + \frac{[\text{BSR}] \cdot K_{\text{m,BSR}}}{(K_{\text{m,BSR}} + [\text{Ca}^{2+}]_{\text{ss}})^2} + \frac{[\text{BSL}] \cdot K_{\text{m,BSL}}}{(K_{\text{m,BSL}} + [\text{Ca}^{2+}]_{\text{ss}})^2}}$$

$$\frac{d[\text{Ca}^{2+}]_{\text{ss}}}{dt} = \beta_{\text{Cass}} \cdot \left(-(I_{\text{CaL}} - 2 \cdot I_{\text{NaCa,ss}}) \cdot \frac{A_{\text{cap}}}{2 \cdot F \cdot v_{\text{ss}}} + J_{\text{rel}} \cdot \frac{v_{\text{jsr}}}{v_{\text{ss}}} - J_{\text{diff,Ca}} \right)$$

$$\frac{d[\text{Ca}^{2+}]_{\text{nsr}}}{dt} = J_{\text{up}} - J_{\text{tr}} \cdot \frac{v_{\text{jsr}}}{v_{\text{nsr}}}$$

$$\beta_{\text{Cajsr}} = \frac{1}{1 + \frac{[\text{CSQN}] \cdot K_{\text{m,CSQN}}}{(K_{\text{m,CSQN}} + [\text{Ca}^{2+}]_{\text{jsr}})^2}}$$

$$\frac{d[\text{Ca}^{2+}]_{\text{jsr}}}{dt} = \beta_{\text{Cajsr}} \cdot (J_{\text{tr}} - J_{\text{rel}})$$

ORd Human Model Transmural Heterogeneity

	epi/endo	M/endo
G_{NaL}	0.6	1
G_{to}	4.0	4.0
$P_{Ca}, P_{CaNa}, P_{CaK}$	1.2	2.5
G_{Kr}	1.3	0.8
G_{Ks}	1.4	1
G_{K1}	1.2	1.3
$G_{NaCa,i}, G_{NaCa,ss}$	1.1	1.4
G_{NaK}	0.9	0.7
G_{Kb}	0.6	1
$J_{rel,NP,\infty}, J_{rel,CaMK,\infty}$	1	1.7
$J_{up,NP}, J_{up,CaMK}$	1.3	1
[CMDN]	1.3	1

Scaling Factors for Model Implementation of Transmural Heterogeneity

Formulation changes to account for epi I_{to} differences are:

$$\delta_{epi} = 1.0 - \frac{0.95}{1.0 + \exp\left(\frac{V + 70.0}{5.0}\right)}$$

$$\tau_{i,epi,fast} = \tau_{i,fast} \cdot \delta_{epi}$$

$$\tau_{i,epi,slow} = \tau_{i,slow} \cdot \delta_{epi}$$

Computational Methodology

Hardware and Software

For simulation of the basic human model, we used custom code developed and run using Microsoft Visual C++ 2008 Express Edition on a Windows Vista Dell desktop PC, with an Intel

Core 2 Quad processor. Integration was performed as described below (Rapid Integration). We also used custom C++ code run on an array of Dell cluster nodes with 64-bit Intel Xeon processors, running Linux and Sun Microsystems Grid Engine. Execution scripts were written in Python. A fixed time step of 0.01 ms was applied, and the Rush-Larsen Method(Rush and Larsen 1978) was used. All simulations were paced to true steady state(Livshitz and Rudy 2009), unless otherwise noted.

Validation and fitting of individual model components (i.e. time constants, steady state curves) was performed using custom code written in Matlab 2009a running on a Windows Vista Dell desktop PC, with an Intel Core 2 Quad processor. Integration of currents was performed as described below (Rapid Integration). Automated parameter estimation used a sum of least squares objective function, minimized by Matlab functions “fmincon”, “ga”, and “lsqcurvefit” (interior reflexive Newton’s Method for “fmincon” and “lsqcurvefit”, genetic algorithm for “ga”). See Matlab documentation for details and references. We used the parallel implementation of “fmincon” and “ga” by opening a matlabpool (size 4). Manual parameter estimation was also used, where minimization was by simple guess and check.

Rapid Integration

The Rush-Larsen Method(Rush and Larsen 1978), applied by Victorri et al.(Victorri, Vinet et al. 1985), relies on the assumption that during sufficiently small time intervals, a system of differential algebraic equations becomes effectively uncoupled. One can then readily solve uncoupled differential equations one-by-one to obtain expressions for time evolution of state variables.

Here, identification of sufficiently small time intervals (dt) was determined by comparison to gold standard simulations with fixed dt = 0.005 ms. We match the gold standard when we apply the following rules:

- 1) dt = 0.005 ms from the start of the stimulus until 25 ms thereafter
- 2) maximum allowed dt = 1.0 ms

3) dt was adjusted dynamically with changes in membrane voltage, as described in LR1(Luo and Rudy 1991):

a. if $\Delta V \leq 0.2$ mV, $dt = 0.8 \cdot \frac{dV}{dt}$

b. if $\Delta V \geq 0.8$ mV, $dt = 0.2 \cdot \frac{dV}{dt}$

i. while $\Delta V \geq 0.8$ mV, dt is reduced tenfold until the condition, $\Delta V < 0.8$ mV, is met (minimum dt = 0.005 ms)

Equations for updating gates (e.g. generic gate, s)

$$s = s_{\infty} - (s_{\infty} - s) \cdot \exp\left(\frac{-dt}{\tau_s}\right)$$

Equations for updating the n gate, $J_{rel,NP}$, and $J_{rel,CaMK}$

$$n = \alpha_n \cdot \frac{k_{+2,n}}{k_{-2,n}} - \left(\alpha_n \cdot \frac{k_{+2,n}}{k_{-2,n}} - n \right) \cdot \exp(-k_{-2,n} \cdot dt)$$

$$J_{rel,NP} = J_{rel,NP,\infty} - (J_{rel,NP,\infty} - J_{rel,NP}) \cdot \exp\left(\frac{-dt}{\tau_{rel,NP}}\right)$$

$$J_{rel,CaMK} = J_{rel,CaMK,\infty} - (J_{rel,CaMK,\infty} - J_{rel,CaMK}) \cdot \exp\left(\frac{-dt}{\tau_{rel,CaMK}}\right)$$

The Forward Euler Method was applied to update membrane voltage, concentrations, and $CaMK_{trap}$ at each time step.

Using the above method, it took less than one minute of runtime to pace the model to true and accurate steady state at 1 Hz (Microsoft Visual C++ 2008 Express Edition on a Windows Vista Dell desktop PC, with a 2.83 GHz Intel Core 2 Quad processor).

Chapter 2 Supplementary Figures

Additional Details for Currents

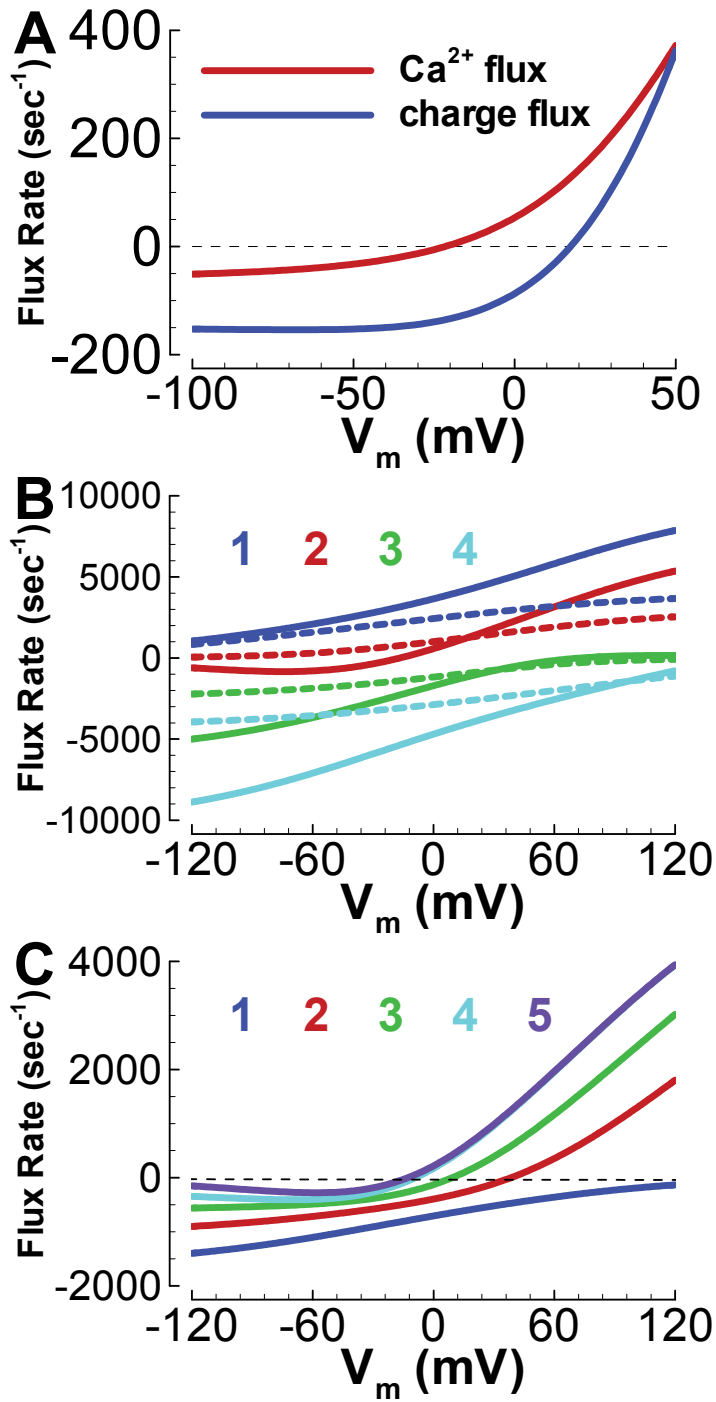


Figure 2.S01. Human I_{NaCa} model faithfully reproduces Kang and Hilgemann(Kang and Hilgemann 2004) observations. Compare Figures 3C, 4A, 4C from Kang and Hilgemann(Kang and Hilgemann 2004) with the simulations from our human I_{NaCa} model, presented here (same protocols were used). A) Charge flux reversal potential is more depolarized than Ca^{2+} flux, a feature of this model which includes the observed Na^+ leak mode. B) Charge flux (solid lines) and Ca^{2+} flux (dashed lines) versus voltage, for a variety of substrates (in mM, condition 1: $[Na^+]_o=0$, $[Na^+]_i=40$, $[Ca^{2+}]_o=4$, $[Ca^{2+}]_i=0$; condition 2: $[Na^+]_o=120$, $[Na^+]_i=40$, $[Ca^{2+}]_o=4$, $[Ca^{2+}]_i=0$; condition 3: $[Na^+]_o=120$, $[Na^+]_i=40$, $[Ca^{2+}]_o=0$, $[Ca^{2+}]_i=0.1$; condition 4: $[Na^+]_o=120$, $[Na^+]_i=4$, $[Ca^{2+}]_o=0$, $[Ca^{2+}]_i=0.1$). C) Reversal potential is sensitive to ionic substrate (in mM, $[Na^+]_o=100$, $[Ca^{2+}]_o=1.2$, $[Ca^{2+}]_i=0.0005$, condition 1: $[Na^+]_i=0$; condition 2: $[Na^+]_i=5$; condition 3: $[Na^+]_i=10$; condition 4: $[Na^+]_i=20$; condition 5: $[Na^+]_i=20$, $[Ca^{2+}]_i=0$).

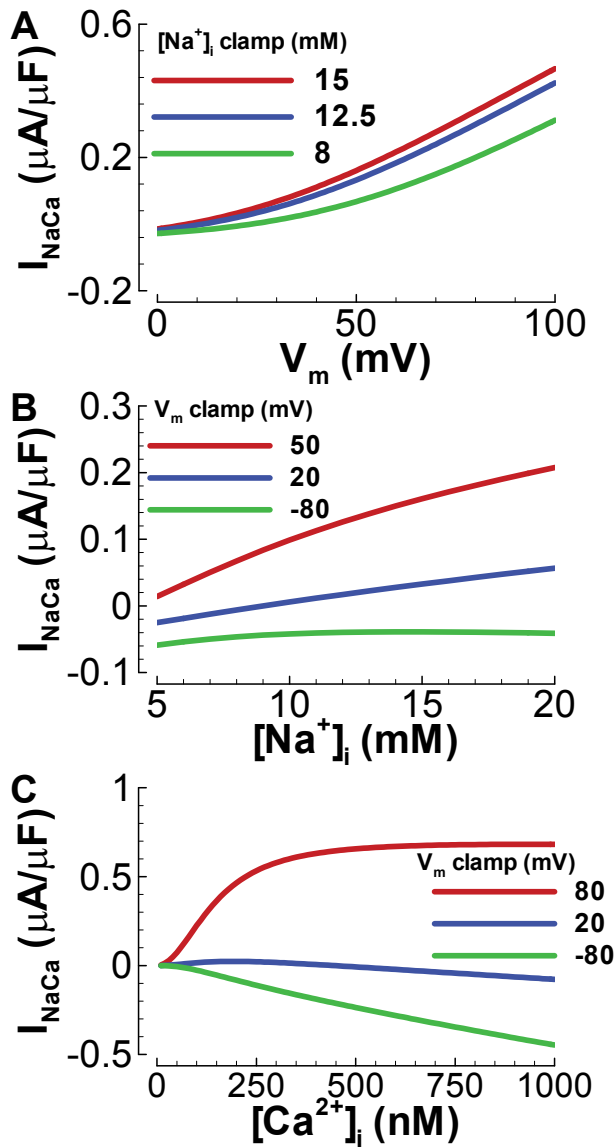


Figure 2.S02. Human I_{NaCa} model faithfully reproduces observations of Weber et al. (Weber, Piacentino et al. 2003). Compare Weber et al. (Weber, Piacentino et al. 2003), their Figure 2, with simulations from our human I_{NaCa} model, shown here (same protocols were used). A) Voltage dependence of I_{NaCa} under different intracellular Na^+ clamp conditions. B) Intracellular Na^+ dependence of I_{NaCa} under different voltage clamp conditions. C) Intracellular Ca^{2+} dependence of I_{NaCa} under different voltage clamp conditions. The model incorporates Weber's "allosteric activation", seen at depolarized voltages.

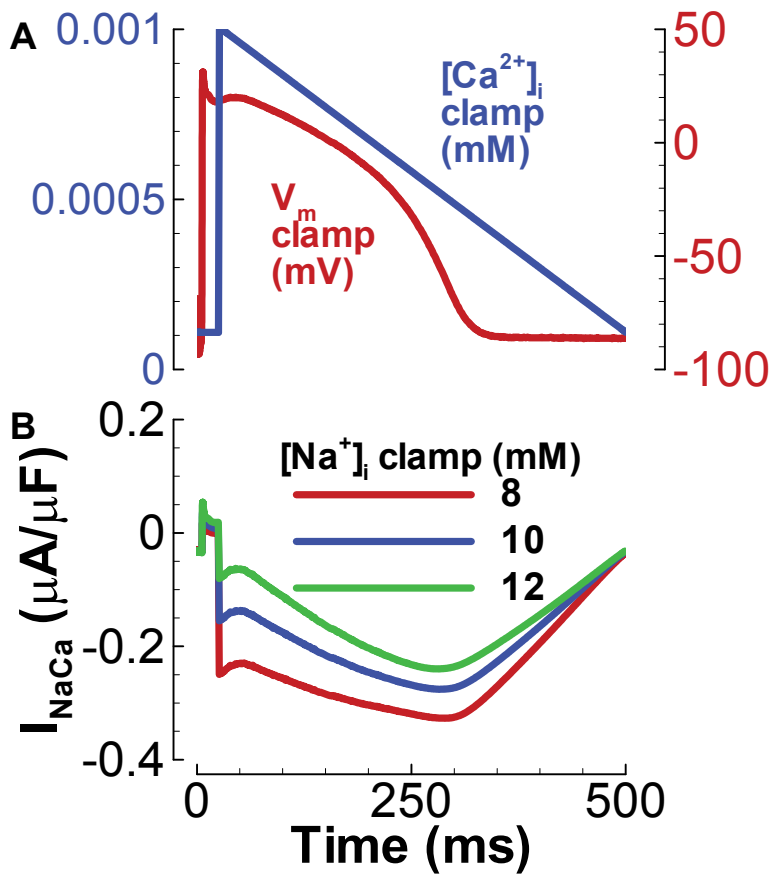


Figure 2.S03. Human I_{NaCa} model faithfully reproduces Weber et al. (Weber, Piacentino et al. 2003) intracellular Na^+ dependence under AP and Ca^{2+} clamp conditions. Compare Weber et al. (Weber, Piacentino et al. 2003) Figure 6A with simulations from our I_{NaCa} model, shown here (same protocols were used). A) Clamped Ca^{2+} transient (similar to Weber et al. (Weber, Piacentino et al. 2003), increasing instantaneously from 0.01 to 0.1 μM , and decaying over 500 ms), and action potential waveform measured in undiseased human ventricular myocytes (microelectrode recording, see Experimental Methods section of this supplement for more details). B) Due to depolarization, exchange current was outward, briefly, until $[Ca^{2+}]_i$ rose. When $[Na^+]_i$ was relatively low, maximal inward exchange current increased, as Weber showed.

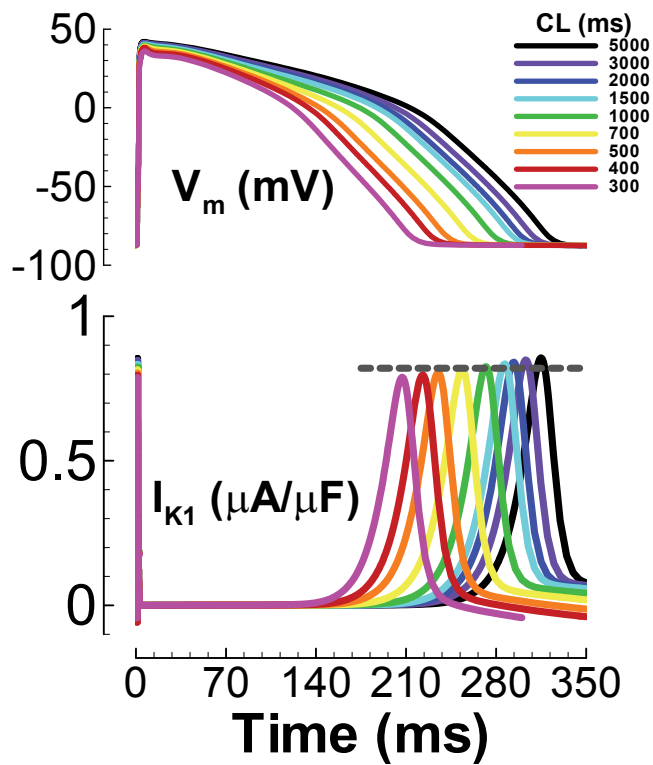


Figure 2.S04. I_{K1} shows voltage dependence, but not rate dependence. Top panel: Simulated action potentials, paced at different cycle lengths. Bottom panel: I_{K1} in the model, at the different pacing rates. Note that the peak current reached was largely rate independent, as was shown by Jost et al. (Jost, Acsai et al. 2009) in undiseased human ventricle experiments.

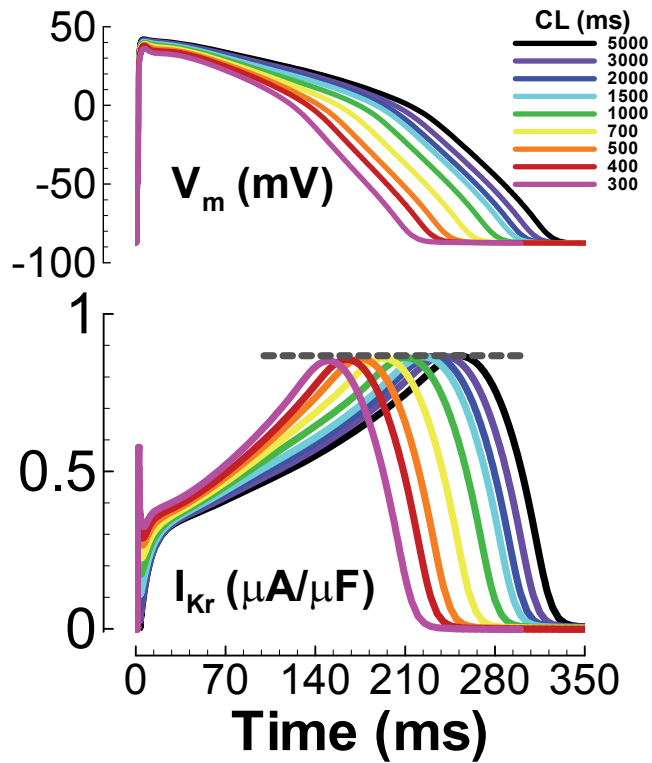


Figure 2.S05. I_{Kr} shows voltage dependence, but not rate dependence. Top panel: Simulated action potentials, paced at different cycle lengths. Bottom panel: I_{Kr} in the model, at the different pacing rates. Note that the peak current reached was rate independent, as was shown by Jost et al. (Jost, Acsai et al. 2009) in undiseased human ventricle experiments.

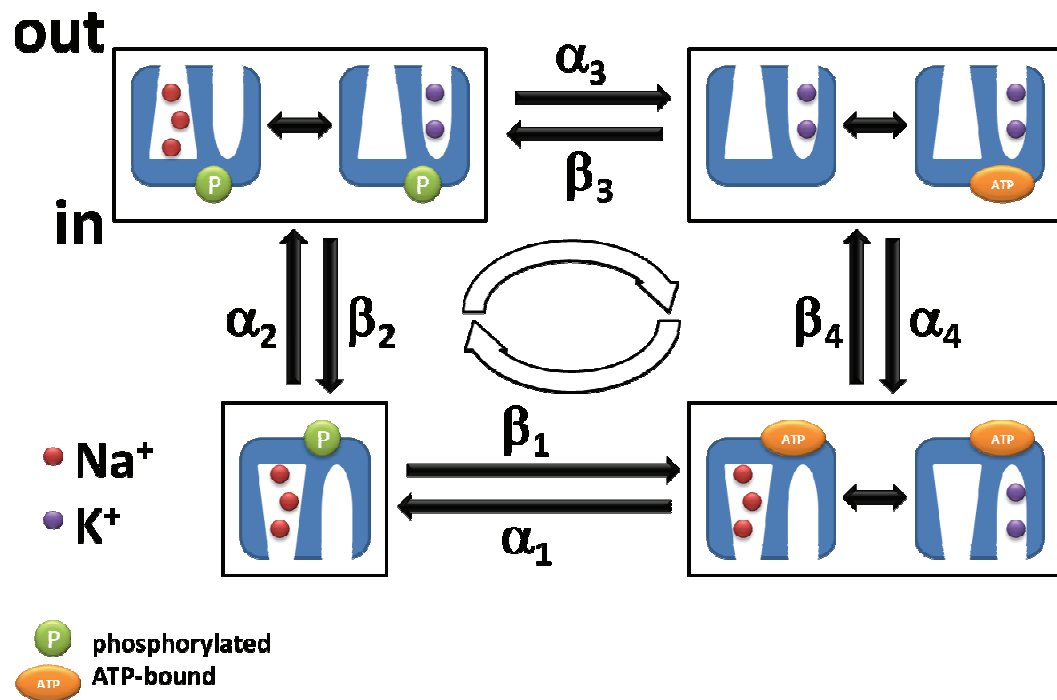


Figure 2.S06. Schematic diagram of the human I_{NaK} model, modified from Smith and Crampin (Smith and Crampin 2004). There are four distinct enzymatic states, with lumped substates where non-rate limiting transitions were assumed to be in rapid equilibrium. Forward pump function is clockwise cycling. From this diagram, we formulated equations for the current using the King-Altman method (King and Altman 1956).

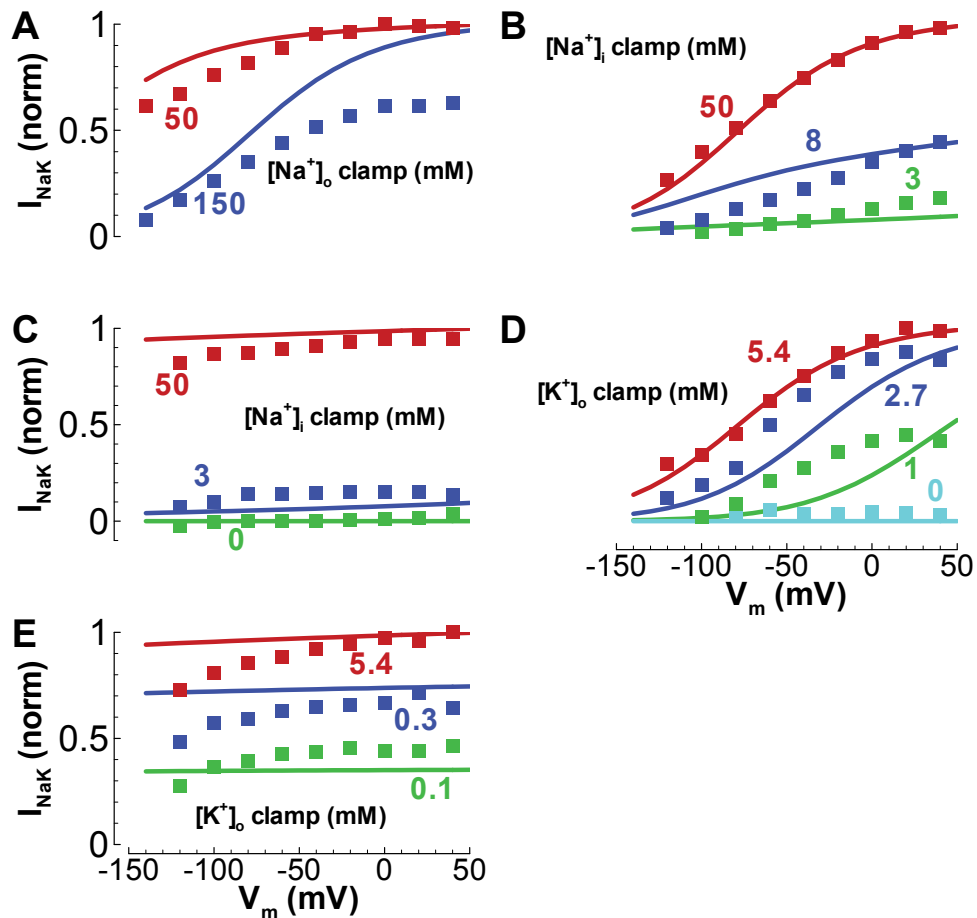


Figure 2.S07. Human I_{NaK} model faithfully reproduces major observations of Nakao and Gadsby (Nakao and Gadsby 1989). Data (squares) are from Nakao and Gadsby (Nakao and Gadsby 1989), their Figures 2A, 4C, 7A, 9B, 10B. I_{NaK} model simulations are solid lines (same protocols used). The model is not a perfect match to these data, measured in guinea pig ventricle, but the basic voltage and concentration dependencies are duplicated, demonstrating that the model is dynamically and mechanistically correct. A) Voltage dependence of I_{NaK} under different extracellular Na^+ clamp conditions. B) Voltage dependence of I_{NaK} under different intracellular Na^+ clamp conditions, and $[Na^+]_o=150$ mM. C) Voltage dependence of I_{NaK} under different intracellular Na^+ clamp conditions, and $[Na^+]_o=0$ mM. D) Voltage dependence of I_{NaK} under different extracellular K^+ clamp conditions, and $[Na^+]_o=150$ mM. E) Voltage dependence of I_{NaK} under different extracellular K^+ clamp conditions, and $[Na^+]_o=0$ mM.

APD Rate Dependence in Homogeneous Multicellular Fiber

We used microelectrode action potentials, measured in the undiseased human ventricle at 37 °C, for model validation. Since these data were measured in a multicellular preparation, the experimental protocol was simulated in a 1-dimensional multicellular fiber(Decker, Heijman et al. 2009). In Decker et al.(Decker, Heijman et al. 2009), the subtle but complex differences in APD adaptation between single cell and a multicellular fiber were investigated. We used the conduction equations as in Decker et al. (-200 $\mu\text{A}/\mu\text{F}$, 1 ms stimulus delivered to fiber end, zero flux boundary conditions), and measured the model APD at the 50th cell in a 100-cell homogeneous subendocardial strand. Fiber results were similar to single cell results, as in Decker et al, and match the experimental data. Conduction velocity was 45 cm/sec at 1 Hz pacing, consistent with available (canine) experiments(Spach, Heidlage et al. 2000).

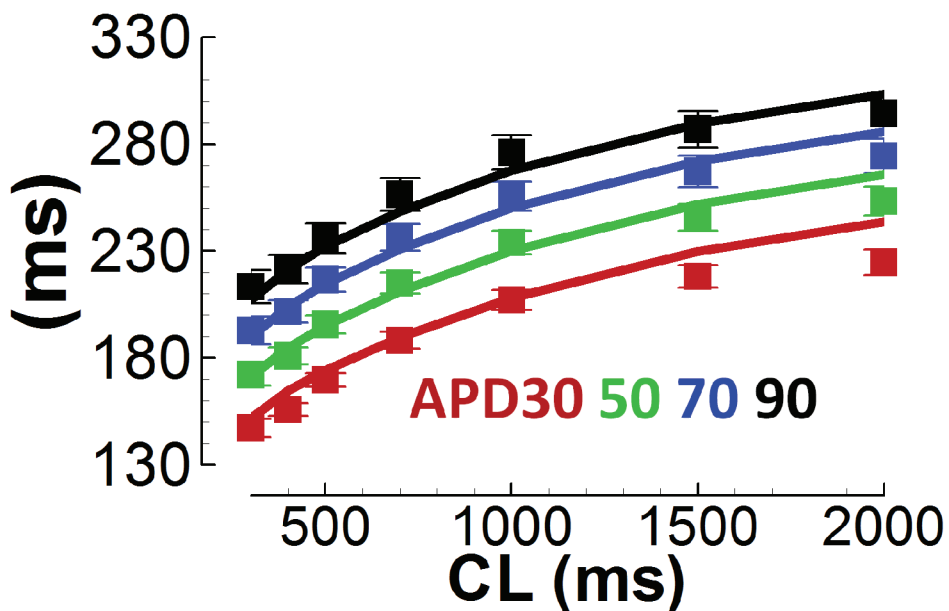


Figure 2.S08. Multicellular strand simulations compared to measurements. APD30, APD50, APD70, and APD90 shown in red, green, blue, and black, respectively. Squares are experimentally measured human subendocardial action potentials, at 37°C, N=140. Solid lines are simulation results from the 50th cell in a 100-cell strand (zero flux boundary).

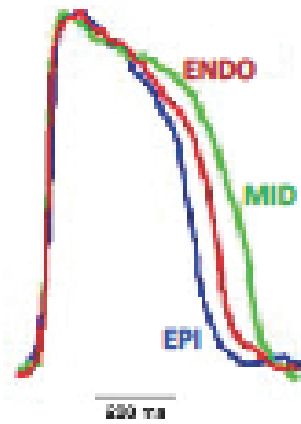
Transmural AP Simulations Compared with Nonfailing Human Optical Mapping Experiments

Experiments

experiments

heart #5

CL = 1000 ms



simulations, CL = 1000 ms

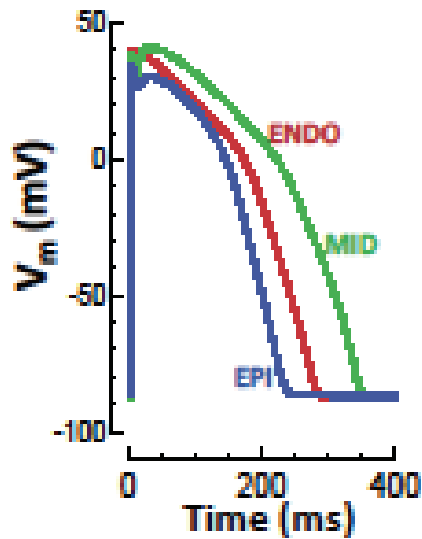


Figure 2.S09. Experiments (top) are from an undiseased human heart (heart #5, male, age 20, death from Tylenol overdose), measured by Glukhov et al.(Glukhov, Fedorov et al. 2010), reproduced with permission. Simulations are below. Cell types are color coded and labeled. CL = 1000 ms.

Alternans Simulation in Coupled Tissue

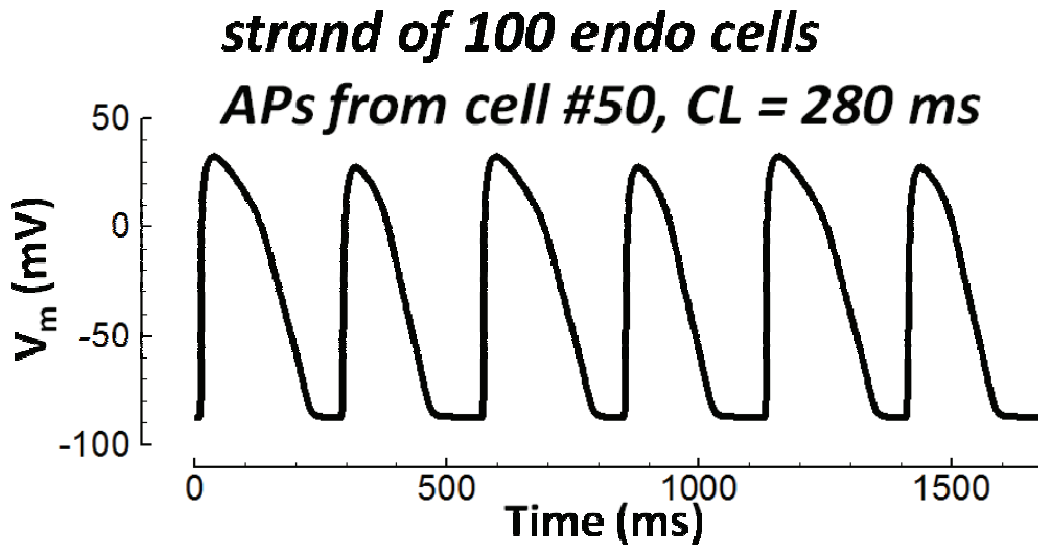


Figure 2.S10. A strand composed of 100 endo cells was paced at CL = 280 ms until steady state was reached. Beat to beat APD alternans were evident at the central cell (#50, isolated from edge effects).

Alternans were Eliminated by SERCA2a Upregulation

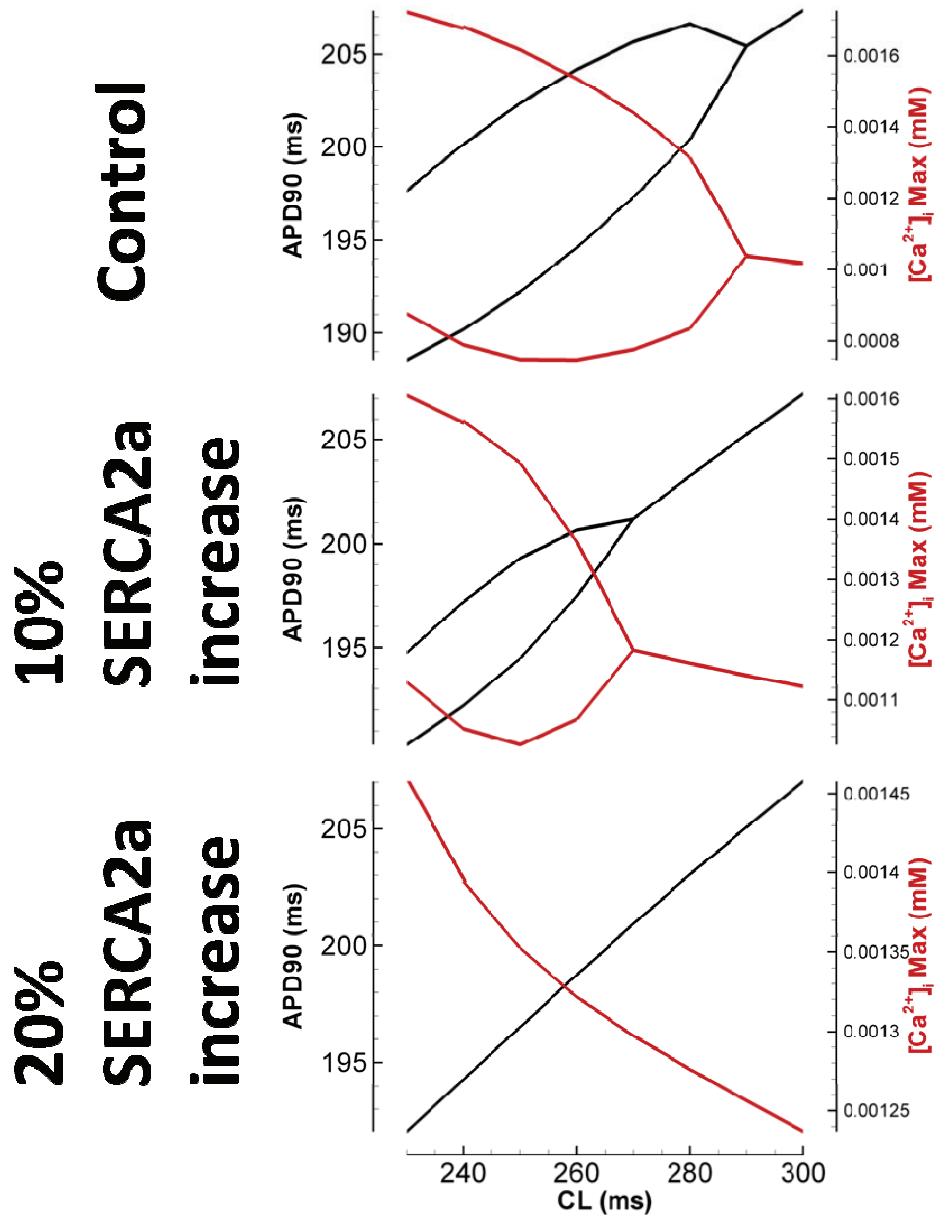


Figure 2.S11. Alternans were eliminated by upregulation of SERCA2a (J_{up} in the model), as in experiments by Cutler et al. (Cutler, Wan et al. 2009). APD90 is on the left axes in black. Peak intracellular Ca^{2+} concentration ($[Ca^{2+}]_i$ Max) is on the right axes in red. From top to bottom, J_{up} was increased from control by 10, and 20 %. For 10% increase in J_{up} , the alternans bifurcation shifted to faster rates. For 20% increase, the bifurcation was eliminated.

Effects of H^+ , CO_2 and HCO_3^- on Na^+ Handling, I_{NaK} and APD Rate Dependence

We kept Cl^- concentration constant, since the ORd model does not systematically include Cl^- handling (20 mM intracellular and 100 mM extracellular, as in Decker et al.(Decker, Heijman et al. 2009)). Otherwise, all Crampin and Smith equations were included exactly as described(Crampin and Smith 2006). The I_{NaK} formulation we used, based on Smith and Crampin(Smith and Crampin 2004), includes pH dependence. The simulations below allow I_{NaK} to respond dynamically to pH.

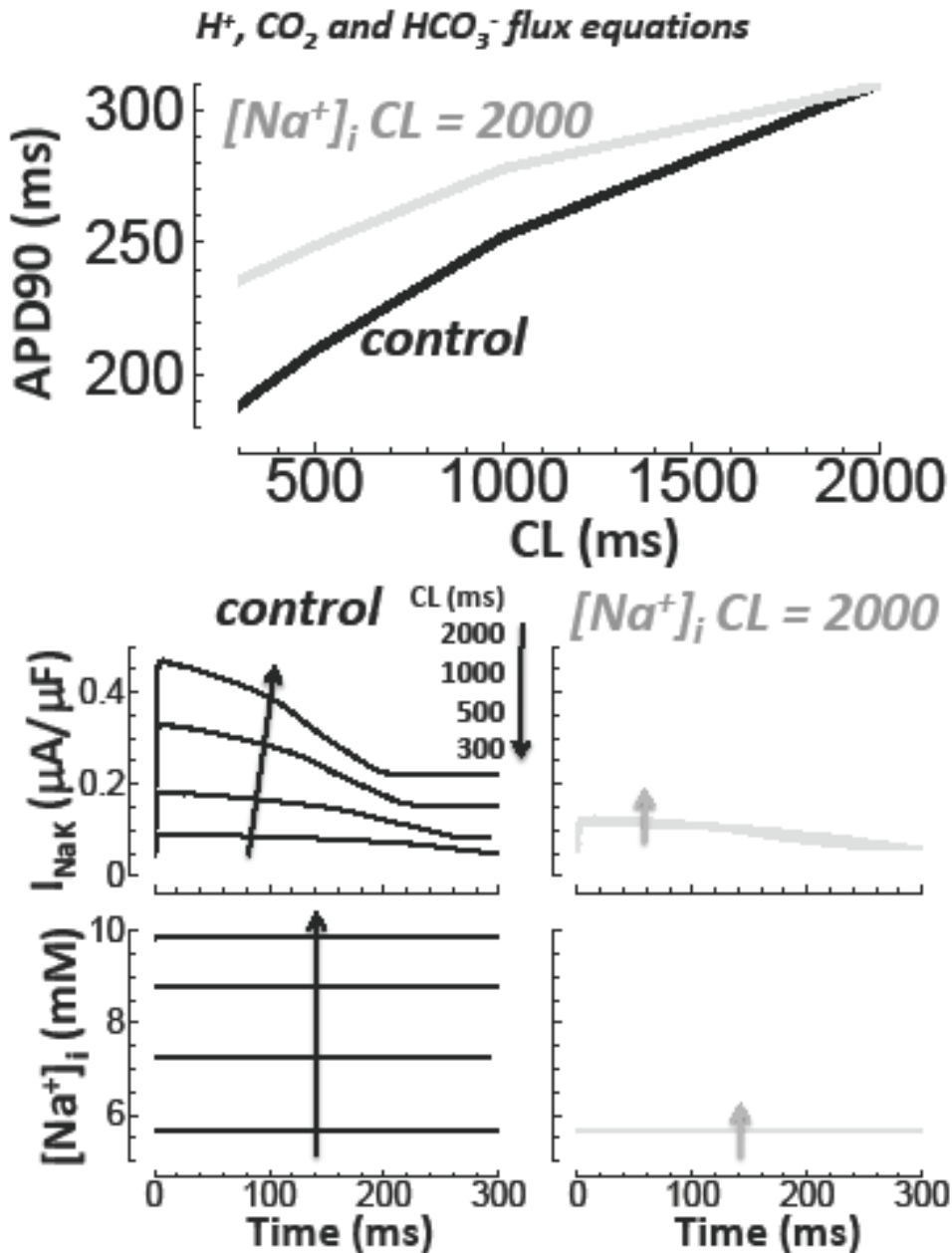


Figure 2.S12. H^+ , CO_2 and HCO_3^- fluxes did not change the relationship between Na^+ accumulation, I_{NaK} and APD rate dependence. Top) APD90 rate dependence with incorporation of the Crampin and Smith equations (Crampin and Smith 2006) (black line). When intracellular Na^+ concentration ($[Na^+]_i$) was artificially kept low, at the CL = 2000 ms value, the ability of the APD to shorten at fast rates was substantially reduced (gray line). Bottom) Left) As pacing rate increased (indicated by arrows) I_{NaK} increased due to $[Na^+]_i$ accumulation. Right) However, when $[Na^+]_i$ was clamped at the low CL = 2000 ms value, I_{NaK} became rate independent. This hampered APD shortening at fast pacing rates.

Effect of KCNE1 Heterogeneity on Transmural I_{Ks} and AP Simulations

Protein forming the β -subunit of I_{Ks} , KCNE1 was measured to be transmurally heterogeneous in the undiseased human ventricle (Szabo, Szentandrássy et al. 2005). Western blots showed about two-fold greater intensity for KCNE1 in M-cells compared to epi cells. Considering that KCNE1:KCNQ1 stoichiometry is variable (Nakajo, Ulbrich et al. 2010), and that the presence of KCNE1 slows I_{Ks} activation by about five fold and increases I_{Ks} conductance by about five fold, we simulated the effect of KCNE1 transmural heterogeneity on I_{Ks} and the AP. Thus, for heterogeneous KCNE1 simulations in M-cells, I_{Ks} activation was five times slower and conductance was five times greater than in the control M-cell. For epi cells, activation was five times faster, and conductance was five times smaller than in the control epi cell. These conditions are exaggerated (five fold changes compared KCNE1 overabundance to total KCNE1 absence (Sanguinetti, Curran et al. 1996)), showing possible KCNE1 transmural heterogeneity effects in the extreme. As shown, even for the extreme case there was little effect on I_{Ks} or especially on the AP.

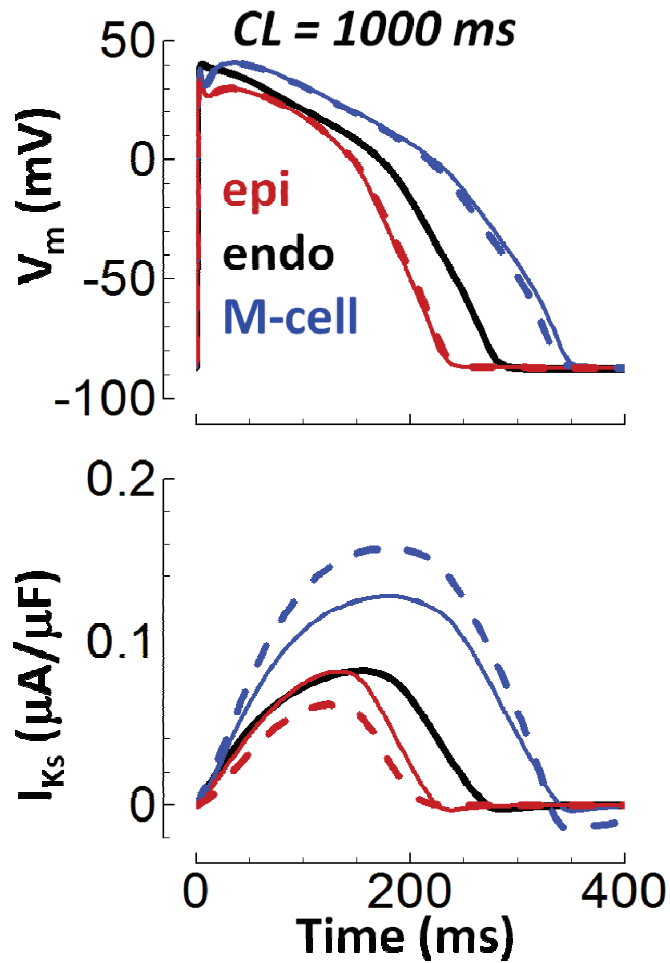


Figure 2.S13. Transmural heterogeneity of KCNE1 β -subunit had minimal effect on transmural heterogeneity of I_{Ks} and the AP. Results for control conditions are solid lines (black is endo, blue is M-cell, red is epi). Dashed lines show the effect of the KCNE1 heterogeneity. Top) AP. Bottom) I_{Ks} .

APD Accommodation

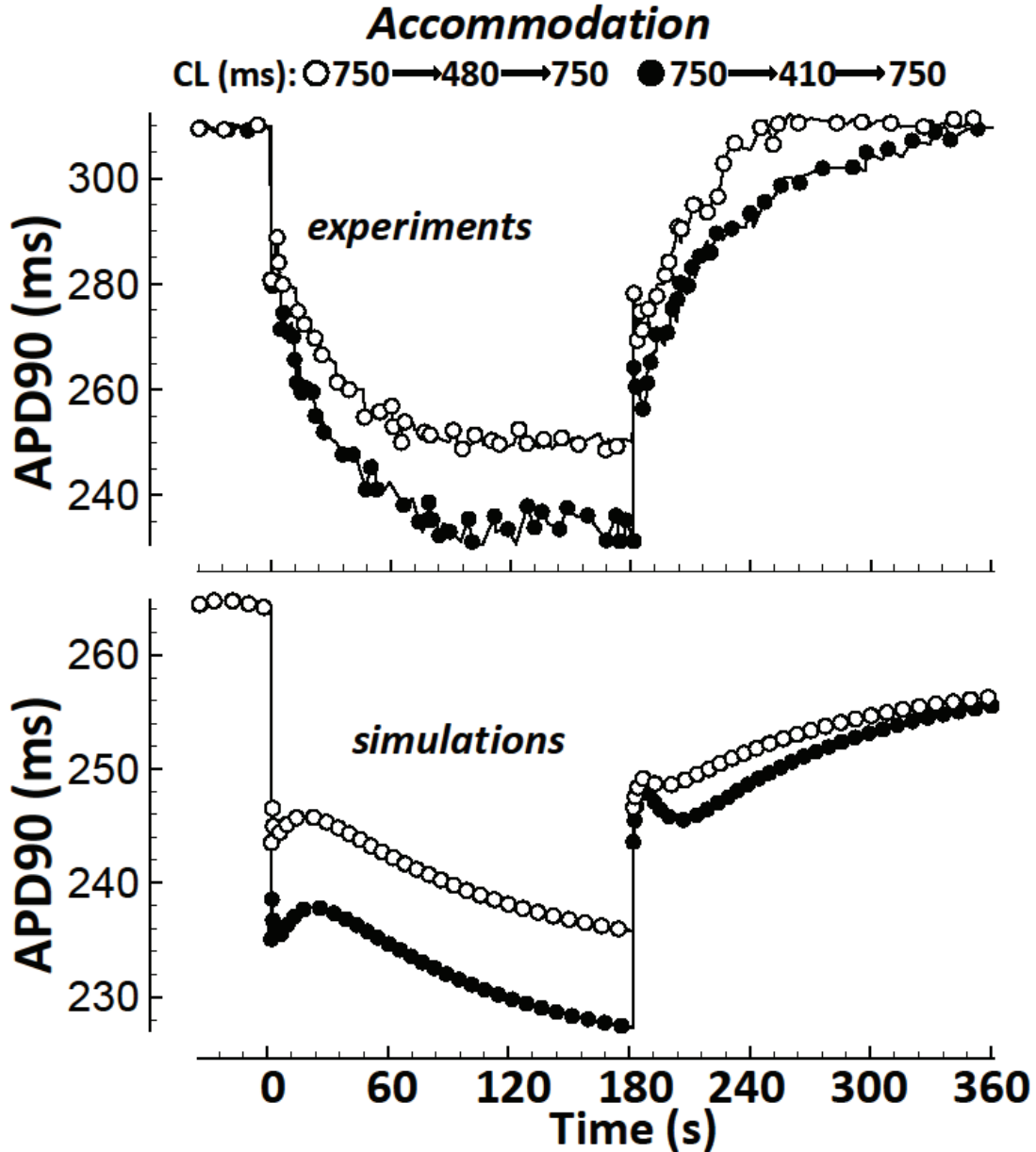


Figure 2.S14. APD90 Accommodation. At time = 0 seconds, pacing CL was abruptly reduced. At time = 180 seconds, the pacing CL was abruptly increased to its original value. CL change from 750 to 480 ms is shown with white circles. Black circles show CL change from 750 to 410 ms. Experiments (top) are from in vivo nonfailing human hearts, measured by Franz et al. (Franz, Swerdlow et al. 1988). Simulations are below.

Parameter Sensitivity Analysis

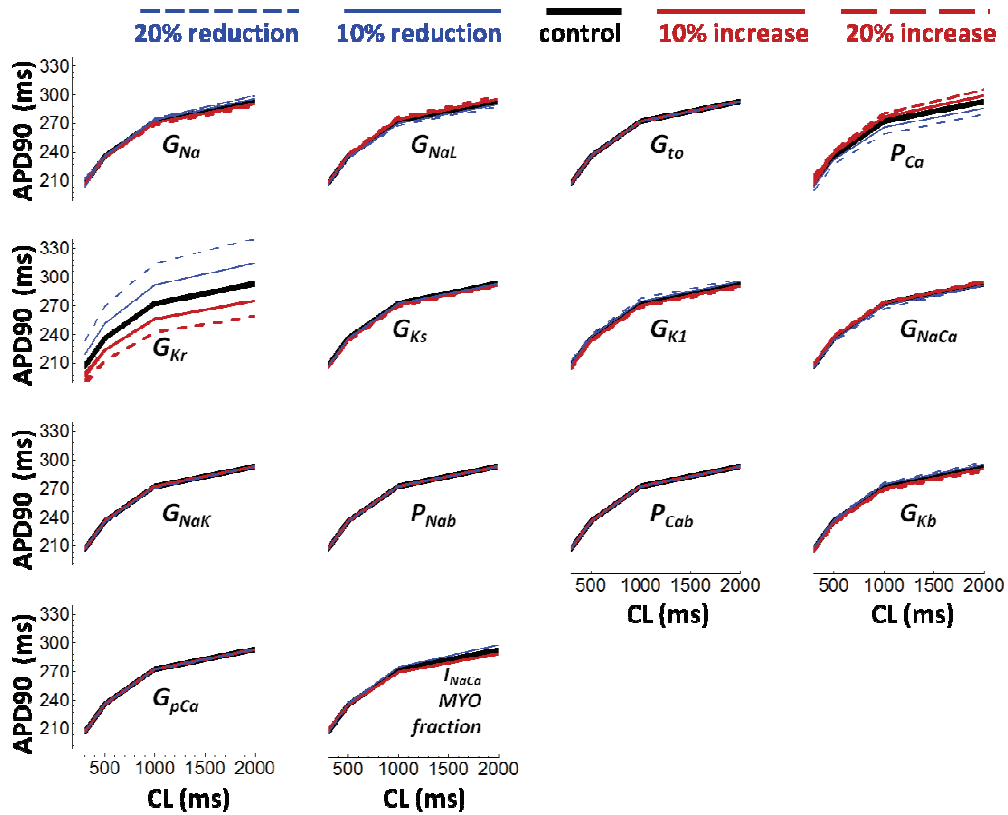


Figure 2.S15. Sensitivity of steady state APD90 rate dependence to variations in current conductances and to the fraction of I_{NaCa} in the myoplasm (80% in the control case). The control case is shown with the thick black line. Parameter reductions are in blue (20% dashed blue, 10% solid blue). Parameter increases are shown in red (10% solid red, 20% dashed red).

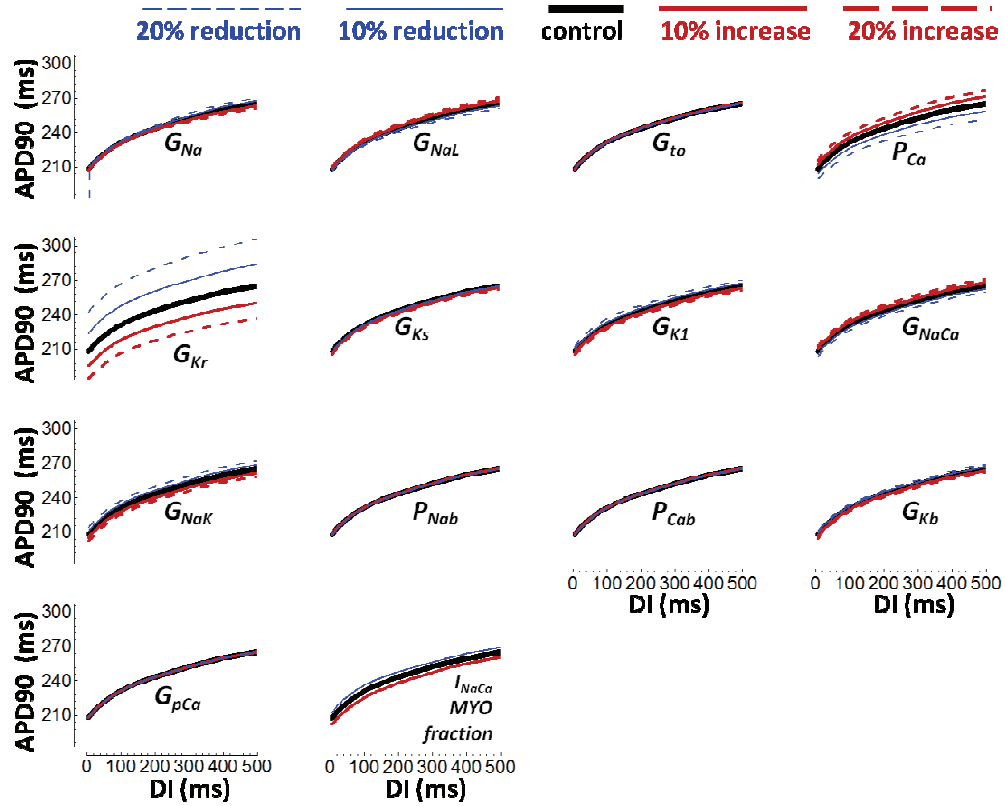


Figure 2.S16. Sensitivity of S1S2 restitution of APD90 to variations in current conductances and to the fraction of I_{NaCa} in the myoplasm (80% in the control case). The control case is shown with the thick black line. Parameter reductions are in blue (20% dashed blue, 10% solid blue). Parameter increases are shown in red (10% solid red, 20% dashed red).

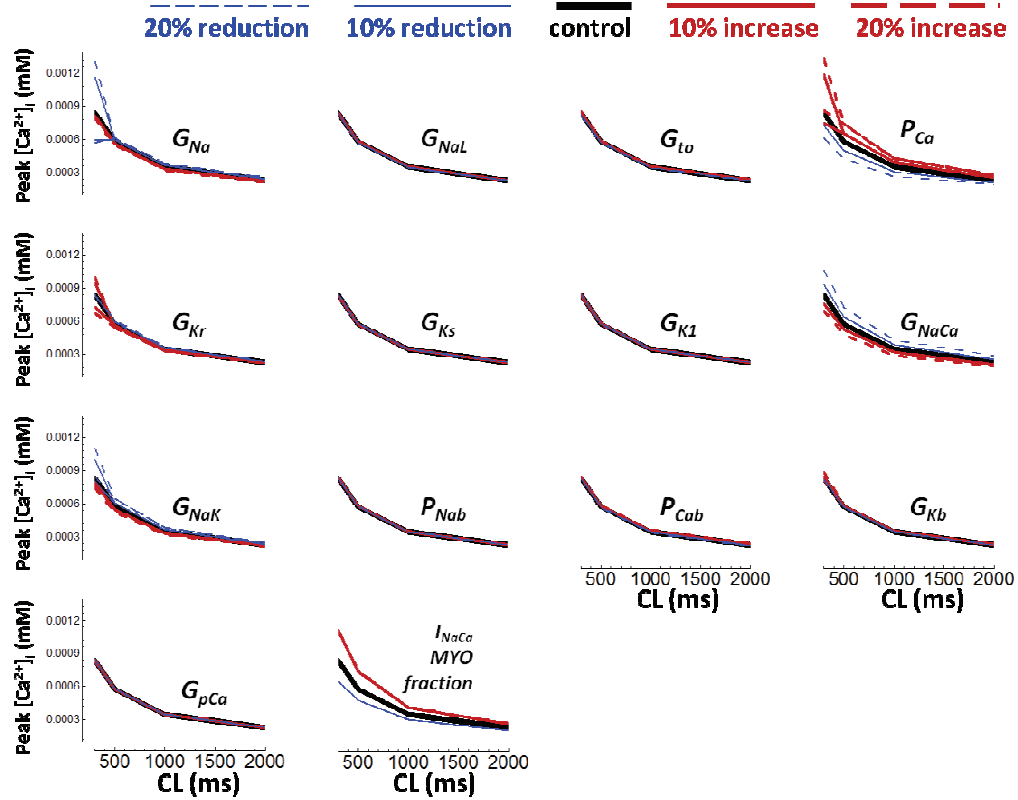


Figure 2.S17. Sensitivity of rate dependence of maximum (systolic) intracellular Ca^{2+} concentration (peak $[\text{Ca}^{2+}]_i$) to variations in current conductances and to the fraction of I_{NaCa} in the myoplasm (80% in the control case). The control case is shown with the thick black line. Parameter reductions are in blue (20% dashed blue, 10% solid blue). Parameter increases are shown in red (10% solid red, 20% dashed red).

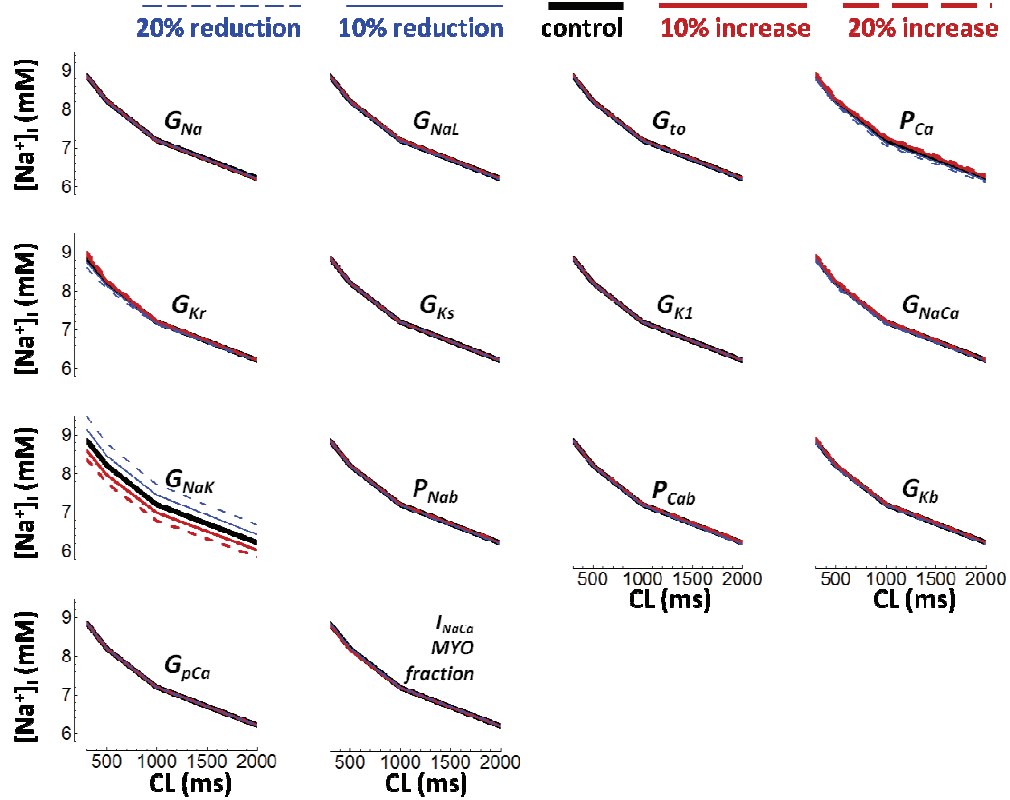


Figure 2.S18. Sensitivity of rate dependence of intracellular Na^+ concentration ($[\text{Na}^+]_i$) to variations in current conductances and to the fraction of I_{NaCa} in the myoplasm (80% in the control case). The control case is shown with the thick black line. Parameter reductions are in blue (20% dashed blue, 10% solid blue). Parameter increases are shown in red (10% solid red, 20% dashed red).

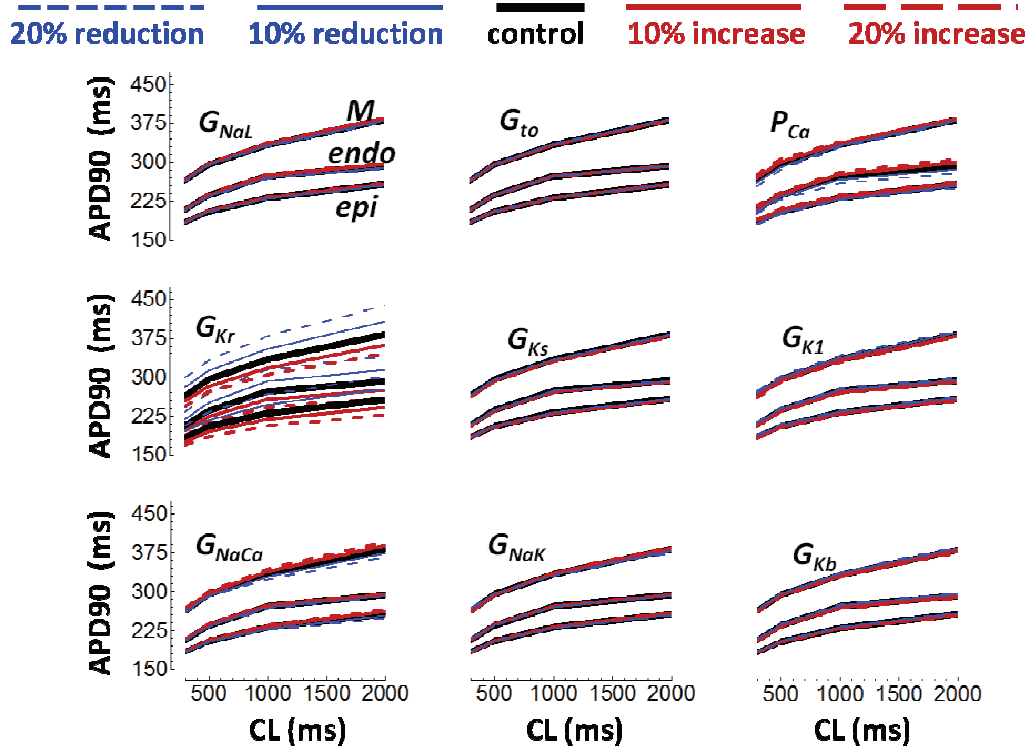


Figure 2.S19. Sensitivity of steady state rate dependence of APD90 in the different transmural cell types to changes in current conductances. The control case is shown with the thick black line. Parameter reductions are in blue (20% dashed blue, 10% solid blue). Parameter increases are shown in red (10% solid red, 20% dashed red).

Chapter 3: Multiple Hits Evince Arrhythmic Phenotype in Subclinical Long QT Syndrome: Simulation Studies of the Silent KCNQ1 Mutation Q357R

Introduction

Long QT syndrome (LQTS) causes sudden death due to cardiac arrhythmia in the absence of structural heart disease in otherwise healthy people (Roden 2008). LQTS prevalence is estimated to be quite high, affecting as many as 1 in 2000 among caucasians (Schwartz, Stramba-Badiale et al. 2009). The most common form of LQTS is type-1 (LQT1) (Priori, Schwartz et al. 2003) with KCNQ1 as the locus of mutations. This gene transcribes the Kv7.1 protein, forming the α -subunit of the ventricular repolarizing slow delayed rectifier K^+ current, I_{Ks} (Sanguinetti, Curran et al. 1996).

Though LQT1 is less deadly than other forms of LQTS, its lethality increases considerably under conditions of emotional/physical stress or exercise (Schwartz, Priori et al. 2001). These conditions accelerate pacing rate and activate the β -adrenergic response, which increases L-type Ca^{2+} current (I_{CaL}) (Nagykaldi, Kem et al. 1999; Antoons, Volders et al. 2007). I_{Ks} is also increased with pacing rate and β -adrenergic stimulation (Volders, Stengl et al. 2003). The additional outward current provided by I_{Ks} is required for proper repolarization in opposition to enhanced inward I_{CaL} . Conditions other than β -adrenergic stimulation which increase demand on I_{Ks} for proper repolarization include reduction in other repolarizing currents, especially the rapid delayed rectifier K^+ current, I_{Kr} . The inner pore lining of the hERG protein, forming I_{Kr} α -subunits, has uncommon affinity for a variety of clinically used pharmacological agents causing I_{Kr} block (Sanguinetti and Tristani-Firouzi 2006). Thus, the presence of β -adrenergic stimulation and drug-induced (acquired) LQTS compounds risk for LQT1 patients (Roden 2004) by challenging their genetically compromised repolarization reserve (Roden and Yang 2005).

β -adrenergic stimulation, consequent fast pacing, and/or drug block of I_{Kr} act as additional hits on top of congenital LQT1. As stated recently by Wilde, a double hit hurts more

(Wilde 2010). Multiple hits, each individually innocuous, may combine synergistically to create arrhythmia substrates.

An interesting case of silent LQT1 (Varro and Papp 2006) has been observed; missense mutation Q357R near the S6/C-terminal junction of Kv7.1 (Boulet, Raes et al. 2006). Q357R was discovered in a 40 year old female proband with a history of syncope. However, her measured QTc interval was within the normal range (0.43 seconds) (Chen, Zhang et al. 2003). The phenotype associated with silent mutations alone cannot always account for clinical outcomes. Arrhythmia is caused by multiple hits in silent LQTS. Motivated to explain this phenomenon, we investigated Q357R as an instructive example, using quantitative computational models in computer simulations.

Methods

Markov I_{Ks} and Human Ventricular Myocyte Models

Using experimental data from Boulet et al. (Boulet, Raes et al. 2006), human I_{Ks} models for wild-type (WT) and KCNQ1 mutant Q357R were developed. Action potential (AP) simulations were conducted using the O'Hara-Rudy dynamic (ORd) model for the human ventricular myocyte (described in detail in Chapter 2). Simulations were performed in two transmural cell types: epicardial (epi) and mid-myocardial (M). Simulations were also performed in a heterogeneous transmural wedge model from which we computed the pseudo-ECG as previously (Gima and Rudy 2002) mimicking experiments (Yan and Antzelevitch 1996). Further details are in the Chapter 3 Supplement.

β -Adrenergic Stimulation by Isoproterenol (ISO)

In order to determine β -adrenergic stimulation effects on I_{Ks} and changes to its role in the AP, we adapted the recent model by Heijman et al. (Heijman, Volders et al. 2011), including signaling cascade details from isoproterenol (ISO) application to compartmentalized PKA concentration and fractional phosphorylation of targets. Targets are: 1) I_{Ks} (Volders, Stengl et al. 2003), 2) fast Na^+ current (Baba, Dun et al. 2004) (fast I_{Na}), 3) I_{CaL} (Nagykaldi, Kem et al. 1999; Antoons, Volders et al. 2007), 4) Na^+/K^+ ATPase (Despa, Bossuyt et al. 2005) (I_{NaK}), 5) ultra-rapid K^+ current (Sridhar, da Cunha et al. 2007) (I_{Kur} , represented by K^+ background current, I_{Kb} in ORd), 6) ryanodine receptor (Ginsburg and Bers 2004) (RyR, J_{rel}), 7) SERCa pump (Odermatt, Taschner et al. 1996) (J_{up}), and 8) troponin (Robertson, Johnson et al. 1982) (trpn). Equations and details are in the Chapter 3 Supplement.

Results

Silent Mutant Q357R Kinetics and Behavior

Boulet et al. (Boulet, Raes et al. 2006) observed the following regarding Q357R compared to WT I_{Ks} channels: 1) steady state activation was shifted to more depolarized potentials, 2) activation was slowed, 3) deactivation was unchanged, 4) current was reduced, and 5) channel expression at the membrane was reduced (confocal image data; not quantified). We developed and tested mechanistic explanations for these observations using Markov models for I_{Ks} .

WT I_{Ks} was represented by a Markov model shown in Figure 3.01A, left (Silva and Rudy 2005). WT channels activate after relatively slow transitions from left to right (zone 2 closed states), followed by relatively rapid transitions from top to bottom (zone 1 closed states). Rapid activation from zone 1 states which are near to the open states provides an available reserve (Silva and Rudy 2005). By contrast, we hypothesized that Q357R mutant channels do not have available reserve. That is, Q357R channels activate with two identical relatively slow zone 2-like transitions. To implement this in the Markov model, we replaced top to bottom transition

rates (“g” and “d” in WT) with the left to right transition rates (“a” and “b” in WT, slightly modified to “A” and “B” in Q357R). In addition, compared to WT, the Q357R model includes depolarization directed shifts in the voltage dependence of transition rates. Conductance was reduced by 50% to represent the observed lower expression at the membrane. We tested whether these changes account for the differences in Q357R channel kinetics compared to WT, as observed by Boulet et al. (Boulet, Raes et al. 2006).

Heterotetramer Assembly and Function

In addition to the homozygous Q357R case, Boulet created the heterozygous case by injecting CHO-K1 cells with equal amount of Q357R and WT cDNA. Thus, when subunits come together to form the main components of I_{Ks} , the resulting channel could be heteromeric. There are six permutations of WT and Q357R subunit pairings that can form a channel tetramer (Figure 3.01B). We tested whether dominant negative mutant behavior could account for heterozygous (het) results. That is, the model assumes 1) WT and Q356R tetramer assembly is random, 2) presence of ≥ 1 Q357R subunit(s) slows gating for the entire channel, and 3) presence of ≥ 1 Q357R subunit(s) attenuates membrane expression. These assumptions (schematized in Figure 3.01B) allowed us to develop and test a putative model for the het case. Accordingly, het current calculation was the weighted average of computed Q357R and WT currents, added together in a 5:1 mixture.

Validation of WT, Q357R, and het models

Using the assumptions and corresponding models described, we were able to reproduce the kinetics of the Q357R and het currents compared to WT. Simulations are compared to experiments in Figure 3.02. Specifically, as determined by Boulet et al., for mutant current simulation compared to WT, 1) steady state activation was shifted to more depolarized potentials,

2) activation rate was slowed, 3) deactivation rate was unaffected, and 4) tail current was reduced. The correspondence between simulations and experiments (Figure 3.02) supports the hypothesis that Q357R kinetic changes can be considered as loss of available reserve and that Q357R has dominant negative consequences.

β -Adrenergic Stimulation

As in previous simulations(Heijman, Volders et al. 2011) and experiments(Volders, Stengl et al. 2003), human I_{Ks} was augmented by PKA in part due to accelerated activation. In brief, PKA phosphorylation was represented by the following changes to ORd: I_{CaL} conductance was larger and steady state activation, as well as inactivation, were shifted toward more hyperpolarized potentials; I_{Ks} activation transition rates were accelerated, and the conductance increased; I_{Kb} larger conductance; fast I_{Na} larger conductance and hyperpolarization directed shifts in steady state inactivation; J_{rel} larger amplitude and faster decay; J_{up} increase in Ca^{2+} affinity; troponin) decrease in Ca^{2+} affinity; I_{NaK} increase in Na^+ affinity. The changes were validated using available experiments (Figure 3.03A, details in the caption). With these changes, simulated AP duration (APD) with ISO (30 nM) relative to control was within the experimentally observed range for nonfailing human ventricular myocytes, measured using monophasic AP recordings at pacing cycle length CL = 500 ms (Shimizu et al.(Shimizu, Ohe et al. 1991)). The slope of APD restitution (S1 pacing CL = 400 ms, diastolic interval, DI, was relative to APD90) was more steep with ISO than without, as observed by Taggart et al. using monophasic AP recordings in nonfailing human hearts(Taggart, Sutton et al. 2003).

Figure 3.03B shows the simulated effects of 1 μ M ISO on the AP and PKA targets. As in nonfailing human ventricle experiments(Shimizu, Ohe et al. 1991), the AP upstroke and plateau were elevated and APD was slightly reduced with ISO (4 ms reduction, top row of Figure 3.03B). Increased I_{Na} caused the elevated upstroke. The plateau potential was elevated by I_{CaL} increase. AP duration shortening was caused by increase in I_{Ks} (and also I_{NaK} , I_{Kb}). Changes to Ca^{2+} fluxes and buffers led to an increase in the Ca^{2+} transient amplitude.

Phenotype is Silent under Basal Conditions

We tested the effect of replacing WT with Q357R or het I_{Ks} in different cell types at normal heart rate under basal conditions (CL = 1000 ms, no ISO, Figure 3.04). In epi cells, Q357R and het had very little effect on the APD. Prolongation was 14 and 12 ms, respectively. For M-cells, Q357R and het increased APD by 30 and 23 ms, respectively. These are relatively small increases ($\leq 8.5\%$ increase), though larger than for epi cells ($\leq 6.0\%$ increase). Minor AP prolongation under basal conditions duplicates the silent phenotype.

Occupancy in rapidly activating zone 1 closed states, near the open states, was lower for Q357R compared to WT in both epi and M cells. In M cells, zone 2 occupancy actually exceeded zone 1 occupancy (note crossover). These results indicate that mutant current reduction was due in part to altered channel kinetics, not expression differences alone. For simplicity, the intermediate zone occupancy for the weighted sum het case was not shown.

Multiple Hits Cause AP Prolongation and Early Afterdepolarizations (EADs)

In Figure 3.05, hits to the repolarization reserve were sequentially added in epi cell simulations. Layered hits were: 1) fast pacing (CL = 300 ms, second column), 2) β -adrenergic stimulation (1 μ M ISO dose, third column), and 3) partial I_{Kr} block (30% block, far right column). With fast pacing, Q357R and het prolonged the AP by only negligible amounts (8 and 7 ms, respectively). Note that the prolongation was less than observed at the slower resting heart rate (CL = 1000 ms, far left column, 14 and 12 ms prolongation for Q357R and het, respectively). This is accurate to the typical LQT1 clinical phenotype, where prolongation is more severe at slower rates, though arrhythmic events are associated with fast pacing (Schwartz, Priori et al. 2001; Roden 2008). When ISO was added at fast pacing, APD was increased by 27 and 21 ms for Q357R and het respectively, relative to WT. The increase due to ISO was 15 ms (Q357R)

and 10 ms (het) compared to without ISO. This was due to an increase in inward I_{CaL} , which was not countered sufficiently by the increase in compromised outward I_{Ks} . By contrast, ISO slightly decreased WT APD (4 ms, shown in Figure 3.03B).

Adding partial I_{Kr} block (30%) to ISO at fast rate caused WT APD to increase by 31 ms. For Q357R and het, APD was severely prolonged under these conditions; extended time at depolarized plateau voltages allowed I_{CaL} reactivation, triggering EADs (mechanism shown in Chapter 2). The Q357R and het APs following the EAD were shortened due to incompletely deactivated I_{Ks} during the short diastolic interval.

With fast pacing alone, the Q357R and het I_{Ks} changes had a strong effect in the M-cell (Chapter 3 Supplement Figure 3.S01). The first hit alone – fast pacing – caused substantial changes to the M-cell AP with the silent LQT mutation.

Silent Mutant I_{Ks} Gating Kinetics in Presence of Multiple Hits

At CL = 1000 ms, zone 1 occupancy was greater than zone 2 occupancy for both WT and Q357R cases (Figure 3.05, bottom row). Interestingly, after the first hit (fast pacing), zones 1 and 2 occupancy showed crossover for WT. For Q357R, there was no crossover. Instead, zone 2 occupancy always remained larger. Thus, mutant loss of I_{Ks} was due in part to kinetics differences (relative reduction in zone 1 available reserve (Silva and Rudy 2005)), not just reduced conductance. Occupancy of zone 1 available reserve states was always larger for WT than for Q357R. However, conductance loss was the more important consequence of the Q357R mutation. This was determined from simulations shown in Chapter 3 Supplement Figure 3.S02. We created two component mutants: one with altered conductance alone (mutant type A); another with altered gating kinetics alone (mutant type B).

Qualitative results for mutant types A and B were the same as for Q357R and het. That is, under basal conditions at normal heart rate, mutant AP prolongation was mild. When pacing rate was increased, the AP differences were reduced. Adding ISO and then ISO plus partial I_{Kr} block caused AP prolongation to become more dramatic for mutants A and B. As expected,

mutant type B (altered kinetics alone) showed reduced zone 1 occupancy compared to WT, while mutant type A (reduced conductance alone) showed zone occupancy similar to WT (not shown).

Reduced conductance alone caused EADs with ISO plus I_{Kr} block. However, altered kinetics alone (mutant type B) did not produce an EAD. These results signify that although the kinetics changes, which reduce the available reserve for Q357R, are important, the more severe consequence of Q357R is reduced channel expression at the membrane.

Mechanisms

In Figure 3.06, we investigated the mechanisms underlying previous results. Essentially, the function of human I_{Ks} is to be “augmentable” in proportion to need and prevent excessive AP prolongation (Roden 2004; Jost, Virag et al. 2005). This “repolarization reserve” function was quantified as the cumulative charge delivered by I_{Ks} . We also quantified cumulative charge delivered by I_{Kr} and other relevant ISO-dependent currents during the AP.

As the AP progresses, ISO-dependent depolarizing currents, fast I_{Na} and I_{CaL} , deliver inward current, resulting in a negative charge contribution ($Q_{Na}+Q_{CaL}$) with a rapid phase (I_{Na}) followed by a slower phase (I_{CaL}). Outward repolarizing currents counteract negative $Q_{Na}+Q_{CaL}$. Other than I_{Ks} , the ISO-dependent outward currents are I_{NaK} and I_{Kb} . Adding positive $Q_{NaK}+Q_{Kb}$ to $Q_{Na}+Q_{CaL}$ reduces the overall net negative charge. So does Q_{Kr} , and finally, also Q_{Ks} .

Under basal conditions at normal pacing rate, by the end of the AP, $Q_{NaK}+Q_{Kb}$ played a minor role in countering $Q_{Na}+Q_{CaL}$. Large outward Q_{Kr} provided the majority of positive charge, causing cumulative charge to cross the zero line. Additional effects of Q_{Ks} were negligibly small. Q_{Ks} became slightly larger with the hit of fast pacing, but was still small. Results for WT, Q357R, and het were indistinguishable under these conditions.

When ISO was applied in addition to fast pacing, Q_{Ks} contribution became pronounced. The cumulative charge from $Q_{NaK}+Q_{Kb}$ was also larger. However, negative $Q_{Na}+Q_{CaL}$ also increased. Even adding Q_{Kr} to $Q_{NaK}+Q_{Kb}$ was not enough to fully overcome cumulative $Q_{Na}+Q_{CaL}$, and cause a zero line crossing. Only with addition of Q_{Ks} , enhanced by ISO, was the zero line

crossed ensuring proper repolarization. With ISO, proper repolarization required much larger Q_{Ks} contribution than without ISO to counteract larger $Q_{Na}+Q_{CaL}$. For WT, ISO caused a remarkable 8-fold increase in Q_{Ks} . The increase was only ~5-fold for Q357R and het.

When partial I_{Kr} block was added to fast pacing and ISO application, the need for Q_{Ks} to help counteract $Q_{Na}+Q_{CaL}$ became even more critical. Only in the WT case did the contributions of outward $Q_{NaK}+Q_{Kb}$ + (reduced) Q_{Kr} + Q_{Ks} fully counteract inward $Q_{Na}+Q_{CaL}$ to cause a zero line crossing. Zero line crossings did not occur for the silent mutant cases.

Under normal and slow pacing conditions alone (no ISO, no I_{Kr} block), there were no important differences between WT and silent mutant types. It was loss of augmentability of silent mutant I_{Ks} , necessary in the presence of multiple hits, which caused AP prolongation and EADs.

The bar charts in Figure 3.06B show Q_{Ks} delivered at $t = 250$ ms when hits were layered for WT, Q357R, and het cases. Multiple hits increased Q_{Ks} ; for silent mutant cases, Q_{Ks} increase was smaller than for WT, illustrating reduced augmentability. For silent mutant cases, I_{Ks} augmentation was insufficient to prevent AP prolongation and EADs with ISO and with ISO plus I_{Kr} block, respectively.

Heterogeneous Transmural Wedge

To determine how the Q357R mutation affects repolarization in the more realistic context of heterogeneous tissue, we performed transmural wedge (pseudo-ECG) simulations (Figure 3.07). Under basal conditions, the silent mutation barely affected the QT interval (15 and 13 ms longer for Q357R and het, respectively, compared to WT). With ISO application, QT interval lengthening increased. Prolongation was 24 and 23 ms for Q357R and het relative to WT, and T-wave amplitude increased. When the second hit of partial I_{Kr} block was added, the degree of prolongation relative to WT became severe for Q357R and het (>80 ms). ISO plus I_{Kr} block-induced prolongation for Q357R and het was nearly twice (1.8 fold) that for WT. Dispersion of repolarization, measured as T-peak to T-end duration, was 2-fold larger for the mutant cases.

Onset of Emotional/Physical Stress or Exercise

Fatal arrhythmias in LQT1 typically occur at the transition to a state of emotional/physical stress (e.g. exercise onset(Schwartz, Priori et al. 2001) or diving into a pool(Roden 2008)). To simulate this arrhythmic scenario, we accelerated the pacing rate and applied a bolus of ISO (using the more mutation-sensitive M-cell, Figure 3.08). The pacing rate was doubled, from CL = 1000 to 500 ms, in a graded fashion over ~7 seconds, as observed in human subjects during exercise onset(Nobrega and Araujo 1993) (caused by rapid removal of vagal heart rate suppression(Robinson, Epstein et al. 1966)). For I_{CaL} , the fraction of channels phosphorylated by PKA increased more rapidly than for I_{Ks} (validation by Heijman et al.(Heijman, Volders et al. 2011)). Eventually, the resulting imbalance between inward and outward current ISO responses led to pronounced EADs in the silent mutant cases.

Discussion

Under basal conditions, as seen clinically(Chen, Zhang et al. 2003), simulated silent LQT current resulted in silent phenotype in human epi and M-cells and in the pseudo-ECG. As shown by Jost et al.(Jost, Virag et al. 2005), otherwise small human I_{Ks} is augmentable, helping to terminate the AP when repolarization reserve is compromised(Roden 2004). Also, Silva and Rudy simulations showed that I_{Ks} augmentation can overcome an EAD due to I_{Kr} block and restore normal repolarization(Silva and Rudy 2005). However, with silent mutant I_{Ks} , the combined presence of acceleration/fast pacing, β -adrenergic stimulation and I_{Kr} reduction caused LQTS phenotype to be revealed. Indeed, multiple hits hurt more(Wilde 2010).

In guinea pig simulations(Faber, Silva et al. 2007), arrhythmic Q357R and het phenotypes were revealed under basal conditions alone, without additional hits (EADs, Chapter 3 Supplement Figure 3.S03). The very different genotype-phenotype relationship in guinea pig versus human, caused by different ionic profile of their ventricular myocytes(Jost, Virag et al.

2004), highlights the fact that caution must be taken when extrapolating results and conclusions from animal experiments to human disease and its clinical manifestation.

Clinical Attributes Determine Protocols

Exercise and emotional/physical stress are arrhythmia triggers for LQT1(Schwartz, Priori et al. 2001). The hit of β -adrenergic stimulation is clinically important for discovery of silent LQT1 pathology(Vyas, Hejlik et al. 2006). Thus, we applied continuous pacing protocols (normal, fast and acceleration to fast rates; not pause protocols, appropriate for LQTS type-2(Tan, Bardai et al. 2006)) and applied β -adrenergic stimulation in the human myocyte model. Simulation results agreed with clinical observations. That is, fast or accelerating pacing with β -adrenergic stimulation caused robust AP shortening for WT, but not for the silent LQTS mutation Q357R. In the silent LQTS case, the additional repolarization hit of mild I_{Kr} block evinced EADs (not observed for WT). The additional hits differentiated mutant phenotypes from WT. In Figure 3.07, we showed that the reduced I_{Ks} augmentability determined silent mutant pathology. An important distinction is that reduced augmentability of I_{Ks} , not its mere reduction, causes substantial AP prolongation and EADs, revealing the LQT phenotype.

Dominant Negative Loss of Available Reserve

Missense mutation Q357R is an exchange of neutral glutamine for positively charged arginine at the junction between S6 and the C-terminus. Boulet experiments showed that due to the influence of the positive arginine, voltage dependent gating was affected(Boulet, Raes et al. 2006). We speculate that placement of the mutant arginine adjacent to the positive-negative charge interactions between S4 and S2 segments(Wu, Delaloye et al. 2010) could disrupt I_{Ks} gating. However, in the absence of further experimental analysis based on structural detail, it remains unclear exactly how this might amount to the observed slowing of activation.

Boulet et al.(Boulet, Raes et al. 2006) were not able to determine whether the dominant negative behavior of Q357R was due to trafficking or assembly abnormalities. Relying on the assumption of no assembly abnormalities (i.e. WT and Q356R tetramer assembly is random), simulations tested whether current reductions in the het case could be due to the same trafficking defect observed for homotetrameric Q357R. The reduction of expression at the membrane(Boulet, Raes et al. 2006) was represented by halved macroscopic conductance for Q357R and het I_{Ks} . That is, heterotetrameric channels were assumed identical to homotetrameric Q357R channels with respect to both kinetics and trafficking properties. With this dominant negative het model, we were able to accurately reproduce experimentally measured het behaviors (Figure 3.02). Thus, our theoretical analysis suggests that the dominant negative behavior for Q357R may be due to impaired trafficking alone, because simulations were accurate without including assembly abnormality. Additional experiments are needed to determine the basic mechanisms underlying trafficking defects (i.e. whether Q357R introduces a retainer motif).

Cell Type and Pacing Rate

Transmural cell types for the ORd human ventricular AP model were developed previously (see Chapter 2). Human data showed that I_{Ks} was 1.4 times larger in epi than in M-cells. However, as shown in Figure 3.04, M-cell I_{Ks} peak magnitude is actually larger than in epi cells. This is explained by the fact that the longer M-cell plateau allows additional time for smaller conductance I_{Ks} to become more fully activated. The longer M-cell AP is therefore more reliant on I_{Ks} than the epi cell to bring about complete repolarization. Thus, I_{Ks} loss of function in Q357R has greater consequence in M-cells. The fractional difference in I_{Ks} peak magnitude between cell types during fast pacing was even greater than at slower rates, indicating increased importance of I_{Ks} for successful M-cell repolarization at accelerated rates.

Limitations

The effects of β -adrenergic stimulation were validated on a target-by-target basis using the ORd human ventricular AP model. The overall result of β -adrenergic stimulation on the AP and APD restitution are in agreement with nonfailing human ventricular measurements by Shimizu et al.(Shimizu, Ohe et al. 1991) and Taggart et al.(Taggart, Sutton et al. 2003). However, the experimental dataset available for β -adrenergic effects on target proteins is nearly all from experiments performed in non-human mammals (dog)(Heijman, Volders et al. 2011); adapted here for human simulations.

The ORd model is essentially gender-neutral; validated based on more than 100 undiseased human hearts, of which 56% were male (see Chapter 2). Recent data showed K^+ current reduction in females compared to males(Gaborit, Varro et al. 2010). Female gender may be an additional risk factor for LQTS patients. The I_{Kr} block simulations presented relate to, but do not specifically account for, gender differences.

Figures

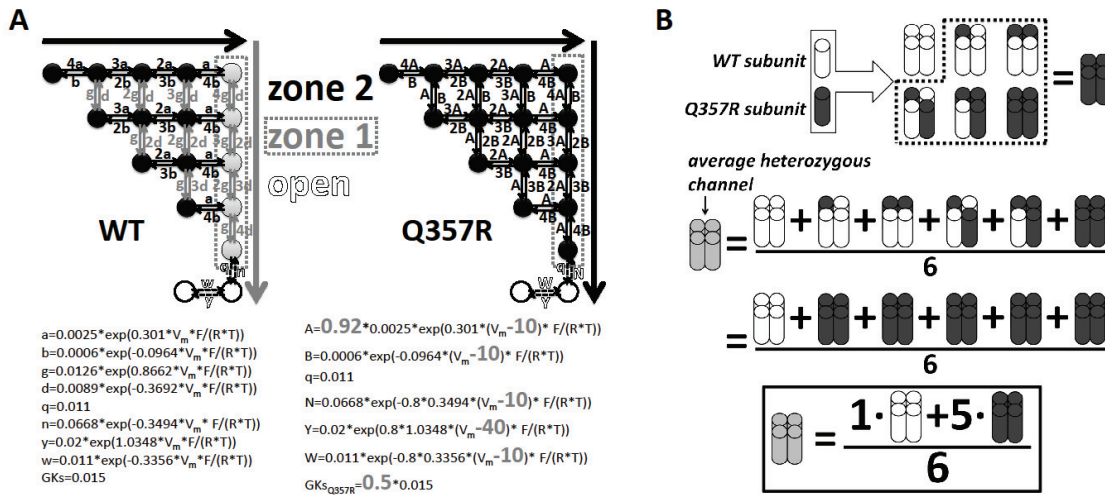


Figure 3.01. Markov models for I_{Ks} . A) Schematic diagrams and transition rate equations. The wild type (WT) model is on the left. The Q357R mutant model is on the right. Equations for each are below the diagrams (differences from WT are large bold gray text). The WT model activation, as proposed by Silva and Rudy (Silva and Rudy 2005), represents two voltage sensor transitions. First transitions from left to right (large black arrow), and second transitions are vertical from top to bottom (large gray arrow). Channel kinetic states are divided into two zones. Different from WT where zone 1 (gray circles) transitions are relatively rapid, for Q357R these transitions are the same as the slower zone 2 (black circles) transitions. B) WT (white) and Q357R (black) subunits combine to form six distinct tetramer permutations in the heterozygous (het) case (gray). In the model, we considered that the mutation was dominant negative. Thus, the behavior of the average het channel was determined by averaging the behavior of the permutations: $\text{het} = (1 \cdot \text{WT} + 5 \cdot \text{Q357R})/6$.

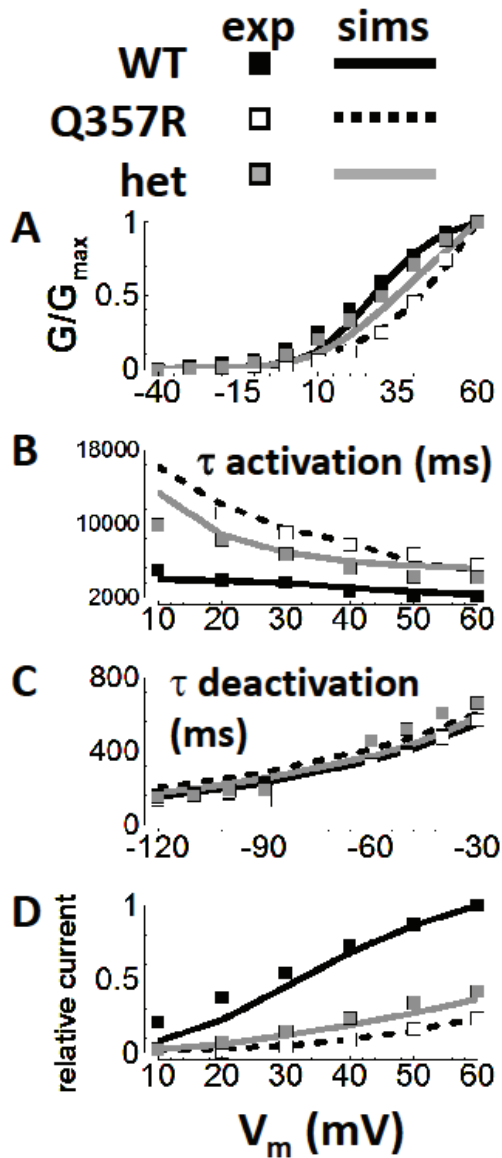


Figure 3.02. Validation for WT, Q357R, and het I_{K_S} . Experiments are from Boulet et al.(Boulet, Raes et al. 2006) (squares: WT is black, Q357R is white, and het is gray). Simulations are shown with lines (WT is black, Q357R is dashed black, and het is gray). A) Steady state activation of tail currents. B) Time constant for step current activation. C) Time constant for deactivation. D) Relative current after 5 second steps to potentials shown. Simulated protocols were the same as those used in Boulet experiments. exp - experiments; sims - simulations.

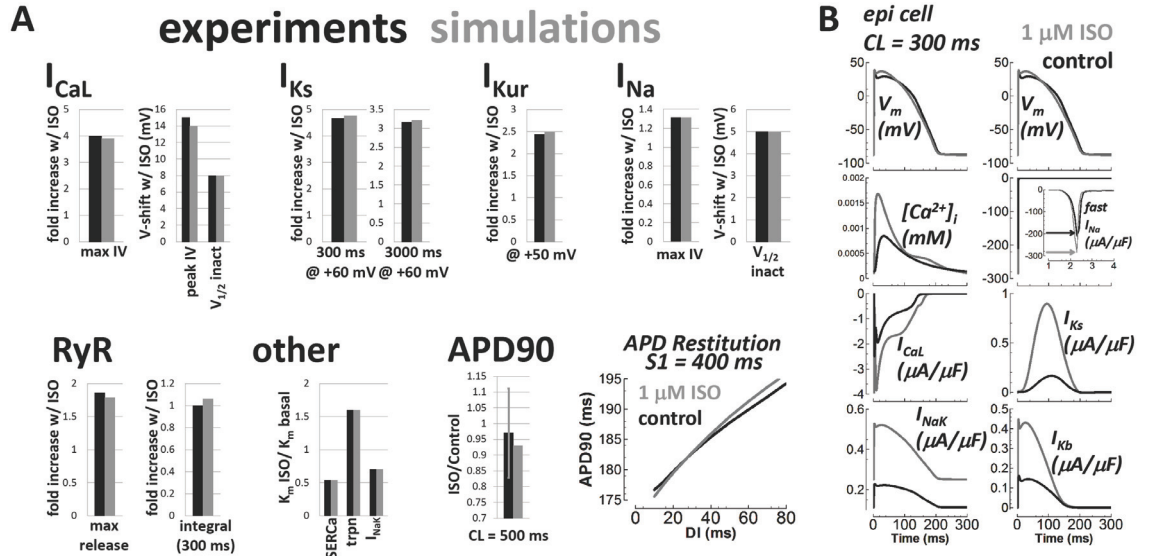


Figure 3.03. Validation of the effects of ISO on target channels and processes in human. A) Bar charts showing experimental data from various sources (black bars). Simulations using the ORd human myocyte model (details in Chapter 2) with the WT I_{Ks} Markov model are shown with gray bars. ISO effects were as follows. I_{CaL}) Maximum of the current-voltage curve (max IV) was increased, the voltage of the IV curve peak (peak IV) and the voltage of half maximum ($V_{1/2}$ inact) steady state inactivation were shifted toward more hyperpolarized potentials(Nagykaldi, Kem et al. 1999; Antoons, Volders et al. 2007). I_{Ks}) Step current at +60 mV was increased at both short (300 ms) and long (3000 ms) time points(Volders, Stengl et al. 2003). I_{Kur}) Current (step: +50 mV) was increased(Sridhar, da Cunha et al. 2007). I_{Na}) Maximum of the IV curve (max IV) was increased, and $V_{1/2}$ for steady state inactivation ($V_{1/2}$ inact) was shifted toward more hyperpolarized potentials(Baba, Dun et al. 2004). RyR) The maximum release flux (J_{rel} , max release) and the integral of release after 300 ms were increased(Ginsburg and Bers 2004). Other) Ca^{2+} affinity for SERCa flux (J_{up}) was increased(Odermatt, Taschner et al. 1996). It was decreased for trpn(Robertson, Johnson et al. 1982). Na^+ affinity for I_{NaK} was increased(Despa, Bossuyt et al. 2005). APD90) At CL = 500 ms, APD90 was decreased(Shimizu, Ohe et al. 1991). APD Restitution) The slope was increased(Taggart, Sutton et al. 2003). B) Simulated effects of ISO (1 μ M) on the human AP and targets are shown (gray lines) in comparison to control (no

ISO, black lines). From left to right, top to bottom: AP (repeated for timing purposes), myoplasmic Ca^{2+} concentration ($[\text{Ca}^{2+}]_i$), fast I_{Na} , I_{CaL} , I_{Ks} , I_{NaK} , and I_{Kb} . Epi cell paced at CL = 300 ms.

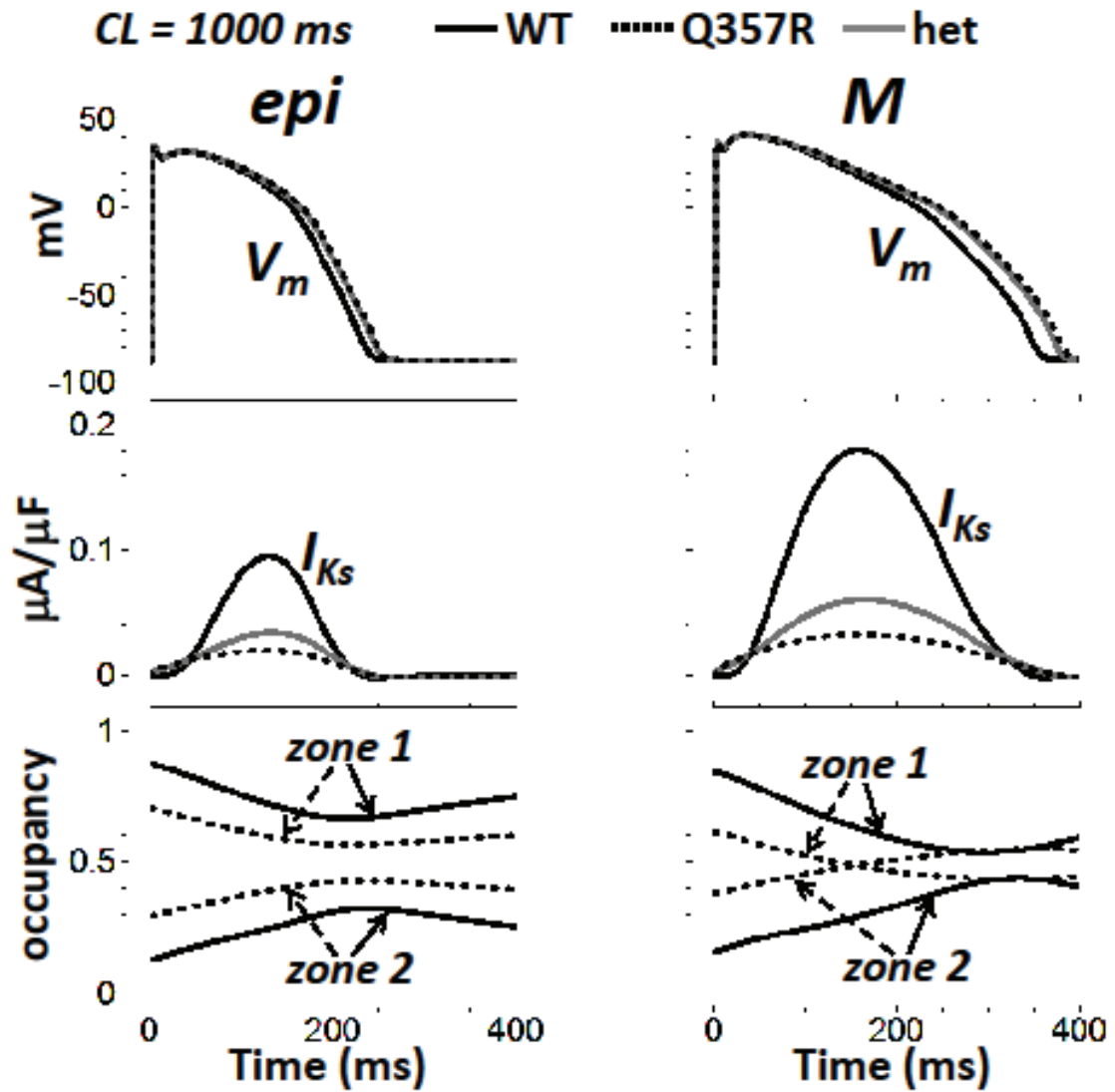


Figure 3.04. Transmural cell type dependence of the Q357R mutation at normal pacing rate (CL = 1000 ms). Results for WT, Q357R, and het are black, dashed black, and gray lines, respectively. Epi (left) versus M-cell (right) under basal conditions (no ISO). The top row shows APs. I_{Ks} is the middle row. Closed state zone occupancy is below.

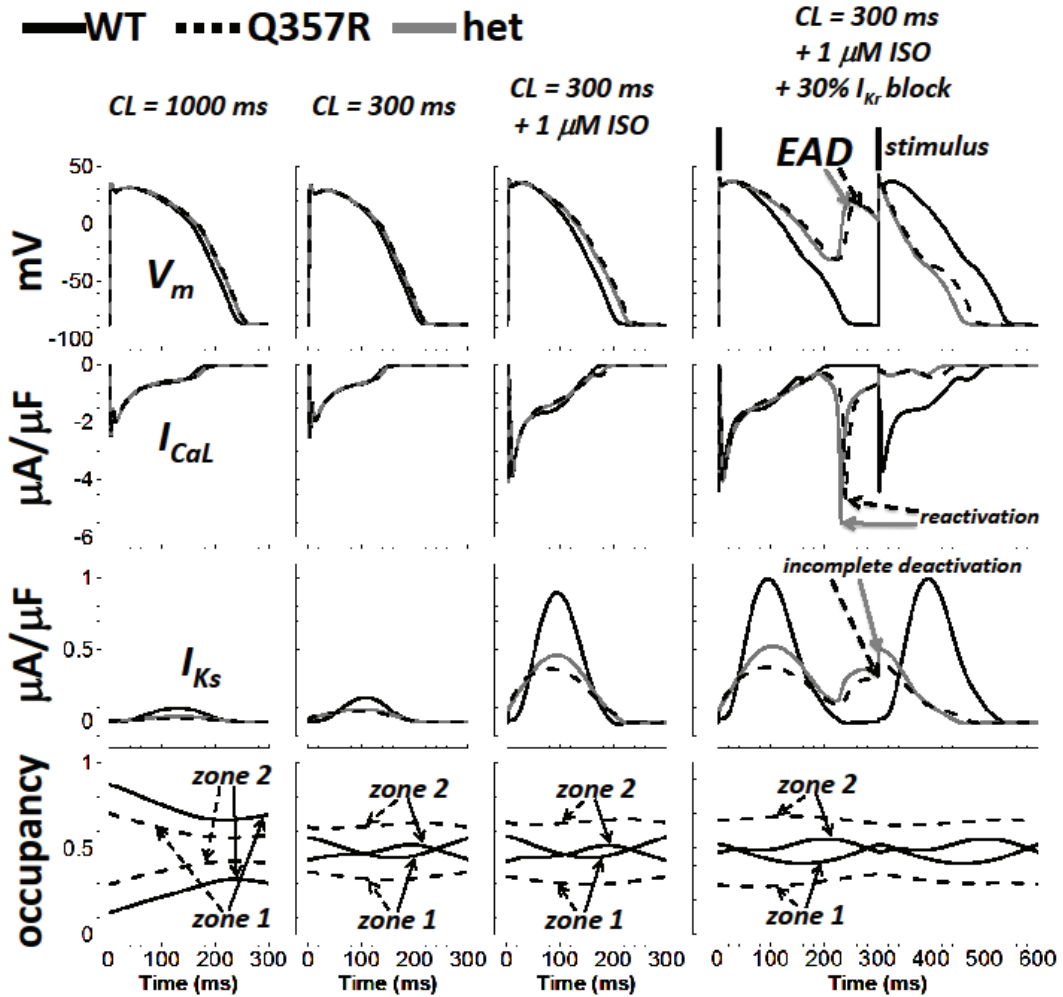


Figure 3.05. Effect of pacing, ISO and partial I_{Kr} block on the AP in epi cells. WT, Q357R, and het are black, dashed black, and gray lines, respectively. Descending rows show the AP, I_{CaL} , I_{Ks} , and closed state zone occupancy. Columns, from left to right, show the cases for normal pacing under basal conditions, fast pacing under basal conditions, fast pacing with application of ISO, and 30% I_{Kr} block in addition to fast pacing and ISO. EADs in the rightmost column (top row, arrows) were caused by I_{CaL} reactivation (second row, arrows) due to prolongation of AP plateau (deficient I_{Ks} , third row). The AP following the EAD is short, because of residual activation of I_{Ks} (incomplete deactivation, arrows).

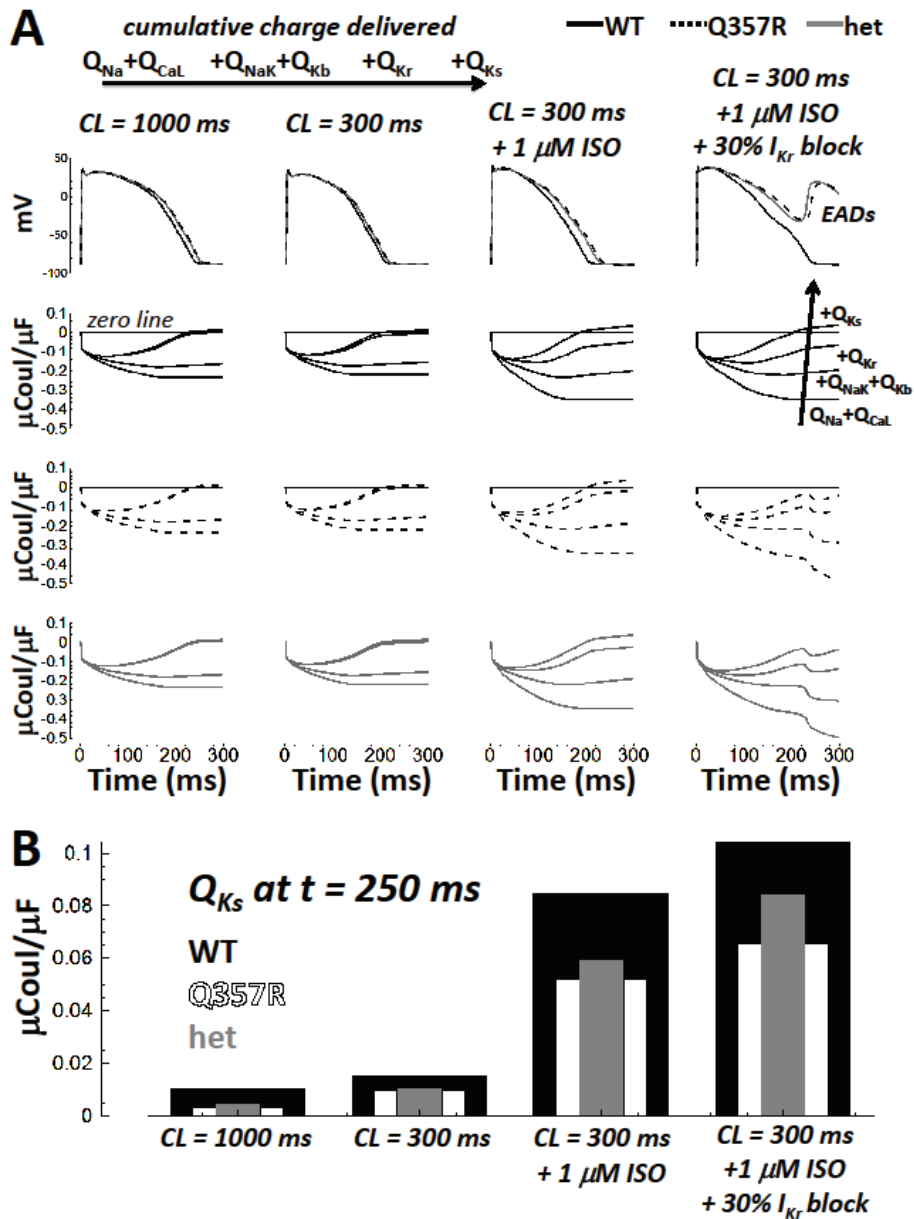


Figure 3.06. Mechanism by which layered hits reveal pathology. WT, Q357R, and het are black, dashed black, and gray lines, respectively. A) The top row shows APs. Bottom rows show cumulative charge delivered for ISO dependent currents and I_{Kr} : namely, $Q_{Na}+Q_{CaL}$, $Q_{NaK}+Q_{Kb}$, Q_{Kr} , and Q_{Ks} (order indicated by the arrow and labels). B) Charge contributed by I_{Ks} (Q_{Ks}) as hits were layered (left to right) for WT, Q357R and het.

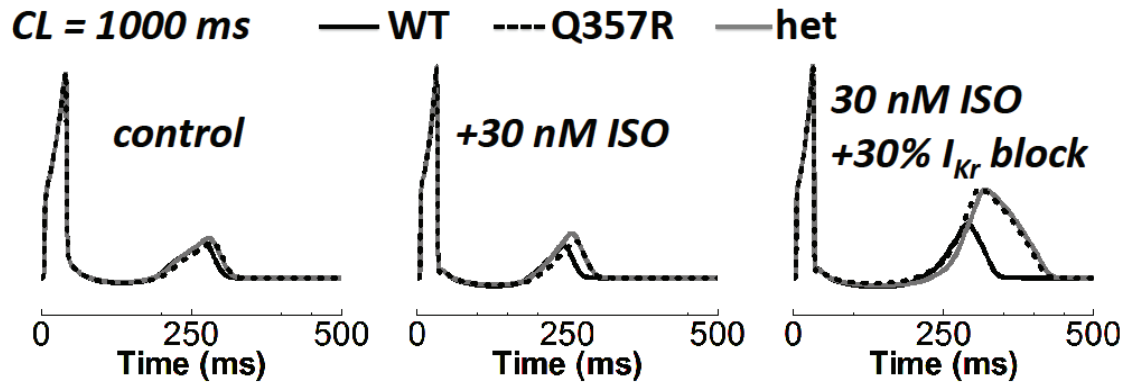


Figure 3.07. Effects of ISO and I_{Kr} reduction on the transmural wedge pseudo-ECG. Results for WT, Q357R, and het are black, dashed black, and gray lines, respectively. The simulated pseudo-ECG is plotted using a shared, normative scale. On the left, middle, and right the cases of control, ISO, and 30% I_{Kr} block plus ISO are shown.

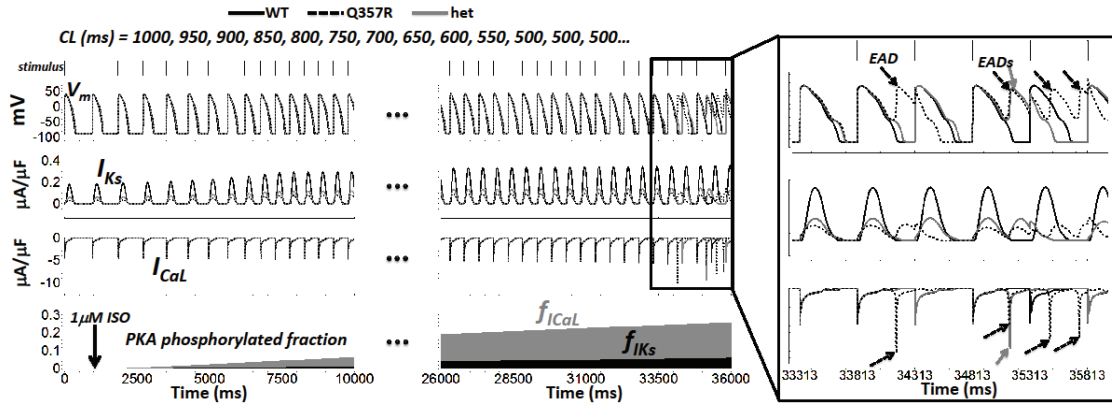


Figure 3.08. Emotional/physical stress or exercise onset. Simulations in M-cells with WT, Q357R, and het are black, dashed black, and gray lines, respectively. Shown from top to bottom: APs, I_{Ks} , I_{CaL} and fraction of I_{CaL} (f_{ICaL} , gray) and I_{Ks} (f_{IKs} , black) channels phosphorylated by PKA. Bars along the top show the accelerating stimulus delivery. An ISO bolus of 1 μM was applied at $t = 1000$ ms (arrow in bottom panel). Time axis is broken (dots), skipping an uneventful midsection. The box on the far right shows the final paced beats on expanded time scale. Arrows show EADs caused by I_{CaL} reactivation.

Chapter 3 Supplementary Material

Markov I_{Ks} Models

Using experimental data from Boulet et al. (Boulet, Raes et al. 2006), human I_{Ks} models for wild-type (WT) and KCNQ1 mutation Q357R were developed. Experiments conducted with the β -subunit KCNE1 included best represent I_{Ks} (Sanguinetti, Curran et al. 1996) and therefore were used for model development and validation. Boulet experiments were conducted at room temperature (20-23 °C). Accordingly, model validation was at room temperature (Figure 3.02). To create models representing behavior at body temperature (37 °C), we used $Q_{10} = 3.5$, as determined for I_{Ks} by Seeböhm et al. (Seeböhm, Lerche et al. 2001). Other simulations and the equations are at body temperature. The I_{Ks} Markov model paradigm was based on the work of Silva and Rudy (Silva and Rudy 2005).

Simulations Using the O'Hara-Rudy dynamic (ORd) Human Ventricular Model

AP simulations were conducted using the ORd model for the human ventricular myocyte (see Chapter 2). The Hodgkin-Huxley I_{Ks} formulation was replaced by Markov models for WT or mutant I_{Ks} . Simulations were performed in two transmural cell types: epicardial (epi) and mid-myocardial (M).

To measure the AP duration (APD), we used APD90, defined as the time between the maximum AP upstroke velocity and 90% repolarization. The duration of the pseudo-ECG (QT interval) was from the start of the stimulus to the time when the computed pseudo-ECG was less than 0.1% of its maximal value.

The simulated pseudo-ECG, though it carries a remarkable resemblance to the clinical ECG and simulates many of its properties, is not intended to represent the same physical entity. The choice to use the simulated transmural wedge was for its incorporation of coupled transmural

heterogeneity into the study, and its extensive use in experimental studies by Antzelevitch and others.

Equations for PKA Phosphorylation

As in Heijman et al.(Heijman, Volders et al. 2011), we used the population based approach to adjust currents and fluxes for PKA phosphorylation. That is, using the fraction of phosphorylated channels computed by the Heijman model of the β -adrenergic signaling pathway, we add the weighted sum of basal and phosphorylated currents or fluxes to obtain the total current or flux. As in experiments, pacing was to quasi-steady state (100 beats, using ORd 1Hz steady state initial conditions) in single cell simulations, and 10 beats in multicellular fiber simulations.

For guinea pig simulations, I_{Ks} conductance (GKs), was set so that WT I_{Ks} would give APDs that were the same as in the original model(Faber, Silva et al. 2007).

Below are equations for the parameters affected by PKA phosphorylation. Changes to ORd equations are highlighted using bold type.

L-type Ca^{2+} Current: I_{CaL}

$$d_{\infty,PKA} = \frac{1}{1 + \exp\left(\frac{-(V + 3.940 + \mathbf{16.0})}{4.230}\right)}$$

$$f_{\infty,PKA} = \frac{1}{1 + \exp\left(\frac{V + 19.58 + \mathbf{2.8}}{3.696}\right)}$$

$$P_{Ca,PKA} = \mathbf{2.5} \cdot P_{Ca}$$

$$\Psi_{Ca,PKA} = z_{Ca}^2 \cdot \frac{VF^2}{RT} \cdot \frac{y_{Cai} \cdot [Ca^{2+}]_{ss} \cdot \exp\left(\frac{z_{Ca}VF}{RT}\right) - y_{Cao} \cdot [Ca^{2+}]_o}{\exp\left(\frac{z_{Ca}VF}{RT}\right) - 1.0}$$

Where $[Ca^{2+}]_{ss}$ is given a 0.03 mM ceiling, representing flux saturation, to prevent non-physiological outward current during the peak of the $[Ca^{2+}]_{ss}$ spike.

Slow Delayed Rectifier K⁺ Current: I_{Ks}

$$a_{PKA} = 1.2 \cdot a$$

$$g_{PKA} = 1.2 \cdot g$$

$$GK_{SPKA} = 3.2 \cdot GK_S$$

Background K⁺ Current: I_{Kb}

$$GK_{bPKA} = 2.5 \cdot GK_b$$

Fast Na⁺ Current: I_{Na}

$$h_{\infty,PKA} = \frac{1}{1 + \exp\left(\frac{V + 82.9 + 5.0}{6.086}\right)}$$

$$h_{CaMK,\infty,PKA} = \frac{1}{1 + \exp\left(\frac{V + 89.1 + 5.0}{6.086}\right)}$$

$$GNa_{PKA} = 2.7 \cdot GNa$$

SR Ca²⁺ Release Flux, via Ryanodine Receptor: J_{rel}

$$\alpha_{rel,PKA} = 1.75 \cdot \alpha_{rel}$$

$$T_{rel,NP,PKA} = 0.5 \cdot T_{rel,NP}$$

$$\alpha_{rel,CaMK,PKA} = 1.75 \cdot \alpha_{rel,CaMK}$$

$$T_{rel,CaMK,PKA} = 0.5 \cdot T_{rel,CaMK}$$

Calcium Uptake via SERCa Pump: J_{up}

$$J_{up,NP,PKA} = \frac{0.004375 \cdot [Ca^{2+}]_i}{0.54 \cdot 0.00092 + [Ca^{2+}]_i}$$

$$J_{\text{up,CaMK,PKA}} = (1 + \overline{\Delta J_{\text{up,CaMK}}}) \cdot \frac{0.004375 \cdot [\text{Ca}^{2+}]_i}{0.54 \cdot (0.00092 - \overline{\Delta K_{\text{m,PLB}}}) + [\text{Ca}^{2+}]_i}$$

Troponin

$$K_{\text{m,TRPN,PKA}} = 1.6 \cdot K_{\text{m,TRPN}}$$

Na⁺/K⁺ ATPase Current: I_{NaK}

$$K_{\text{Nai,PKA}} = 0.7 \cdot K_{\text{Nai}}$$

Chapter 3 Supplementary Figures

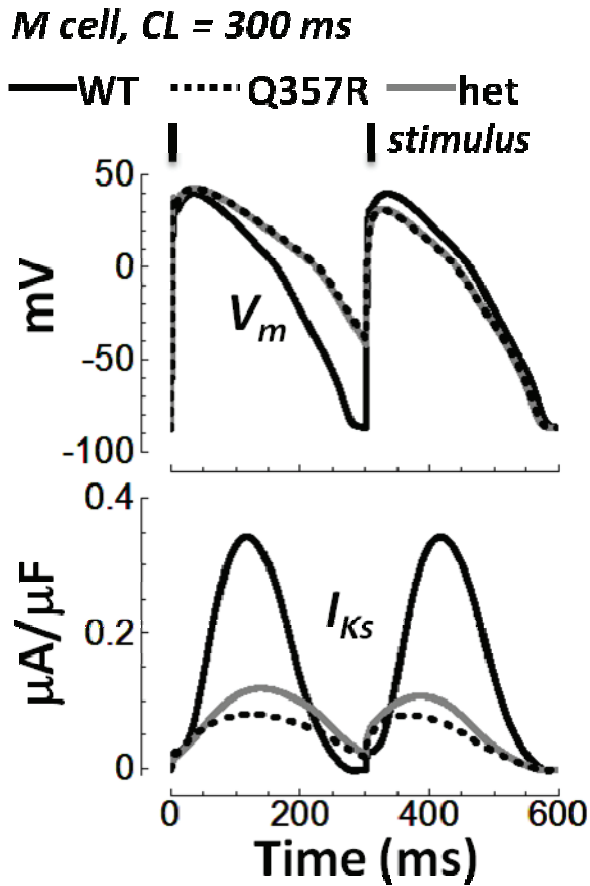


Figure 3.S01. M-cell dependence of the Q357R mutation at fast pacing rate (CL = 300 ms). Results for WT, Q357R and het are black, dashed black, and gray lines, respectively. The top row shows APs. I_{Ks} is below. For Q357R and het, the M-cell AP failed to repolarize before the next pacing stimulus (stimuli are indicated by black bars above the APs). Over the course of two consecutive beats, the AP eventually returned to rest. The first AP was severely prolonged, leaving the membrane voltage elevated at the start of the following beat. This left I_{Ks} slightly activated since deactivation requires time at resting potentials; consequently, repolarization was completed on the second beat. Thus, the first hit alone - fast pacing - proved challenging to the M-cell with silent LQTS mutation.

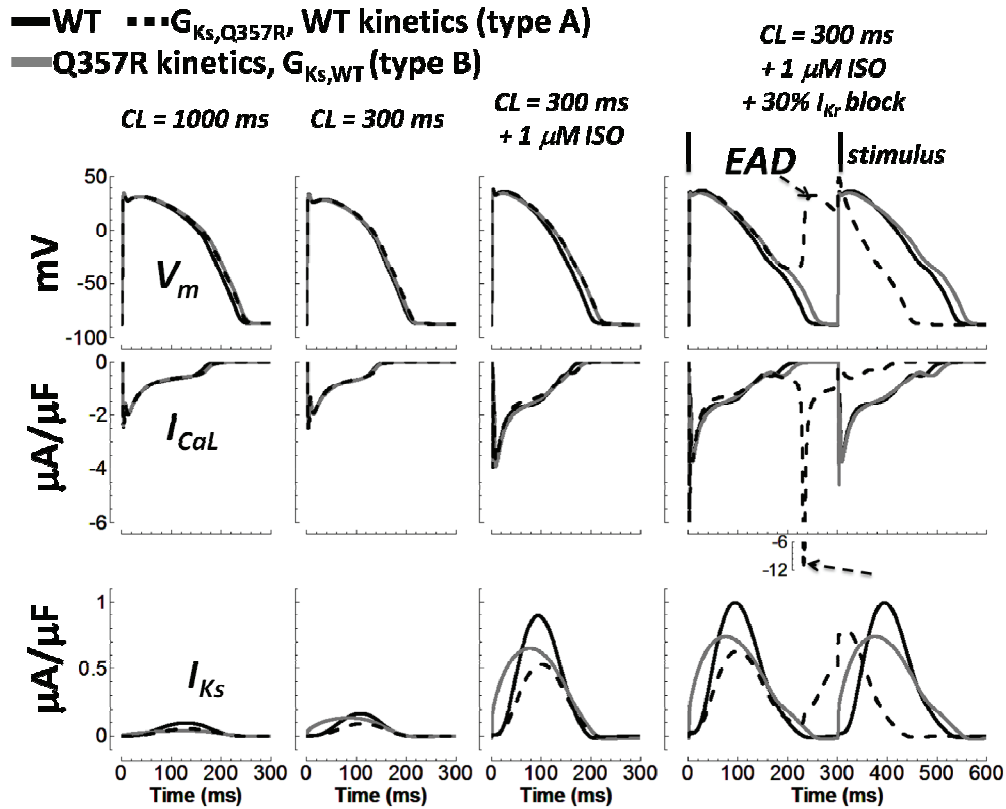


Figure 3.S02. Effect of reduced conductance versus kinetics changes in the silent mutation. The layout is the same as Figure 3.05. WT, WT with Q357R conductance (mutant type A), and Q357R with WT conductance (mutant type B) are black, dashed black, and gray lines, respectively. Descending rows show the AP, I_{CaL} , and I_{Ks} . The four columns, from left to right, show the cases for normal pacing under basal conditions, fast pacing under basal conditions, fast pacing with application of ISO, and 30% I_{Kr} block in addition to fast pacing and ISO. Hit of fast pacing with ISO caused AP prolongation relative to WT. With addition of I_{Kr} reduction, kinetics changes alone did not cause EAD formation, but reduced conductance alone did (arrows, rightmost column).

guinea pig, epi cell

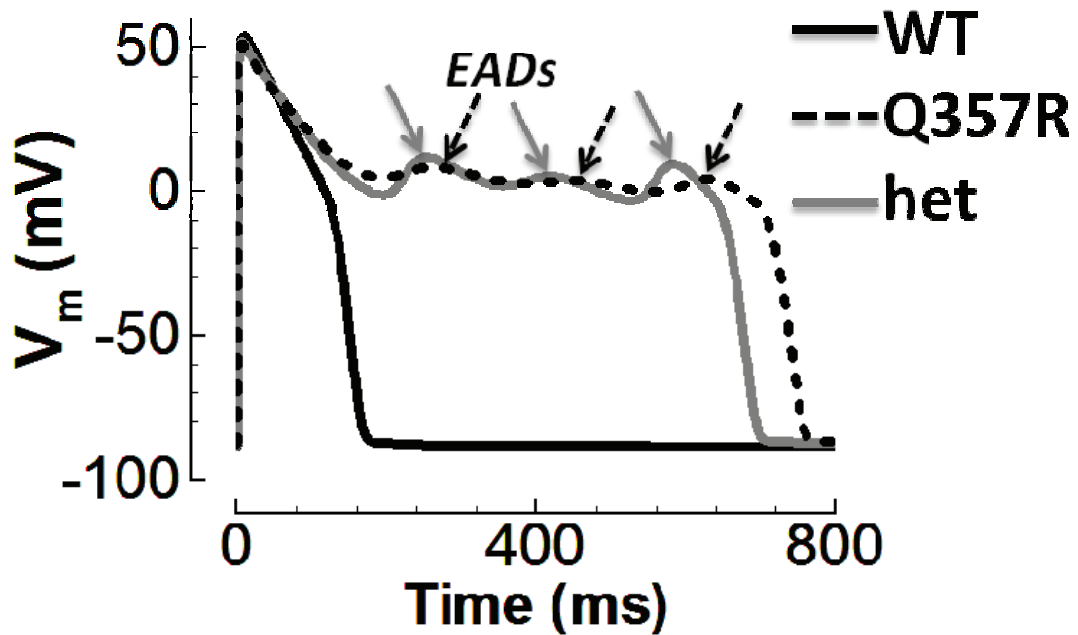


Figure 3.S03. In guinea pig simulations (Faber, Silva et al. 2007), Q357R mutation is not silent. WT, Q357R, and het are black, dashed black and gray lines, respectively. When Q357R and het channels were used for I_{Ks} in the guinea pig epi cell simulations, there was marked AP prolongation compared to WT and development of EADs, even at normal pacing (CL = 1000 ms), and without β -adrenergic stimulation or I_{Kr} -reduction. At fast pacing rate (CL = 300 ms, not shown), AP prolongation was also severe (not silent, but without EADs). Q357R APD was 41 ms or 35% longer than WT, and het APD was 30 ms or 25% longer than WT.

Chapter 4: Insights and Conclusions

The ORd model, validated and characterized in Chapter 2, and applied to investigate subclinical or “silent” LQT1 in Chapter 3, is a novel tool for testing hypotheses related to electrical phenomena in the human ventricular AP. In Chapter 2, the ORd model was compared with other human models. The ability of the ORd model to reproduce both EADs and beat to beat alternans under the appropriate physiological conditions is not matched by other models. When applied to subclinical LQT1, the appearance of EADs after multiple hits to the repolarization reserve was the mark of arrhythmogenic behavior.

Modeling studies which investigate arrhythmia mechanisms require that normal physiology be accurately represented. Extensive validation, using data from over 100 undiseased human hearts, confers accuracy to ORd and lends veracity to model predictions of mechanism. Moreover, in order to study the effects of specific channelopathy and/or application of drugs on arrhythmia, a model must first be capable of demonstrating relevant, dynamic arrhythmia markers at the single cell level, i.e. EADs or alternans. Thus, well designed ORd simulation studies may be capable of offering relatively plausible explanations regarding how a mutation can cause arrhythmia in human patients, and how drugs may ameliorate or exacerbate electro-pathology.

APD with Dynamic Pacing in Human

Previous simulation studies have addressed the topic of APD steady state rate dependence and restitution mechanisms in the human ventricle(Iyer, Mazhari et al. 2004; ten Tusscher, Noble et al. 2004; Ten Tusscher and Panfilov 2006; Grandi, Pasqualini et al. 2010). However, disagreement between models and lack of undiseased or nonfailing human data for model validation left opportunity for further investigation using the more realistic ORd model.

Similar to the Iyer-Winslow(Iyer, Mazhari et al. 2004) and GB models, Na^+ accumulation at fast pacing rate was a major cause of APD rate dependence at steady state in ORd. Unlike

the Iyer-Winslow model, Na^+ accumulation affected I_{NaK} in GB and ORd. In Iyer-Winslow simulations, the major consequence of Na^+ accumulation was to reverse I_{NaCa} , producing additional repolarizing current at fast rates. All models showed that at fast pacing rates, I_{Ks} deactivation was incomplete, providing more repolarizing current. However, this mechanism only played a significant role in the TP model (under basal conditions) because I_{Ks} density was extremely large. In the other models, I_{Ks} was essentially inconsequentially small under basal conditions.

Unlike in the other models, ORd includes late I_{Na} and accurate I_{CaL} . We hypothesized that these currents were secondary contributors to steady state rate dependence of the APD. A complex and subtle aspect of this finding was that roles for late I_{Na} and I_{CaL} were substantial only with Na^+ clamping, but not without. Na^+ clamping alone, and affects on I_{NaK} , failed to completely eliminate APD rate dependence, especially at faster pacing rates within the tachycardia range (CL = 300 to 700 ms). The hypothesized role for late I_{Na} and I_{CaL} could not have been determined using models other than ORd, which have no late I_{Na} and which include I_{CaL} inaccuracies due to lack of experimental validation. Although roles for Na^+ clamping, late I_{Na} and have I_{CaL} are interesting and plausible, these findings are model predictions. Experiments in human ventricular myocytes are needed to test whether the proposed mechanisms are indeed true.

Mechanisms responsible for causing APD restitution are not the same as those responsible for causing steady state rate dependence. Using ORd, we made the observation that ion accumulation had no effect on the former, while it played an important role in determining the latter. Other human ventricular simulation studies did not make this distinction. Again, ORd displayed nuanced mechanisms: late I_{Na} and I_{CaL} inactivation gating was the primary determinant of APD restitution, but not the only mechanism. At very short DIs, incomplete deactivation of I_{Kr} caused early spiking which helped to shorten the APD. Neither I_{Kr} spiking nor late I_{Na} and I_{CaL} effects were proposed as restitution mechanisms in other modeling studies. Other models, lacking late I_{Na} and proper I_{Kr} and I_{CaL} validation, could not have reached these conclusions. Experiments are needed to determine whether these ORd predictions are observed in reality.

As in any theoretical study, knowledge is gained whether predictions are shown to be correct or incorrect. Hopefully, our simulation findings will inspire and direct new experimental research for mechanisms of human ventricular APD dynamics. As described in Chapter 1, understanding such basic issues is a prerequisite for SCD therapy. Computer modeling tools and carefully designed simulation studies can contribute to this understanding.

Role of I_{Ks} in Human

As mentioned just previously, and in Chapter 3, the role of I_{Ks} in the human ventricle was found to be minimal under basal conditions (Jost, Virag et al. 2005). However, I_{Ks} is needed in the presence of β -adrenergic stimulation to help counter β -enhanced inward I_{CaL} . This idea was the basis for explaining potential arrhythmia susceptibility in subclinical, or “silent” LQT1.

With fast pacing and β -adrenergic stimulation, I_{Ks} increase was substantial for normal, WT current. The Q357R mutation in KCNQ1 reduced I_{Ks} . However, the reduction was inconsequential with respect to the AP unless fast pacing and β -adrenergic stimulation were applied. With the addition of partial I_{Kr} block, EADs appeared in mutant simulations but not for WT simulations, and the pathology of the otherwise silent phenotype was revealed.

Multiple hits to the repolarization reserve were required to evince arrhythmia for subclinical LQT1. In human, I_{Ks} is augmentable. It is a failsafe against extreme AP prolongation. Without a fully functioning augmentable safety, AP behavior remains normal only under basal conditions. However, after insults, the safety afforded by I_{Ks} became crucial to prevent arrhythmogenic AP prolongation leading to EADs. These results were presented as a clinically interesting and human ventricle specific example of ORd model application.

Transmural Heterogeneity

As shown by Yan, Antzelevitch and colleagues (Yan and Antzelevitch 1996; Yan and Antzelevitch 1998; Yan, Shimizu et al. 1998), transmural dispersion of repolarization in the heterogeneous wedge offers a rich substrate for the investigation and explanation of a variety of electrical phenotypes relevant to SCD arrhythmia. With these results in mind, transmural cell type models were made. We and others are interested in studying arrhythmia in cell types other than the endo cell (thoroughly validated in ORd using data from over 100 undiseased human hearts). To make the transmural models, we used available undiseased and nonfailing human experimental data (Drouin, Charpentier et al. 1995; Nabauer, Beuckelmann et al. 1996; Szabo, Szentandrassy et al. 2005; Gaborit, Le Bouter et al. 2007; Soltysinska, Olesen et al. 2009; Glukhov, Fedorov et al. 2010). Limitations of these methods were elaborated in Chapter 2. As shown in human ventricle experiments (Drouin, Charpentier et al. 1995; Glukhov, Fedorov et al. 2010), due to substantially longer APD of the M-cell, transmural types are important to consider. Simulations showed that in subclinical LQT1, the M-cell was more sensitive to channelopathy.

Development and validation of ventricular apex and base ORd models would be useful for whole heart simulation studies (e.g. (Bayer, Narayan et al.)). Some data are available for apico-basal gradients in mRNA from undiseased human ventricles (Szentandrassy, Banyasz et al. 2005). However, this dataset is less extensive than the transmural heterogeneity dataset, so we did not make use of it here.

Species Differences and the Need for an Accurate Human Specific Model

In Chapter 1, we showed AP rate dependence and its ionic mechanisms in human, dog, and guinea pig. We also compared the AP consequences of block of delayed rectifier K^+ currents, I_{Kr} and I_{Ks} , in these three species. The fact that ion channel currents in the human ventricular myocyte are different than those in dog or guinea pig is well established experimentally. However, the consequences of these species dependent differences in ion-channel profile in terms of whole cell electrophysiology are difficult to predict. The difficulty stems from the nonlinear and complex interrelatedness of the processes that determine whole-cell AP

behaviors. Thus, a quantitatively accurate computer model of the human case is needed. This reasoning motivated us to develop and use the ORd tool.

Species Differences in the Role of Delayed Rectifier K⁺ Currents

I_{Kr} and I_{Ks} are critical for AP repolarization in the ventricle. Mutations which reduce these currents cause the majority of cases of inherited long QT syndrome (Schwartz, Stramba-Badiale et al. 2009), leading to lethal arrhythmia (SCD). Acquired long QT syndrome, caused by block of I_{Kr} by any of a variety of pharmacological agents (including clinically useful non-cardiac drugs terfenadine, fexofenadine, risperidone, sertindole, erythromycin, and cisapride (Brown 2004)), can also lead to fatal arrhythmias (Roden 2004). Dangers of pro-arrhythmic effect and promiscuity of I_{Kr} block are so great that the FDA requires I_{Kr} block testing to prove drug safety. However, these safety experiments are generally not performed in human myocytes.

When I_{Kr} is blocked, I_{Ks} is indirectly affected (Jost, Virag et al. 2005) leading to loss of repolarization reserve (Roden and Yang 2005). The interplay elevates the importance of these currents in the ventricle. I_{Ks} is tightly regulated by the β -adrenergic pathway and plays a critical role in proper repolarization during exercise and emotional stress (e.g. Chapter 3 “silent” LQT1 mutation, and Volders et al. (Volders, Stengl et al. 2003)). At fast pacing rate, I_{Ks} participates in rate dependent adaptation by building available reserve (Silva and Rudy 2005). Inherited I_{Ks} loss is the single most common cause of long QT syndrome (Schwartz, Stramba-Badiale et al. 2009).

Delayed rectifier K⁺ current differences between species exist. Moreover, the role played by I_{Kr} and I_{Ks} is species dependent. It is in this context that these issues should be addressed quantitatively using accurate mathematical models. Jost et al. (Jost, Virag et al. 2004) showed comparative AP recordings from human, dog, and guinea pig ventricular myocytes in control and with specific drug block of I_{Kr} and I_{Ks} (by 1 mM E-4031 and 100 nM L-735,821, respectively), after long-term pacing at CL = 1000 ms. Important features of these experiments were reproduced by model simulations (Figure 1.01). The small amplitude of human and dog I_{Ks} is in sharp contrast to guinea pig ventricle, where I_{Ks} is the major repolarizing current. For human and dog (Decker,

Heijman et al. 2009), I_{Kr} is the most important repolarizing current. However, it is not the underlying mechanism of APD rate dependence (see below).

Species Differences in APD Steady State Rate Dependence

We found that APD shortening at fast rates was caused primarily by I_{NaK} increase secondary to intracellular $[Na^+]$ accumulation in human and in dog, but not guinea pig. Similar findings have been reported previously for human(Grandi, Pasqualini et al. 2010), dog(Decker, Heijman et al. 2009), and guinea pig(Faber and Rudy 2000) using other protocols. However, the direct and quantitative comparison between species presented yields novel insights. After phase-1 of the AP, the guinea pig AP can be approximated as a two current I_{CaL} - I_{Ks} model, while human and dog APs are more complicated. Human and dog repolarization is due mainly to I_{Kr} , which is not rate dependent (models and experiments(Jost, Acsai et al. 2009)). In these species, rate dependent I_{Ks} is small under basal conditions (no β -adrenergic stimulation) but builds an available repolarization reserve at fast rate(Silva and Rudy 2005). I_{NaK} is the major rate sensitive current in both human and dog. Outward I_{NaK} increases (secondary to $[Na^+]$ accumulation) at fast rate, shortening the APD. Compared to the human, the dog epi cell AP is further complicated by effects of large magnitude I_{to1} and I_{to2} , as described previously(Hund and Rudy 2004; Decker, Heijman et al. 2009).

The AP morphology and its rate dependence are determined by a time-dependent balance between inward and outward currents. For guinea pig, rate dependent changes in I_{NaK} secondary to $[Na^+]$ changes were large; indeed larger than for human or dog. However, as Faber and Rudy showed, there are even larger rate dependent changes in guinea pig I_{Ks} . In contrast to dog and human, this makes I_{NaK} only a minor participant in rate dependence of the guinea pig AP(Faber and Rudy 2000).

References

- Ackerman, M. J. and P. J. Mohler (2010). "Defining a new paradigm for human arrhythmia syndromes: phenotypic manifestations of gene mutations in ion channel- and transporter-associated proteins." Circ Res **107**(4): 457-65.
- Acsai, K., A. Kun, et al. (2007). "Effect of partial blockade of the Na(+)/Ca(2+)-exchanger on Ca(2+) handling in isolated rat ventricular myocytes." Eur J Pharmacol **576**(1-3): 1-6.
- Aggarwal, R. and P. A. Boyden (1995). "Diminished Ca²⁺ and Ba²⁺ currents in myocytes surviving in the epicardial border zone of the 5-day infarcted canine heart." Circ Res **77**(6): 1180-91.
- Akar, F. G., R. C. Wu, et al. (2004). "Phenotypic differences in transient outward K⁺ current of human and canine ventricular myocytes: insights into molecular composition of ventricular I_{to}." Am J Physiol Heart Circ Physiol **286**(2): H602-9.
- Amos, G. J., E. Wettwer, et al. (1996). "Differences between outward currents of human atrial and subepicardial ventricular myocytes." J Physiol **491** (Pt 1): 31-50.
- Antoons, G., P. G. Volders, et al. (2007). "Window Ca²⁺ current and its modulation by Ca²⁺ release in hypertrophied cardiac myocytes from dogs with chronic atrioventricular block." J Physiol **579**(Pt 1): 147-60.
- Baba, S., W. Dun, et al. (2004). "Can PKA activators rescue Na⁺ channel function in epicardial border zone cells that survive in the infarcted canine heart?" Cardiovasc Res **64**(2): 260-7.
- Bailly, P., M. Mouchoniere, et al. (1998). "Extracellular K⁺ dependence of inward rectification kinetics in human left ventricular cardiomyocytes." Circulation **98**(24): 2753-9.
- Bayer, J. D., S. M. Narayan, et al. "Rate-dependent action potential alternans in human heart failure implicates abnormal intracellular calcium handling." Heart Rhythm **7**(8): 1093-101.
- Bernabeu, M. O., R. Bordas, et al. (2009). "CHASTE: incorporating a novel multi-scale spatial and temporal algorithm into a large-scale open source library." Philos Transact A Math Phys Eng Sci **367**(1895): 1907-30.

- Blehschmidt, S., V. Haufe, et al. (2008). "Voltage-gated Na⁺ channel transcript patterns in the mammalian heart are species-dependent." Prog Biophys Mol Biol **98**(2-3): 309-18.
- Boulet, I. R., A. L. Raes, et al. (2006). "Functional effects of a KCNQ1 mutation associated with the long QT syndrome." Cardiovasc Res **70**(3): 466-74.
- Brown, A. M. (2004). "Drugs, hERG and sudden death." Cell Calcium **35**(6): 543-7.
- Chen, S., L. Zhang, et al. (2003). "KCNQ1 mutations in patients with a family history of lethal cardiac arrhythmias and sudden death." Clin Genet **63**(4): 273-82.
- Clancy, C. E. and Y. Rudy (1999). "Linking a genetic defect to its cellular phenotype in a cardiac arrhythmia." Nature **400**(6744): 566-9.
- Crampin, E. J. and N. P. Smith (2006). "A dynamic model of excitation-contraction coupling during acidosis in cardiac ventricular myocytes." Biophys J **90**(9): 3074-90.
- Cutler, M. J., X. Wan, et al. (2009). "Targeted SERCA2a gene expression identifies molecular mechanism and therapeutic target for arrhythmogenic cardiac alternans." Circ Arrhythm Electrophysiol **2**(6): 686-94.
- Decker, K. F., J. Heijman, et al. (2009). "Properties and ionic mechanisms of action potential adaptation, restitution, and accommodation in canine epicardium." Am J Physiol Heart Circ Physiol **296**(4): H1017-26.
- Despa, S., J. Bossuyt, et al. (2005). "Phospholemman-phosphorylation mediates the beta-adrenergic effects on Na/K pump function in cardiac myocytes." Circ Res **97**(3): 252-9.
- Dong, H., J. Dunn, et al. (2002). "Stoichiometry of the Cardiac Na⁺/Ca²⁺ exchanger NCX1.1 measured in transfected HEK cells." Biophys J **82**(4): 1943-52.
- Drouin, E., F. Charpentier, et al. (1995). "Electrophysiologic characteristics of cells spanning the left ventricular wall of human heart: evidence for presence of M cells." J Am Coll Cardiol **26**(1): 185-92.
- Dzhura, I., Y. Wu, et al. (2000). "Calmodulin kinase determines calcium-dependent facilitation of L-type calcium channels." Nat Cell Biol **2**(3): 173-7.
- Faber, G. M. and Y. Rudy (2000). "Action potential and contractility changes in [Na⁺]_i overloaded cardiac myocytes: a simulation study." Biophys J **78**(5): 2392-404.

- Faber, G. M., J. Silva, et al. (2007). "Kinetic properties of the cardiac L-type Ca²⁺ channel and its role in myocyte electrophysiology: a theoretical investigation." Biophys J **92**(5): 1522-43.
- Ferreira, G., J. Yi, et al. (1997). "Ion-dependent inactivation of barium current through L-type calcium channels." J Gen Physiol **109**(4): 449-61.
- Findlay, I. (2002). "Voltage- and cation-dependent inactivation of L-type Ca²⁺ channel currents in guinea-pig ventricular myocytes." J Physiol **541**(Pt 3): 731-40.
- Fink, M., D. Noble, et al. (2008). "Contributions of HERG K⁺ current to repolarization of the human ventricular action potential." Prog Biophys Mol Biol **96**(1-3): 357-76.
- Forbes, M. and N. Sperelakis (1989). Ultrastructure of Mammalian Cardiac Muscle. Physiology and Pathophysiology of the Heart. 2nd edition. N. Sperelakis. Boston, MA, Kluwer Academic: 3-41.
- Frank, J. S., G. Mottino, et al. (1992). "Distribution of the Na⁺-Ca²⁺ exchange protein in mammalian cardiac myocytes: an immunofluorescence and immunocolloidal gold-labeling study." J Cell Biol **117**(2): 337-45.
- Franz, M. R., C. D. Swerdlow, et al. (1988). "Cycle length dependence of human action potential duration in vivo. Effects of single extrastimuli, sudden sustained rate acceleration and deceleration, and different steady-state frequencies." J Clin Invest **82**(3): 972-9.
- Fujioka, Y., M. Komeda, et al. (2000). "Stoichiometry of Na⁺-Ca²⁺ exchange in inside-out patches excised from guinea-pig ventricular myocytes." J Physiol **523 Pt 2**: 339-51.
- Fulop, L., T. Banyasz, et al. (2004). "Reopening of L-type calcium channels in human ventricular myocytes during applied epicardial action potentials." Acta Physiol Scand **180**(1): 39-47.
- Gaborit, N., S. Le Bouter, et al. (2007). "Regional and Tissue Specific Transcript Signatures of Ion Channel Genes in the Non-diseased Human Heart." J Physiol.
- Gaborit, N., S. Le Bouter, et al. (2007). "Regional and tissue specific transcript signatures of ion channel genes in the non-diseased human heart." J Physiol **582**(Pt 2): 675-93.
- Gaborit, N., A. Varro, et al. (2010). "Gender-related differences in ion-channel and transporter subunit expression in non-diseased human hearts." J Mol Cell Cardiol **49**(4): 639-46.

- Gima, K. and Y. Rudy (2002). "Ionic current basis of electrocardiographic waveforms: a model study." Circ Res **90**(8): 889-96.
- Ginsburg, K. S. and D. M. Bers (2004). "Modulation of excitation-contraction coupling by isoproterenol in cardiomyocytes with controlled SR Ca²⁺ load and Ca²⁺ current trigger." J Physiol **556**(Pt 2): 463-80.
- Glukhov, A. V., V. V. Fedorov, et al. (2010). "Transmural dispersion of repolarization in failing and nonfailing human ventricle." Circ Res **106**(5): 981-91.
- Gogelein, H., A. Bruggemann, et al. (2000). "Inhibition of IKs channels by HMR 1556." Naunyn Schmiedebergs Arch Pharmacol **362**(6): 480-8.
- Grandi, E., S. Morotti, et al. (2010). "Interplay of voltage and Ca-dependent inactivation of L-type Ca current." Prog Biophys Mol Biol **103**(1): 44-50.
- Grandi, E., F. S. Pasqualini, et al. (2010). "A novel computational model of the human ventricular action potential and Ca transient." J Mol Cell Cardiol **48**(1): 112-21.
- Greenstein, J. L., R. Wu, et al. (2000). "Role of the calcium-independent transient outward current I_(to1) in shaping action potential morphology and duration." Circ Res **87**(11): 1026-33.
- Guo, D., Q. Liu, et al. (2011). "Electrophysiological properties of HBI-3000: a new antiarrhythmic agent with multiple-channel blocking properties in human ventricular myocytes." J Cardiovasc Pharmacol **57**(1): 79-85.
- Hanck, D. A. and M. F. Sheets (1992). "Time-dependent changes in kinetics of Na⁺ current in single canine cardiac Purkinje cells." Am J Physiol **262**(4 Pt 2): H1197-207.
- Hawkins, C., A. Xu, et al. (1994). "Sarcoplasmic reticulum calcium pump in cardiac and slow twitch skeletal muscle but not fast twitch skeletal muscle undergoes phosphorylation by endogenous and exogenous Ca²⁺/calmodulin-dependent protein kinase. Characterization of optimal conditions for calcium pump phosphorylation." J Biol Chem **269**(49): 31198-206.
- Heijman, J., P. G. Volders, et al. (2011). "Local control of beta-adrenergic stimulation: Effects on ventricular myocyte electrophysiology and Ca⁽²⁺⁾-transient." J Mol Cell Cardiol **50**: 863-871.

- Hodgkin, A. L. and A. F. Huxley (1952). "A quantitative description of membrane current and its application to conduction and excitation in nerve." J Physiol **117**(4): 500-44.
- Hund, T. J., J. P. Kucera, et al. (2001). "Ionic charge conservation and long-term steady state in the Luo-Rudy dynamic cell model." Biophys J **81**(6): 3324-31.
- Hund, T. J., N. F. Otani, et al. (2000). "Dynamics of action potential head-tail interaction during reentry in cardiac tissue: ionic mechanisms." Am J Physiol Heart Circ Physiol **279**(4): H1869-79.
- Hund, T. J. and Y. Rudy (2004). "Rate dependence and regulation of action potential and calcium transient in a canine cardiac ventricular cell model." Circulation **110**(20): 3168-74.
- Iribe, G., P. Kohl, et al. (2006). "Modulatory effect of calmodulin-dependent kinase II (CaMKII) on sarcoplasmic reticulum Ca²⁺ handling and interval-force relations: a modelling study." Philos Transact A Math Phys Eng Sci **364**(1842): 1107-33.
- Iyer, V., R. Mazhari, et al. (2004). "A computational model of the human left-ventricular epicardial myocyte." Biophys J **87**(3): 1507-25.
- Jansen, M. A., H. Shen, et al. (2003). "Energy requirements for the Na⁺ gradient in the oxygenated isolated heart: effect of changing the free energy of ATP hydrolysis." Am J Physiol Heart Circ Physiol **285**(6): H2437-45.
- Ji, Y., W. Zhao, et al. (2006). "Targeted inhibition of sarcoplasmic reticulum CaMKII activity results in alterations of Ca²⁺ homeostasis and cardiac contractility." Am J Physiol Heart Circ Physiol **290**(2): H599-606.
- Jost, N., K. Acsai, et al. (2009). "Contribution of I_{Kr} and I_{K1} to ventricular repolarization in canine and human myocytes: is there any influence of action potential duration?" Basic Res Cardiol **104**(1): 33-41.
- Jost, N., L. Virag, et al. (2004). "A kesoi egyeniranyito kaliumaram gyors (IKr) es lassu komponensenek (IKs) összehasonlito vizsgalata egeszseges emberi, kutya, nyul es tengerimalac kamrai szivizomsejteken." Cardiologia Hungarica **34**: 103-113.

- Jost, N., L. Virag, et al. (2005). "Restricting excessive cardiac action potential and QT prolongation: a vital role for IKs in human ventricular muscle." Circulation **112**(10): 1392-9.
- Kang, T. M. and D. W. Hilgemann (2004). "Multiple transport modes of the cardiac Na⁺/Ca²⁺ exchanger." Nature **427**(6974): 544-8.
- Keenan, N. L. and K. M. Shaw (2011). "Coronary heart disease and stroke deaths - United States, 2006." MMWR Surveill Summ **60 Suppl**: 62-6.
- Kieval, R. S., R. J. Bloch, et al. (1992). "Immunofluorescence localization of the Na-Ca exchanger in heart cells." Am J Physiol **263**(2 Pt 1): C545-50.
- Kim, J., S. Ghosh, et al. (2004). "Identification of the components controlling inactivation of voltage-gated Ca²⁺ channels." Neuron **41**(5): 745-54.
- King, E. L. and C. Altman (1956). "A Schematic Method of Deriving the Rate Laws for Enzyme-Catalyzed Reactions." J. Phys. Chem. **60**: 1375-1378.
- Kobayashi, T., Y. Yamada, et al. (2007). "Regulation of Cav1.2 current: interaction with intracellular molecules." J Pharmacol Sci **103**(4): 347-53.
- Koivumaki, J. T., T. Korhonen, et al. (2011). "Impact of sarcoplasmic reticulum calcium release on calcium dynamics and action potential morphology in human atrial myocytes: a computational study." PLoS Comput Biol **7**(1): e1001067.
- Koller, M. L., S. K. Maier, et al. (2005). "Altered dynamics of action potential restitution and alternans in humans with structural heart disease." Circulation **112**(11): 1542-8.
- Konarzewska, H., G. A. Peeters, et al. (1995). "Repolarizing K⁺ currents in nonfailing human hearts. Similarities between right septal subendocardial and left subepicardial ventricular myocytes." Circulation **92**(5): 1179-87.
- Li, G. R., J. Feng, et al. (1996). "Evidence for two components of delayed rectifier K⁺ current in human ventricular myocytes." Circ Res **78**(4): 689-96.
- Livshitz, L. and Y. Rudy (2009). "Uniqueness and stability of action potential models during rest, pacing, and conduction using problem-solving environment." Biophys J **97**(5): 1265-76.

- Livshitz, L. M. and Y. Rudy (2007). "Regulation of Ca²⁺ and electrical alternans in cardiac myocytes: role of CAMKII and repolarizing currents." Am J Physiol Heart Circ Physiol **292**(6): H2854-66.
- Luo, C. H. and Y. Rudy (1991). "A model of the ventricular cardiac action potential. Depolarization, repolarization, and their interaction." Circ Res **68**(6): 1501-26.
- Luo, C. H. and Y. Rudy (1994). "A dynamic model of the cardiac ventricular action potential. I. Simulations of ionic currents and concentration changes." Circ Res **74**(6): 1071-96.
- Magyar, J., N. Iost, et al. (2000). "Effects of endothelin-1 on calcium and potassium currents in undiseased human ventricular myocytes." Pflugers Arch **441**(1): 144-9.
- Mahajan, A., Y. Shiferaw, et al. (2008). "A rabbit ventricular action potential model replicating cardiac dynamics at rapid heart rates." Biophys J **94**(2): 392-410.
- Maltsev, V. A., H. N. Sabbah, et al. (1998). "Novel, ultraslow inactivating sodium current in human ventricular cardiomyocytes." Circulation **98**(23): 2545-52.
- Maltsev, V. A. and A. I. Undrovinas (2006). "A multi-modal composition of the late Na⁺ current in human ventricular cardiomyocytes." Cardiovasc Res **69**(1): 116-27.
- Myerburg, R. J. (2002). "Scientific gaps in the prediction and prevention of sudden cardiac death." J Cardiovasc Electrophysiol **13**(7): 709-23.
- Nabauer, M., D. J. Beuckelmann, et al. (1996). "Regional differences in current density and rate-dependent properties of the transient outward current in subepicardial and subendocardial myocytes of human left ventricle." Circulation **93**(1): 168-77.
- Nagatomo, T., Z. Fan, et al. (1998). "Temperature dependence of early and late currents in human cardiac wild-type and long Q-T DeltaKPQ Na⁺ channels." Am J Physiol **275**(6 Pt 2): H2016-24.
- Nagykaldi, Z., D. Kem, et al. (1999). "Canine ventricular myocyte beta2-adrenoceptors are not functionally coupled to L-type calcium current." J Cardiovasc Electrophysiol **10**(9): 1240-51.
- Nakajo, K., M. H. Ulbrich, et al. (2010). "Stoichiometry of the KCNQ1 - KCNE1 ion channel complex." Proc Natl Acad Sci U S A **107**(44): 18862-7.

- Nakao, M. and D. C. Gadsby (1989). "[Na] and [K] dependence of the Na/K pump current-voltage relationship in guinea pig ventricular myocytes." J Gen Physiol **94**(3): 539-65.
- Nanasi, P. P., S. Sarkozi, et al. (2000). "Biphasic effect of bimocloamol on calcium handling in mammalian ventricular myocardium." Br J Pharmacol **129**(7): 1405-12.
- Noble, D. (2007). "From the Hodgkin-Huxley axon to the virtual heart." J Physiol **580**(Pt 1): 15-22.
- Nobrega, A. C. and C. G. Araujo (1993). "Heart rate transient at the onset of active and passive dynamic exercise." Med Sci Sports Exerc **25**(1): 37-41.
- Odermatt, A., P. E. Taschner, et al. (1996). "Mutations in the gene-encoding SERCA1, the fast-twitch skeletal muscle sarcoplasmic reticulum Ca²⁺ ATPase, are associated with Brody disease." Nat Genet **14**(2): 191-4.
- Peterson, B. Z., C. D. DeMaria, et al. (1999). "Calmodulin is the Ca²⁺ sensor for Ca²⁺ - dependent inactivation of L-type calcium channels." Neuron **22**(3): 549-58.
- Pieske, B., L. S. Maier, et al. (2002). "Rate dependence of [Na⁺]_i and contractility in nonfailing and failing human myocardium." Circulation **106**(4): 447-53.
- Priebe, L. and D. J. Beuckelmann (1998). "Simulation study of cellular electric properties in heart failure." Circ Res **82**(11): 1206-23.
- Priori, S. G., P. J. Schwartz, et al. (2003). "Risk stratification in the long-QT syndrome." N Engl J Med **348**(19): 1866-74.
- Pueyo, E., Z. Husti, et al. (2010). "Mechanisms of ventricular rate adaptation as a predictor of arrhythmic risk." Am J Physiol Heart Circ Physiol **298**(5): H1577-87.
- Rajamani, S., C. L. Anderson, et al. (2006). "Specific serine proteases selectively damage KCNH2 (hERG1) potassium channels and I(Kr)." Am J Physiol Heart Circ Physiol **290**(3): H1278-88.
- Ramanathan, C., P. Jia, et al. (2006). "Activation and repolarization of the normal human heart under complete physiological conditions." Proc Natl Acad Sci U S A **103**(16): 6309-14.
- Robertson, S. P., J. D. Johnson, et al. (1982). "The effect of troponin I phosphorylation on the Ca²⁺-binding properties of the Ca²⁺-regulatory site of bovine cardiac troponin." J Biol Chem **257**(1): 260-3.

- Robinson, B. F., S. E. Epstein, et al. (1966). "Control of heart rate by the autonomic nervous system. Studies in man on the interrelation between baroreceptor mechanisms and exercise." Circ Res **19**(2): 400-11.
- Rocchetti, M., A. Besana, et al. (2001). "Rate dependency of delayed rectifier currents during the guinea-pig ventricular action potential." J Physiol **534**(Pt 3): 721-32.
- Roden, D. M. (2004). "Drug-induced prolongation of the QT interval." N Engl J Med **350**(10): 1013-22.
- Roden, D. M. (2008). "Clinical practice. Long-QT syndrome." N Engl J Med **358**(2): 169-76.
- Roden, D. M. and T. Yang (2005). "Protecting the heart against arrhythmias: potassium current physiology and repolarization reserve." Circulation **112**(10): 1376-8.
- Roger, V. L., A. S. Go, et al. (2011). "Heart disease and stroke statistics--2011 update: a report from the American Heart Association." Circulation **123**(4): e18-e209.
- Romero, L., E. Pueyo, et al. (2009). "Impact of ionic current variability on human ventricular cellular electrophysiology." Am J Physiol Heart Circ Physiol **297**(4): H1436-45.
- Rudy, Y., M. J. Ackerman, et al. (2008). "Systems approach to understanding electromechanical activity in the human heart: a national heart, lung, and blood institute workshop summary." Circulation **118**(11): 1202-11.
- Rudy, Y. and J. R. Silva (2006). "Computational biology in the study of cardiac ion channels and cell electrophysiology." Q Rev Biophys **39**(1): 57-116.
- Rush, S. and H. Larsen (1978). "A practical algorithm for solving dynamic membrane equations." IEEE Trans Biomed Eng **25**(4): 389-92.
- Sakakibara, Y., T. Furukawa, et al. (1993). "Sodium current in isolated human ventricular myocytes." Am J Physiol **265**(4 Pt 2): H1301-9.
- Sanguinetti, M. C., M. E. Curran, et al. (1996). "Coassembly of K(V)LQT1 and minK (IsK) proteins to form cardiac I(Ks) potassium channel." Nature **384**(6604): 80-3.
- Sanguinetti, M. C. and N. K. Jurkiewicz (1990). "Two components of cardiac delayed rectifier K⁺ current. Differential sensitivity to block by class III antiarrhythmic agents." J Gen Physiol **96**(1): 195-215.

- Sanguinetti, M. C. and M. Tristani-Firouzi (2006). "hERG potassium channels and cardiac arrhythmia." Nature **440**(7083): 463-9.
- Sarkar, A. X. and E. A. Sobie (2010). "Regression analysis for constraining free parameters in electrophysiological models of cardiac cells." PLoS Comput Biol **6**(9): e1000914.
- Saucerman, J. J., S. N. Healy, et al. (2004). "Proarrhythmic consequences of a KCNQ1 AKAP-binding domain mutation: computational models of whole cells and heterogeneous tissue." Circ Res **95**(12): 1216-24.
- Schmidt, U., R. J. Hajjar, et al. (1998). "Contribution of abnormal sarcoplasmic reticulum ATPase activity to systolic and diastolic dysfunction in human heart failure." J Mol Cell Cardiol **30**(10): 1929-37.
- Schwartz, P. J., S. G. Priori, et al. (2001). "Genotype-phenotype correlation in the long-QT syndrome: gene-specific triggers for life-threatening arrhythmias." Circulation **103**(1): 89-95.
- Schwartz, P. J., M. Stramba-Badiale, et al. (2009). "Prevalence of the congenital long-QT syndrome." Circulation **120**(18): 1761-7.
- Seebomh, G., C. Lerche, et al. (2001). "Dependence of I(Ks) biophysical properties on the expression system." Pflugers Arch **442**(6): 891-5.
- Shimizu, W. and C. Antzelevitch (1998). "Cellular basis for the ECG features of the LQT1 form of the long-QT syndrome: effects of beta-adrenergic agonists and antagonists and sodium channel blockers on transmural dispersion of repolarization and torsade de pointes." Circulation **98**(21): 2314-22.
- Shimizu, W., T. Ohe, et al. (1991). "Early afterdepolarizations induced by isoproterenol in patients with congenital long QT syndrome." Circulation **84**(5): 1915-23.
- Silva, J. and Y. Rudy (2005). "Subunit interaction determines IKs participation in cardiac repolarization and repolarization reserve." Circulation **112**(10): 1384-91.
- Smith, N. P. and E. J. Crampin (2004). "Development of models of active ion transport for whole-cell modelling: cardiac sodium-potassium pump as a case study." Prog Biophys Mol Biol **85**(2-3): 387-405.

- Sobie, E. A., L. S. Song, et al. (2005). "Local recovery of Ca²⁺ release in rat ventricular myocytes." J Physiol **565**(Pt 2): 441-7.
- Soltysinska, E., S. P. Olesen, et al. (2009). "Transmural expression of ion channels and transporters in human nondiseased and end-stage failing hearts." Pflugers Arch.
- Soltysinska, E., S. P. Olesen, et al. (2009). "Transmural expression of ion channels and transporters in human nondiseased and end-stage failing hearts." Pflugers Arch **459**(1): 11-23.
- Spach, M. S., J. F. Heidlage, et al. (2000). "Electrophysiological effects of remodeling cardiac gap junctions and cell size: experimental and model studies of normal cardiac growth." Circ Res **86**(3): 302-11.
- Sridhar, A., D. N. da Cunha, et al. (2007). "The plateau outward current in canine ventricle, sensitive to 4-aminopyridine, is a constitutive contributor to ventricular repolarization." Br J Pharmacol **152**(6): 870-9.
- Szabo, G., N. Szentandrassy, et al. (2005). "Asymmetrical distribution of ion channels in canine and human left-ventricular wall: epicardium versus midmyocardium." Pflugers Arch **450**(5): 307-16.
- Szabo, G., N. Szentandrassy, et al. (2005). "Asymmetrical distribution of ion channels in canine and human left-ventricular wall: epicardium versus midmyocardium." Pflugers Arch.
- Szentadrassy, N., T. Banyasz, et al. (2005). "Apico-basal inhomogeneity in distribution of ion channels in canine and human ventricular myocardium." Cardiovasc Res **65**(4): 851-60.
- Taggart, P., P. Sutton, et al. (2003). "Effect of adrenergic stimulation on action potential duration restitution in humans." Circulation **107**(2): 285-9.
- Taggart, P., P. M. Sutton, et al. (2000). "Inhomogeneous transmural conduction during early ischaemia in patients with coronary artery disease." J Mol Cell Cardiol **32**(4): 621-30.
- Tan, H. L., A. Bardai, et al. (2006). "Genotype-specific onset of arrhythmias in congenital long-QT syndrome: possible therapy implications." Circulation **114**(20): 2096-103.
- ten Tusscher, K. H., D. Noble, et al. (2004). "A model for human ventricular tissue." Am J Physiol Heart Circ Physiol **286**(4): H1573-89.

- Ten Tusscher, K. H. and A. V. Panfilov (2006). "Alternans and spiral breakup in a human ventricular tissue model." Am J Physiol Heart Circ Physiol **291**(3): H1088-100.
- Tessier, S., P. Karczewski, et al. (1999). "Regulation of the transient outward K(+) current by Ca(2+)/calmodulin-dependent protein kinases II in human atrial myocytes." Circ Res **85**(9): 810-9.
- Thomsen, M. B., P. G. Volders, et al. (2003). "Electrophysiological safety of sertindole in dogs with normal and remodeled hearts." J Pharmacol Exp Ther **307**(2): 776-84.
- Tohse, N. (1990). "Calcium-sensitive delayed rectifier potassium current in guinea pig ventricular cells." Am J Physiol **258**(4 Pt 2): H1200-7.
- Toyofuku, T., K. Curotto Kurzydowski, et al. (1994). "Identification of Ser38 as the site in cardiac sarcoplasmic reticulum Ca(2+)-ATPase that is phosphorylated by Ca²⁺/calmodulin-dependent protein kinase." J Biol Chem **269**(42): 26492-6.
- Varro, A. and J. G. Papp (2006). "Low penetrance, subclinical congenital LQTS: concealed LQTS or silent LQTS?" Cardiovasc Res **70**(3): 404-6.
- Victorri, B., A. Vinet, et al. (1985). "Numerical integration in the reconstruction of cardiac action potentials using Hodgkin-Huxley-type models." Comput Biomed Res **18**(1): 10-23.
- Virag, L., N. Iost, et al. (2001). "The slow component of the delayed rectifier potassium current in undiseased human ventricular myocytes." Cardiovasc Res **49**(4): 790-7.
- Viswanathan, P. C., R. M. Shaw, et al. (1999). "Effects of IKr and IKs heterogeneity on action potential duration and its rate dependence: a simulation study." Circulation **99**(18): 2466-74.
- Volders, P. G., M. Stengl, et al. (2003). "Probing the contribution of IKs to canine ventricular repolarization: key role for beta-adrenergic receptor stimulation." Circulation **107**(21): 2753-60.
- Vyas, H., J. Hejlik, et al. (2006). "Epinephrine QT stress testing in the evaluation of congenital long-QT syndrome: diagnostic accuracy of the paradoxical QT response." Circulation **113**(11): 1385-92.

- Wagner, S., N. Dybkova, et al. (2006). "Ca²⁺/calmodulin-dependent protein kinase II regulates cardiac Na⁺ channels." J Clin Invest **116**(12): 3127-38.
- Wagner, S., E. Hacker, et al. (2009). "Ca/calmodulin kinase II differentially modulates potassium currents." Circ Arrhythm Electrophysiol **2**(3): 285-94.
- Walsh, K. B., J. Zhang, et al. (2007). "Adenoviral-mediated expression of dihydropyridine-insensitive L-type calcium channels in cardiac ventricular myocytes and fibroblasts." Eur J Pharmacol **565**(1-3): 7-16.
- Wang, D. W., K. Yazawa, et al. (1997). "Pharmacological targeting of long QT mutant sodium channels." J Clin Invest **99**(7): 1714-20.
- Wang, Z. G., L. C. Pelletier, et al. (1990). "Effects of flecainide and quinidine on human atrial action potentials. Role of rate-dependence and comparison with guinea pig, rabbit, and dog tissues." Circulation **82**(1): 274-83.
- Warren, M., P. K. Guha, et al. (2003). "Blockade of the inward rectifying potassium current terminates ventricular fibrillation in the guinea pig heart." J Cardiovasc Electrophysiol **14**(6): 621-31.
- Watanabe, M., N. F. Otani, et al. (1995). "Biphasic restitution of action potential duration and complex dynamics in ventricular myocardium." Circ Res **76**(5): 915-21.
- Weber, C. R., V. Piacentino, 3rd, et al. (2003). "Dynamic regulation of sodium/calcium exchange function in human heart failure." Circulation **108**(18): 2224-9.
- Wehrens, X. H., S. E. Lehnart, et al. (2004). "Ca²⁺/calmodulin-dependent protein kinase II phosphorylation regulates the cardiac ryanodine receptor." Circ Res **94**(6): e61-70.
- Weiss, J. N., A. Garfinkel, et al. (2010). "Early afterdepolarizations and cardiac arrhythmias." Heart Rhythm **7**(12): 1891-9.
- Wilde, A. A. (2010). "Long QT syndrome: a double hit hurts more." Heart Rhythm **7**(10): 1419-20.
- Winslow, R. L., S. Cortassa, et al. "Integrative modeling of the cardiac ventricular myocyte." Wiley Interdiscip Rev Syst Biol Med.
- Winslow, R. L., S. Cortassa, et al. (2010). "Integrative modeling of the cardiac ventricular myocyte." Wiley Interdiscip Rev Syst Biol Med.

- Witcher, D. R., R. J. Kovacs, et al. (1991). "Unique phosphorylation site on the cardiac ryanodine receptor regulates calcium channel activity." J Biol Chem **266**(17): 11144-52.
- Wu, D., K. Delaloye, et al. (2010). "State-dependent electrostatic interactions of S4 arginines with E1 in S2 during Kv7.1 activation." J Gen Physiol **135**(6): 595-606.
- Yan, G. X. and C. Antzelevitch (1996). "Cellular basis for the electrocardiographic J wave." Circulation **93**(2): 372-9.
- Yan, G. X. and C. Antzelevitch (1998). "Cellular basis for the normal T wave and the electrocardiographic manifestations of the long-QT syndrome." Circulation **98**(18): 1928-36.
- Yan, G. X., W. Shimizu, et al. (1998). "Characteristics and distribution of M cells in arterially perfused canine left ventricular wedge preparations." Circulation **98**(18): 1921-7.
- Yuan, W. and D. M. Bers (1994). "Ca-dependent facilitation of cardiac Ca current is due to Ca-calmodulin-dependent protein kinase." Am J Physiol **267**(3 Pt 2): H982-93.
- Yue, D. T. and E. Marban (1988). "A novel cardiac potassium channel that is active and conductive at depolarized potentials." Pflugers Arch **413**(2): 127-33.
- Zeng, J., K. R. Laurita, et al. (1995). "Two components of the delayed rectifier K⁺ current in ventricular myocytes of the guinea pig type. Theoretical formulation and their role in repolarization." Circ Res **77**(1): 140-52.
- Zeng, J. and Y. Rudy (1995). "Early afterdepolarizations in cardiac myocytes: mechanism and rate dependence." Biophys J **68**(3): 949-64.
- Zheng, Z. J., J. B. Croft, et al. (2001). "Sudden cardiac death in the United States, 1989 to 1998." Circulation **104**(18): 2158-63.
- Zicha, S., I. Moss, et al. (2003). "Molecular basis of species-specific expression of repolarizing K⁺ currents in the heart." Am J Physiol Heart Circ Physiol **285**(4): H1641-9.